UiT
THE ARCTIC
UNIVERSITY
OF NORWAY

Faculty of Science and Technology
Department of Physics and Technology

Novel strategies for super-resolution fluorescence microscopy

Marcel Lahrberg

A dissertation for the degree of Philosophiae Doctor – October 2019

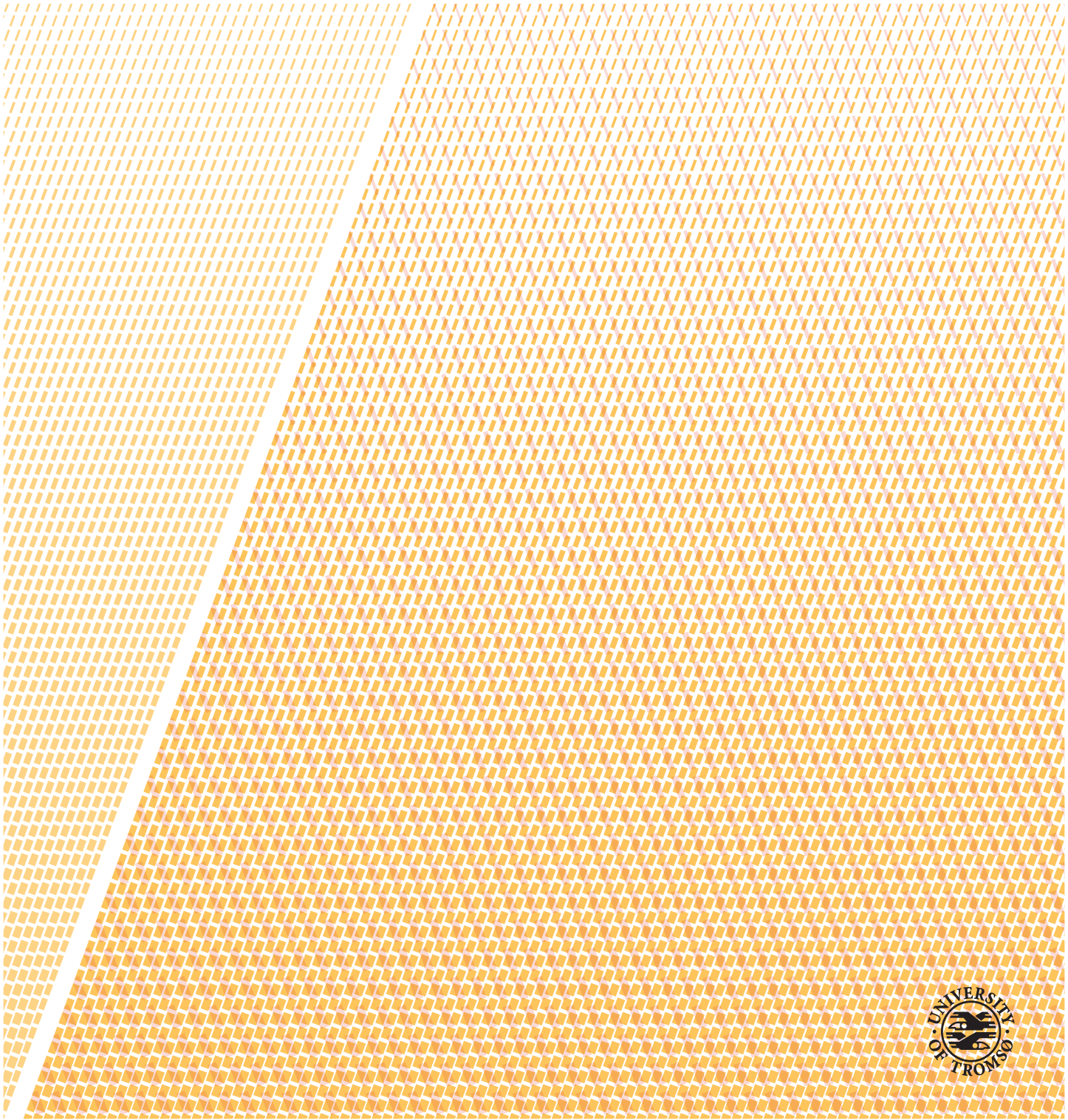

Abstract

Minimally invasive technologies to characterize the structure and functionality of biological samples on the cellular and molecular scale are fundamental to life sciences. Optical fluorescence imaging at visible wavelengths is able to acquire to do so. Due to the wavelike nature of light the maximum achievable resolution in conventional microscopy is limited by diffraction, about half the wavelength of the considered light. Although this diffraction limit is fundamental, techniques have been developed to perform imaging at a resolution of two to a hundred times better than this. All these techniques come with their specific benefits and trade-offs and the presented thesis seeks to make a contribution in the filed of super-resolution microscopy. Structured illumination microscopy (SIM) is a technique that improves the image resolution by acquiring images under non-planar illumination and subsequent image reconstruction. This image reconstruction requires a prior parameter estimation of the illumination pattern from the acquired data. A contribution to improve this parameter estimation is presented and demonstrated using simulation frame work developed for this purpose. It can be shown, that the deviation of the pattern parameters from their actual value can be reduced by up to 80 percent as compared to a more conventional method.

A common way to generate sinusoidal illumination patterns in SIM is to interfere two coherent beams of light using the the imaging objective lens, the epifluorescence configuration. Two new methods to generate those interference patterns, namely transillumination structured illumination microscopy (tSIM), and chip structured illumination microscopy (cSIM) are presented. A pattern generation independent of the objective lens allows to improve the space-bandwidth product (SBP) of SIM by increasing the resolution without sacrificing the field of view (FoV). Imaging simulations are shown to demonstrate this effect when mirrors are used to generate the patterns in tSIM. A theoretical improvement of the SBP of almost five times the SBP of a conventional setup is discussed. Instead of using mirrors, optical waveguides may be used to generate those illumination patterns a presented in cSIM. These waveguides are simulated using Comsol. Imaging is simulated according to expected pattern parameters and the improved imaging is illustrated.

The advantages of optical waveguides as discussion for cSIM are then examined regarding their implementation for light sheet fluorescence microscopy (LSFM). The image quality in wide-field imaging can be improved by limiting the sample illumination to the plane that is actually imaged. This is commonly done in LSFM and requires appropriate beam shaping. The implementation of different waveguide designs to perform beam shaping with waveguides are investigated performing a variety of simulations in Comsol. Chip based axicons with a total width of 20 micrometer and a wedge angle of six degree show to generate promising beam profiles with a propagation length of about 150 micrometer. A possible lattice light sheet generation using two counter propagation axicons is investigated as well as double axicon for the generation of bottle beams. The use of optical phased arrays to perform dynamic beam shaping using sets of 16 and 32 elements of 1 micrometer width is shown and the beam tilting and shifting capabilities a visible wavelength are presented.

Acknowledgements

This thesis was written as part of the Nanoscopy project grant 336716 of the European Research Council, granted to Balpreet Singh Ahluwalia.

I want thank the following people without whose help I could not have finished my work. Balpreet supervised my research and guided me along the way. I thank him for his encouraging enthusiasm and support, helping me to develop my skills as a scientist. Jean-Claude Tinguely co-supervised my work and did a great job helping me to keep things on track. Thanks to all my open-minded colleagues of the Optics group at UiT. They managed to provide a pleasant working atmosphere and made my decision to come to Tromsø worthwhile. Many thanks to Kedar Khare and Joby Joseph for hosting me at IIT Delhi.

Contents

List of Figures

List of Tables

List of Abbreviations

AFM atomic force microscopy

ATF amplitude transfer function

CAD computer-aided design

CLSM confocal laser scanning microscopy

COMSOL COMSOL Multiphysics

cSIM chip SIM

DFT discrete Fourier transform

DOF depth of field

dSTORM direct STORM

EM electromagnetic

ESI entropy-based SR imaging

FEM finite element method

FFT fast Fourier transform

FoV field of view

FPALM fluorescence photoactivation localization microscopy

GSD ground-state-depletion

HILO highly inclined and laminated optical sheet

LSFM light sheet fluorescence microscopy

NA numerical aperture

NSOM near-field scanning optical microscopy

OPA optical phased array

OPFOS orthogonal-plane fluorescence optical sectioning

OTF optical transfer function

PALM photo activated localization microscopy

PDE partial differential equation

PSF point spread function

QBB quasi-Bessel beam

RESOLFT reversible saturable optical fluorescence transitions

S/N signal-to-noise ratio

SBB superimposed Bessel beams

SBP space-bandwidth product

SEM scanning electron microscopy

SHIM scanning helium ion microscopy

Si_3N_4 silicon nitride

SIM structured illumination microscopy

SiO_2 silicon dioxide

SLM spatial light modulator

SMLM single-molecule localization microscopy

SNOM scanning near-field optical microscope

SOFI SR optical fluctuation imaging

SPIM selective plane illumination microscopy

SPM scanning probe microscopy

SR super-resolution

SR-SIM super-resolution structured illumination microscopy

SRM SR microscopy

STED stimulated emission depletion

STEM scanning TEM

STM scanning tunneling microscopy

STORM stochastic optical reconstruction microscopy

SWFM standing-wave fluorescence microscopy

Ta_2O_5 tantalum pentoxide

TE transverse electric

TEM transmission electon microscopy

TiO_2 titanium dioxide

TIR total internal reflection

TIRF TIR fluorescence

TM transverse magnetic

tSIM transillumination SIM

UV ultraviolet

WF wide-field

1

Introduction

Life sciences are driven by the understanding of biological cells and tissues on the microscopic scale. This includes the structure of fixed samples and even more, dynamic processes in living cells and tissues. Optical microscopy allows the study of phenomena on the level of biological cells, down to single molecules, that are invisible to the naked eye. It allows for a minimally invasive observation of a sample in conditions that preserve original functionality, even if the sample is taken out of its actual context; a tissue sample taken out of a liver for instance. In fluorescence microscopy the sample is treated prior to imaging, by labeling structures of interest specifically in order to allow for optical contrast in the first place in some cases, but at least to improve the contrast. This way, even dynamic processes may be observed, leading to fundamental understanding of relevant relationships in biology and medicine.

The contrast, that is provided by the microscope in the image is the vital point that decides what kind of conclusions can be made from what is presented in the image. Modern optics allows for almost aberration free imaging, leaving the resolution of the imaging system to be what limits the contrast. Whether or not two close objects are presented as two distinct entities in the image depends on the resolution of the microscope. A fundamental limit is based on the wavelike nature of light; the diffraction limit. A rough estimate of that limit is about half the wavelength of the light that is used to acquire the image. At a visible wavelength of 500 nm, two objects closer than 0.25 µm appear as one object in the image, they are not resolved.

Nowadays capabilities of modern optics, digital image processing and control of fluorophore chemistry allow for super-resolution (SR) fluorescence microscopy. It is optical microscopy that exploits the physical and chemical properties of fluorophores such that images with a resolution well beyond the diffraction limit are possible without sacrificing the minimally invasive nature of the technique. The 2014 Nobel Prize in Chemistry was awarded to Eric Betzig, William Moerner, and Stefan Hell, for their development of SR fluorescence imaging as it is among the most important tools in life sciences. These techniques are commercially available, thus making them more accessible to the scientific community. However, current implementations of SR fluorescence imaging techniques are still complex and exist in a variety of home-made setups, including obligatory image processing and image reconstruction algorithms. This yield a lot of opportunities to improve and develop fluorescence based high resolution imaging.

1.1 Thesis outline

The presented thesis is much focused on the development of the actual microscope and image processing that are ultimately used to image all sorts of samples. It is part of H2020 Nanoscopy project of the European Research Council. The overall goal of the project is to reduce the complexity of current SR microscopy (SRM) implementations using photonic-chip based waveguide technology. In chapter 2 fundamental principles of optics are introduced paving the way to understand the contributions described in the following chapters. Microscopy is motivated, its fundamental limitations are described and Fourier optics is introduced. Then the field of SRM is described with the aid of exemplary techniques in order to provide a general background. Light sheet fluorescence microscopy is introduced more specifically and the fundamental working principle of optical waveguides is described. In chapter 3 the theoretical background of structured illumination microscopy (SIM) is described in more detail and a framework for the required image reconstruction is presented. A contribution to parameter estimation, necessary for the successful image reconstruction in SIM is investigated and discussed. An improved way to perform parameter estimation is presented and examined using simulated data. It is attached as a peer reviewed article (paper 1) on page 47. Contributions to improve the space-bandwidth product (SBP) of SIM are presented in techniques as transillumination SIM (tSIM) and chip SIM (cSIM). tSIM is a novel implementation of SIM that uses a set of mirrors to perform pattern generation. Its potential advantage lies the increased field of view (FoV) that ultimately increases the SBP. Theoretical considerations are discussed and correspondign simulations regarding the imaging process are presented. A peer reviewed article (paper 2) is attached on page 65.

The approach of cSIM uses a set of photonic waveguides to generate well defined illumination patterns for SIM. The choice of waveguide material and geometry allow not only for a large FoV imaging area, but also for fine illumination patterns that potentially improve the resolution of SIM. The principle of such waveguide designs is investigated based on COMSOL Multiphysics (COMSOL) simulations, considerations regarding the imaging process are analyzed using a framework similar to the simulations in tSIM. An article under review (paper 3) is attached on page 89. Optical waveguides may not only provide evanescent field excitation in microscopy as in cSIM. In chapter 4, different waveguide designs are investigated regarding their usability with respect to free-space beam shaping. This covers static and dynamic beam shaping with applications like light sheet and lattice light sheet microscopy in mind. Different waveguide models are simulated using COMSOL. A peer reviewed article (paper 4) is attached on page 141. A conclusion and an outlook for future work are given in chapter 5.

1.2 Peer reviewed articles

- **Paper 1:** Marcel Lahrberg, Mandeep Singh, Kedar Khare, and Balpreet Singh Ahluwalia. “Accurate estimation of the illumination pattern’s orientation and wavelength in sinusoidal structured illumination microscopy.” In: *Appl. Opt.* 57.5 (Feb. 2018), pp. 1019–1025, published

- **Paper 2:** Joby Joseph, Faiz KP, Marcel Lahrberg, Jean-Claude Tinguely, and Balpreet Singh Ahluwalia. “Improving the space-bandwidth product of structured illumination microscopy using a transillumination configuration.” In: *Journal of Physics D: Applied Physics* (2019), accepted for publication

- **Paper 3:** Øystein I. Helle, Firehun T. Dullo, Marcel Lahrberg, Jean-Claude Tinguely, and Balpreet S. Ahluwalia. “Structured illumination microscopy using a photonic chip.” In: *arXiv preprint arXiv:1903.05512* (Mar. 2019), under revision

- **Paper 4:** Marcel Lahrberg, Firehun Tsige Dullo, and Balpreet Singh Ahluwalia. “Photonic-chip based free space beam shaping and steering for advanced optical microscopy application.” In: *OSA Continuum* 2.11 (2019), accepted for publication

2

Basic concepts

In this chapter, the basic concepts used throughout the thesis are discussed. First, the term of optical resolution is introduced. Microscopy is motivated as a solution to the limited optical resolution capabilities of the bare human eye. The theoretical imaging process in the microscope is described in terms of Fourier optics. A basic introduction to fluorescence microscopy is given as it is the imaging technique under consideration in the presented thesis. A general introduction to SR microscopy is given. Light sheet fluorescence microscopy (LSFM) is introduced as a motivation for the presented work on waveguide chips. Optical waveguides, especially planar waveguides, are introduced. A short description of the finite element method (FEM) is provided as it is used to perform simulations of different waveguide designs using COMSOL.

2.1 Human vision and the Rayleigh criterion

Humans use the naked eye for general visual perception of their environment. This applies to many kinds of objects of any scale. As for the scope of the presented thesis, the ability to observe small scale objects is of interest. The basis for this process is the image formation in the naked eye. In simple terms, light coming from an object falls onto the the eye's lens that creates an image on the retina. The ability of the human eye to discern two close objects instead of perceiving them as one object is termed resolution, with the resolution of the naked eye being limited due to its physiology and fundamental physical

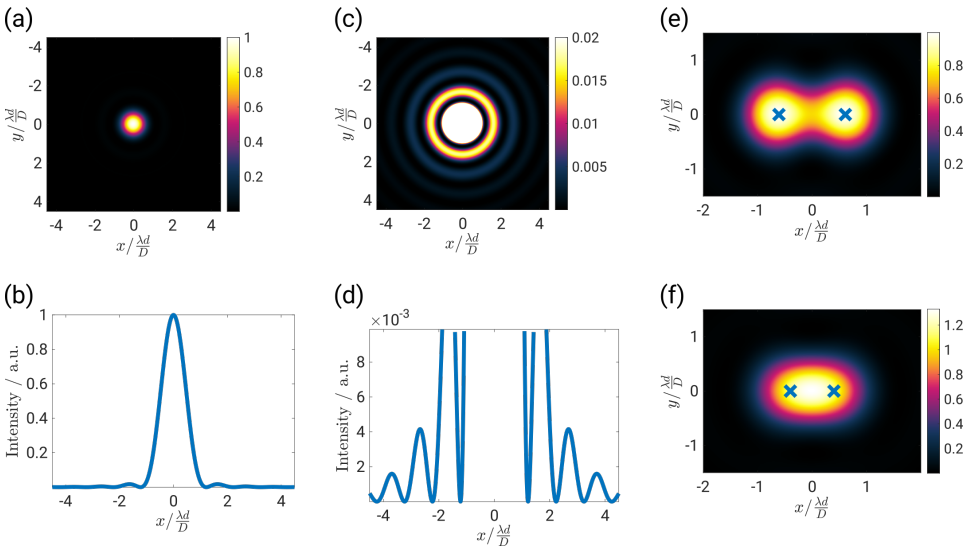

Figure 2.1: The image intensity (arbitrary units) of a point source is described by an Airy disk. **(a)** and **(b)** show the Airy disk and its profile respectively. The ring structures are more prominent when only displaying a fraction of the intensity range as in **(c)** with its profile in **(d)**. The image of an object consisting of two point sources will show a superposition of two Airy patterns (centers marked with "x"). **(e)** If their distance is large enough (here $1.22\lambda d/D$), two well separated patterns are visible; the two objects are resolved. **(f)** If the two objects are too close (here $0.80\lambda d/D$), no intensity dip is seen between the two Airy disks and the objects are not resolved in the image.

principles. This is the reason why optical instruments are developed and used in order to perform optical investigations on phenomena that are not resolved by the bare eye.

2.1.1 Spatial resolution of the human eye

The spatial resolution limit of the human eye is best explained by describing a visible object as a composition of light emitting points. An image of each of those points is generated on the retina by the eye's lens. The whole image of the object is made up in a pointillism style. As in actual pointillism, the points in the image are not points in the mathematical sense, they are patterns of finite extend, thus limiting the spatial resolution of the bare eye.

Due to the wavelike nature of light and the circular aperture of the imaging lens, light emerging from a point source will generate a spot of light intensity in the image plane, the so-called Airy disk (see Figure 2.1). This phenomenon was first described in 1828 by John Herschel [53]. In 1835, George Biddell Airy

gave its first theoretical description [6]. Depending on the superposition of the Airy disks of two point sources, these point sources are said to be resolved if an intensity dip in between them can be identified as described in Figure 2.1. This is reflected in the Rayleigh criterion of resolution [37]. It states that the resolution limit for two point sources is reached when the center of the Airy pattern of one point source falls on the first minimum of the Airy pattern of the second point source. This resolution limit is expressed as

$$\delta = 0.61 \frac{\lambda}{\sin\left(\frac{\alpha}{2}\right)} = 1.22 \frac{\lambda d}{D}. \tag{2.1}$$

Here, δ is the minimum distance between the two point sources at which they are resolved according to the given resolution criterion, 0.61 is a fixed factor given by the Airy pattern resulting from a circular aperture, λ is the wavelength of light under consideration, α is the acceptance angle of the lens, d is the distance of the object from the aperture and D is the size of the aperture. A related term is the angle of resolution that defines a minimum angular distance of two objects for them to be resolved;

$$\theta = \frac{1.22\lambda}{D}. \tag{2.2}$$

Two close objects, here consisting of a point source each, can be resolved when the conditions in eqs. (2.1) and (2.2) are fulfilled. Looking at Equation (2.2), it is favorable to get the object as close to the eye as possible in order to increase the resolution. This has its natural limit in the eye's ability to accommodate, to generate an image on the retina according to geometrical optics. The said near(est) point is age dependent and a standard value is $d = 0.25\,\mathrm{m}$ ([107], Table 9-20-2).

Under well-lit conditions, the pupil size of the eye is given as $D = 4\,\mathrm{mm}$ [107]. In this case, eq. (2.1) predicts that two point objects emitting at a wavelength of $\lambda = 550\,\mathrm{nm}$ must have a minimum distance of $\delta = 42\,\mu\mathrm{m}$ to be resolved by the eye. Since the pupil size increases with decreased brightness, the maximum size of the pupil can reach a value of $D = 8\,\mathrm{mm}$ which results in $\delta = 21\,\mu\mathrm{m}$. These values are based on the assumption that the object is brought to the eye as close as possible ($d = 0.25\,\mathrm{m}$).

In order for the observer to resolve small details on objects, optical instruments ranging from simple magnifying glasses to compound microscopes are employed to generate an image of the object. This image has the property to display details with a larger angular distance at a given viewing distance than achievable by looking at the object with the bare eye. The ratio between the angular size of the object as seen through the instrument to the angular size given by the bare eye is the magnification.

2.2 The Abbe resolution limit

Before going into a more detailed description of optical resolution with respect to microscopy the Abbe resolution limit, another widely used term, is discussed. In the original publication [1], this resolution limit was specifically derived for a microscope considering a thin sample. In optical microscopy, the Abbe resolution limit of the system is the resolution that may be reached if any kind of misalignment and aberration can be ruled out. In order to understand the underlying idea, here a periodic sample (a grating) is illuminated with a plane wave and a lens is used to generate an image of the sample. Depending on the resolution limit of the setup, the grating structure may be resolved in the generated image.

Given a transmissive diffraction grating (see fig. 2.2) with a grating spacing d between its slits, a monochromatic plane wave of wavelength λ incident on the grating at an angle θ_i will generate intensity maxima due to constructive interference at an angle θ_m behind the grating. These interference maxima appear due to the different path lengths and according phase differences of light from different slits reaching the same spot on the aperture. They repeat whenever the angle dependent path difference is a multiple (integer m) of the wavelength; the different so-called diffraction orders. The relation between the angles and the wavelength is given by

$$d\,(\sin\theta_i - \sin\theta_m) = m\lambda. \tag{2.3}$$

The smaller the grating period, the larger the first order diffraction angle.

In order to render the grating structure in an image generated by a lens behind the grating, the lens must be able to capture at least two diffraction orders to generate intensity modulation in the image. It is this intensity modulation in the image that indicates the sample structure. This puts a limit to the minimal size d at a given wavelength, aperture size, and working distance of the lens. A smaller grating period results in a larger diffraction angle for the first order. The larger the diffraction angle, the larger the aperture (diameter of the lens) has to be to be able to capture the diffraction order and the grating structure.

Since $\theta_m = \arcsin(\sin(\theta_i) - m\lambda/d)$, θ_1 can be shifted by increasing θ_i so that the first diffraction order may be captured by the entrance aperture. The optimum is reached once $\theta_i = \theta_1$ and eq. (2.3) can be written as $d = \lambda/(2\sin\theta)$. Scaling the wavelength by the refractive index n of the medium the famous equation

$$d = \frac{\lambda}{2\mathrm{NA}} \tag{2.4}$$

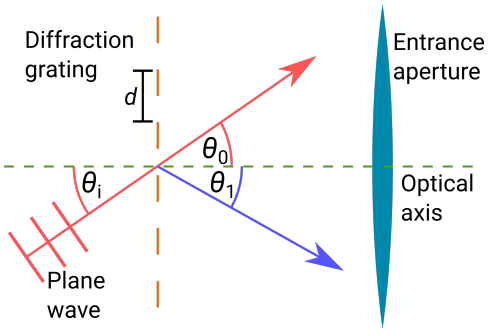

Figure 2.2: Working principle of a transmissive diffraction grating (grating spacing d). The grating and the entrance aperture of the imaging system are aligned with the optical axis. A plane wave is incident on the diffraction grating under an angle θ_i. The zero order diffraction maximum appears at an angle $\theta_0 = \theta_i$ after the diffraction grating. A first order diffraction maximum appears at an angle θ_1.

using the numerical aperture (NA) with

$$\mathrm{NA} = n \sin \theta \tag{2.5}$$

is obtained. Although the resolution limit has been derived for the imaging of a periodic diffraction grating it holds for the imaging of an arbitrary sample with the following restrictions:

- The Abbe resolution limit for a microscope considers **coherent imaging** conditions.
- The highest resolution is achieved under **oblique illumination** of the sample.
- So far no phase alteration by the sample has been considered.
- Within the scope of the presented thesis the Abbe resolution limit is only of partial interest since fluorescence microscopy is highly incoherent.

2.3 Optical resolution and Fourier optics

After introducing two fundamental and more descriptive concepts of resolution in optics, now a more mathematical description is given. In order to get a more in depth understanding of what spatial resolution means and what it is limited by, Fourier optics is employed. Following the notation in [37], fundamental principles and concepts are introduced that are needed to understand in what way the spatial resolution of a microscope is limited and how it can be improved.

In general, the microscope is an optical imaging system that transforms an input signal $g_1(x_1, y_1)$ into an output signal $g_2(x_2, y_2)$. Three properties of the system are assumed to be given. First, the system is linear, which means that it shows superposition property. The systems response to a signal can thus be expressed as the composition of its responses to each point of the signal. Derived from that, the system's response to a point source is described by the point spread function (PSF). This could be the Airy disk as described earlier. Second, it is shift invariant and the PSF does not change its shape depending on the position of a given point source. Third, the system is distortion free and image plane coordinates have a linear relation to the object plane coordinates. The imaging process can then be formulated as

$$g_2(x_2, y_2) = \iint_{-\infty}^{\infty} g_1(\xi, \eta)\, h(x_2 - \xi, y_2 - \eta)\, d\xi\, d\eta. \tag{2.6}$$

This is the convolution of the object with the PSF h and may be noted as $g_2 = g_1 \otimes h$. The coordinates ξ and η have been introduced as the system's response to g_1 is now described as a summation of all responses to a point source at the new sample locations. With respect to fluorescence microscopy, the input signal may be the fluorescence intensity of the sample and the output signal the recorded intensity. Then the PSF can be regarded as the image of a point source. On the other hand, the PSF is generally an impulse response even with respect to a complex input and output. This refers to the fact that under coherent imaging conditions, the complex amplitude must be considered and instead of the optical transfer function (OTF), the amplitude transfer function (ATF) describes the impulse response. This is discussed in section 2.3.1.

At this point the Fourier transform and inverse Fourier transform are introduced as they provide the basis for many descriptions with respect to imaging using wave optics. In general, the Fourier transform $\mathcal{F}$ of a two-dimensional (complex) function $g(x, y)$ of spatial coordinates x and y can be written as [37]

$$G(f_x, f_y) = \iint_{-\infty}^{\infty} g(x, y) \exp\left(-i2\pi(f_x x + f_y y)\right) dxdy, \tag{2.7}$$

which is itself a two-dimensional complex function of the spatial frequencies f_x and f_y. In addition to the Fourier transform, the inverse Fourier transform $\mathcal{F}^{-1}$ is defined as

$$g(x, y) = \iint_{-\infty}^{\infty} G(f_x, f_y) \exp\left(i2\pi(f_x x + f_y y)\right) df_x df_y. \tag{2.8}$$

The usefulness of the transform pair is quite obvious when having in mind that whether or not fine details are resolved in an image depends on the content of high spatial frequencies in its Fourier transform.

The reason to introduce Fourier optics is that the integral in eq. (2.6) (a convolution) takes a rather simple form of $G_2(f_x, f_y) = G_1(f_x, f_y)H(f_x, f_y)$

with the Fourier transforms G_2, G_1, and H of g_2, g_1 and h respectively as stated by the convolution theorem [37]. The convolution becomes a simple multiplication in Fourier or frequency space. This means that every frequency component of the input is changed in its phase and amplitude by the transfer function H in order to generate the output.

2.3.1 Image formation in the microscope

The image formed by the microscope is basically an intensity map either directly seen by the eye or recorded by a camera. Two different imaging conditions are distinguished; coherent and incoherent imaging. Reviewing the pointillism idea that an image is made of the light coming from different points of an object, the coherence of the light determines how to describe the system. In general, the image intensity $I_i(u, v)$ is given by the absolute square of the phasor $U_i(u, v)$, a complex function describing phase and amplitude of the electromagnetic (EM) wave.

Diffraction-limited coherent imaging

If the light is coherent, meaning that its phase varies in the same way in all object points, the image intensity needs to be calculated based on the complex amplitude. This means that the phase distribution over all object points determines the image formation; the integrated intensity distribution. An example is the diffraction grating described above. In this case the phasor in the image plane is given by the phasor of the ideal image (as predicted by geometric optics) $U_g(\tilde{\xi}, \tilde{\eta})$ and the amplitude impulse response $h(u, v; \tilde{\xi}, \tilde{\eta})$ as described in eq. (2.6)

$$U_i(u, v) = \iint_{-\infty}^{\infty} U_g(\tilde{\xi}, \tilde{\eta})\, h(u - \tilde{\xi}, v - \tilde{\eta})\, d\tilde{\xi}\, d\tilde{\eta}. \tag{2.9}$$

This equation contains the reduced coordinates $\tilde{\xi} = M\xi$ and $\tilde{\eta} = M\eta$ to accommodate the magnification M as given by geometrical optics. If the imaging system generates the image in the far field, meaning that the distance between the aperture and the image is much larger than the square of the aperture size divided by the wavelength, the Fraunhofer approximation is valid. In that case, the amplitude impulse response is given by the Fourier transform of

$$H(f_x, f_y) = P(\lambda z_i f_x, \lambda z_i f_y), \tag{2.10}$$

with the pupil function P, the imaging wavelength λ and the distance from the exit pupil to the image plane z_i. For a circular aperture and pupil function, the

ATF is given by

$$H(f_x, f_y) = \text{circ}\left(\frac{\sqrt{f_x^2 + f_y^2}}{w/\lambda z_i}\right) \tag{2.11}$$

with the circle function circ (see fig. 2.3) and the radius of the pupil w. The Fourier transform of eq. (2.9) can be written as

$$G_i(f_x, f_y) = G_g(f_x, f_y)H(f_x, f_y). \tag{2.12}$$

Since the ATF H is the Fourier transform of h which itself is a scaled Fourier transform of the pupil function, under coherent imaging conditions the pupil of the imaging system directly acts as a band-pass filter to the spatial frequencies present in the image. That is intuitively seen from the example of the diffraction grating describing the Abbe resolution limit as presented in fig. 2.2.

Diffraction-limited incoherent imaging

In the case of imaging using incoherent light, the interference effects of the relative phases in U_g are averaged out over the integration time of the detector. The image is thus calculated based on the time averaged intensity distribution that is predicted by geometrical optics as $I_g(\tilde{\xi}, \tilde{\eta})$. The final image intensity distribution is then given by

$$I_i(u, v) = \kappa \iint_{-\infty}^{\infty} I_g(\tilde{\xi}, \tilde{\eta}) \left|h(u - \tilde{\xi}, v - \tilde{\eta})\right|^2 d\tilde{\xi}\, d\tilde{\eta}, \tag{2.13}$$

scaled with a constant κ. Defining $\mathcal{G}_g$ and $\mathcal{G}_i$ as the normalized frequency spectra of I_g and I_i and the normalized frequency spectrum of $|h|^2$ as the OTF $\mathcal{H}$, eq. (2.13) can be rewritten using the convolution theorem as

$$\mathcal{G}_i(f_x, f_y) = \mathcal{G}_g(f_x, f_y)\mathcal{H}(f_x, f_y). \tag{2.14}$$

Similar to eq. (2.10), where a relation between H and the pupil function P is shown, the relation between $\mathcal{H}$ and P has been shown to be [37]

$$\mathcal{H}(f_x, f_y) = \frac{\iint_{-\infty}^{\infty} P\left(x + \frac{\lambda z_i f_x}{2}, y + \frac{\lambda z_i f_y}{2}\right) P\left(x - \frac{\lambda z_i f_x}{2}, y - \frac{\lambda z_i f_y}{2}\right) dx\, dy}{\iint_{-\infty}^{\infty} P^2(x, y)\, dx\, dy}. \tag{2.15}$$

The geometrical interpretation of eq. (2.15) is that the value of $\mathcal{H}$ at each point is the ratio between the overlap of two pupil functions, each shifted by $\pm f_{x/y}$ and divided by the size of the pupil function, given that $P = 1$ inside and $P = 0$ outside the pupil. In other words, the OTF can be calculated as the normalized autocorrelation function of the pupil function.

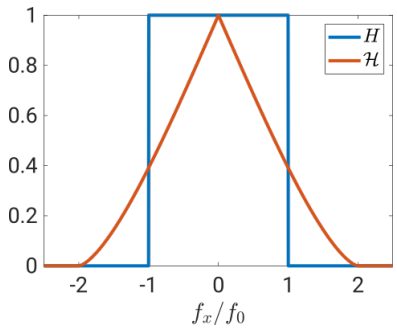

Figure 2.3: Comparing the ATF H and the OTF $\mathcal{H}$ generated by a circular pupil function. The functions are rotationally symmetric with respect to the origin. A cross section at $f_y = 0$ is presented. The frequencies have been normalized to the cutoff frequency f_0 of the coherent imaging system.

Resolution limit of the coherent and incoherent system

Assuming a circular pupil function, the ATF H and the OTF $\mathcal{H}$ are calculated and presented in fig. 2.3. It is obvious from this representation that any imaging system is limited in its spatial resolution by the finite support of its transfer function. Although the highest supported spatial frequency is twice as high for the incoherent imaging system compared to a coherent one, this does not necessarily mean that it provides a better resolution. As described above, $\mathcal{H}$ affects an intensity distribution whereas H manipulates a complex amplitude. In the coherent case, depending on the phase distribution, two point sources separated by the Rayleigh criterion may be not resolved or resolved with an even higher contrast than in the incoherent case. This his is more meaningful with respect to noise and background signal in the acquired image. In the end, the contrast in the recorded image determines whether or not the sought after information is provided. The respective cutoff frequencies for H and $\mathcal{H}$ have been derived to be

$$f_0 = \frac{w}{\lambda z_i} \tag{2.16}$$

for H and $2f_0$ for $\mathcal{H}$ [37]. Here w is the radius of the pupil. Keeping in mind that the magnification in the whole derivation of H and $\mathcal{H}$ has been omitted, the magnification equals one. For a thin lens this would be the case if object and image distance are equal to twice the focal length of the lens. In doing so, the inverse of eq. (2.4), the cutoff frequency, can be written as

$$\frac{1}{d} = \frac{2\mathrm{NA}}{\lambda} = \frac{2n\sin\theta}{\lambda} = \frac{2nw}{\lambda z_i}. \tag{2.17}$$

The reason for this value to be twice as large as given in eq. (2.16), although working under coherent conditions, is the oblique illumination of the sample that is described by Abbe [1].

2.3.2 Fluorescence microscopy

The achievable resolution of a microscopy technique determines if a structure or process in a sample like a biological cell or tissue section may be observed. However, the process by which a contrast is to be generated will finally determine if the final data set, an image or a time series contains the desired information. If the sample itself does not provide a high contrast with respect to a specific target structure using techniques like bright-field, dark-field, or phase-contrast microscopy, fluorescent labels (endogenous or exogenous) may generate that contrast. This is the general concept of fluorescence microscopy.

Fluorescence is a process where a molecule can emit light. It is the response of this fluorophore to a preceding excitation through absorption of light. Due to the Stokes shift the wavelength of the exciting light is different (usually shorter) than that of the emitted light. A detailed description of fluorescence follows further down in this section.

Fluorescence microscopy has become popular in life science. One of the first descriptions dates back to 1904, published by Köhler [63]. It was known by then that the optical resolution of a microscope depends on the wavelength, see section 2.2. Using a wavelength shorter than that of visible light, i.e. ultraviolet (UV) light, would increase the resolution. In Köhler's manuscript, a type of fluorescence (autofluorescence) is basically described as an imaging artefact when imaging with UV light. Autofluorescence is fluorescence that is present in a given sample without the supplement of (artificial) fluorophores. As Köhler already implied, fluorescence would find application due to its specificity. Nowadays it is used for example in imaging of biological cells [7, 82] as well as clinical application like imaging of the retina [88]. Also localization based techniques have employed it in label-free SR imaging, or SRM [61]. All these techniques rely on the localized fluorescence response of specific molecules in the sample.

The majority of fluorescence microscopy is based on a sample preparation process in which fluorophores are attached to target structures. A large variety of labeling strategies exists from which a suitable method has to selected to achieve the intended specific labeling of a structure. Among these techniques are chemical labeling, enzymatic labeling, genetic labeling, and protein labeling using a short tag [84]. In these cases, the aforementioned autofluorescence may be an unwanted, unspecific signal (noise). Since the excitation and emission of a fluorophore can be separated by wavelength it is possible to filter out most of the light not coming from specific places of the fluorescent label, scattered excitation light for example. This a way, one path for the excitation light and a separate path for signal detection can be used.

Limiting factors of fluorescence microscopy are photobleaching and phototoxicity. Photobleaching is a photochemical process, an alteration in a molecule such that it loses its ability to fluoresce. It causes a reduction in the signal strength and degrades the signal-to-noise ratio (S/N). Phototoxicity describes the impact of light in the sample. In live cells, the excitation light may damage macromolecules, limiting their functionality, possibly up to the point where the cell dies [58]. Thus, the amount of excitation light the cell is exposed to should be kept as small as possible.

Fluorescence

Fluorescence based microscopy techniques play a major role within the scope of the presented thesis . The spontaneous emission of a photon by a molecule is called luminescence [98]. This does not include thermal radiation. Fluorescence is described by the behavior of an electron in the quantum mechanical system, a fluorescent molecule for example. This quantum mechanical system provides different energy levels or states which the electron can occupy. Based on these energy states as shown in the Jablonski diagram in fig. 2.4, the fluorescence property of a molecule can be described. The fluorophore in its electronic ground state S_0 can be excited through absorption of a photon $h\nu_{\mathrm{ex}}$ (Planck's constant h, frequency ν) into an excited state S_1. This transitions is said to happen "instantaneously" (within 10^{-15} s [66]). After non-radiative transitions (internal conversion in less than 10^{-12} s) from a higher vibrational energy level to the vibrational ground state in S_1, fluorescence is possible. Fluorescence is then the emission of a photon $h\nu_{\mathrm{em}}$ through the transition of the molecule from an electronically excited state S_1 to its ground state S_0, commonly into a higher vibrational state of S_0. From there, the thermal equilibrium, the vibrational ground state of S_0, is reached again through internal conversion. The time a molecule spends in the circle from absorption of a photon in its thermal equilibrium until the return to it upon emission of a fluorescence photon is given by the fluorescence lifetime (typically about 10^{-8} s). Since the internal conversion happens on a much smaller time scale than the fluorescence lifetime, fluorescence mainly takes place by a transition from the thermal equilibrium state of the excited electronic state. The selection of a higher vibrational state of the molecule, while changing the electronic state for absorption and emission of a photon, is governed by the Franck-Condon principle [35]. It says that the transition probability for a molecule involving a change in the vibrational and the electronic state (vibronic transition) depends on the overlap between the involved wave function at the given nuclear coordinate. Since the discussed transitions (absorption and emission of a photon) mostly start from the thermal equilibrium of the given electronic state while the vibrational energy levels and their wave functions look similar in each electronic state, the absorption and emission spectra show mirror symmetry.

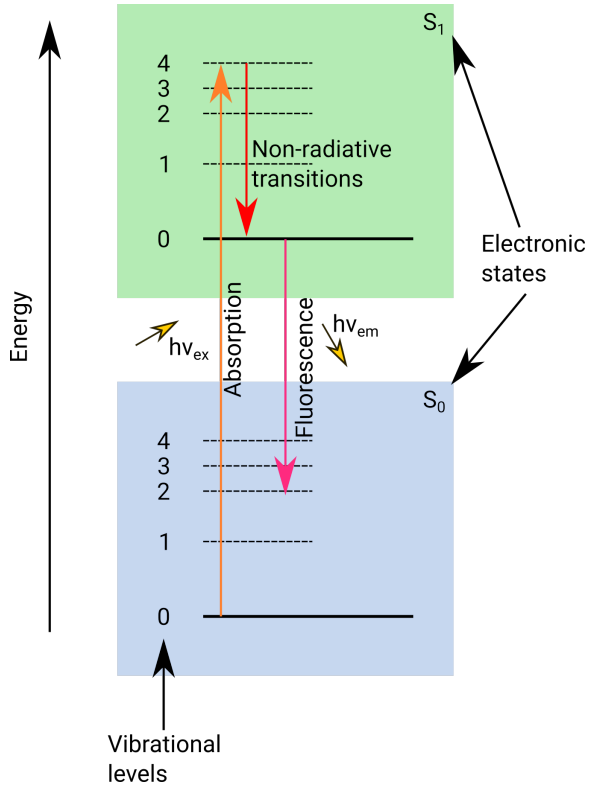

Figure 2.4: The Jablonski diagram [59] showing the electronic ground state S_0 and an excited state S_1 of a fluorophore, including the vibrational levels in each electronic state. The molecule may undergo a transition from S_0 to S_1 by absorption of a photon $h\nu_{\text{ex}}$. It then undergoes non-radiative transitions into the vibrational ground level of S_1. From there, the molecule goes back into S_0 by spontaneous emission of a photon $h\nu_{\text{em}}$. This phenomenon is called fluorescence.

The description of fluorescence using the Jablonski diagram explains two major properties of fluorescence that make it so useful in microscopy. First, the excitation and emission spectra show distinct peaks due to the discrete energy levels as presented in the Jablonski diagram. Second, those peaks are separated in their wavelength due to the Stokes shift. Based on the internal conversion, the wavelength of the emission is longer than the wavelength of the absorption since part of the energy the system took up by absorbing a photon is dissipated as heat. This means that fluorescence can be excited at a specific wavelength (using a laser for instance), and it can then be distinguished from the emission. If the fluorophores are specifically bound to structures of interest in e.g. a biological cell, a spatially unspecific excitation (illumination) of the sample may still lead to a highly specific fluorescence response of the sample depending on the staining strategy. The excitation light can simply be filtered out depending on its wavelength thus removing a lot of what would otherwise appear as background signal, improving the S/N. For the further consideration with respect to image resolution, the spontaneous nature of the fluorescence after excitation and the comparably long fluorescent lifetime are of interest. Fluorescent emission is a random process [66], the imaging process thus qualifies as incoherent and relevant considerations as described in section 2.3.1 apply. Another fundamentally related figure of merit is the quantum yield, the ratio of number of photons emitted to the number of photons absorbed, $\Phi = \frac{h\nu_{\mathrm{em}}}{h\nu_{\mathrm{ex}}}$. Since the excited fluorophore may return to the ground state through a non-radiative process, the quantum yield is less than one. The quantum yield is of major concern since it determines the exposure of the sample needed to generate sufficient signal strength. The exposure to excitation light on the other hand promotes unwanted photobleaching and phototoxicity. This makes a sufficient quantum yield so important.

Fluorescence is only one possible pathway for a molecule to relax from an excited state back into the ground state. Phosphorescence involves the transition from S_1 through a triplet state T_1 (not shown in fig. 2.4) that is located below between S_1 and S_0 on the energy axis. This involves the electron in the excited state to have the same spin as the remaining electron in the ground state. A transition back into the ground state is quantum mechanically said to be forbidden which manifests itself in a comparably long phosphorescence lifetime of up to several seconds. This is mentioned here for the sake of completeness and is not regarded further on.

2.4 Super-resolution microscopy

The idea of resolution in microscopy and the criteria given by Abbe and Rayleigh are described in sections 2.1 and 2.2. Before going into the description of some of the techniques that are used nowadays to circumvent theses limits it should be pointed out that different resolution criteria may be defined depending on the character of the question that should be answered. In case of an unknown sample this can be based on the Nyquist–Shannon sampling theorem [24]. The whole sample, for instance a complex biomolecule, has to be imaged including spatial frequencies twice as high as the intended resolution (see section 2.4.4 on SMLM). If the distance between two objects is of interest, the Rayleigh criterion could be of interest. In three-dimensional imaging it may be the resolution based on the smallest observation volume [86]. Since the microscope is developed as a tool to answer a variety of questions in different fields, there can not be the one resolution criterion to find the best technique [24]. As the resolution criterion is not well defined, it is hard to clearly distinguish SRM from conventional microscopy. A generally accepted limit for conventional optical microscopy is a resolution of $\approx 0.2\,\mu m$ in the lateral and $\approx 0.6\,\mu m$ in the axial direction [24]. Some of the concepts that have been developed to circumvent this limit are described in the following.

2.4.1 Towards shorter wavelengths

As described in section 2.3.2 one way to increase the resolution of the imaging technique is the use of a shorter wavelength like in the UV microscope [80, 63]. This rather low resolution improvement may be increased by using an even shorter wavelength. X-ray microscopy, using absorption contrast or phase contrast, was proposed and achieves a resolution below 15 nm [19]. Matter waves have an even shorter wavelength. Louis de Broglie related the momentum of a particle to its wavelength via the Planck constant [16]. Applied to the electron, transmission electon microscopy (TEM) and scanning TEM (STEM) have been developed and achieve 50 pm resolution [33]. The scanning electron microscopy (SEM) uses a focused electron beam to scan the sample surface, while detecting various signals at each position [8]. Scanning helium ion microscopy (SHIM) is not only used for SR imaging of the sample, but also provides possible sample manipulation like ion milling [57]. These are techniques that improve the resolution by using lower than optical wavelengths. This requires not only the lens based optics (UV, X-ray, electron optics) to be changed in order to manipulate the imaging wavelength, but also requires partially severe sample preparation and imaging conditions like electric conductivity of the sample, or imaging in a vacuum. For many questions of life science this may disqualify those techniques.

2.4.2 Near-field and scanning probe microscopy

The commonly accepted Abbe limit of resolution is a result of far-field optics. If an aperture, smaller than the employed wavelength is brought to the sample, at a distance less than the wavelength, the sample can be scanned by detecting the near-field intensity distribution [96]. These techniques are named near-field scanning optical microscopy (NSOM) or scanning near-field optical microscope (SNOM) [18, 77]. A variety of implementation, using the probe for excitation or detection only is possible. Using visible light, a spatial resolution of 500 Å is reported [68]. Similar to the near-field optical microscopes, scanning probe microscopy (SPM) has been developed. Scanning the sample with a physical probe and measuring different kinds of interaction, thus generating an image without the use of (electron) optics. In scanning tunneling microscopy (STM) voltage is applied between an electrically conducting sample an the probe. The probe is scanned over the surface and the electrical current due to quantum tunneling is measured. Since the measured current depends on the distance between probe and surface, the surface structure can be measured at an atomic level [13]. A direct progression of STM is atomic force microscopy (AFM). The surface is scanned with a small apex on a cantilever measuring interatomic forces between single atoms. It can be applied to electrically non-conducting samples without the need for a vacuum [12].

2.4.3 Confocal microscopy and optical sectioning

Before introducing some principles of optical SRM, a fundamental technique that provides optical sectioning in three-dimensional imaging is described. Although not actually providing SR capabilities it is mentioned here as it emphasizes the difference between axial resolution and optical sectioning. Confocal microscopy, implemented as confocal laser scanning microscopy (CLSM) has an edge over wide-field (WF) microscopy as it is able to reject out-of-focus light [78]. It is a scanning technique in which a limited volume of the sample is illuminated at a time and the response is detected. While the conventional WF microscope will detect light coming from beyond the focal plane, an aperture in the conjugate plane of the CLSM will reject this light thus allowing for optical sectioning and improving the contrast. Although this technique allows for a 1.4-fold improvement in lateral resolution its main advantage is the optical sectioning capability [24]. Another technique that provides comparable optical sectioning is light sheet fluorescence microscopy as described in section 2.5.

2.4.4 Optical far-field SR microscopy

Different far-field SR microscopy techniques operating at visible wavelengths are implemented for fluorescence based bioimaging. For these techniques the term “nanoscopy” has been coined and a quick overview is given. These techniques can be divided into three categories based on their approach to overcome the conventional resolution limit [87].

Structured illumination microscopy

The first category is SIM. These techniques rely on different kinds of non-planar illumination of the sample and multiple image acquisitions with varying illumination patterns. Subsequent image reconstruction yields a resolution of usually up to twice the resolution of the respective WF image [105, 47]. It has been shown, that the exploitation on nonlinear effects may further increase the resolution [41]. Techniques like standing-wave fluorescence microscopy and spatially modulated illumination microscopy are described in the literature [24]. They are based on a modulated illumination intensity along the optical axis thus increasing the axial resolution. More common are implementations using a standard WF microscope, where the lateral resolution can be improved by generating an illumination pattern that is modulated in the sample plane as well as along the optical axis [46, 42]. By interfering coherent light in the sample space, a well defined illumination pattern is generated. The resolution improvement is based on the frequency mixing of the sample’s spatial frequency with the pattern’s spatial frequency. As a result, a moiré pattern is generated. An illustrative example is the superposition of two periodic functions with only a small difference in their spatial frequencies; two semitransparent curtains for instance. This generates coarse moiré patterns. With respect to the microscope, these moiré fringes may be transmitted by the OTF support. Knowledge of the illumination pattern will then allow for reconstruction of the underlying sample structures that are originally to fine to be captured by the microscope. The mathematical details are described in section 3.1 and it should be pointed out that the mathematical principle that generates the coarse interference pattern is not only valid for periodic sample structures. It is possible to implement interference based SIM on a TIR fluorescence (TIRF) microscope. This allows for increased lateral resolution while limiting the excitation of the sample to the size of the evanescent field [62, 108]. A derivative of these interference based approaches are point scanning SIM techniques like image scanning microscopy [32, 40] that also rely on a non-planar illumination. Classifying SIM as nanoscopy is controversial as those techniques are still limited in their resolution improvement due to diffraction, although they do achieve a resolution better than the classical limit.

Reversible saturable optical fluorescence transitions microscopy

This leads to the second category of nanoscopy techniques that are based on deterministic on/off-switching of fluorescent molecules. These techniques may be summarized under reversible saturable optical fluorescence transitions (RESOLFT) microscopy [55, 49, 24]. The sample (fluorophore distribution) is measured in a point-by-point fashion using a point detector. The resolution is determined by the size of the volume that emits the fluorescence signal. In stimulated emission depletion (STED) [50] a focused laser and a high NA objective lens are used to generated a diffraction limited excitation volume. This excitation spot is overlayed with a toroidal intensity distribution (the STED beam) that generates stimulated emission. Stimulated emission is the radiative deexcitation of a molecule by an incoming photon. The emitted photon propagates in the same direction as the photon stimulating the emission and has the same wavelength. As the spontaneous fluorescence emission covers a relatively broad spectrum, it can be distinguished from the well defined excitation and STED beam including the stimulated emission. Depending on the intensity distribution of the STED beam, the volume of the sample that undergoes spontaneous emission can thus be reduced to achieve a lateral resolution of 15 nm to 20 nm [29]. Since the size of the detected volume decreases with increased intensity in the STED beam, the resolution is limited by the photodamage that is acceptable in the regarded experiment [87]. A related technique is ground-state-depletion (GSD) microscopy [48, 15]. In GSD microscopy, instead of deexciting fluorophores outside the volume of interest, fluorophores are excited from the ground state into a non-fluorescent triplet state. For a short period of time after that (the lifetime of the triplet state in the range of ns–µs) only fluorophores in a well defined small volume are fluorescent.

Single-molecule localization microscopy

The third group are techniques based on WF illumination and stochastic on/off-switching of the fluorophores. The general term single-molecule localization microscopy (SMLM) has been established for this second group of nanoscopy techniques whose resolution is not limited by diffraction. They are based on the idea that fluorophores can be characterized as individual point emitters, and the possibility to switch their fluorescent state on and off randomly. In order to generate a SR image, a series of raw data images of the sample is acquired. In each of those images only a fraction of fluorophores is actually fluorescent such that the raw data image consists of a diffraction limited image of several, spatially well separated point sources. By determining the center position of those point sources in the image (fitting a Gaussian function for instance), a list of coordinates is collected. This is done for each frame and the coordinate

distribution can be displayed as a probability density map. Although the single emitters can be localized to a fairly high precision (20 nm lateral and 50 nm [87]) the resolution of the final image depends on the label density in the sample (Nyquist-Shannon sampling). Different implementations of the SMLM principle are used. In photo activated localization microscopy (PALM)[11] and fluorescence photoactivation localization microscopy (FPALM)[54] fluorescent proteins are used as labels (exogenous). The switching between the fluorescent and non-fluorescent state is achieved through illumination with a suitable wavelength. On the other hand stochastic optical reconstruction microscopy (STORM)[83] and direct STORM (dSTORM)[45] are based on immunolabeling (endogenous). Here the random switching of the molecule during the fluorescence cycle at high excitation powers is used. In order to successfully perform an image reconstruction using these techniques, the distribution of fluorescent molecules in the on-state has to be sparse enough. A post-processing technique using statistical analysis of a time series based on independently blinking molecules is used in SR optical fluctuation imaging (SOFI)[25]. With this technique it is possible to achieve SR from the raw data set, even if the sparsity constraint in each frame is not fulfilled, as long as the molecules cycle through fluorescent on/off-states.

2.5 Light sheet fluorescence microscopy

As already discussed in section 2.4.3, the lack of optical sectioning capability in conventional WF imaging significantly reduces the image contrast as a lot of background signal is generated. A way to introduce optical section without scanning the sample as in confocal microscopy is LSFM[34]. LSFM, or selective plane illumination microscopy (SPIM)[56], originally developed as orthogonal-plane fluorescence optical sectioning (OPFOS)[100], uses orthogonal illumination of the sample with respect to the imaging objective lens, minimizing out-of-focus light and providing exceptional optical sectioning capability. This has made LSFM a most suitable method for live cell imaging of thick specimens. The main advantage over confocal microscopy is the fast, because WF based image acquisition. Since the excitation of the sample is limited to the areas being imaged, also the the area where photodamage occurs is reduced to a necessary minimum. This is especially relevant with respect to imaging living biological samples [94].

The light sheet is generated by focusing an extended beam of light in one plane only, using a cylindrical lens, possibly in combination with a high NA objective lens [39]. Alternatively a single objective lens, generating the light sheet and acquiring the image as in the highly inclined and laminated optical sheet (HILO) implementation may be used [97]. Another way to generate a

light sheet is by the use of an axicon [26]. This is investigated and discussed in chapter 4. The image acquisition is done by an imaging objective with its focal plane aligned with the light sheet. This way only the portion of the sample that is actually imaged is also excited. In a HILO configuration the imaging objective also generates the light sheet and the light sheet is at an angle with the focal plane. This limits the advantage of the LSFM approach but allows for a more compact design.

2.6 Optical waveguides

So far, the use of fluorescence as a means to generate contrast has been described. Although discussed with respect to the coherent imaging condition, the illumination or excitation of the sample has not been taken into account. Instead of performing a bulk illumination of the whole sample it may be advantageous to provide more specific illumination of the sample. In order to reduce effects like photobleaching and phototoxicity in areas of the sample that are not intended to be imaged at a given moment, an excitation spatially limited to the imaged area is of interest. Among other means, optical waveguides as introduced in the following section are suitable to perform that task.

The free-space transmission of light from one place to another is possible by means of ray propagation. Since rays of light propagating in free-space show divergence it is necessary to perform tasks like refocusing along the way. An alternative is the propagation of light in dielectric waveguides, systems of dielectric media that are able to guide light along a give path without the necessity of readjusting the beam profile. The fundamental concept of optical waveguides is introduced by discussing the most fundamental planar waveguide followed by the rib waveguide.

2.6.1 Planar waveguides

The planar optical waveguide, or slab waveguide is shown in fig. 2.5. A system of three plane slabs of dielectrics of different refractive indices (substrate (n_s), core (n_1), and cladding (n_0)) is considered. The slabs extended in the xy-plane and a given core thickness presents two parallel interfaces of each two dielectrics with different refractive indices (substrate and core, and core and cladding). According to Snell's law, a ray incident on an interface (n_1, n_2 with $n_1 > n_2$) at an angle θ_i with the normal will propagate beyond the interface at an angle given by $\theta_2 = \arcsin(\sin(\theta_i)n_1/n_2)$ until θ_1 reaches a critical angle upon which the light does not pass the interface but is reflected due to total internal reflection (TIR). If this is repeated at both interfaces of

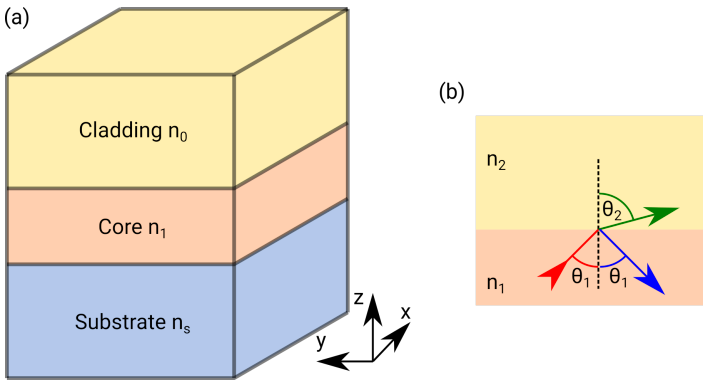

Figure 2.5: A planar waveguide **(a)** consisting of three layers of dielectric media (cladding, core, substrate) with different refractive indices $n_0 < n_1$, $n_s < n_1$. The layers extend in the xy-plane and light is guided in the core layer due to total internal reflection. A light ray (red) incident on the interface between two dielectric media (dashed normal) at an angle θ_1 changes its direction of propagation (green, θ_2) according to Snell's law until θ_1 equals the critical angle and $\theta_2 = 90°$. Increasing θ_1 beyond this point leads to total internal reflection (blue).

the slab waveguide, the ray of light coupled into it propagates in the core due to repeated TIR. The necessity to overcome the critical angle at the interfaces translates to a maximum acceptance angle, the NA of the waveguide, at the facet where light is to be coupled in.

Beyond the conditions imposed by the NA there are further limitations to the way light may propagate within the waveguide. At this point the wavelike nature of light has to be taken into consideration. Light is propagating as a wave in the waveguide and a self-consistency condition is imposed [85]. Assuming a plane wave associated with the incident beam, propagating in the waveguide by TIR, an angle $\phi = \pi/2 - \theta_1$ with the x-direction is formed. This is the intended direction of net propagation. At this point, propagation constants along x and y can be defined

$$\beta = kn_1 \cos\phi \tag{2.18}$$

$$\kappa = kn_1 \sin\phi \tag{2.19}$$

with the wavenumber $k = 2\pi/\lambda$ and the considered vacuum wavelength λ. The wavefront of a plane wave is perpendicular to its direction of propagation. An angle ϕ is sought after such that after two-times reflection of the beam, once at each interface, its wavefront is consistent with the initial wave. Each field distribution that satisfies this phase-matching condition is called a mode of the waveguide [76]. It is only fulfilled at discrete angles ϕ and accordingly for discrete propagation constants β and κ. In addition, an effective index for

each mode is defined as

$$n_e = \frac{\beta}{k} = n_1 \cos\phi. \tag{2.20}$$

So far, the phenomenon of guided wave optics has only been described in terms of ray and wave optics. To fully understand the further discussion of waveguides, the EM description of light has to be taken into account. There light is described as an EM field that propagates through space with the electric field $\mathrm{E}(\mathrm{r}, t)$ and the magnetic field $\mathrm{H}(\mathrm{r}, t)$, both functions of space $\mathrm{r} = (x, y, z)$ and time t. More specifically, the described wave consists of oscillating electric and magnetic fields at angular frequency $\omega = ck$

$$\begin{aligned}\mathrm{E}(\mathrm{r}) &= \mathrm{E}(y, z)\exp[i(\omega t - \beta x)]\\ \mathrm{H}(\mathrm{r}) &= \mathrm{H}(y, z)\exp[i(\omega t - \beta x)].\end{aligned}$$

Maxwell's equations govern the behaviour of the EM field. The dielectric waveguide under consideration qualifies for a description using the following equations

$$\nabla \times \mathrm{H} = \epsilon \frac{\partial \mathrm{E}}{\partial t} \tag{2.21}$$

$$\nabla \times \mathrm{E} = -\mu_0 \frac{\partial \mathrm{H}}{\partial t} \tag{2.22}$$

$$\nabla \cdot \mathrm{E} = 0 \tag{2.23}$$

$$\nabla \cdot \mathrm{H} = 0, \tag{2.24}$$

with the electric permittivity $\epsilon = \epsilon_0 n^2$, the vacuum permittivity ϵ_0 and the refractive index n of the medium, and the magnetic permeability in vacuum μ_0. For a plane wave propagating in x-direction in the slab waveguide it can be shown that two modes exist [76]. For one mode, $E_x = E_z = H_y = 0$, which means that the electric field does not have a component along the direction of propagation, but only transversal to it; the transverse electric (TE) mode. In the second mode, $H_x = H_z = E_y = 0$, the magnetic field does not have a component along the direction of propagation and is therefore called transverse magnetic (TM) mode. These results are based on the boundary condition at the interface of two dielectrics, that the tangential components of the electric and the magnetic field must be continuous [85]. Given that the modes are confined in the core at $-a \leq z \leq a$ (thickness of the core = $2a$), and the the substrate and the cladding are extending away from the core, the field distribution for the TE-mode can be expressed as

$$E_y = \begin{cases} A\cos(\kappa a - \phi)\exp(-\sigma(z-a)) & z > a \\ A\cos(\kappa z - \phi) & -a \leq z \leq a \\ A\cos(\kappa a + \phi)\exp(\xi(z+a)) & z < -a \end{cases} \tag{2.25}$$

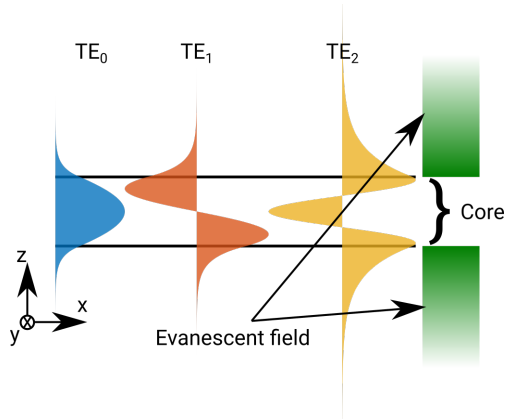

Figure 2.6: The electric field (y-component) of the fundamental, first and second order TE modes of a slab waveguide in blue, red and yellow respectively (see also fig. 2.5). All guided modes show a portion of the field extending beyond the core. This evanescent field (green) decays in an exponential fashion.

with the wavenumbers along the z-axis

$$\kappa = \sqrt{k^2 n_1^2 - \beta^2}$$
$$\sigma = \sqrt{\beta^2 - k^2 n_0^2}$$
$$\xi = \sqrt{\beta^2 - k^2 n_s^2}.$$

In fig. 2.6, the magnitude of E_y for a symmetric ($n_0 = n_s$) slab waveguide for the fundamental (TE_0, blue), first order (TE_1, red) and second order (TE_2, yellow) mode are illustrated qualitatively. Additionally, the exponentially decaying evanescent field (green) in substrate and cladding are also represented. It can be seen that the evanescent field is stronger for higher order modes as they are less confined in the slab. The decay of the evanescent field is given by the extinction coefficients σ and ξ. Similar results are obtained for the TM-modes of the waveguide where H_y shows the oscillating behaviour along z in the core and the exponential decay outside of it [76].

Solving for the effective index

The effective index n_e can be calculated as described below [76]. By defining the normalized frequency for an asymmetric ($n_s > n_0$) waveguide as

$$v = ka(n_1^2 - n_s^2) \tag{2.26}$$

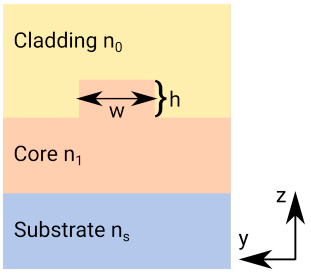

Figure 2.7: The schematic profile of a rib waveguide. Compared to the slab waveguide the core is etched down by the rib height h, leaving a rib of width w. With such a design the light is not only spatially confined in the z-direction, but also in the y-direction.

and the normalized propagation constant

$$b = \frac{n_e^2 - n_s^2}{n_1^2 - n_s^2} \tag{2.27}$$

as well as a measure of the asymmetry

$$\gamma = \frac{n_s^2 - n_o^2}{n_1^2 - n_s^2}, \tag{2.28}$$

the following dispersion equation can be derived

$$\begin{aligned} 2v\sqrt{1-b} =& m\pi \\ &+ \frac{1}{2}\arctan\left[\left(\frac{n_1^2}{n_s^2}\right)^p \sqrt{\frac{b}{1-b}}\right] \\ &+ \frac{1}{2}\arctan\left[\left(\frac{n_1^2}{n_0^2}\right)^p \sqrt{\frac{b+\gamma}{1-b}}\right]. \end{aligned} \tag{2.29}$$

Here m is determining the order of the mode ($m = 0$ for the fundamental mode) and p selects between TE ($p = 0$) and TM ($p = 1$) modes. By numerically finding the root of this function, the normalized propagation constant b can be determined and thus also the effective index n_e of the mode by using eq. (2.27).

2.6.2 Two-dimensional confinement in the rib waveguide

The rib waveguide is a structure that does not only provide one-dimensional confinement of light as in a slab but also in the y-direction. This is done by limiting the width w of the core and etching a rib height h around it (see fig. 2.7). When calculating the effective indices of comparable slab waveguides

for the etched core height as well as for the untreated core height, a change in the refractive index along the y direction appears. The higher refractive index in the rib region promotes the confinement in the y-direction. Due to the two-dimensional confinement, the guided modes are no pure TE- or TM-modes. This means that the previously defined way of naming the TE-mode ($E_x = E_z = H_y = 0$) does not work anymore. Still, these modes will have major and minor field components such that a mode with a major E_y and a minor H_y component is called (quasi)-TE-mode and vice versa [106].

2.6.3 Finite element method in COMSOL Multiphysics

The behaviour of EM radiation is described using partial differential equations (PDEs) as presented in eq. (2.21). It can be difficult, if possible at all, to find analytical solutions for non-trivial geometries [76]. For a part of the presented thesis FEM as implemented in COMSOL [22] is used to determine the EM field distribution for different waveguide designs and the light propagation outside of the waveguide. Since an analytical solution may be impossible to find, an approximation is sought after. Historically the idea to approximate an unknown function using a set of functions over subdomains is described by Courant [23]. The concept of the FEM is well documented in the literature [81] and here a short description of the idea is given.

For the user in COMSOL the task is to first generate a model consisting of a computer-aided design (CAD) geometry, the distribution of material properties, the refractive index of the waveguide for instance and the correct (physical) boundary conditions like a perfect electric/magnetic conductor or the perfectly matched layer. In addition, on the input and possibly the output of a waveguide model numeric ports are used in order to find the guided modes and propagate them through the model.

The model domain is subdivided in small parts, hence finite element. These elements are separated by nodes. In each of those elements the solution to the concerned PDEs is approximated as a linear combination of basis functions (polynomials for instance). To each node belongs a basis function that has a limited support and the whole domain is covered by such basis functions. The discretization and the basis functions can be selected depending on the problem under consideration. This allows for an exact representation of the geometry as well as the solution. A region in which the solutions variation is expected to be larger may then be equipped with higher order approximation functions to accommodate strong variation. The actual mesh is generated by a function of the software although the user will select the form of the mesh elements, for instance triangular in a two-dimensional model, tetrahedral in a three-dimensional model, and parameters like the maximum element size

and growth rate. At this point the problem can be formulated such that the parameters of the approximation functions can be calculated considering the physical boundary conditions. The solution is then the assembly of the solutions found at each node.

3

Structured illumination microscopy

The details of interference-based, linear two-dimensional SIM are discussed in the first part of this chapter in order to provide the background for the work included at the end. The chapter includes a contribution to the most relevant parameter estimation in SIM in section 3.1.1 and simulations regarding two novel implementations of the technique in sections 3.2.1 and 3.2.2. Historically the foundation of SIM can be seen in the work by Lukosz [69, 70] in the late 1960s. This is discussed in the reviews by Cremer and Masters [24], and Heintzmann and Huser [47]. Special note should be given to the fact that although providing an analysis of optical systems and resolution improvement that can be related to today's SIM, the cited work by Lukosz regards coherent imaging conditions. SIM based on elastically scattered light of the sample does not improve the resolution beyond the Abbe limit under oblique, planar (as opposed to structured) illumination [102]. Here, SIM, implemented as a technique to overcome the resolution limit in the object plane using a single lens WF setup, as by Heintzmann and Cremer [46], and Gustafsson [42] is discussed in detail. This way earlier approaches aiming at a resolution improvement in the axial direction such as standing-wave fluorescence microscopy (SWFM) [67, 10] are disregarded.

The SIM technique regarded in detail in this thesis is what is called super-resolution structured illumination microscopy (SR-SIM) for the purpose of

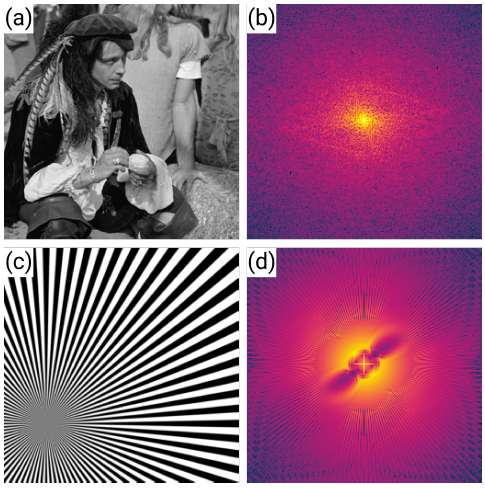

Figure 3.1: The pirate sample **(a)** and its Fourier spectrum **(b)**, and the Siemens star sample **(c)** and its Fourier spectrum **(d)** for comparison. The Fourier spectrum of the pirate sample is almost isotropic, whereas the Fourier spectrum of the Siemens star is clearly not. The Siemens star is thus useful for the illustration of data processing steps that involve a shift in the Fourier domain. Furthermore, since the spokes of the Siemens star get closer towards its center, the resolution of the image is directly indicated.

differentiation from other techniques using a somehow structured illumination, as discussed in the review by Heintzmann and Huser [47]. It is described as a technique using a sinusoidal interference pattern for illumination of the sample in order to achieve lateral resolution improvement. In the following SR-SIM will simply be referred to as SIM.

Throughout this chapter imaging is simulated using one of the samples as presented in fig. 3.1. The Fourier spectrum of the pirate sample is almost isotropic, whereas the Fourier spectrum of the Siemens star is clearly not. The Siemens star is thus useful for the illustration of data processing steps that involve a shift of the data in the Fourier domain. The color map "Morgenstemning" [36] will be used for better visual representation, when appropriate.

3.1 Image reconstruction in SIM

The theoretical background for SIM is introduced using the notation as given by Wicker and co-workers [103, 104]. The image formation for WF microscopy under planar illumination can be described as

$$D(\mathrm{r}) = [S(\mathrm{r})I] \otimes h(\mathrm{r}), \tag{3.1}$$

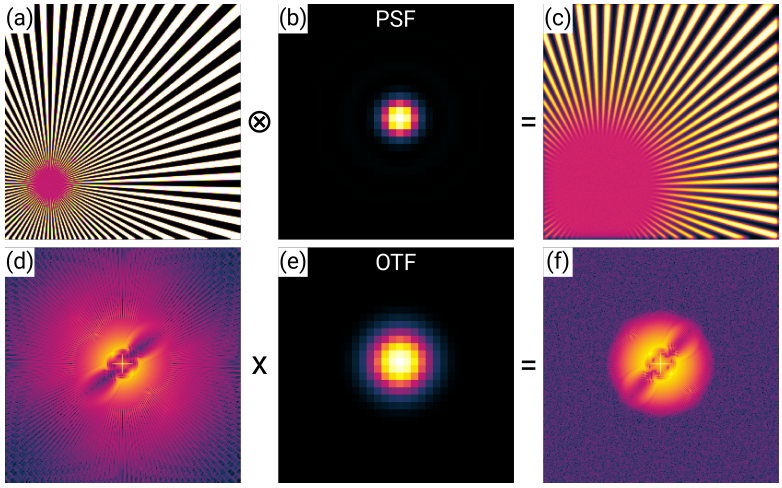

Figure 3.2: The WF imaging process under planar illumination (see eq. (3.1)) is simulated as a convolution of the emission **(a)** with the PSF **(b)** (cropped representation) resulting in the WF image **(c)**. The same process is described in the Fourier domain as multiplication of the sample's Fourier spectrum **(d)** with the OTF **(e)**, resulting in the Fourier spectrum of the WF image **(f)**. Note that the limited support of the OTF cuts off high frequency components, limiting the resolution in the image.

with the acquired image D, the fluorophore distribution S, the planar illumination intensity I, the PSF h and the spatial coordinate r. Note that h, introduced as the amplitude impulse response in section 2.3.1 is now the PSF of the system. Since the whole fluorescence imaging process can be described in terms of intensity as it is an incoherent process, the amplitude transfer function is not used. The whole change of notation is done to stay in accordance with the literature. With respect to eq. (2.13) this means that $I_i = D$, $I_g = [S \times I]$, and $|h|^2 = h$.

The process described by eq. (3.1) is illustrated in fig. 3.2. It is a convolution of the emission **(a)** with the PSF **(b)** resulting in the WF image **(c)**. The same process is described in the Fourier domain as multiplication of the sample's Fourier spectrum **(d)** with the OTF **(d)**, resulting in the Fourier spectrum of the WF image **(f)**. The fact that the finer details of the sample (pattern closer to the center of the Siemens star) are not visible in the WF image **(d)** is due to the limited resolution. The reason for that is the suppression of high frequency components by the limited support of the OTF, clearly visible when comparing **(d)** and **(f)**.

In SIM, the planar illumination I is replaced by a sinusoidal illumination pattern

$$I(\mathrm{r}) = \sum_{m=-1}^{1} a_m \exp[im(2\pi \mathrm{pr} + \phi)], \tag{3.2}$$

with the modulation depth a_m, its wave vector $\mathrm{p} = p_x\hat{k}_x + p_y\hat{k}_y$, with the unit vectors $\hat{k}_x$ and $\hat{k}_y$, and the phase ϕ. The Fourier transform of this expression yields

$$\tilde{D}(\mathrm{k}) = \left[\tilde{I}(\mathrm{k}) \otimes \tilde{S}(\mathrm{k})\right] \tilde{h}(\mathrm{k}) \tag{3.3}$$

where tilde ($\sim$) indicates the Fourier transform and k is the Fourier space coordinate or spatial frequency. The term $\tilde{h}$ is the OTF, written as $\mathcal{H}$ in section 2.3.1. It has the property to limit the highest spatial frequency of the sample represented in the image to a cutoff frequency $\|\mathrm{k}\|_2 \leq k_{\max}$ and thus the maximum resolution of the image.

The full expression of eq. (3.3) using eq. (3.2) yields

$$\tilde{D}(\mathrm{k}) = \sum_{m=-1}^{1} \exp(im\phi) \underbrace{a_m \tilde{S}(\mathrm{k} - m\mathrm{p})\tilde{h}(\mathrm{k})}_{\tilde{C}_m(\mathrm{k})}. \tag{3.4}$$

It can be seen that $\tilde{D}(\mathrm{k})$ contains frequency components, or bands $\tilde{S}_m(\mathrm{k}) = \tilde{S}(\mathrm{k} - m\mathrm{p})$ that are shifted by $m\mathrm{p}$ (highlighted in eq. (3.5)) with respect to their original position in frequency space prior to multiplication with the OTF. This is illustrated in fig. 3.3. The sample is excited with a sinusoidal illumination pattern **(a)** resulting in a raw data image **(b)**. The three peaks of the illumination pattern in the Fourier domain (schematically in **(c)**) generate three copies of the original sample spectrum in the Fourier domain **(d)**.

In this way, high spatial frequency components of the sample that are not observable under planar illumination are transferred into the image, although the bands are shifted and summed up. By taking N images of the sample with different phases ϕ_n with $n = 1, \cdots, N$, the resulting Fourier transforms of the images $\tilde{D}_n(\mathrm{k})$ can be written as

$$\begin{pmatrix} \tilde{D}_1 \\ \vdots \\ \tilde{D}_N \end{pmatrix} = \begin{pmatrix} \exp(-im\phi_1) & 1 & \exp(im\phi_1) \\ \vdots & \vdots & \vdots \\ \exp(-im\phi_N) & 1 & \exp(im\phi_N) \end{pmatrix} \begin{pmatrix} a_{-1}\tilde{S}(\mathrm{k} + \mathrm{p})\tilde{h}(\mathrm{k}) \\ a_0\tilde{S}(\mathrm{k})\tilde{h}(\mathrm{k}) \\ a_1\tilde{S}(\mathrm{k} - \mathrm{p})\tilde{h}(\mathrm{k}) \end{pmatrix}, \tag{3.5}$$

or

$$\tilde{\mathrm{D}}(\mathrm{k}) = \mathrm{M}\tilde{\mathrm{C}}(\mathrm{k}), \tag{3.6}$$

with the acquired images in the vector $\tilde{\mathrm{D}} = [\tilde{D}_1, \cdots, \tilde{D}_N]^\intercal$, the matrix $\mathrm{M}_{nm} = \exp(im\phi_n)$ and a vector $\tilde{\mathrm{C}}(\mathrm{k}) = [\tilde{C}_{-1}, \tilde{C}_0, \tilde{C}_+ 1]^\intercal$. If the inverse of M ($\mathrm{M}^{-1}$) exists,

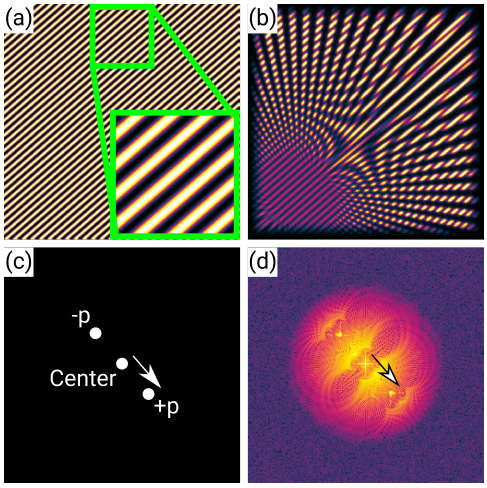

Figure 3.3: Simulation of image acquisition using a sinusoidal illumination pattern **(a)**, as described in eq. (3.2). This results in a single raw data image **(b)**. The multiplication of the illumination pattern with the fluorophore (sample) distribution in real space results in a convolution of the Fourier transform of the illumination pattern **(c)** with the sample's Fourier spectrum (fig. 3.2**(d)**) **prior** to multiplication with the OTF. The acquired data **(d)** contains shifted versions of the samples Fourier spectrum. The wave vectors $m\mathrm{p}$ (see eq. (3.2)) are indicated.

the different components can be separated by

$$\tilde{\mathrm{C}}(\mathrm{k}) = \mathrm{M}^{-1}\tilde{\mathrm{D}}(\mathrm{k}). \tag{3.7}$$

This is illustrated in fig. 3.4.

The final image is the inverse Fourier transform of $\hat{\tilde{S}}(\mathrm{k})$, the final estimate in the Fourier domain. It is obtained by shifting each band to its original position and recombining them using a generalized Wiener filter

$$\hat{\tilde{S}}(\mathrm{k}) = \frac{\sum_{m,d} a_m \tilde{C}_{m,d}(\mathrm{k} + m\mathrm{p}_d)\tilde{h}^*(\mathrm{k} + m\mathrm{p}_d)}{\sum_{m,d} \left|a_m \tilde{h}(\mathrm{k} + m\mathrm{p}_d)\right|^2 + w} A(\mathrm{k}). \tag{3.8}$$

The Wiener filter reduces the degrading influence of the OTF and weights the bands in regions where they overlap according to their expected S/N. The Wiener parameter w is determined empirically, $A(\mathrm{k})$ is an apodization function decreasing linearly from unity at the center to zero near the end of the extended OTF support, shaping the overall spectrum in order to prevent ringing artifacts in the final image, and the asterisk $(*)$ indicates the complex conjugate. Since the resolution improvement only takes place in the direction of p, the process of image acquisition and band separation is repeated for different orientations d to obtain isotropic resolution enhancement. The reconstruction for three different, equally distributed pattern orientations d is shown in fig. 3.5 **(c)** and

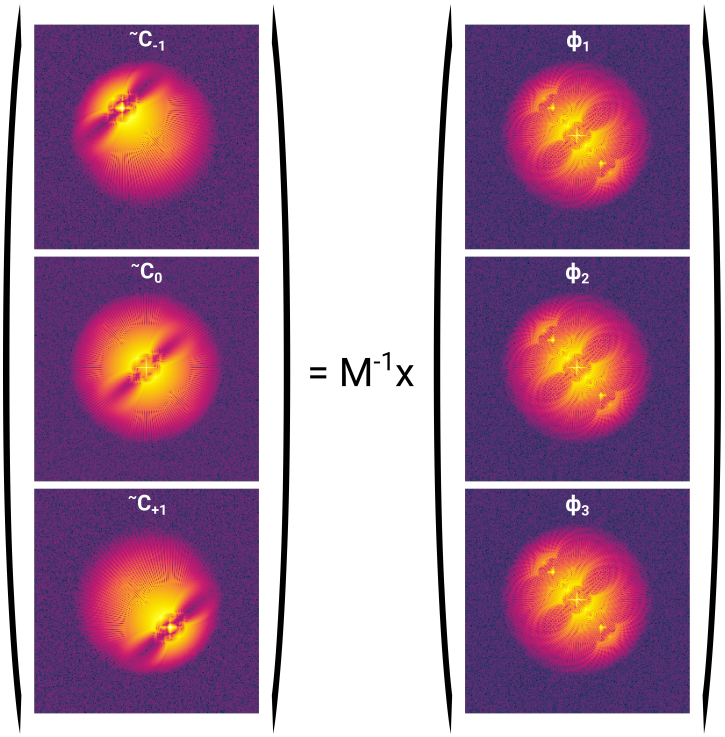

Figure 3.4: Illustration of the separation of the different spectral components as described in eq. (3.7). The vector containing the Fourier spectra of the raw data images at different phase angles ϕ_1, ϕ_2, and ϕ_3 is multiplied by the inverse of M. This results in the separated components $\tilde{C}(k)$. Shifting $\tilde{C}_{\pm 1}$ by $\mp p$ such that they interlock correctly with $\tilde{C}_0$ will then extend the Fourier space in direction of p.

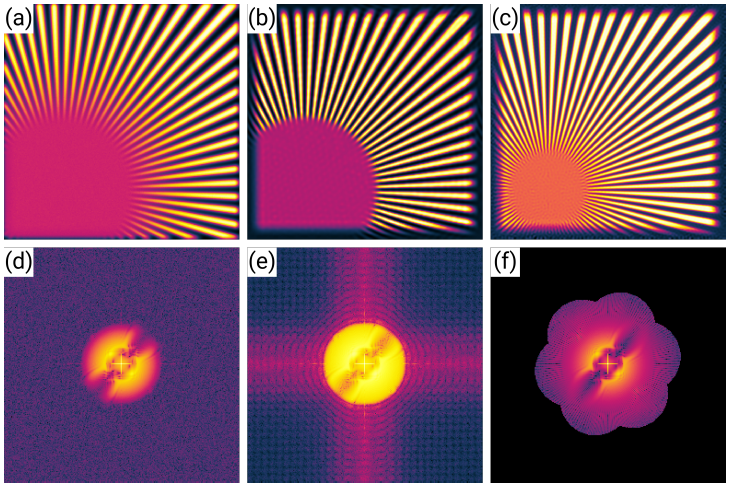

Figure 3.5: Comparison of a WF, planar illumination image **(a)** and its Fourier spectrum **(d)** with a deconvolution result **(b)** and its Fourier spectrum **(e)**, and the SIM reconstruction **(c)** and its Fourier spectrum **(f)**. The deconvolution of the WF image improves the contrast, but the resolution is the same. In the SIM reconstruction the resolution is actually improved. This is also visible in the extend of relevant components in the Fourier spectrum.

compared to a WF image **(a)** and a deconvolution result **(b)**. The deconvolution is the WF image corrected for the OTF within its support. It can be implemented using eq. (3.8) with $m = 0$ for instance.

As can be seen from eqs. (3.7) and (3.8) the phases ϕ_n and the wave vectors p need to be known in order to perform the reconstruction. The parameter estimation is the most critical part in the image reconstruction of SIM. Depending on the implementation of the experimental setup, different approaches to estimate the required parameters are described in the literature.

If an equidistant phase distribution of ϕ_n can be assumed and p lies well within the OTF, retrieval of p is straight forward [43, 74]. Then eq. (3.7) can be applied by using these relative phases in M that differ from the true phases only by a constant offset ϕ_Δ. This also allows for the calculation of the factors a_m. If these assumptions about the phase distribution can not be made, but p is known, the phase of the illumination pattern can be determined based on the phase of the peak at p in $\tilde{D}_n$ [90, 89]. Alternatively the spectrum's autocorrelation can be evaluated at p and the phase can be determined as

$$\phi_n = \arg\left[(\tilde{D}'_n \odot \tilde{D}'_n)(\mathrm{p})\right], \tag{3.9}$$

where $\tilde{D}$ is filtered by the complex conjugated OTF yielding $\tilde{D}'_n = \tilde{D}_n \tilde{h}^*$ in order to reduce the influence of noise and asymmetries in the PSF [103]. Here $\odot$ represents the auto-correlation. Due to its non-iterative and flexible nature

it is the method of choice for the work presented here. It is applied after p is estimated as described in section 3.1.1. The mentioned methods above are described in more detail in the attached paper in section 3.1.1. There also a reference to an iterative phase determination [104] is given.

3.1.1 Subpixel peak detection - Paper 1

The contribution presented here is the determination of the unknown p from the acquired raw data with subpixel precision and subsequent determination of ϕ using eq. (3.9). Although there is a variety of custom-build SIM setups, what they have in common is the need for image reconstruction in which, in one way or another, the parameters of the illumination patter need to be estimated. An error in the estimation of those parameters will manifest itself as artifacts in the reconstructed image, compromising the contrast and resolution. Thus any contribution improving the parameter estimation will increase the benefit of SIM.

The sinusoidal illumination pattern will appear as three distinct peaks in the Fourier transform of the raw data. One peak in the center and each one peak at ±p. If p is not known, it can be estimated from the peak location. Since the raw data is presented as a discretized image (pixels), also the Fourier transform is performed as a discrete Fourier transform (DFT), implemented as the fast Fourier transform (FFT).

A discretized image consists of $N_x \times N_y$ pixels ($N_{x,y}$ being even integers) with indices $\mathrm{x} = [1, \cdots, N_x]$ and $\mathrm{y} = [1, \cdots, N_y]$ and spatial coordinates from $\left(-\frac{N_{x,y}}{2}\right)$ to $\left(\frac{N_{x,y}}{2} - 1\right)$ px (pixels) in steps of 1 px in $\hat{x}$- and $\hat{y}$-direction. The conventional FFT returns an array of the same size with indices u = x and v = y which correspond to frequency coordinates from $\left(-\frac{1}{2}\right)$ px^{-1} to $\left(\frac{1}{2} - \frac{1}{N_{x,y}}\right)$ px^{-1} in steps of $\left(\frac{1}{N_{x,y}}\right)$ px^{-1} in the $\hat{k}_x$- and $\hat{k}_y$-directions. Here $\hat{k}_x$ and $\hat{k}_y$ are frequency domain analogues of $\hat{x}$ and $\hat{y}$. The localization precision of a maximum in the FFT thus depends on the step size $\frac{1}{N_{x,y}}$. This can be improved by padding the image with zeros prior to the Fourier transformation. Depending on the padding size this approach may become computationally expensive.

The idea is to first localize the peaks in $\tilde{D}(\mathrm{k})$ without any padding, giving the indices (u_0, v_0) with a localization precision equal to the step size $\frac{1}{N_{x,y}}$ in the frequency domain. In the second step, the Fourier transform of the input image is calculated in a selected region in the frequency domain around the position of the peak with a chosen oversampling [93, 91] using a twofold matrix

multiplication

$$\tilde{D}(\hat{u},\hat{v}) = \exp\left(\frac{-2\pi i}{N_y}\hat{v}^\intercal y\right) D(x,y) \exp\left(\frac{-2\pi i}{N_x} x^\intercal \hat{u}\right), \tag{3.10}$$

where exp(Z) is the exponential of each element in array Z.

The indices in $\hat{u}$ and $\hat{v}$ can now be chosen as fractional numbers around u_o and v_0. An adequate choice is to select an upsampling factor α and an area around the initial pixel location of 1.5 px in each direction such that $\hat{u},\hat{v} = [-\frac{1.5}{2}, -\frac{1.5}{2} + \frac{1}{\alpha}, \cdots, \frac{1.5}{2} - \frac{2}{\alpha}, \frac{1.5}{2} - \frac{1}{\alpha}] + u_0, v_0$ represent subpixel indices around the original position of the peak. The corresponding frequency space coordinates range from $\left\{-\frac{1}{2} + \left[\frac{1}{N_{x,y}} \cdot \left(u_0, v_0 - \frac{1.5}{2} - 1\right)\right]\right\}$ to $\left\{-\frac{1}{2} + \left[\frac{1}{N_{x,y}} \cdot \left(u_0, v_0 + \frac{1.5}{2} - 1\right)\right] - \frac{1}{\alpha N_{x,y}}\right\}$ px^{-1} in steps of $\frac{1}{\alpha N_{x,y}}\mathrm{px}^{-1}$. The position of the maximum localization in $\tilde{D}(\hat{u},\hat{v})$ will then be as precise as if it had been localized in the FFT of the original image after increasing its size by a factor of α in both directions using zero padding, but at a negligible computational cost. This is illustrated in fig. 3.6. A raw data image under stripe pattern illumination **(a)** and its Fourier spectrum **(b)** (comparable to what is shown in fig. 3.3 for the Siemens star) are show. Although the illumination pattern is hardly visible in the image, the three distinct peaks in its Fourier spectrum indicating the sinusoidal illumination pattern are clearly visible. Determining p by localizing the peak (red cross) in the cropped region of the Fourier spectrum using the conventional FFT leads to a certain deviation from its actual location (green cross) **(c)**. Localizing the maximum in the same region using the presented subpixel resolution improves the precision **(d)**. The cropped regions presented in **(c)** and **(d)** are the same. The peak localization is clearly improved and yield a value for p that is closer to its actual value.

Simulations

Simulations are performed in order to test the subpixel precision estimation of the illumination pattern. Raw data images for two different samples (Siemens star and pirate, see fig. 3.1) are simulated, similar to what was done by Wicker et al. [103, 104]. In the first step the samples (pixel size of 65 nm) are scaled such that their brightest pixel would have a photon count of 5×10^1, 5×10^2, 5×10^3 and 5×10^4 (four data sets) and the darkest a photon count of zero, in order to add noise of the Poisson distribution in the last step. No further offset or noise is added. The illumination patterns are generated based on a fringe spacing

$$L = \left(p_x^2 + p_y^2\right)^{-1/2}, \tag{3.11}$$

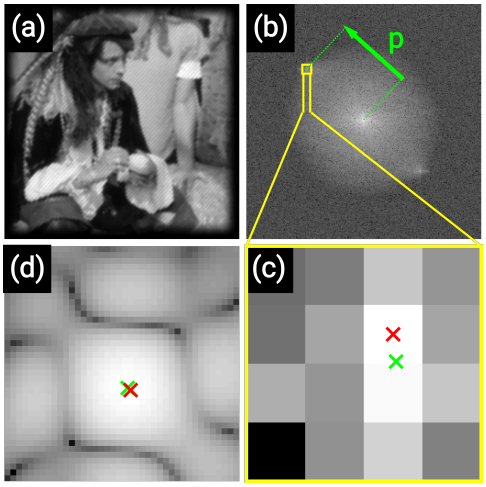

Figure 3.6: A raw data image under stripe pattern illumination **(a)** and its Fourier spectrum **(b)** (comparable to what is shown in fig. 3.3 for the Siemens star). Determining p by localizing the peak (red cross) in the cropped region of the Fourier spectrum using the conventional FFT leads to a certain deviation from its actual location (green cross) **(c)**. Localizing the maximum in the same region using the presented subpixel resolution improves the precision **(d)**. The cropped regions presented in **(c)** and **(d)** are the same. [65]

set to 200 nm and 20 randomly distributed orientation angles

$$\gamma = \arctan\left(p_y/p_x\right), \tag{3.12}$$

see eq. (3.2). For each orientation a set of three phases is generated. The phases are set to 0°, 120° and 240°, with a random variation of a Gaussian distribution at a standard deviation of 10° for each phase step. In order to maintain the maximum possible photon count in each raw data image, the sinusoidal illumination patterns are scaled such that they only vary in a range from zero to one. This way 60 raw data images are simulated per set. Each image is convolved with a point spread function, simulated using a two-dimensional distribution based on the Bessel function of first kind and first order [73], given a numerical aperture of the imaging objective of NA = 1.4. The emission wavelength was set to $\lambda_{\text{em}} = 515$ nm. Finally noise is simulated based on the Poisson distribution. For each raw data image the parameter estimation was performed as described above for upsampling factors of $\alpha = 1$ to 10. First the peaks in the Fourier domain that come from the sinusoidal illumination pattern in real space were localized applying eq. (3.10). From those peak positions the orientation and fringe period of the illumination pattern in each raw data image are calculated using eqs. (3.11) and (3.12).

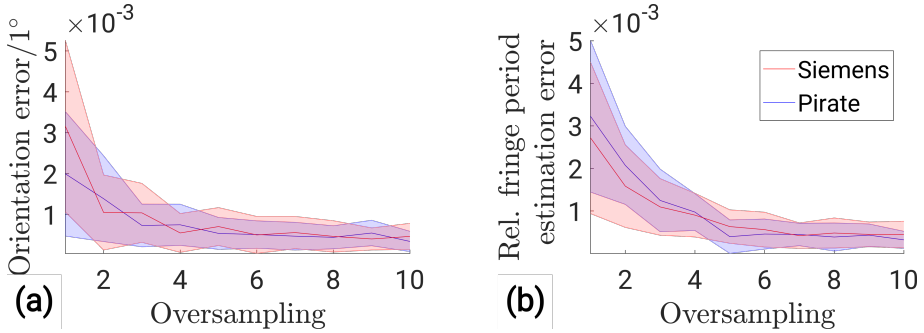

Figure 3.7: The pattern orientation and fringe spacing as calculated per eqs. (3.11) and (3.12) using the detected p, deviate from their actual values as presented in **(a)** and **(b)** respectively. The deviations are calculated using the proposed method at oversampling factors of 1 to 10. The calculations are performed for a maximum expected photon count of 5×10^1 in the brightest pixel. The solid line represents the mean deviation for all 60 samples and the shaded area shows the standard deviation. This is done for two different samples (Siemens star (red) and Pirate (blue)). [65]

Results

It is possible to improve SIM image reconstruction under the described conditions using a subpixel peak detection in the Fourier spectrum of the raw data images. First the improvement of the parameter estimation is demonstrated and then the improvement in the actual reconstructed data.

The orientation γ as calculated from the peak location in Fourier space deviates from the actual orientation $\hat{\gamma}$ by $\Delta\gamma = |\hat{\gamma} - \gamma|$. Only 20 different values for γ are used for the simulations, but for each individual raw data image (three phases per angle) the deviation $\Delta\gamma$ is calculated since the pattern phase and noise may change the result of the peak localization. Thus each raw data image yields a value for γ and $\Delta\gamma$. In fig. 3.7 **(a)** the mean (solid line) and standard deviation (shaded area) of the 60 values for $\Delta\gamma$ in a data set are presented for parameter estimation based on peak localization at different oversampling factors α and for the two different samples. Here only data sets simulated with a maximum photon count of 50 are regarded since the result does not show significant variations for the other selected photon counts. The determination of the pattern orientation is significantly improved through subpixel peak localization.

In a similar way, the fringe spacing L as calculated per eq. (3.11) has a deviation from the initially set 200 nm. This deviation is calculated as $\Delta L = \frac{|L - 200\,\mathrm{nm}|}{200\,\mathrm{nm}}$ in order to free the measure from scaling. The evaluation in fig. 3.7 **(b)** shows the mean (solid line) and standard deviation (shaded area) of the 60 values

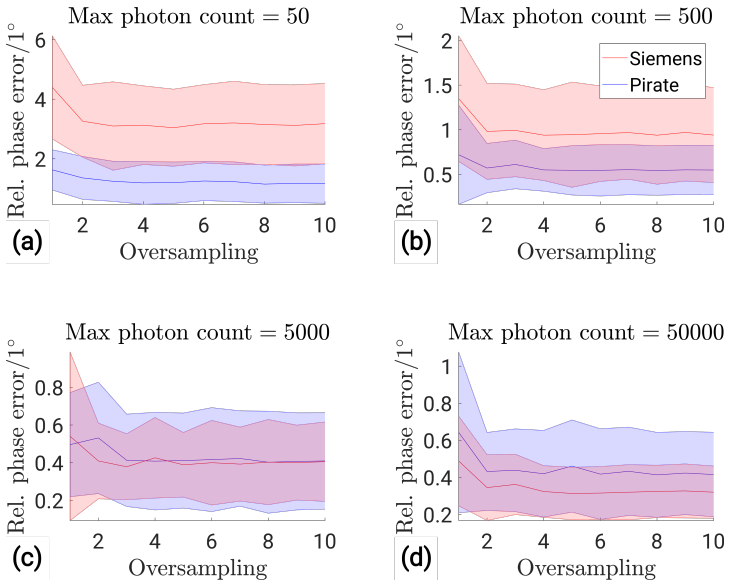

Figure 3.8: The relative error of the phase estimation depending on the oversampling in the wave vector estimation for four different maximum photon counts of 5×10^1, 5×10^2, 5×10^3 and 5×10^4 in **(a)**, **(b)**, **(c)**, and **(d)** is shown. For both samples the solid lines represent the mean value and the shaded areas the standard deviation of the phase error. [65]

for ΔL in a data set. This evaluation is presented for parameter estimation based on peak localization at different oversampling factors α and for two different samples. The underlying data sets are simulated using a maximum photon count of 50. As for the orientation deviation, this result is exemplary for all selected photon counts. Since the determination of the pattern period depends on the precision of the peak localization in a similar manner as the determination of the pattern angle, it shows a related improvement behavior.

The pattern phase for each raw data image is calculated using eq. (3.9) and the determined value for p. The goodness of the determined values for the phases are evaluated following [103, 104]. For each orientation γ, the deviation of the three phases was calculated as $\delta\phi = \phi - \hat{\phi}$. The relative error E_γ^r for one orientation is then calculated as the standard deviation of all three $\delta\phi_\gamma$ in a subset. As described in [103, 104], this way a global phase offset is rejected. The mean (solid line) and standard deviation (shaded area) of E_γ^r are shown in fig. 3.8 as a function of α. A different evaluation of the estimated phases is shown in fig. 3.9. Instead of the relative error E_γ^r, the absolute error E_γ^a is presented. It is calculated as the mean of the absolute values of all three $\delta\phi_\gamma$ in a subset. This way a global phase offset is not rejected in the evaluation. The relative phase error does not significantly change when determining the

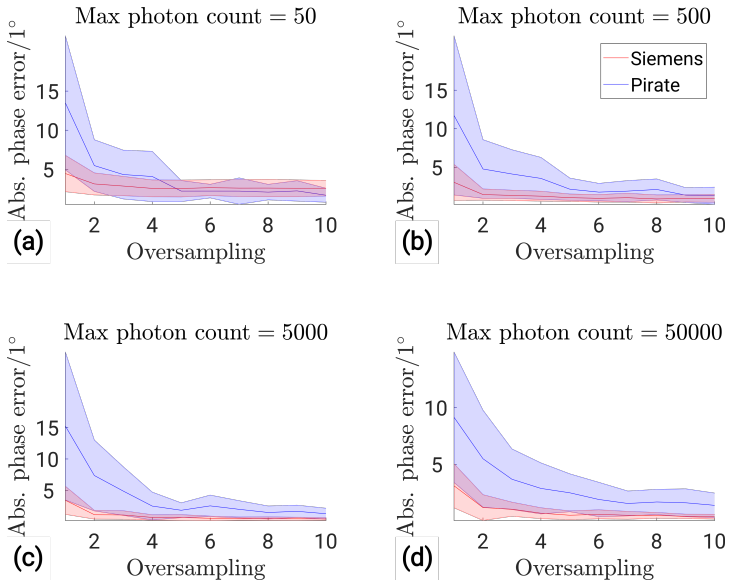

Figure 3.9: The absolute error of the phase estimation depending on the oversampling in the wave vector estimation for four different maximum photon counts of 5×10^1, 5×10^2, 5×10^3 and 5×10^4 in **(a)**, **(b)**, **(c)**, and **(d)** is shown. For both samples the solid lines represent the mean value and the shaded areas the standard deviation of the phase error. [65]

pattern's phase values using eq. (3.9) for high precision determination of p as presented above. However the absolute phase error is reduced significantly such that the determination of a global phase offset ϕ_Δ.

Finally fig. 3.10 shows the influence of the proposed parameter estimation at subpixel precision. A raw data set is simulated as described above with three pattern angles of 11°, 71° and 131° (similar to [90]) and three phases each at a maximum photon count of 5×10^4. The data sets used to generate actual image reconstructions only contain nine raw images; three pattern orientations with three phases each. Although the pattern angles are selected such that an isotropic resolution improvement can be achieved, the selected phases are still displaced from an equidistant distribution as described above. In addition to the SIM raw data, a WF image under planar illumination is simulated and the result of a Wiener deconvolution is shown in **(a)**. The SIM reconstruction based on the actual input parameters yields the optimal result in **(b)** with the expected resolution enhancement compared to **(a)**. Panels **(c)** and **(d)** show the reconstruction results based on parameter estimation for oversampling factors of 1 and 10. In the last row panels **(e)** and **(f)** show the deviations of the results in **(c)** and **(d)** from **(b)** respectively. It is the absolute value of the difference of the values in corresponding pixels and it can be seen, that a reconstruction based on subpixel precision parameter estimation at an oversampling factor

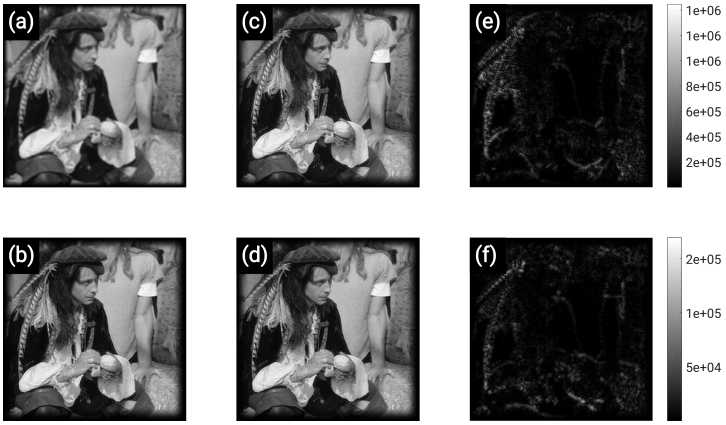

Figure 3.10: Simulated imaging of the pirate sample for a raw data set of nine images (three orientations with three phases each). Panel **(a)** shows the result of a conventional WF deconvolution under planar illumination. The SIM reconstruction with known pattern parameters in **(b)** shows the expected resolution enhancement. In **(c)** and **(d)** the image reconstruction based on the proposed parameter estimation for oversampling of 1 and 10 respectively are show. In **(e)** and **(f)** the absolute deviation of the reconstruction as shown in **(c)** and **(d)** from the reconstruction with know pattern parameters are presented. [65]

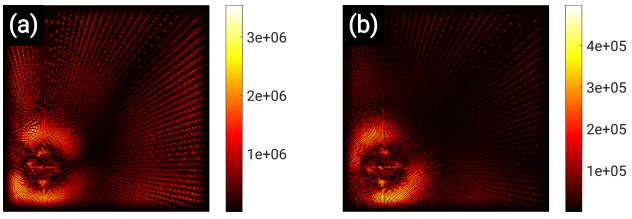

Figure 3.11: Similar to fig. 3.10 **(e)** and **(f)**, the absolute deviation of the reconstruction from the reconstruction with know pattern parameters are presented for oversampling factors of one and ten in **(a)** and **(b)** respectively. [65]

of 10 yields a result whose deviation from the optimal reconstruction can be reduced by almost one order of magnitude around sharp edges in the image. For the presented data an oversampling larger than 10 does not improve the result of the reconstruction in terms of the shown deviation. The same evaluation has been done for the Siemens star as presented in fig. 3.11. Here the absolute deviations of the reconstructions for one- and ten-fold oversampling are shown in **(a)** and **(b)** similar to fig. 3.10 **(e)** and **(f)**.

Conclusion

Peak localization in the Fourier spectrum of SIM raw data, in order to determine the wave vector of the imposed sinusoidal illumination pattern in real space does improve with subpixel peak localization. Fourier space based determination of the orientation and fringe spacing of sinusoidal patterns in real space is presented and its feasibility demonstrated on simulated data. The subsequent improvement of the autocorrelation based pattern phase estimation does show an improvement for the absolute phase value. This way the precise parameter estimation without prior knowledge on the illumination pattern that is necessary for a successful reconstruction of the data is possible. Furthermore, no iterative process is needed and the computational cost are marginal. Simulation results show, that the presented method can reduce the deviation from an optimal reconstruction by one order of magnitude as compared to a conventional parameter estimation.

Paper 1: Accurate estimation of the illumination pattern's orientation and wavelength in sinusoidal structured illumination microscopy

- Published in Applied Optics, February 2018
- Authors:
  - Marcel Lahrberg,
  - Mandeep Singh,
  - Kedar Khare,
  - and Balpreet Singh Ahluwalia
- *Author contributions:* M.L. implemented the simulations framework, designed the study and wrote the manuscript. M.S. contributed to the implementation of algorithm. K.K. conceived the idea and proposed the implementation. B.S.A. supervised the project. All authors reviewed and commented on the manuscript.

Research Article Vol. 57, No. 5 / 10 February 2018 / Applied Optics 1019

applied optics

Accurate estimation of the illumination pattern's orientation and wavelength in sinusoidal structured illumination microscopy

Marcel Lahrberg,[1] Mandeep Singh,[2] Kedar Khare,[2] and Balpreet Singh Ahluwalia[1,*]

[1]Department of Physics and Technology, University of Tromsø, Tromsø N-9037, Norway
[2]Department of Physics, Indian Institute of Technology Delhi, New Delhi 110016, India
*Corresponding author: balpreet.singh.ahluwalia@uit.no

Received 6 September 2017; revised 31 December 2017; accepted 31 December 2017; posted 5 January 2018 (Doc. ID 305681); published 2 February 2018

Structured illumination microscopy is able to improve the spatial resolution of wide-field fluorescence imaging by applying sinusoidal stripe pattern illumination to the sample. The corresponding computational image reconstruction requires precise knowledge of the pattern's parameters, which are its phase (ϕ) and wave vector (p). Here, a computationally inexpensive method for estimation of p from the raw data is proposed and illustrated with simulations. The method estimates p through a selective discrete Fourier transform at tunable subpixel precision. This results in an accurate p estimation for all the illumination patterns and subsequently improves the superresolution image recovery by a factor of 10 around sharp edges as compared to an integer pixel approach. The technique as presented here is of major interest to the large variety of custom-build systems that are used. The feasibility of the presented method is proven in comparison with published data.

OCIS codes: (100.6640) Superresolution; (180.2520) Fluorescence microscopy; (100.2000) Digital image processing; (100.2650) Fringe analysis.

https://doi.org/10.1364/AO.57.001019

1. INTRODUCTION

Wide-field fluorescence microscopy is limited in its maximum spatial resolution to what is commonly known as the Abbe diffraction limit [1]. The diffraction limit is a result of the finite range of spatial frequencies that a microscope's objective can capture depending on its aperture. The 2D image formation under plain illumination can be formulated as a convolution ($\otimes$), giving $D(\mathbf{r}) = [S(\mathbf{r})I] \otimes h(\mathbf{r})$, with the acquired image D, the sample S, the plain illumination intensity I, the point spread function (PSF) h and the spatial coordinate $\mathbf{r}$. In the Fourier transform of this expression, the convolution is replaced by a multiplication and vice versa $\tilde{D}(\mathbf{k}) = [\tilde{I}(\mathbf{k}) \otimes \tilde{S}(\mathbf{k})]\tilde{h}(\mathbf{k})$, where tilde ($\sim$) indicates the Fourier transform, $\mathbf{k}$ is the Fourier space coordinate or spatial frequency, and $\tilde{h}$ is called the optical transfer function (OTF), which has the property of limiting the highest spatial frequency of the sample represented in the image to a cutoff frequency $\|\mathbf{k}\|_2 \leq k_{\max}$ and thus the maximum resolution of the image. Introducing non-uniform illumination of the sample will mix high spatial frequency information lying beyond the OTF's support into its passband [2]. In structured illumination microscopy (SIM), this idea can be used by implementing a sinusoidal stripe pattern illumination. It is described by a wave vector $\mathbf{p} = p_x\hat{k}_x + p_y\hat{k}_y$, with the unit vectors $\hat{k}_x$ and $\hat{k}_y$, that determines a pattern angle

$$\gamma = \arctan(p_y/p_x), \tag{1}$$

a fringe spacing of

$$L = (p_x^2 + p_y^2)^{-1/2}, \tag{2}$$

and a phase ϕ yielding the pattern's shift along the wave vector. Computational image reconstruction upon raw data acquisition may now separate spatial frequency components shifted from their original position into the passband and those naturally lying within the passband [3]. Relocating shifted components to their original position eventually results in a larger information content in the Fourier domain and equivalently in a higher resolution of the reconstructed image. For a single SIM reconstruction, multiple raw images of the sample with different illumination patterns are needed. In the 2D case, a typical configuration of three different illumination wave vectors $\mathbf{p}$ (with constant fringe period and three different orientations) and three different phases ϕ each yielding a total of nine images can be used to reconstruct one image. Image reconstruction in SIM for the described stripe pattern illumination is well known and can be derived from the more general 3D case [4]. Software

implementations for SIM reconstruction are readily available [5,6]. Given a sinusoidal illumination pattern in the object plane, its wave vector **p** and phase ϕ need to be known for each of the raw data images to perform the well-established direct reconstruction. Estimation of **p** and ϕ is a critical task in SIM and is addressed here because a wrong parameter estimation for one of the nine raw data images is sufficient to corrupt the overall reconstruction. Common methods used to estimate the phase rely on precise knowledge of the wave vector [7–10] or require the pattern phases to be equally distributed [4,6]. This means that an incorrect estimation of **p** will inevitably lead to a wrong value for ϕ if no further assumptions on the phase distribution can be made and thus prevent correct image reconstruction. Furthermore, some of the methods for parameter estimation involve iterative steps that come with an increased computational cost [6,7]. This problem is usually addressed by gaining experimental control over the illumination pattern, using expensive hardware like spatial light modulators, vibration-free suspension systems, and piezo actuators to introduce predefined phase shifts. The idea of the proposed method is to determine the wave vector **p**, based on the raw data images in a noniterative way at a precision that is sufficient to apply a direct solution for the phase estimation as presented by Wicker [8].

As can be seen in Fig. 1, the sinusoidal illumination pattern results in three peaks in the Fourier spectrum of each input image, and **p** is estimated by localizing these peaks. Because the input images are real valued, one peak will be located at the center (zero frequency), and the other two peaks will be distributed symmetrically around the center along the vector **p** in the Fourier space. In essence, the algorithm presented here localizes one of the outer peaks with subpixel precision in the absolute value map of the Fourier transform. First a conventional Fourier transform as given by the fast Fourier transform (FFT) is applied on the raw image. To rule out contributions of the low frequencies, a mask is applied. Frequencies smaller than 95% of the actual pattern frequency are masked. This corresponds to a rough estimate in an actual setup. The maximum in the masked FFT image is identified with integer pixel precision offered by the FFT routine. Then the Fourier transform in a small region around the peak position with a higher sampling is calculated, where the peak can be localized with improved precision. As opposed to padding the raw image with zeros prior to applying the FFT, which increases the precision of the peak localization in the same way albeit at a high computational cost, the proposed method calculates the Fourier transform in a significantly smaller area at a specific sampling rate around the pre-estimated peak location. This reduces the computational cost to a fraction of an approach based on zero padding [11,12].

In Section 2, the theoretical background for sinusoidal SIM, including current methods of parameter estimation and the proposed subpixel peak detection for SIM, is described. In Section 3, the presented method is applied to simulated data, and the results are compared to published data. Finally, Section 4 provides concluding remarks on where the presented method integrates within published methods for parameter estimation.

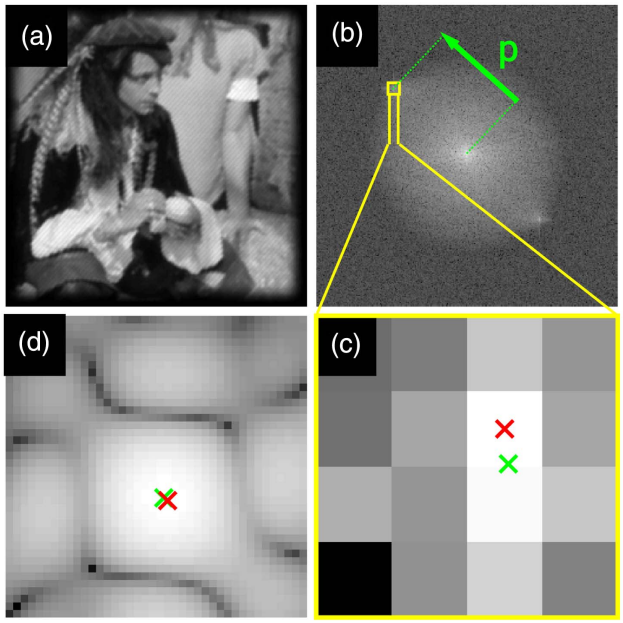

Fig. 1. Illustration of the subpixel peak localization in Fourier space. Panel (a) shows a raw data image of the sample pirate under stripe pattern illumination as described in the text. The edges of the image have been dampened to avoid discontinuities. In (b), the Fourier spectrum of (a) calculated by the FFT routine is shown. The pattern wave vector **p** is indicated in green. Estimating **p** based on the integer pixel location of the maximum in the Fourier spectrum will lead to a peak location mismatch as shown in the cropped Fourier spectrum (c). The red cross is the location of the maximum, the green cross the actual peak location based on the numerical value of the fringe period and orientation used. Panel (d) shows the result of the proposed selective Fourier transform of (a). The center has been selected to be the location of the maximum found in (c). The upsampling factor is $\alpha = 10$, and the size of the area is the same as in (c). Now the maximum (red) is much closer to the actual peak position (green).

2. THEORY

The theoretical background is described widely using the notation of Wicker *et al.* [7,8]. First, the general framework for SIM using a sinusoidal illumination pattern is presented. Then an overview of current parameter estimation methods is outlined, and the proposed approach for computationally inexpensive peak localization at subpixel precision is presented.

A. Sinusoidal SIM

Given a sinusoidal illumination pattern, the image formation can be described as

$$D(\mathbf{r}) = [S(\mathbf{r})I(\mathbf{r})] \otimes h(\mathbf{r}), \tag{3}$$

where

$$I(\mathbf{r}) = \sum_{m=-1}^{1} a_m \exp[im(2\pi \mathbf{p}\mathbf{r} + \phi)] \tag{4}$$

denotes the illumination pattern with the modulation depth a_m. The Fourier transform of $D(\mathbf{r})$ can be written as

$$\tilde{D}(\mathbf{k}) = \sum_{m=-1}^{1} \exp(im\phi)\underbrace{a_m \tilde{S}(\mathbf{k} - m\mathbf{p})\tilde{h}(\mathbf{k})}_{\tilde{C}_m(\mathbf{k})}. \quad (5)$$

It can be seen that $\tilde{D}(\mathbf{k})$ contains frequency components or bands $\tilde{S}_m(\mathbf{k}) = \tilde{S}(\mathbf{k} - m\mathbf{p})$ that are shifted by $m\mathbf{p}$ with respect to their original position in frequency space prior to multiplication with the OTF. In this way, high spatial frequency components of the sample that are not observable under plain illumination are transferred into the image, although the bands are shifted and summed up. By taking N images of the sample with different phases ϕ_n with $n = 1, \ldots, N$, the resulting Fourier transforms of the images $\tilde{D}_n(\mathbf{k})$ can be written as

$$\tilde{\mathbf{D}}(\mathbf{k}) = \mathbf{M}\tilde{\mathbf{C}}(\mathbf{k}), \quad (6)$$

with the acquired images in the vector $\tilde{\mathbf{D}} = [\tilde{D}_1, \ldots, \tilde{D}_N]^\intercal$, the matrix $\mathbf{M}_{nm} = \exp(im\phi_n)$, and a vector $\tilde{\mathbf{C}}(\mathbf{k}) = [\tilde{C}_{-1}, \tilde{C}_0, \tilde{C}_{+}1]^\intercal$. If the inverse of $\mathbf{M}$ ($\mathbf{M}^{-1}$) exists, the different components can be separated by

$$\tilde{\mathbf{C}}(\mathbf{k}) = \mathbf{M}^{-1}\tilde{\mathbf{D}}(\mathbf{k}). \quad (7)$$

The final image is the inverse Fourier transform of $\hat{\tilde{S}}(\mathbf{k})$, the final estimate in the Fourier domain. It is obtained by shifting each band to its original position and recombining them using a generalized Wiener filter:

$$\hat{\tilde{S}}(\mathbf{k}) = \frac{\sum_{m,d} a_m \tilde{C}_{m,d}(\mathbf{k} + m\mathbf{p}_d)\tilde{h}^*(\mathbf{k} + m\mathbf{p}_d)}{\sum_{m,d}|a_m \tilde{h}(\mathbf{k} + m\mathbf{p}_d)|^2 + w} A(\mathbf{k}). \quad (8)$$

The Wiener filter reduces the degrading influence of the OTF and weights the bands in regions where they overlap according to their expected SNR. The Wiener parameter w is determined empirically, $A(\mathbf{k})$ is an apodization function decreasing linearly from unity at the center to zero near the end of the extended OTF support, shaping the overall spectrum to prevent ringing artifacts in the final image, and the asterisk ($*$) indicates the complex conjugate. Because the resolution improvement only takes place in the direction of $\mathbf{p}$, the process of image acquisition and band separation is repeated for different orientations d to obtain isotropic resolution enhancement. As can be seen from Eqs. (7) and (8), the phases ϕ_n and the wave vectors $\mathbf{p}$ need to be known to perform the reconstruction.

B. Conventional Parameter Estimation Techniques

Following Gustafsson *et al.* [4] and Müller *et al.* [6], if an equidistant phase distribution of ϕ_n can be assumed, retrieval of $\mathbf{p}$ is straightforward. Then Eq. (7) can be applied by using these relative phases in $\mathbf{M}$ that differ from the true phases only by a constant offset ϕ_Δ. Given a large enough OTF support with respect to $\mathbf{p}$, and the OTF corrected components $\tilde{C}'_m = \frac{\tilde{C}_m \tilde{h}^*}{|\tilde{h}|^2}$, $\tilde{C}'_{\pm 1}$ will have an overlapping region $\mathbf{k}'$ with $\tilde{C}'_0$, where they will be different by a complex factor a'_m only for the correct $\mathbf{p}$ (see Fig. 2). Thus, by maximizing the cross correlation ($\star$) for $m \neq 0$,

$$[\tilde{C}'_0 \star \tilde{C}'_m](\mathbf{p}) = \sum_{\mathbf{k}'} \tilde{C}'^*_0(\mathbf{k}')\tilde{C}'_m(\mathbf{k}' + m\mathbf{p}), \quad (9)$$

the vector $\mathbf{p}$ can be determined, and the complex factor a'_m is calculated as

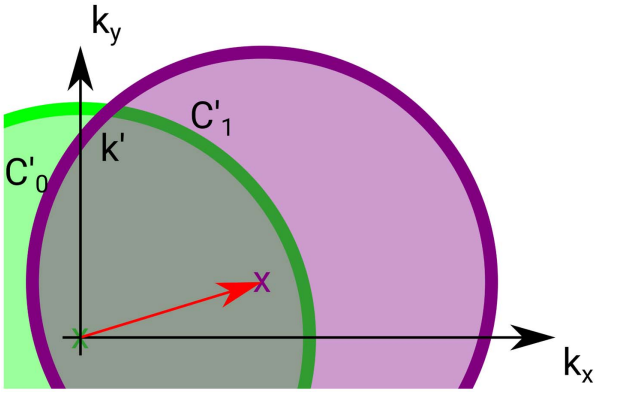

Fig. 2. Spectral overlap. The separated components $\tilde{C}'_0$ and $\tilde{C}'_1$ in Fourier space ($\mathbf{k}_x$, $\mathbf{k}_y$). If $\tilde{C}'_1$ is shifted by $\mathbf{p}$ (red arrow) to its correct position in Fourier space, both bands will have a region of overlap $\mathbf{k}'$ in which they differ only by a complex factor [see Eq. (10)].

$$a'_m = \frac{\sum_{\mathbf{k}'} \tilde{C}'^*_0(\mathbf{k}')\tilde{C}'_m(\mathbf{k}' + m\mathbf{p})}{\sum_{\mathbf{k}'}|\tilde{C}_0(\mathbf{k}')|^2}. \quad (10)$$

Furthermore, $\phi_\Delta = \arg(a'_m)$, with $\arg(\cdot)$ giving the angle of a complex number, and $a_m = |a'_m|$ for $a_0 = 1$. The workflow described so far is applied when equidistant phase steps within one pattern orientation are provided in the experimental setup.

However, if the assumptions about the phase distribution cannot be made but $\mathbf{p}$ is known, the phase of the illumination pattern can be determined based on the phase of the peak at $\mathbf{p}$ in $\tilde{D}_n$ as

$$\phi_n = \arg[\tilde{D}_n(\mathbf{p})], \quad (11)$$

as described by Shroff *et al.* [9,10]. Alternatively the spectrum's autocorrelation can be evaluated at $\mathbf{p}$, and the phase can be determined as

$$\phi_n = \arg[(\tilde{D}'_n \odot \tilde{D}'_n)(\mathbf{p})], \quad (12)$$

as described by Wicker, where $\tilde{D}$ is filtered by the complex conjugated OTF yielding $\tilde{D}'_n = \tilde{D}_n \tilde{h}^*$ to reduce the influence of noise and asymmetries in the PSF [8]. Here $\odot$ represents the autocorrelation. Due to its noniterative and flexible nature, it is the method of choice for the work presented here. It is applied after $\mathbf{p}$ is estimated as described in Section 2.C.

A related method is mentioned for the sake of completeness. It determines the phase values by an iterative optimization. The idea is that two separated bands $\tilde{C}_i(\mathbf{k})$ and $\tilde{C}_j(\mathbf{k} - l\mathbf{p})$ (l being an integer) should not have common information in the region where they overlap for $i \neq j + l$ if they are separated correctly. They have similar components, if $\mathbf{M}$ in Eq. (7) contains the wrong phase values. The phases in the separation matrix $\mathbf{M}$ are then found by minimizing a cost function that evaluates the cross correlation in the overlapping regions [7].

C. Subpixel Peak Detection

Because it may not be possible to do a parameter estimation based on a given prior knowledge like the phase distribution or the pattern wave vector, these parameters need to be extracted from the acquired raw data [13]. We address the situation where no assumption can be made about phase

distribution, and the values of $\mathbf{p}$ are unknown to begin with. We propose to reconstruct $\mathbf{p}$ using the approach we describe as follows and then use the reconstructed value of $\mathbf{p}$ with Eq. (12) for reconstructing the phase value ϕ. This way the precision of the peak localization does not only govern the accuracy for the determined value of $\mathbf{p}$ but also the fidelity of the estimated ϕ. One approach is to localize the peaks in $\tilde{D}(\mathbf{k})$ that come from the sinusoidal illumination pattern. For a discretized image consisting of $N_x \times N_y$ pixels ($N_{x,y}$ being even integers) with indices $\mathbf{x} = [1, \ldots, N_x]$ and $\mathbf{y} = [1, \ldots, N_y]$ and spatial coordinates from $(-\frac{N_{x,y}}{2})$ to $(\frac{N_{x,y}}{2} - 1)$ px in steps of 1 px in $\hat{x}$ and $\hat{y}$ direction, the conventional FFT returns an array of the same size with indices $\mathbf{u} = \mathbf{x}$ and $\mathbf{v} = \mathbf{y}$, which correspond to frequency coordinates from $(-\frac{1}{2})\text{px}^{-1}$ to $(\frac{1}{2} - \frac{1}{N_{x,y}})\text{px}^{-1}$ in steps of $(\frac{1}{N_{x,y}})\text{px}^{-1}$ in the $\hat{k}_x$ and $\hat{k}_y$ directions, $\hat{k}_x$ and $\hat{k}_y$ being frequency domain analogs of $\hat{x}$ and $\hat{y}$. The localization precision of a maximum in the FFT thus depends on the step size $\frac{1}{N_{x,y}}$. This can be improved by padding the image with zeros prior to the Fourier transform. Depending on the padding size, this approach may become computationally expensive.

Our approach to this problem is to first localize the peaks in $\tilde{D}(\mathbf{k})$ without any padding, giving the indices (u_0, v_0) with a localization precision equal to the step size $\frac{1}{N_{x,y}}$ in the frequency domain. In the second step, the Fourier transform of the input image is calculated in a selected region in the frequency domain around the position of the peak with a chosen oversampling [11,12] using a twofold matrix multiplication:

$$\tilde{D}(\hat{\mathbf{u}}, \hat{\mathbf{v}}) = \exp\left(\frac{-2\pi i}{N_y}\hat{\mathbf{v}}^{\mathsf{T}}\mathbf{y}\right) D(\mathbf{x}, \mathbf{y}) \exp\left(\frac{-2\pi i}{N_x}\mathbf{x}^{\mathsf{T}}\hat{\mathbf{u}}\right), \quad \textbf{(13)}$$

where $\exp(\mathbf{Z})$ is the exponential of each element in array $\mathbf{Z}$. The indices in $\hat{\mathbf{u}}$ and $\hat{\mathbf{v}}$ can now be chosen as fractional numbers around u_o and v_0. An adequate choice is to select an upsampling factor α and an area around the initial pixel location of 1.5 px in each direction such that $\hat{\mathbf{u}}, \hat{\mathbf{v}} = [-\frac{1.5}{2}, -\frac{1.5}{2} + \frac{1}{\alpha}, \ldots, \frac{1.5}{2} - \frac{2}{\alpha}, \frac{1.5}{2} - \frac{1}{\alpha}] + u_0, v_0$ represent subpixel indices around the original position of the peak. The corresponding frequency space coordinates range from $\{-\frac{1}{2} + [\frac{1}{N_{x,y}} \cdot (u_0, v_0 - \frac{1.5}{2} - 1)]\}$ to $\{-\frac{1}{2} + [\frac{1}{N_{x,y}} \cdot (u_0, v_0 + \frac{1.5}{2} - 1)] - \frac{1}{\alpha N_{x,y}}\}\text{px}^{-1}$ in steps of $\frac{1}{\alpha N_{x,y}}\text{px}^{-1}$. The position of the maximum localization in $\tilde{D}(\hat{\mathbf{u}}, \hat{\mathbf{v}})$ will then be as precise as if it had been localized in the FFT of the original image after increasing its size by a factor of α in both directions using zero padding at a negligible computational cost. Performing the peak localization for a set of nine raw input images, for a fivefold oversampling the computation times are 0.03 s and 0.43 s and for a tenfold oversampling 0.04 s and 1.80 s for the subpixel approach and the zero padding approach, respectively, on an Intel Core i7 at 2.10 GHz, using MATLAB. With respect to the computational complexity for a raw SIM image of dimension $M \times M$, a fivefold zero padded FFT in both row and column directions will have a computational complexity of $\mathcal{O}(25M^2 \log(25M^2))$, whereas the proposed method has complexity of $\mathcal{O}(5M^2)$. For a tenfold oversampling, these numbers are $\mathcal{O}(100M^2 \log(100M^2))$ versus $\mathcal{O}(10M^2)$. The timing numbers provided can be seen in this context. When the oversampling factor is much smaller than M, as in this case, this is significant computational gain for achieving the same level of accuracy.

3. SIMULATIONS

To test the subpixel precision estimation of the illumination pattern, raw data images for two different samples (Siemens star and pirate; see Fig. 3) have been simulated, similar to what was done by Wicker *et al.* [7,8]. In the first step, the samples (pixel size of 65 nm) have been scaled such that their brightest pixel would have a photon count of 5×10^1, 5×10^2, 5×10^3, and 5×10^4 (four data sets), and the darkest photon count of zero, to add noise of the Poisson distribution in the last step. No further offset or noise was added. The illumination patterns of 200 nm fringe spacing are generated based on 20 randomly distributed orientation angles γ. For each orientation, a set of three phases (0°, 120°, and 240°, with a random variation of a Gaussian distribution at a standard deviation of 10° for each phase step) is generated. To maintain the maximum possible photon count in each raw data image, the sinusoidal illumination patterns are scaled such that they only vary in a range from zero to one. This way 60 raw data images are simulated per set. Each image is convolved with a point spread function, simulated using a 2D distribution based on the Bessel function of first kind and first order [14], given a numerical aperture of the imaging objective of NA = 1.4. The emission wavelength was set to $\lambda_{\text{em}} = 515$ nm. Finally, noise is simulated based on the Poisson distribution. For each raw data image, the parameter estimation was performed as described previously for upsampling factors of $\alpha = 1$–10. First the peaks in the Fourier domain that come from the sinusoidal illumination pattern in real space were localized applying Eq. (13). From those peak positions, the orientation and fringe period of the illumination pattern in each raw data image are calculated using Eqs. (1) and (2).

The orientation γ as calculated from the peak location in Fourier space deviates from the actual orientation $\hat{\gamma}$ by $\Delta\gamma = |\hat{\gamma} - \gamma|$. Although only 20 different values for γ were used for the simulations, for each individual raw data image, the deviation $\Delta\gamma$ was calculated because the pattern phase and noise may change the result of the peak localization. Thus, each raw data image yields a value for γ and $\Delta\gamma$. In Fig. 4(a), the

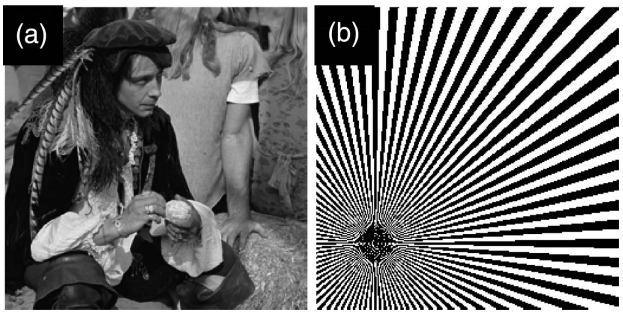

Fig. 3. Samples (a) pirate and (b) Siemens star as they have been used in the simulations. They are represented in a size of 256 × 256 px.

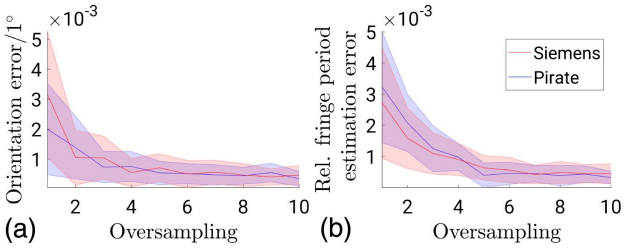

Fig. 4. (a) Deviation of the pattern orientation and (b) fringe spacing calculated from the detected peak position from the actual value for oversampling factors of 1–10. The calculations are performed for a maximum expected photon count of 5×10^1 in the brightest pixel. The solid line represents the mean deviation for all 60 samples, and the shaded area shows the standard deviation. This is done for two different samples [Siemens star (red) and pirate (blue)].

mean (solid line) and standard deviation (shaded area) of the 60 values for $\Delta\gamma$ in a data set are presented for parameter estimation based on peak localization at different oversampling factors α and for the two different samples, for data sets simulated with a maximum photon count of 50. This result does not show significant variations for the other selected photon counts and is thus exemplary.

Similar to the orientation, the fringe spacing L as calculated per Eq. (2) has a deviation from the initially set 200 nm. This deviation is calculated as $\Delta L = \frac{|L-200\ \text{nm}|}{200\ \text{nm}}$ to free the measure from scaling. The evaluation in Fig. 4(b) shows the mean (solid line) and standard deviation (shaded area) of the 60 values for ΔL in a data set. This evaluation is presented for parameter estimation based on peak localization at different oversampling factors α and for two different samples. The underlying data sets are simulated using a maximum photon count of 50. As for the orientation deviation, this result is exemplary for all selected photon counts. The pattern phase for each raw data image is calculated with Eq. (12) and the determined value for $\mathbf{p}$. The values for the phases are evaluated following [7,8]. For each orientation γ, the deviation of the three phases was calculated as $\delta\phi = \phi - \hat{\phi}$. The relative error E_γ^r for one orientation is then calculated as the standard deviation of all three $\delta\phi_\gamma$ in a subset. As described in Refs. [7,8], this way a global phase offset is rejected. The mean (solid line) and standard deviation (shaded area) of E_γ^r are shown in Fig. 5 as a function of α.

A second evaluation of the estimated phases is shown in Fig. 6. Instead of the relative error E_γ^r, the absolute error E_γ^a is presented. It is calculated as the mean of the absolute values of all three $\delta\phi_\gamma$ in a subset. This way a global phase offset is not rejected in the evaluation.

Finally, Fig. 7 shows the influence of the proposed parameter estimation at subpixel precision. A raw data set was simulated as described earlier with three pattern angles of 11°, 71°, and 131° (similar to Shroff *et al.* [9]) and three phases each at a maximum photon count of 5×10^4. The data sets used to generate actual image reconstructions only contain nine raw images. Although the pattern angles are selected such that an isotropic resolution improvement can be achieved, the selected phases are still displaced from an equidistant distribution as described previously. In addition to the SIM raw data, a wide-field image under plain illumination was simulated,

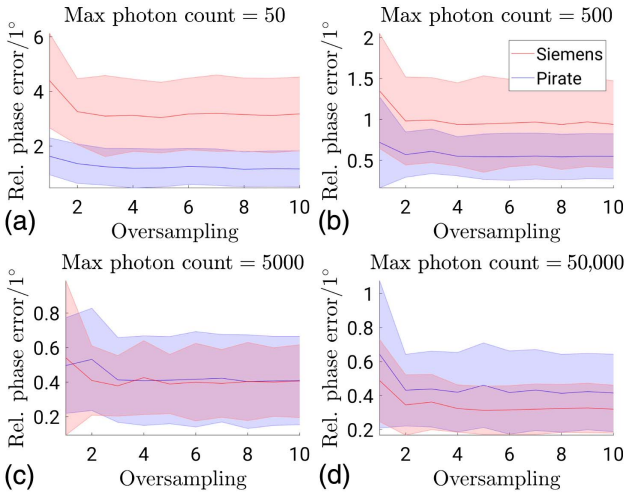

Fig. 5. Relative phase error at oversampling of 1–10 for four different photon levels (a) 5×10^1, (b) 5×10^2, (c) 5×10^3, and (d) 5×10^4, and two different samples [Siemens star (red) and pirate (blue)]. The solid lines represent the mean value and the shaded areas the standard deviation of the phase error.

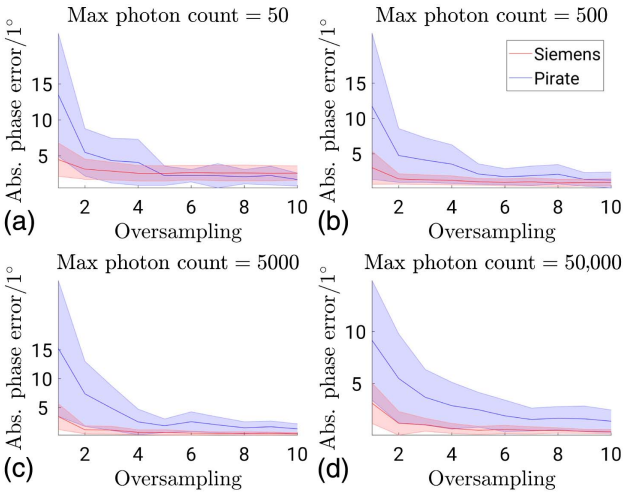

Fig. 6. Absolute phase error at oversampling of 1–10 for four different photon levels (a) 5×10^1, (b) 5×10^2, (c) 5×10^3, and (d) 5×10^4, and two different samples [Siemens star (red) and pirate (blue)]. The solid lines represent the mean value and the shaded areas the standard deviation of the phase error.

and the result of a Wiener deconvolution is shown in Fig. 7(a). The SIM reconstruction based on the actual input parameters yields the optimal result in Fig. 7(b) with the expected resolution enhancement compared to Fig. 7(a). Figures 7(c) and 7(d) show the reconstruction results based on parameter estimation for oversampling factors of 1 and 10. Figures 7(e) and 7(f) show the deviations of the results in Figs. 7(c) and 7(d) from Fig. 7(b), respectively. It is the absolute value of the difference of the values in corresponding pixels, and it can be seen that a reconstruction based on subpixel precision parameter estimation at an oversampling factor of 10 yields a result whose deviation from the optimal

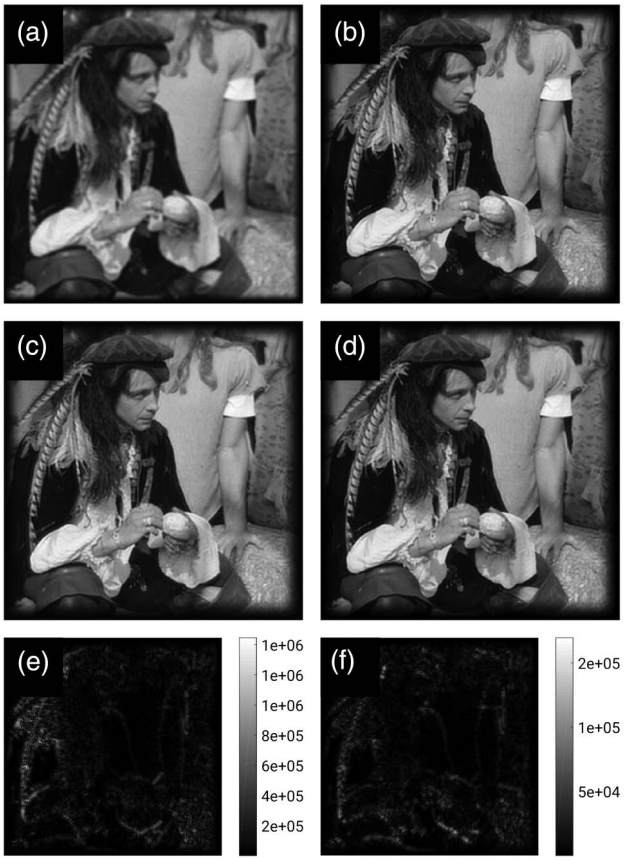

Fig. 7. Reconstruction of simulated SIM data. For a raw data set of nine images (three orientations with three phases each), parameter estimation and reconstruction were performed for oversampling factors of 1 and 10. Panel (a) shows the result of a conventional wide-field deconvolution under plain illumination. The SIM reconstruction with known pattern parameters in (b) shows the expected resolution enhancement. In (c) and (d), the image reconstruction based on the proposed parameter estimation for oversampling of 1 and 10, respectively, is shown. In (e) and (f), the absolute deviation of the reconstruction as shown in (c) and (d) from the reconstruction with known pattern parameters is presented.

reconstruction can be reduced by almost 1 order of magnitude around sharp edges in the image. For the presented data, an oversampling larger than 10 does not improve the result of the reconstruction in terms of the shown deviation. The same evaluation has been done for the Siemens star as presented in Fig. 8. Here the absolute deviations of the reconstructions for one- and tenfold oversampling are shown in Figs. 8(a) and 8(b) similar to Figs. 7(e) and 7(f).

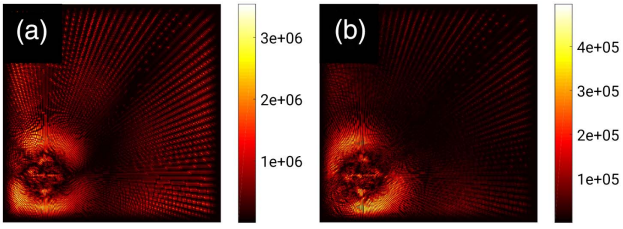

Fig. 8. Similar to Figs. 7(e) and 7(f), the absolute deviation of the reconstruction from the reconstruction with known pattern parameters is presented for oversampling factors of (a) 1 and (b) 10.

4. RESULTS AND DISCUSSION

It can be shown that the proposed subpixel precision localization of a maximum in the Fourier domain is suitable to determine the wave vector of a sinusoidal pattern imposed on a structure in real space (Fig. 4). This method achieves an improvement in precision as a method based on zero padding would do, although at a fraction of the computational cost (time and memory), especially at increased oversampling factors. The benefit of this approach can be directly shown when doing phase estimation on 2D SIM data using Eq. (12).

In the introduction of the noniterative phase estimation [8], its feasibility was demonstrated in comparison with an iterative approach [7] that would determine the relative phases in a data set, and a reference to [2] and [15] is given for the estimation of the global phase offset to get the absolute phases. Figure 5 shows that the quality of the phase estimation does not change significantly by increasing the precision of the wave vector estimation in the tested range, and the results, at least for the pirate sample, correspond well to published results in Figs. 2(a) and 2(b) of Ref. [8] for the single-step approach at maximum expected number of photons of 5×10^1, 5×10^2, 5×10^3, and 5×10^4. Disregarding a global phase offset, localizing the pattern wave vector to conventional pixel precision is sufficient, as the error drops below 1° for realistic SNRs.

However, the absolute phase error as shown in Fig. 6 suggests that if Eq. (12) is to be applied for phase estimation, the presented method is of major importance. The high-precision calculation of the wave vector based on subpixel peak localization enables the phase estimation without an additional step to find a global phase offset. A difference in the behavior of both samples is visible. The Siemens star sample enables good phase detection even at lower oversampling. Phase estimation, except for the lowest simulated SNR, performs well. The more generalized sample pirate shows significant improvement with an increased oversampling.

Applying subpixel precision peak localization in the Fourier domain to determine the orientation and fringe spacing of sinusoidal patterns in real space is presented and its feasibility demonstrated on simulated data. Especially the application of the results in an established method for phase estimation shows that this is a way for parameter estimation in sinusoidal structured illumination microscopy for comparably fine (i.e., 200 nm) illumination patterns.

The benefits are twofold because the whole work flow of determining the necessary parameters in SIM reconstruction does not require prior knowledge of the phase distribution or the pattern wave vector, nor does it depend on iterative processes. Furthermore, it was demonstrated that the deviation from the optimal reconstruction can be reduced by about 1 order of magnitude, thus producing a more accurate result using the subpixel peak detection method. In addition, the savings in computational time for SIM reconstruction provided by the proposed subpixel method will be beneficial for real-time reconstruction of the SIM images if the pattern parameters need to be estimated prior to reconstruction.

Funding. H2020 European Research Council (ERC) (336716); Norwegian Centre for International Cooperation in Education, SIU Norway (INCP-2014/10024); University Grants Commission (UGC), India.

Acknowledgment. The authors would like to thank Krishna Agarwal for scientific review of the manuscript. BSA acknowledges ERC and the Norwegian Centre for International Cooperation in Education, SIU-Norway. KK acknowledges University Grant Commission, India funding.

REFERENCES

1. E. Abbe, "Beiträge zur Theorie des Mikroskops und der mikroskopischen Wahrnehmung," Archiv für mikroskopische Anatomie **9**, 413–418 (1873).
2. M. G. L. Gustafsson, "Surpassing the lateral resolution limit by a factor of two using structured illumination microscopy," J. Microsc. **198**, 82–87 (2000).
3. R. Heintzmann and C. G. Cremer, "Laterally modulated excitation microscopy: Improvement of resolution by using a diffraction grating," Proc. SPIE **3568**, 185–196 (1999).
4. M. G. L. Gustafsson, L. Shao, P. M. Carlton, C. J. R. Wang, I. N. Golubovskaya, W. Z. Cande, D. A. Agard, and J. W. Sedat, "Three-dimensional resolution doubling in wide-field fluorescence microscopy by structured illumination," Biophys. J. **94**, 4957–4970 (2008).
5. P. Křížek, T. Lukeš, M. Ovesný, K. Fliegel, and G. M. Hagen, "SIMToolbox: A MATLAB toolbox for structured illumination fluorescence microscopy," Bioinformatics **32**, 318–320 (2015).
6. M. Müller, V. Mönkemöller, S. Hennig, W. Hübner, and T. Huser, "Open-source image reconstruction of super-resolution structured illumination microscopy data in ImageJ," Nat. Comms. **7**, 10980 (2016).
7. K. Wicker, O. Mandula, G. Best, R. Fiolka, and R. Heintzmann, "Phase optimisation for structured illumination microscopy," Opt. Express **21**, 2032–2049 (2013).
8. K. Wicker, "Non-iterative determination of pattern phase in structured illumination microscopy using auto-correlations in Fourier space," Opt. Express **21**, 24692–24701 (2013).
9. S. A. Shroff, J. R. Fienup, and D. R. Williams, "Phase-shift estimation in sinusoidally illuminated images for lateral superresolution," J. Opt. Soc. Am. A **26**, 413–424 (2009).
10. S. A. Shroff, J. R. Fienup, and D. R. Williams, "Lateral superresolution using a posteriori phase shift estimation for a moving object: Experimental results," J. Opt. Soc. Am. A **27**, 1770–1782 (2010).
11. R. Soummer, L. Pueyo, A. Sivaramakristnan, and R. J. Vanderbei, "Fast computation of Lyot-style coronagraph propagation," Astrophys. J. Suppl. Ser. **167**, 81–99 (2006).
12. M. Singh and K. Khare, "Accurate efficient carrier estimation for single-shot digital holographic imaging," Opt. Lett. **41**, 4871–4874 (2016).
13. L. Condat, J. Boulanger, N. Pustelnik, S. Sahnoun, and L. Sengmanivong, "A 2-D spectral analysis method to estimate the modulation parameters in structured illumination microscopy," in *IEEE 11th International Symposium on Biomedical Imaging (ISBI)*, 2014, vol. **11**, pp. 604–607.
14. E. Mudry, K. Belkebir, J. Girard, J. Savatier, E. Le Moal, C. Nicoletti, M. Allain, and A. Sentenac, "Structured illumination microscopy using unknown speckle patterns," Nat. Photonics **6**, 312–315 (2012).
15. J. T. Frohn, "Super-resolution fluorescence microscopy by structured light illumination" Ph.D. dissertation (Swiss Federal Institute of Technology, 2000).

3.2 Large field of view structured illumination microscopy

In the previous section the pattern parameter estimation for SIM using pattern frequencies that lie within the support of the imaging objective's OTF was discussed. This means, that the FoV for high resolution imaging (high NA of the objective) is limited by the small FoV of that objective lens. In this section two approaches to increase the FoV in SIM over what is conventionally achieved are investigated. These techniques are tSIM (paper 2 [60], attached in section 3.2.1) and cSIM (paper 3 [52], attached in section 3.2.2). The idea is that the epifluorescence approach in most SIM implementations uses the same objective lens for illumination pattern generation as for imaging. As can be seen from eq. (3.5), the addition of high frequency components in the Fourier space and thus the resolution improvement, beyond the classical resolution limit, is limited by the maximum size of p, the illumination pattern frequency. Here the classical resolution limit refers to the resolution obtained in WF fluorescence imaging under planar illumination, the Rayleigh criterion for instance. In SIM implementations using an epifluorescence microscope, excitation of the sample and image acquisition are done with the same objective lens. The resolution of the illumination pattern is limited by the imaging objective in a similar way, the resolution of a raw data image is limited. Since NA and FoV of an objective lens are inversely proportional, imaging with an epifluorescence SIM setup will always involve a trade-off between resolution and FoV. This can be expressed in the SBP [37]

$$\mathrm{SBP} = \frac{\mathrm{FoV}}{(0.5\delta)^2}. \tag{3.13}$$

with δ as the system's resolution, and the factor 0.5 stemming from the Nyquist-Shannon sampling theorem. It expresses the information content in the reconstructed image, the optimal number of pixels. Since the FoV of an imaging objective lens is inversely proportional to the NA, and the resolution is proportional to the NA, a high NA objective will allow for a high resolution over a smaller FoV and vice versa, such that the SBP does not change significantly. It is the SBP that ultimately defines the throughput of an imaging system and is thus the interesting figure of merit for application in biomedical fields.

The generation of sinusoidal illumination patterns is achieved by interfering two coherent beams. Although a microscope objective is able to perform that task, this can also be done by much simpler means. Two examples are the techniques tSIM and cSIM. In tSIM a set of mirrors is used to bring the coherent beams to interference in the sample plane. The idea is to increase the SBP by increasing the FoV as compared to a conventional SIM implementation. This means to keep the high frequency pattern generation, but using a low NA imaging objective with a large FoV. In cSIM two coherent waveguide modes

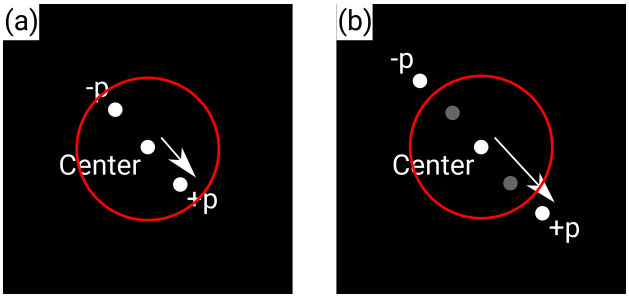

Figure 3.12: Similar to the presentation in fig. 3.3 **(c)** the pattern frequency and OTF support (red circle) are indicated for a single lens epifluorescence setup in **(a)**. If the illumination pattern generation is decoupled from the imaging objective lens, the corresponding peaks in the Fourier domain might theoretically lie outside the support of the OTF as indicated in **(b)**. The illumination pattern would not directly be indicated in the raw data anymore.

are brought to interference and the sinusoidal intensity distribution in the evanescent field on top of the waveguide is used for sample excitation. Here the increase in SBP is mainly based on the reduction in δ, improving the pattern resolution, but using a higher NA objective, as compared to tSIM. In both approaches the image acquisition is done using a standard fluorescence microscope. This way the illumination pattern is generated independently form the imaging objective lens and the frequency shift p depends on the mirror configuration and waveguide design respectively. Both techniques are described in this chapter with main focus on simulation results.

It is important to notice, that the presented work on subpixel peak localization may not directly apply in the reconstruction of tSIM, and cSIM data. Associated with a pattern generation decoupled from the imaging objective lens is the generation of pattern frequencies that possibly lie outside the support of the OTF as presented in fig. 3.12. In **(a)** the wave vector of the sinusoidal illumination pattern lies well within the support of the OTF and may thus be detected using the subpixel peak localization. The pattern frequency in **(b)** may be so high that the associated peaks in the Fourier domain lie outside the OTF support and are not transmitted at all. Thus subpixel peak localization in order to determine the pattern wave vector can not be used. A conclusion regarding the work on tSIM and cSIM is given on page 129.

3.2.1 Transillumination SIM - Paper 2

If the pattern in SIM is generated using an objective lens, the pattern resolution and frequency are limited by the lens' NA as described by the Abbe resolution limit due to its coherent nature. As discussed in section 2.1 the considered

image acquisition can actually not be described using the Abbe limit since it is an incoherent process. However, it is common in the literature to do so in order to provide general understanding of SIM and it yields reasonable results when its limited validity is kept in mind. If the resolution in WF fluorescence imaging is thus described by the Abbe limit as well, the achievable resolution for standard epifluorescence SIM using the same imaging objective for pattern generation as for image acquisition is

$$\delta_{\mathrm{SIM}} = \frac{\lambda}{4\mathrm{NA}}. \tag{3.14}$$

This is half the resolution ("twice as good") as the limit described for planar illumination in eq. (2.4), due to the frequency shift. The use of the Abbe limit here does not indicate that the fluorescence imaging process is a coherent process. This is important since SIM under coherent imaging conditions does not improve the image resolution beyond the classical Abbe limit [102].

In tSIM the pattern generation is not limited by the imaging objective since mirrors are used to interfere coherent beams in the object plane. With respect to the pattern generation these mirrors act like higher NA objective lenses. The mirrors in the proposed setup generate sinusoidal illumination patterns by interfering two beams in the sample plane. The angle of this interference can be associated to a NA of that particular mirror set. If the objective lens was used to generate the interference pattern, the pattern frequency would be limited by the objective's NA. For an illustrative purpose, three mirror sets, named NA_1, NA_2, and NA_3 are used that provide interference patterns equivalent to patterns that are generated, using an objective lens with (1) the given NA, (2) twice the given NA, and (3) three times the given NA of the actual imaging objective lens. A typical objective lens with a 10× (low) magnification and a NA=0.25 has FoV with a diameter of 2.2 mm.

For comparison, if the NAs of the mirror setup are equivalent to one, two, and three times the NA of the imaging objective lens (NA_1, NA_2, NA_3), the achievable SBP of conventional WF imaging, using planar illumination, conventional SIM imaging and tSIM imaging are achieved as described in table 3.1. It is an approximation, assuming that the excitation and emission wavelength are the same (λ) and that the Fourier space is filled sufficiently, using multiple patter orientations and intermediate pattern frequencies (NA_1 and NA_2).

In paper 2, the illumination pattern generation is done using a set of mirrors as shown in fig. 3.13. In order to generate sinusoidal stripe patterns for SIM without using an objective lens, a laser beam is expanded, filtered through a diaphragm and used to illuminate a grating on a SLM (fig. 3.13**(a)**). This way the beam is split into diffraction orders, of which the $\pm 1^{\mathrm{st}}$ orders are brought to interference in the sample plane through a mirror set, the 0^{th} order

Imaging condition	Pattern resolution	Image resolution	δ	$\frac{\text{FoV}}{(0.5\delta)^2}$
planar WF	∞	$\frac{\lambda}{2\text{NA}}$	$\left(\frac{1}{\infty}+\frac{2\text{NA}}{\lambda}\right)^{-1}=\frac{\lambda}{2\text{NA}}$	SBP_{WF}
SIM	$\frac{\lambda}{2\text{NA}}$	$\frac{\lambda}{2\text{NA}}$	$\left(\frac{2\text{NA}}{\lambda}+\frac{2\text{NA}}{\lambda}\right)^{-1}=\frac{\lambda}{4\text{NA}}$	$4\ \text{SBP}_{\text{WF}}$
tSIM	$\frac{\lambda}{2\text{NA}_3}=\frac{\lambda}{6\text{NA}}$	$\frac{\lambda}{2\text{NA}}$	$\left(\frac{6\text{NA}}{\lambda}+\frac{2\text{NA}}{\lambda}\right)^{-1}=\frac{\lambda}{8\text{NA}}$	$16\ \text{SBP}_{\text{WF}}$

Table 3.1: Comparing resolution and SBP of different imaging conditions. Since the imaging objective is the same in all cases, the use of a low NA objective, and mirror based pattern generation in tSIM, the SBP can be improved by a factor of 4 as compared to conventional epifluorescence SIM. Here only the highest possible pattern frequencies are considered, such that the pattern resolution for tSIM is based on the mirror set providing the largest interference angle (NA_3).

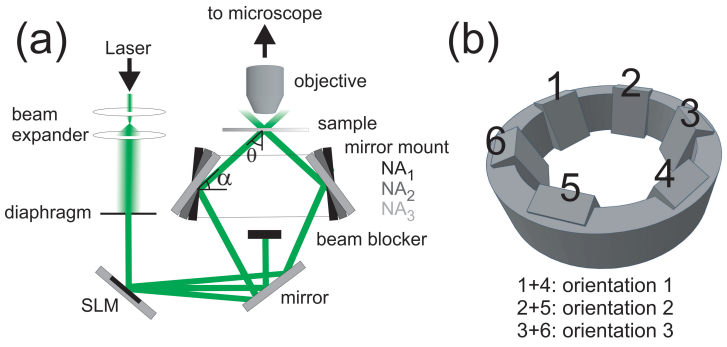

Figure 3.13: The experimental setup for tSIM. **(a)** In order to generate sinusoidal stripe patterns for SIM without using an objective lens, a laser beam is expanded, filtered through a diaphragm and used to illuminate a grating on a spatial light modulator (SLM). This way the beam is split into diffraction orders, of which the $\pm 1^{\text{st}}$ orders are brought to interference in the sample plane through a mirror set, the 0^{th} order is blocked. **(b)** A mirror mount with different sets of mirrors allows for different pattern orientations in the sample plane. The pattern period depends on the mirror angles. [60]

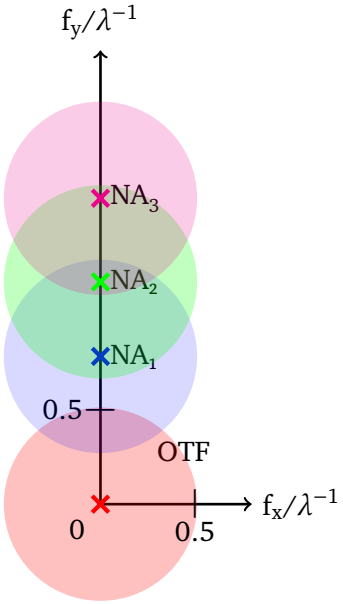

Figure 3.14: Given an imaging objective with NA = 0.25 the OTF support is limited to $\frac{2NA}{\lambda} = 0.5\,\lambda^{-1}$ (red circle). For illumination patterns generated by interfering the excitation light under different angles θ, equivalent NAs of NA_1 (blue cross), NA_2 (green cross), NA_3 (magenta cross) are generated, giving additional information at higher frequencies in the Fourier space in the form of the shifted copies of the conventional OTF (circles of respective color). Although a positive and negative term are always created, here only the information gain in one direction, along the positive y-axis, is shown. [60]

is blocked. A mirror mount (fig. 3.13**(b)**) with different sets of mirrors allows for different pattern orientations in the sample plane. The selected mirror angle α determines the interference angle θ and hence the patter period (α, and θ indicated in **(a)**). Since each pattern generated with given mirror angles can be thought of as a pattern generated by an objective lens with a certain NA, mirror settings are described by equivalent NAs. By rotating the grating structure on the SLM, the pattern orientation (set of two mirrors) is selected. Shifting the grating on the SLM (along the grating wave vector) will introduce a phase shift to the illumination pattern.

The filling of the Fourier space is illustrated in figs. 3.14 and 3.15 using interference angles and corresponding equivalent NAs as shown in table 3.2. In fig. 3.14 the maximum extend in the Fourier domain accessible is illustrated assuming a low NA imaging objective with NA=0.25 and mirror angles such that interference patterns equivalent to those generated by an objective lens of up to NA_3=0.81 are generated. This way the maximum pattern resolution is $\frac{\lambda}{2NA_3} = \frac{\lambda}{1.62}$. Given an unaided WF resolution of $\frac{\lambda}{2NA} = \frac{\lambda}{0.5}$, a resolution

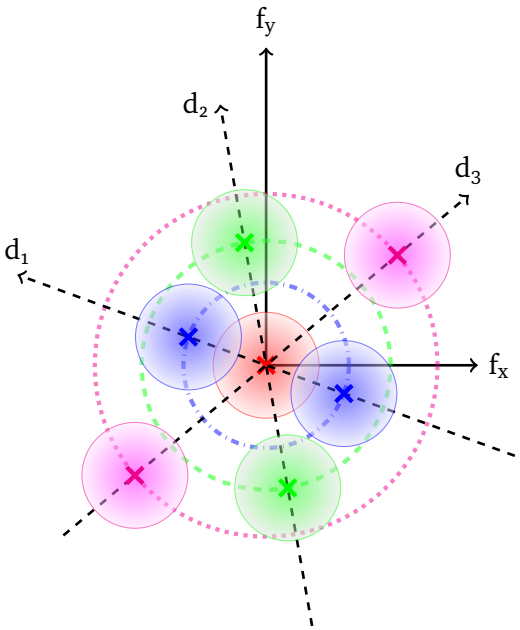

Figure 3.15: In order to fill the Fourier space gapless and isotropically, not only the frequency shifts have to be varied, but the process has also to be repeated for different orientations (d_1, d_2, and d_3). The pattern frequencies and shifted OTFs are depicted as in fig. 3.14. [60]

θ	NA
23°	0.39
36°	0.59
54°	0.81

Table 3.2: Interference angle θ for the pattern generation corresponds to an equivalent NA of an objective lens.

of $\left(\frac{1.62}{\lambda} + \frac{0.5}{\lambda}\right)^{-1} = \frac{\lambda}{2.21}$ can be achieved. Compared to the conventional SIM resolution of $\frac{\lambda}{2\mathrm{NA}}$ (eq. (3.14)), the resolution can be improved by a factor of 2.21 over the FoV of the low NA imaging objective lens. In order to achieve the described resolution improvement isotropically, different pattern orientations as presented in fig. 3.15 are used to fill the Fourier space. This corresponds to an almost fivefold (4.88-fold to be precise) improvement of the SBP as compared to conventional SIM.

Simulations

In order to demonstrate the quality of the reconstructed images, simulations are shown using a variety of NAs (of the mirrors) and pattern wave vectors p. The results are presented in figures 6 through 9 in paper 2. In figure 6 of paper 2 a WF deconvolution result under planar illumination is presented for reference, to compare with the tSIM simulation results. In figure 7 of paper 2 a simulation is done based on raw data using only three pattern orientations as in conventional SIM, but doing so for all the three possible interference angles (table 3.2). As a result the resolution is improved along specific directions in which the Fourier space is filled. This lead to details in the sample being resolved depending on their orientation.

In figure 8 of paper 2, the result, when only acquiring raw data images using NA_2, NA_3, and NA_2 and NA_3 mirror sets, but with six orientations each is simulated. The Fourier space is filled isotropically, but only for certain frequency ranges. In the reconstruction this is reflected as structures of intermediate size that are not resolved. At first glance it could be concluded that this tSIM implementation provides a unique way to point out structures of a specific size in a sample. This only happens in a sample like the presented Siemens star where the spatial frequencies are spatially separated.

Finally, if six orientations per interference angle are used, the Fourier space can be filled isotropically and gapless. This is shown in figure 9 in paper 2. In that case only using NA_1 would require 18 images, using NA_2 and NA_2 would require 36 images, and using NA_1, NA_2, and NA_3 would require 54 raw data images. For NA_1 and NA_2 this does obviously lead to large overlaps in the Fourier space and a reduced number of pattern orientations would be sufficient. However, this would require intermediate pattern orientations on the mirror mount, specifically adapted to the portion of the Fourier space that is to be filled. Exploiting redundant information in SIM has been shown to further reduce the number of required raw data images [28, 95]. This way the image acquisition is speed up which also reduced photo damage of the sample.

Large FoV pattern generation

Preliminary results of the proposed setup as presented in fig. 3.13 are shown in figures 3, 4, and 5 of paper 2. The mirror setup is used to project stripe patterns on a layer of photo resist that is developed and characterized in a SEM. It is demonstrated, that the illumination patterns may be generated using the different mirror sets over an area of 16 mm^2. This is more than sufficient for the mentioned 10× objective lens. The structures are shown to be stable with good phase control needed for optimal raw data acquisition.

Paper 2: Improving the space-bandwidth product of structured illumination microscopy using a transillumination configuration

- Accepted in Journal of Physics D: Applied Physics, October 2019
- Authors:
  - Joby Joseph,
  - Faiz KP,
  - Marcel Lahrberg,
  - Jean-Claude Tinguely,
  - and Balpreet Singh Ahluwalia
- *Author contributions:* J.J. conceived the idea. F.K. and J.C.T. implemented the setup and performed the experiments. M.L. performed the simulation work. B.S.A. supervised the project All authors contributed to the manuscript.

Improving the space-bandwidth product of structured illumination microscopy using a transillumination configuration

JOBY JOSEPH,[1,*] FAIZ KP,[1], MARCEL LAHRBERG,[2], JEAN-CLAUDE TINGUELY,[2] AND BALPREET SINGH AHLUWALIA[2,**]

[1] *Photonics Research Lab, Department of Physics, Indian Institute of Technology Delhi, HauzKhas, New Delhi 110016, India*
[2] *Department of Physics and Technology, UiT The Arctic University of Norway, NO-9037 Tromsø, Norway*
[*] *joby@iitd.ac.in, ** balpreet.singh.ahluwalia@uit.no*

Abstract: Applying structured instead of plane illumination in widefield optical fluorescence microscopy can improve the spatial resolution beyond what is known as the Abbe limit. In general it is not only the resolution of an imaging system that is of interest but also its field of view (FOV). These two parameters are expressed in the space-bandwidth product (SBP). Here we introduce a modified structured illumination microscopy (SIM) approach that offers a larger SBP than any other available implementation. This is achieved through a transillumination geometry instead of the typical epifluorescent configuration. Compared to conventional SIM, the illumination path is decoupled from the objective lens by using a multi-mirror setup to generate the sinusoidal interference pattern for structured illumination in transmission mode. The spatial frequency of the illumination pattern can be controlled by changing the angle of the mirrors, achieving comparably fine patterns over a large FOV. In this work simulation results demonstrate the potential resolution improvement to be expected by the suggested implementation. Preliminary experimental results demonstrate phase-shifting ability and the stability of fringe frequencies over a large FOV of ($\approx 16\,\mathrm{mm}^2$) at different numerical apertures, fulfilling the prerequisites for SIM acquisition.

1. Introduction

In general the resolution of a light microscope is limited due to the wave-like nature of light and the objective's finite aperture. This is commonly known as the Abbe resolution limit and lies around half of the wavelength of the collected light [1, 2]. Different fluorescence techniques have been implemented to overcome the resolution limit [3–6] and they provide what is called super-resolution microscopy or nanoscopy. Structured illumination microscopy (SIM) [5, 7, 8] is one among those super-resolution methods, typically providing around two-fold resolution improvement to the classical limit in the widefield linear optical regime. Instead of uniform illumination as in a conventional microscope, a sinusoidal light pattern is used to illuminate the fluorescently labeled object. The acquired image then consists of a superposition of the illumination pattern and the sample structure, containing previously unobservable information through frequency mixing in the form of Moiré structures. Expressed in the Fourier domain it means that high-frequency sample information that lies outside the support region of the systems's optical transfer function (OTF) is shifted into that region by structured illumination [9]. It is this down conversion of frequency components and computational unmixing and relocation of shifted components that can be used to reconstruct the image with improved resolution. Various realizations as laterally modulated excitation microscopy (LMEM) by Heintzmann et al. [7] or SIM by Gustafsson et al. [5] have been reported. Frohn et al. proposed harmonic excitation light microscopy (HELM) [8], a transillumination type implementation where the illumination pattern

is generated using prisms (glass blocks) on the backside of the sample. Plasmonic structured illumination microscopy (PSIM) was introduced by Wei et al. [10] where surface plasmons are utilized to generate structured excitation of fluorescent beads.

A typical epifluorescent implementation of SIM, using a single objective lens for sample illumination and imaging acting in the linear optical range has a maximum achievable resolution that is limited to approximately half the conventional resolution limit. Since the objective lens does not only limit the image resolution but also the resolution of the illumination pattern on the sample, the achievable image resolution lies around $\delta = \frac{\lambda}{4NA}$, where λ is the wavelength of the collected light and NA is the numerical aperture of the objective lens. As conventional SIM may not be able to resolve features with a size smaller than the described resolution, the nonlinear response of fluorescent molecules to excitation at high power can be used to introduce higher harmonics in the illumination pattern and thus increase the achievable resolution [11–13]. However, photodamage introduced by the high excitation power to the biological structure as well as photobleaching of the fluorescent dyes may prohibit the application of this technique. In addition to the enhancement of the optical resolution, the SIM technique also benefits from an excellent optical sectioning property [14–16]. Optical sectioning removes out of focus blur light, enhancing the contrast and thus image quality. Already only this effect, without resolution enhancement, has been demonstrated as interesting for large specimens such as tissue samples [17, 18].

The motivation of this work is to propose a new method that is capable of acquiring images at higher resolution over large areas (cm^2-scale). A low magnification objective lens, such as 10X/0.45 NA as used in [18], is desirable to use for imaging large areas at high-speed. However, low magnification/NA objective lenses reduce the achievable optical resolution of SIM. One way to avoid this limitation is to decouple the illumination light path from the imaging objective lens. The transmission geometry is the suitable method to do so. Frohn et al. [8] used a prism for illumination at a similar setup and a transmission-based large FOV implementation has been recently demonstrated for periodic samples [19], but a sample independent pattern generation with comparably high spatial frequencies over a large FOV was not investigated yet.

Here we propose transillumination SIM to decouple the illumination from imaging path. A multi-mirror setup [20] generates illumination patterns with higher spatial frequencies than can be achieved using a low magnification/NA imaging objective lens. While a low magnification/NA objective lens enables imaging a large FOV, an independent multi-mirror mount enables to push the resolution limit beyond what is supported by the NA of the objective. The multi-mirror mount is placed beneath the sample stage such that two plane waves interfere at the sample plane generating closely spaced interference fringes. It is demonstrated that the proposed setup generates high-visibility and stable interference pattern over very large areas (cm^2-scale). The proposed transillumination SIM setup is also shown to be capable of generating illumination patterns with different fringe periods (different spatial frequency) and thus supporting isotropic resolution enhancement by filling the Fourier space. Furthermore the capability to introduce well defined phase steps is demonstrated.

2. Transillumination SIM using mirrors

In order to decouple the illumination from the imaging objective and to improve the resolution of conventional SIM we have developed a new transillumination type configuration. Here a set of mirrors [20] is used to generate a sinusoidal interference pattern for SIM imaging.

By making use of a multi-mirror mount to direct a pair of coherent beams to interfere in the sample plane, the spatial frequency of the interference pattern will depend on the reflecting angle of the mirrors α. The half-angle of interference θ can be expressed as the illumination's numerical aperture (NA), where a larger interference angle realizes a higher NA and thus a higher pattern frequency. Especially numerical apertures larger than the NA of the objective lens

are of interest as they provide a resolution improvement. Similar to Fourier ptychography [21], the Fourier space can be filled piece-wise by using different pattern orientations and different interference angles mimicking different NAs. Since the illumination pattern does not depend on the imaging objective's NA anymore, a low NA objective with a large FOV can be used.

The basic concept of high-frequency information collection over a large FOV through a low NA objective using SIM is described in Fig. 1. As depicted in Fig. 1**(a)**, given an imaging objective with NA = 0.25 and an excitation and emission wavelength of λ ($\lambda_{ex} = \lambda_{em}$), the OTF support is limited to $\frac{2NA}{\lambda} = 0.5\,\lambda^{-1}$ (red circle). For illumination patterns generated by interfering the excitation light under an angle of $\theta = 23°, 36°$, and 54°, mimicking NAs of 0.39, 0.59 and 0.81, which again correspond to pattern frequencies of $f = 0.78\,\lambda^{-1}, 1.18\,\lambda^{-1}$, and $1.62\,\lambda^{-1}$, all respectively indicated by NA_1 (blue), NA_2 (green), NA_3 (magenta) are generated. Images acquired using the mentioned illumination patterns contain additional information at higher frequencies in the Fourier space in form of the shifted copies of the conventional OTF. Here only the information gain in one direction, along the y-axis and only the positive direction is shown. In Fig. 1**(b)** the acquisition of additional spectral components along three different directions d_1, d_2, and d_3 is illustrated. These orientations are distributed in even 60° steps with an offset to present a more realistic case. The dash-dotted, the dashed and the dotted circles indicate the pattern frequencies of NA_1, NA_2, and NA_3 respectively, colors as in Fig. 1**(a)**. For each of the represented pattern orientations one set of spectral components acquired using one pattern frequency is illustrated. To fill the Fourier space isotropically, the imaging acquisition is repeated for all three pattern spacings at up to six orientations. The increase in the number of necessary images is thus the cost for the advantages of this approach.

2.1. Space-bandwidth product of transmission SIM

The space bandwidth product (SBP) is a measure to characterize an imaging system, providing the total number of significant samples in the image (pixels) required to represent an image from that system [22]. It can be defined as

$$\mathrm{SBP} = \frac{\mathrm{FOV}}{(0.5\delta)^2} \tag{1}$$

with δ as the system's resolution, and the factor 0.5 stemming from the Nyquist-Shannon sampling theorem. For a conventional widefield epifluorescent system, the maximum achievable resolution is

$$\delta_{\mathrm{wf}} = \frac{\lambda}{2\mathrm{NA}}. \tag{2}$$

SIM achieves a resolution improvement corresponding to a shift of the OTF in the frequency space as illustrated in Fig. 1. In conventional SIM, where this shift is limited by the resolution of the generated illumination pattern, and the NA is the same for illumination and collection, theoretically the resolution $\delta_{\mathrm{convSIM}}$ is half of δ_{wf}. Considering a constant FOV in the imaging process and the fact that $\mathrm{SBP} \propto 1/\delta^2$ this yields

$$\mathrm{SBP}_{\mathrm{convSIM}} = 4 \times \mathrm{SBP}_{\mathrm{wf}}. \tag{3}$$

The spatial frequency of an illumination pattern generated by a conventional imaging objective lens is limited by the objective's NA. For imaging a large FOV it is desirable to use a low magnification and low NA objective lens, e.g., 10x 0.25 NA, rather than using high-magnification and high NA, e.g., 60-100X 1.4 NA. In the proposed transmission setup as outlined later in Section 3.2, we have experimentally obtained illumination fringes with an effective N.A. of 0.8 over centimetre scale. Thus, when comparing this with an imaging objective lens of 10X 0.25 N.A. the proposed set-up allows generation of an illumination pattern with spatial frequencies 3

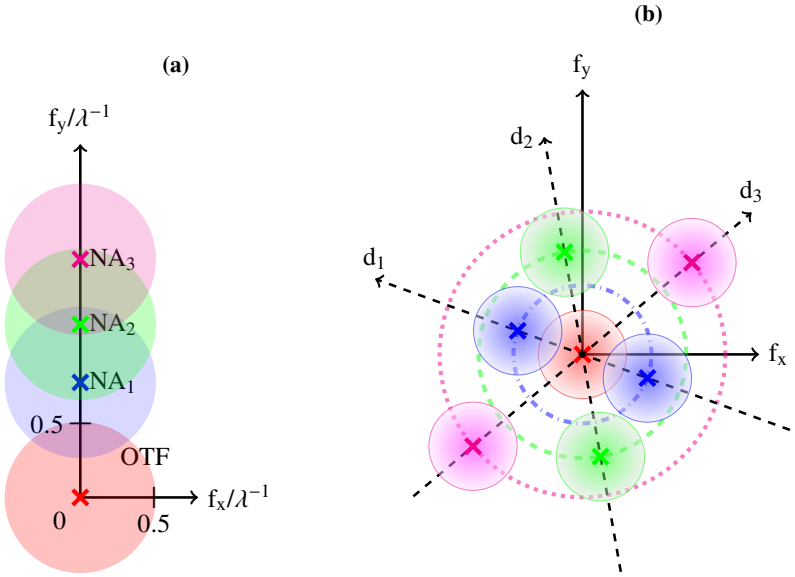

Fig. 1: Illustration of the collection of high frequency information through a low NA objective in transillumination SIM. **(a)** Given an imaging objective with NA = 0.25 the OTF support is limited to $\frac{2\mathrm{NA}}{\lambda} = 0.5\,\lambda^{-1}$ (red). For illumination patterns generated by interfering the excitation light under different angles, NA_1 (blue), NA_2 (green), NA_3 (magenta) are generated, giving additional information at higher frequencies in the Fourier space in the form of the shifted copies of the conventional OTF. Whereas a positive and negative term are always created, here only the information gain in one direction, along the positive y-axis, is shown. **(b)** In order to fill the Fourier space gapless and isotropically, not only the frequency shifts have to be varied, but the process has also to be repeated for different orientations (d_1, d_2, and d_3).

times higher than this imaging objective lens (10X,0.25 N.A.) In such a case, the shift of the OTF and thus the reach towards higher spatial frequencies will be three times as large as well. The final support in the Fourier domain is given by how far the OTF is shifted and its size. Thus shifting the OTF e.g. three times in one direction by its radius (size) will reach to four times its original extent (once for each shift plus once for its size). For this example, the SBP yields:

$$\mathrm{SBP}_{\mathrm{tSIM}} = 4 \times \mathrm{SBP}_{\mathrm{convSIM}} = 16 \times \mathrm{SBP}_{\mathrm{wf}}. \tag{4}$$

Thus the SBP can be increased to 4 times as compared to a conventional SIM approach if the generated illumination pattern corresponds to three times the NA of the imaging objective. This is 16 times the SBP of conventional wide-field imaging. Both the resolution (δ) and the SBP of the proposed transmission SIM are functions of the imaging objective lens' NA and the highest interference angle (equivalent to the highest NA of the illumination side) formed at the sample stage. Thus, for a given experimental setup, i.e. fixed λ and imaging objective lens, the proposed transmission SIM approach supports scalable resolution and SBP simply by altering the interference angles of the multi-mirror setup. However, when it comes to amount of information required to fill the space in the Fourier domain, the larger the shift in the OTF the more orientations will be necessary, as indicated in Fig. 1. The increase in SBP or resolution can thus be seen as a trade-off with the additional number of necessary images.

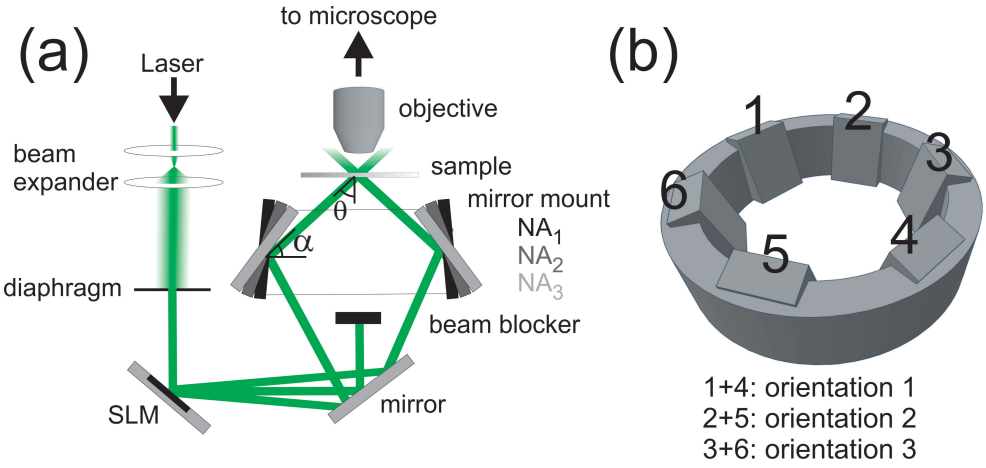

Fig. 2: Illustration of transmission type SIM setup. **(a)** First, the laser beam is expanded using a telescope. Subsequently, a diaphragm is used to select an approximately flat beam profile for a homogeneous intensity over the large illumination area. The light is then directed onto a spatial light modulator (SLM). A grating profile on the SLM is used to split the illumination into different diffraction orders. The two first diffraction orders are guided to the mirror mount while the central beam is blocked. The mirrors on the mount lead the pair of beams to interfere in the sample plane. Different mirror angles α provide interfering beams at angles θ, mimicking different numerical apertures (NA_1, NA_2, and NA_3), and generating interference patterns with varied frequencies. The objective captures the fluorescent response to image the sample in the microscope. **(b)** Design of a mirror mount. Different mirrors around the mount provide the rotated orientation patterns necessary for SIM.

3. Experimental Methods and Results

In this section we expose the experimental results that endorse our transmission-based SIM approach. In the first two sections we demonstrate the capability of the mirror mounts to generate uniform high frequency illumination patterns over a large FOV. In the third part we show the controlled shifting of phase necessary for the SIM method.

3.1. Experimental setup

A schematic of the proposed experimental setup is presented in Fig. 2. It consists of a diode-pumped solid-state laser source (BlueMode, TOPTICA photonics, Germany) emitting at a vacuum wavelength of 405 nm. The spatially filtered/cleaned beam is collimated and widened using a telescope. A region with an approximately flat beam profile is selected with a diaphragm and subsequently projected onto a reflective phase only spatial light modulator (Holoeye LETO). The light is divided into the 0^{th} and two 1^{st} diffraction orders by a grating pattern displayed on the spatial light modulator (SLM). Figure 2**(a)** displays how the 0^{th} order beam is blocked, while the two 1^{st} order beams are reflected at the mirror mounts crossing at the sample plane. By rotating the pattern on the SLM, each pair of opposing mirrors can generate a sinusoidal illumination pattern according to their orientation. The period of the interference pattern τ depends on the wavelength and angle of mirror pair analogue to the resolution: $\tau = \frac{\lambda}{2 \sin \theta}$, with $\theta = 90 - \alpha$. By changing the angle of mirrors α the period can be manipulated. Here three angles of interference corresponding to three different numerical apertures (NA_1, NA_2, and NA_3) are proposed and

studied. Further, by introducing a phase shift to the pattern on the SLM the sinusoidal interference pattern obtains a phase shift (lateral shift) as well. This way the illumination pattern's orientation, periodicity, and phase are controlled.

3.2. Patterns in photoresist

To study the illumination pattern achieved with the presented system, interference patterns are generated and recorded photolithographically so that they can be characterized in a scanning electron microscope (SEM). A glass substrate is spin-coated with a layer of about 1 µm photoresist (AZ 1505, Microchemicals) and placed at the sample plane, where the interference pattern generated by the mirror mount is inscribed. The diameter where the interference fringes are formed and thus ultimately the FOV of this approach can be increased by adjusting the beam diameter. Three different mirror angles, 23°, 36° and 54°, corresponding to NA_1=0.39, NA_2=0.59, NA_3=0.8, respectively, are utilised for different samples. By rotating the beam, three pattern orientations are also inscribed at different photoresist samples. After laser exposure, the pattern is developed and analyzed under a scanning electron microscope (SEM). The diameter of over 4 mm where the sinusoidal pattern was generated is seen in Fig. 3**(a)**. Fig. 3**(b)**-**(d)** displays zoomed in sections from the upper left corner, the central region and the lower right corner of Fig. 3**(a)** respectively, suggesting a homogeneous pattern. The Fourier spectrum of SEM images as in Fig. 3**(b)**-**(d)** is utilized to determine the pattern period. In Fig. 4**(a)**, the exemplary Fourier spectrum of such a SEM image is shown. The delta peaks closest to the DC peak in the center stem from the sinusoidal pattern, with their distance to the DC peak indicating the grating period. This analysis rendered values of 510, 330 and 250 nm for NA_1 to NA_3, respectively. Fig. 4**(b)** depicts the results for different NAs and orientations at different regions of the samples. The results show homogeneity of the pattern with minor variations which may be attributed to the photoresist coating. These variations are likely the cause for the higher order peaks seen at Fig. 4**(a)**. Despite providing a limited comparison with no quantitative information to the visibility of fluorescent fringes, since the exposure time in the photolithographic application is fairly large compared to fluorescence imaging (several seconds vs. 10-100s of milliseconds), the sharpness of the patterns in the photoresist suggests a high temporal sensitivity of the fringes . Further, the sinusoidal pattern is demonstrated without paying attention to polarization. For optimization of the modulation depth, the polarization of a beam could be controlled by, e.g., a waveplate and a Pockels cell [23]. An alternative would be to provide elliptical polarization, which would ensure 50% modulation depth [24].

3.3. Phase shift

Phase shifting of the structured illumination is necessary for the targeted SIM implementation, in order to gather complete information of the sample area. The ability to maintain a stable phase is demonstrated by the fact that the pattern can actually be recorded in photoresist. Since repeated imaging using a shifted pattern is required, the control over the phase shift using the SLM is characterized. For this purpose an interference pattern is generated a low NA and directly projected on a CMOS camera. By introducing phase shift on the SLM, an equivalent phase shift of the pattern on the camera is achieved as presented in Fig. 5. In the plot of Fig. 5, four phase steps and the intensity profiles are shown, demonstrating the capability of phase control over the extent of the modulation frequency.

4. Simulating the imaging performance

In this section the imaging performance of a SIM setup of the proposed type is assessed by reconstructing simulated raw data. First, the theoretical background of SIM as it is used in the presented work is explained. In the second part, the expected results of SIM using different parameters are shown.

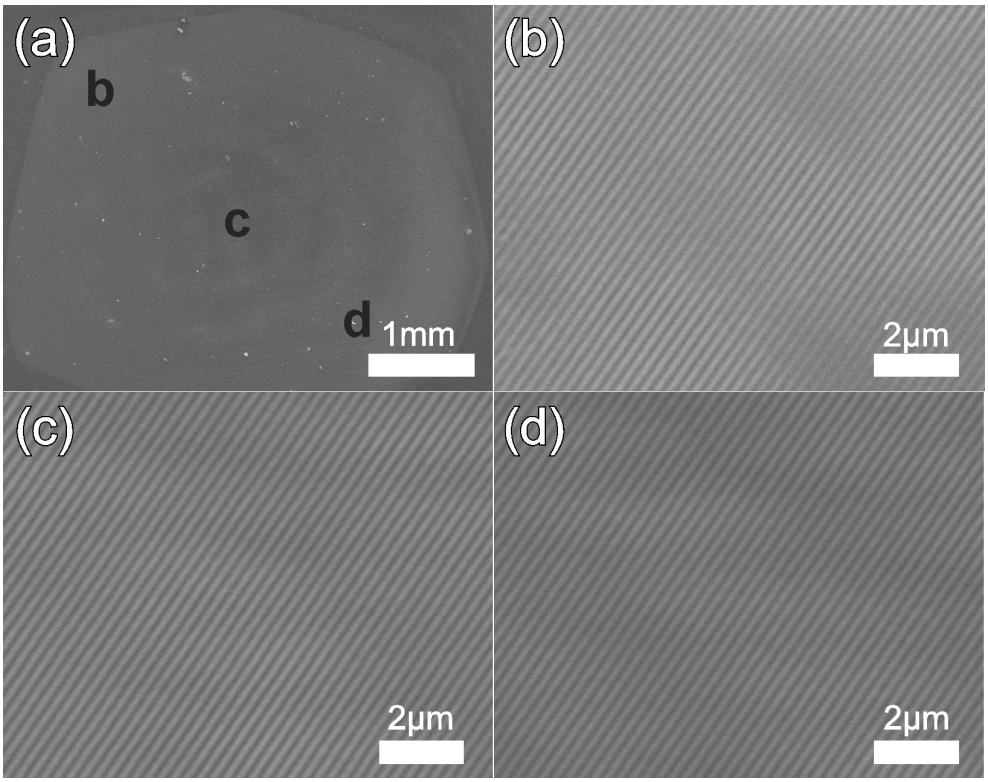

Fig. 3: SEM images of photoresist patterned with the transmission type setup. **(a)** Low magnification image shows exposed area of over 4 mm, with **(b)**-**(d)** being higher magnified regions approximately indicated in **(a)**. The images suggest a homogeneous structured pattern over the exposed region.

4.1. Theoretical formulation of the imaging process

Following the notation of Wicker et al. [25,26], the image formation in two-dimensional widefield fluorescence microscopy using a sinusoidal illumination pattern can be formulated as

$$D(\mathbf{r}) = [S(\mathbf{r})I(\mathbf{r})] \otimes h(\mathbf{r}). \tag{5}$$

The acquired image D is the dye distribution of the fluorescence labeled sample S multiplied with the illumination intensity I and convolved ($\otimes$) with the microscopes point spread function or PSF (h); $\mathbf{r}$ refers to the spatial coordinate. In Fourier space this expression becomes

$$\tilde{D}(\mathbf{k}) = \left[\tilde{I}(\mathbf{k}) \otimes \tilde{S}(\mathbf{k})\right] \tilde{h}(\mathbf{k}). \tag{6}$$

Tilde (~) indicates the Fourier transform, and $\mathbf{k}$ is the Fourier space coordinate or spatial frequency. The extend of the optical transfer function (OTF) $\tilde{h}$ is limited to a cutoff frequency $\|\mathbf{k}\|_2 \leq k_{\max}$. This is a basic property of the imaging objective and results in a limited resolution in the image. If the fluorescence in the sample is excited using a sinusoidal illumination pattern

$$I(\mathbf{r}) = \sum_{m=-1}^{1} a_m \exp[im(2\pi \mathbf{p}\mathbf{r} + \phi)] \tag{7}$$

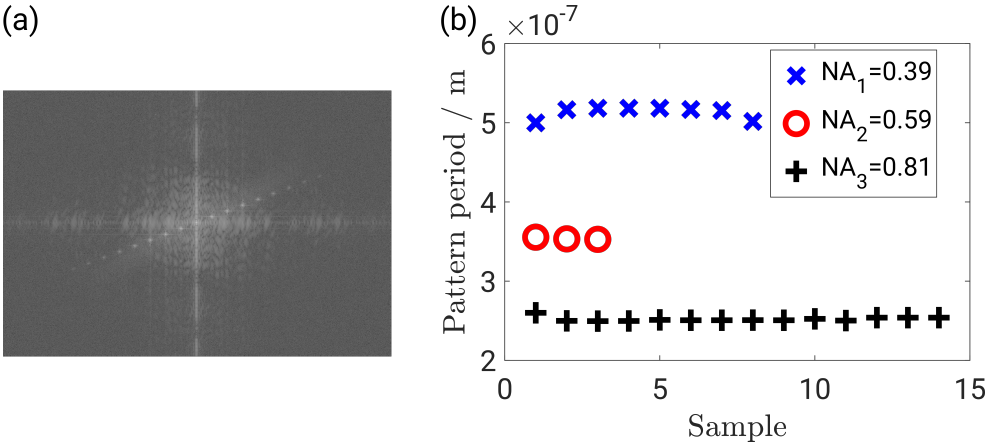

Fig. 4: SEM images of photoresist samples taken at different regions with different NAs and orientations are used to determine pattern uniformity through Fourier analysis. **(a)** Fourier transform of examplifying SEM image as in Fig. 3 **(b)**-**(d)**. The peaks closest to the DC component are localized and the frequency is determined. **(b)** shows these results demonstrating the uniformity of the pattern period. Variations may be attributed to photoresist and not illumination-related effects.

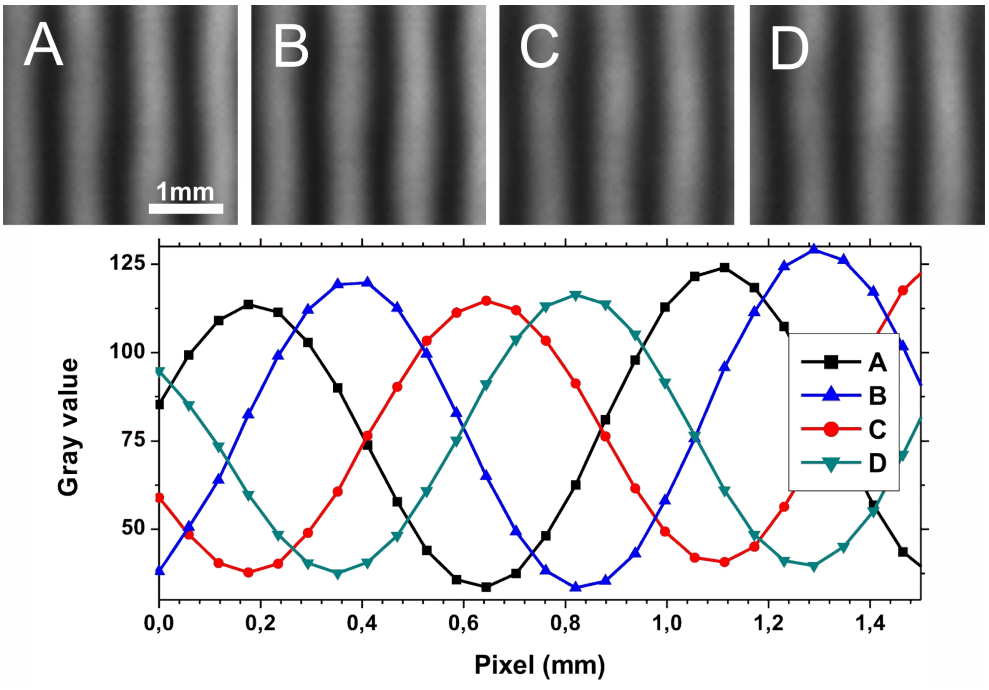

Fig. 5: Demonstration of phase control at the transmission setup. A-D: Low NA interference directly projected onto a camera and shifted in $\lambda/4$ phase steps introduced by the SLM. The plot displays line profiles of these images.

with a modulation depth a_m, a wave vector $\mathbf{p}$ and a phase ϕ, the Fourier transform of an acquired image can be written as

$$\tilde{D}(\mathbf{k}) = \sum_{m=-1}^{1} \exp(im\phi) \underbrace{a_m \tilde{S}(\mathbf{k} - m\mathbf{p})\tilde{h}(\mathbf{k})}_{\tilde{C}_m(\mathbf{k})}. \tag{8}$$

The Fourier transforms of the acquired images $\tilde{D}(\mathbf{k})$ contain bands $\tilde{S}_m(\mathbf{k}) = \tilde{S}(\mathbf{k} - m\mathbf{p})$ that are shifted by $m\mathbf{p}$ with respect to their original position in Fourier space before they are multiplied with the OTF. This way frequency components of the sample that actually lie outside the OTF support are now transmitted into image space. Taking N images of the sample with different phases ϕ_n with $n = 1, \cdots, N$, the resulting Fourier transforms of the images $\tilde{D}_n(\mathbf{k})$ can be written as

$$\tilde{\mathbf{D}}(\mathbf{k}) = \mathbf{M}\tilde{\mathbf{C}}(\mathbf{k}), \tag{9}$$

with the acquired images in the vector $\tilde{\mathbf{D}} = [\tilde{D}_1, \cdots, \tilde{D}_N]^\intercal$, the matrix $\mathbf{M}_{nm} = \exp(im\phi_n)$ and a vector $\tilde{\mathbf{C}}(\mathbf{k}) = [\tilde{C}_{-1}, \tilde{C}_0, \tilde{C}_+1]^\intercal$. If the inverse of $\mathbf{M}$ ($\mathbf{M}^{-1}$) exists, the different components can be separated by

$$\tilde{\mathbf{C}}(\mathbf{k}) = \mathbf{M}^{-1}\tilde{\mathbf{D}}(\mathbf{k}). \tag{10}$$

The final image is the inverse Fourier transform of $\hat{\tilde{S}}(\mathbf{k})$, the final estimate in the Fourier domain. It is obtained by shifting each band to its original position and recombining them using a generalized Wiener filter

$$\hat{\tilde{S}}(\mathbf{k}) = \frac{\sum_{m,d} a_m \tilde{C}_{m,d}(\mathbf{k} + m\mathbf{p}_d)\tilde{h}^*(\mathbf{k} + m\mathbf{p}_d)}{\sum_{m,d} \left|a_m \tilde{h}(\mathbf{k} + m\mathbf{p}_d)\right|^2 + w} A(\mathbf{k}). \tag{11}$$

The Wiener filter reduces the degrading influence of the OTF and weights the bands in regions where they overlap according to their expected SNR. The Wiener parameter w is determined empirically, $A(\mathbf{k})$ is an apodization function decreasing linearly from unity at the center to zero near the end of the extended OTF support, shaping the overall spectrum in order to prevent ringing artifacts in the final image, and the asterisk ($*$) indicates the complex conjugate. Since the resolution improvement only takes place in the direction of $\mathbf{p}$, the process of image acquisition and band separation is repeated for different orientations d to obtain isotropic resolution enhancement.

4.2. Simulations

For the presented simulations, an imaging objective with a numerical aperture of NA = 0.25 is assumed. The excitation and emission wavelength is set to be equal $\lambda = 10\,\text{px}$ in the sample space. In Fig. 6 **(a)**, the sample (Siemens star) for the simulations is introduced. Fig. 6 **(b)** shows a simulation of the widefield deconvolution and Fig. 6 **(c)** shows the corresponding Fourier spectrum. The simulated result for plain illumination is generated in the same way as results for structured illumination, just with an interference angle of 0° generating plane illumination. For the simulation of the raw data for SIM, three interference angles of 23°, 36° and 54° (referred to as NA_1, NA_2, and NA_3) for the generation of the illumination pattern can be used. These interference angles determine the fringe spacing of the sinusoidal illumination pattern. For the orientations, three or six evenly distributed angles with a random overall offset are used. For each direction, a set of three evenly distributed phases, also with a random overall offset, is generated. The raw data images are then simulated according to Eqs. (5) and (7) using a modulation depth of $a_m = 1$. The PSF is simulated using a 2D distribution based on the Bessel function of first kind and first order [27]. The reconstruction results as presented in Figs. 7 to 9 show the resolution improvement that is to be expected in comparison to Fig. 6.

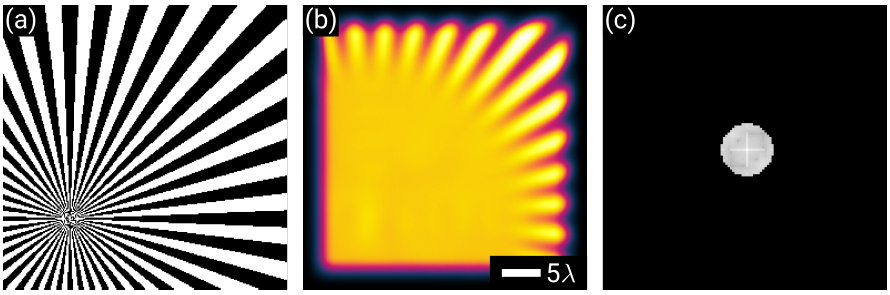

Fig. 6: The Siemens star sample **(a)** of size 256×256 px. In **(b)** the widefield image as obtained with an NA $= 0.25$ objective at a wavelength of $\lambda = 10$ px, after deconvolution is simulated. In panel **(c)** the Fourier spectrum of **(b)** is shown. For best possible contrast the color map "Morgenstemning" [28] is used to represent the intensity here and in the following.

Different NAs and orientations for the illumination pattern result in different pattern frequencies and wave vectors **p** in the description above. Since the data is acquired consecutively, the different frequency components can be separated one at a time and joined as described in Eq. (11) with additional terms d in the sum. In order to generate raw data for the reconstructions in Fig. 8 **(a)**, **(b)** simulated data only based on NA_2 is used. In Fig. 8 **(c)**, **(d)** only NA_3 and in Fig. 8 **(e)**, **(f)** only NA_2 and NA_3 are used. This leaves a gap between the low and the high frequency components. This gap results in artifacts in the reconstruction and is clearly visible in the figure. Furthermore, Fig. 7 shows the reconstructions using only three pattern orientations instead of six in order to create the raw data. This leads to an anisotropic filling of the Fourier space of the reconstruction. Fig. 9 shows the expected reconstruction results using only NA_1 (Fig. 9 **(a)**, **(b)**), NA_1 and NA_2 (Fig. 9 **(c)**, **(d)**) and finally NA_1, NA_2, and NA_3 (Fig. 9 **(e)**, **(f)**). The Fourier space of the images is expanded successively and the resolution improves accordingly. There are no gaps in the Fourier space, neither is the Fourier space filled anisotropically.

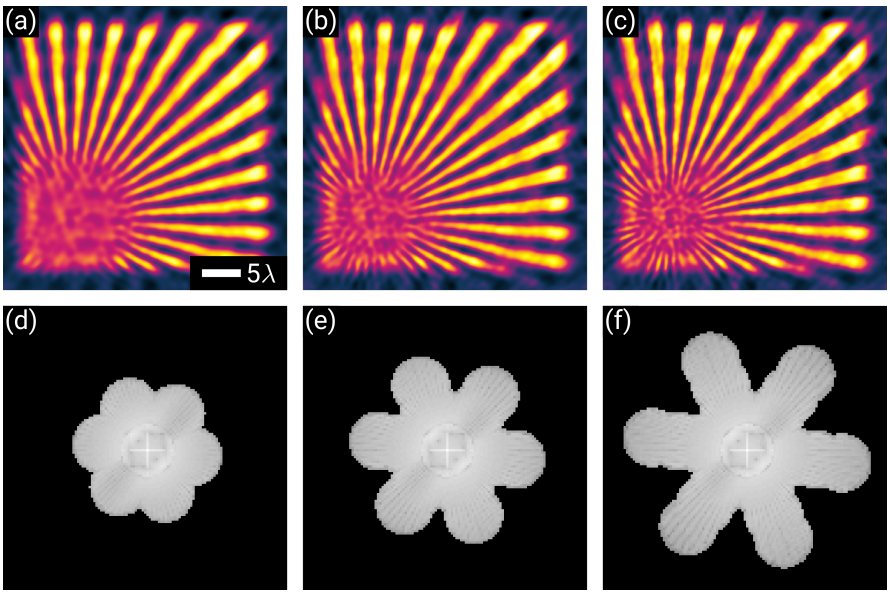

Fig. 7: If the Fourier space is filled successively but only three pattern orientations are used, the Fourier space is not filled isotropically anymore. In **(a)** and the corresponding Fourier spectrum **(d)** the reconstruction is done with simulated data using illumination patterns generated with NA_1. This way three pattern orientations with three phase steps each equals nine raw data images are required. In **(b)** and **(e)** the raw data set is simulated with NA_1 and NA_2. An additional set of nine raw data images, eighteen in total, are required. In **(c)** and **(f)** all three suggested NAs NA_1 & NA_2 & NA_3 are used. A third set of raw data images, in total twenty-seven images are needed.

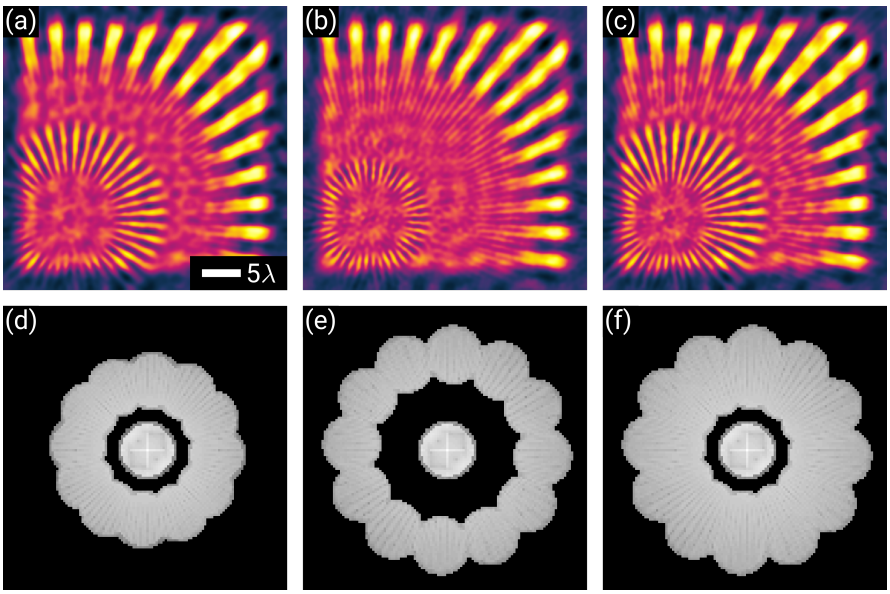

Fig. 8: This figure illustrates what happens if the Fourier space is not filled successively. Panels **(a)** and **(d)** show the image reconstruction based on raw data simulated with patterns of NA_2 only. Since images of six pattern orientations with each three phase steps are required, a total of eighteen raw data images is required for the proposed reconstruction. In panels **(b)** and **(e)** the raw data is simulated using NA_3 only, requiring eighteen raw data images as well. Panels **(c)** and **(f)** show a reconstruction based on raw data using NA_2 and NA_3. This way twice as many raw data images (thirty-six) are needed.

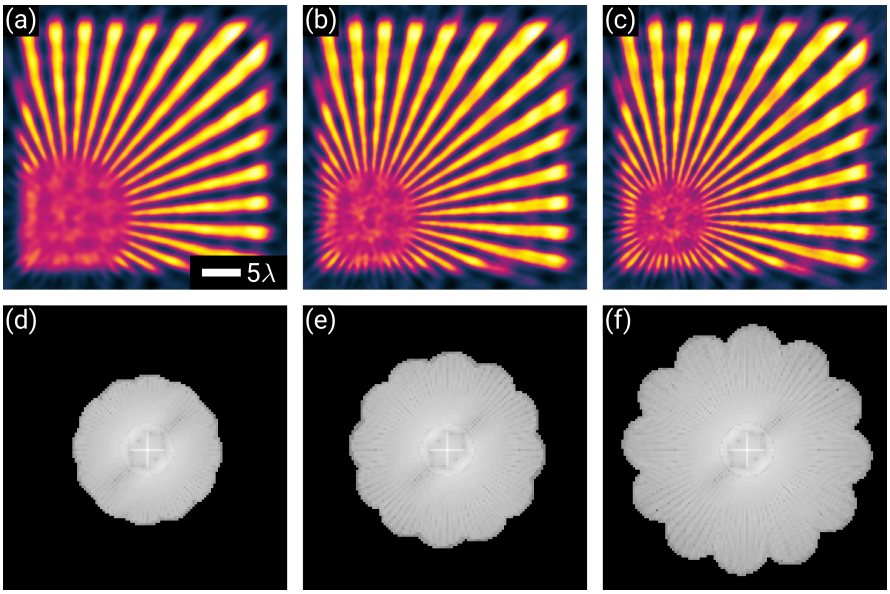

Fig. 9: Simulated SIM reconstruction using six orientations. In **(a)** and the corresponding Fourier spectrum **(d)** the reconstruction is done with simulated data using illumination patterns generated with NA_1. This way six orientations times three phase shift equals 18 images are needed. In **(b)** and **(e)** the raw data set is simulated with NA_1 and NA_2. An additional set of eighteen images, thirty-six images in total, is needed. In **(c)** and **(f)** all three suggested NAs NA_1 & NA_2 & NA_3 are used. Here three sets of eighteen images, fifty-four raw data images are used.

5. Conclusion and Summary

A mirror based transillumination SIM setup is proposed that increases the SBP by maintaining a large FOV while illuminating the sample with a sinusoidal illumination with comparably high spatial frequency. The generation of stable fringe illumination over a large FOV is experimentally demonstrated and the ability for precise phase shifts is shown. The unique characteristic of the presented implementation is not only to decouple the pattern generation from the imaging path, but also the exploitation of the ability to generate uniform interference patterns over a centimeter sized FOV. Simulation work shows the possible resolution enhancement in SIM imaging of fluorescent labeled samples using three different illumination NAs. The approach is flexible towards larger or smaller differences between illumination angles. Larger illumination NAs could be used towards higher resolution or SBP, coming however at the cost of more images and possibly less optical sectioning. This is not a constraint when the sample is thin, e.g., pathologically relevant cryo-tissue sections which are usually few hundred nanometers thick. This technique is expected to be useful for applications in biomedical fields such as pathology, hematology, immunohistochemistry and neuroanatomy, where it is strongly necessary to image large numbers of histology slides for analysis.

The illumination path of the transillumination setup is similar to conventional SIM, but the collection light path is different. Here, the flurorescence light is collected by an upright microscope, which could be adversely affected by the aberration from the mounting media and especially for thick samples. This would be a lesser problem for thin samples, e.g cryo-tissue sections as outlined above. Finally, if the illumination of a fluorescent sample still turns out to be more challenging to control or estimate, SIM reconstruction algorithms such as Blind-SIM are able to perform without ideal and pre-determined fringe patterns [27, 29].

In future work, the proposed mirror based transillumination SIM setup will be employed for high-resolution imaging of pathological tissue samples [30]. 3D SIM can also be pursued by making use of the 0th order diffracted beam [31].

6. Funding and Acknowledgments

B.S.A. acknowledges the funding from the European Research Council, (project number 336716) and Norwegian Centre for International Cooperation in Education, SIU-Norway (Project number INCP- 2014/10024). J.J. acknowledges University Grant Commission (UGC) India for joint funding.

7. Disclosures

All authors have jointly applied for a patent application to protect the invention related to the transmission SIM.

References

1. E. Abbe, "Beiträge zur Theorie des Mikroskops und der mikroskopischen Wahrnehmung," Arch. für mikroskopische Anat. **9**, 413–418 (1873).
2. H. Köhler, "On Abbe's theory of image formation in the microscope," Opt. Acta (1981).
3. E. Betzig, J. K. Trautman, T. D. Harris, J. S. Weiner, and R. L. Kostelak, "Breaking the diffraction barrier: Optical microscopy on a nanometric scale," Science (1991).
4. S. W. Hell and J. Wichmann, "Breaking the diffraction resolution limit by stimulated emission: stimulated-emission-depletion fluorescence microscopy," Opt. Lett. (1994).
5. M. G. L. Gustafsson, "Surpassing the lateral resolution limit by a factor of two using structured illumination microscopy," J. Microsc. **198**, 82–87 (2000).
6. V. Krishnamurthi, B. Bailey, and F. Lanni, "Image processing in 3D standing wave fluorescence microscopy," in *SPIE 2655, Three-Dimensional Microscopy: Image Acquisition and Processing III,* (1996).
7. R. Heintzmann and C. G. Cremer, "Laterally modulated excitation microscopy: improvement of resolution by using a diffraction grating," in *Proc. SPIE 3568, Optical Biopsies and Microscopic Techniques III,* I. J. Bigio,

H. Schneckenburger, J. Slavik, K. Svanberg, and P. M. Viallet, eds. (International Society for Optics and Photonics, 1999), pp. 185–196.
8. J. T. Frohn, H. F. Knapp, and A. Stemmer, "True optical resolution beyond the Rayleigh limit achieved by standing wave illumination." Proc. Natl. Acad. Sci. United States Am. **97**, 7232–6 (2000).
9. I. Amidror and R. D. Hersch, "The role of Fourier theory and of modulation in the prediction of visible moire effects," J. Mod. Opt. (2009).
10. F. Wei, D. Lu, H. Shen, W. Wan, J. L. Ponsetto, E. Huang, and Z. Liu, "Wide field super-resolution surface imaging through plasmonic structured illumination microscopy," Nano Lett. **14**, 4634–4639 (2014).
11. R. Heintzmann, T. M. Jovin, and C. Cremer, "Saturated patterned excitation microscopy—a concept for optical resolution improvement," J. Opt. Soc. Am. A **19**, 1599–1609 (2002).
12. M. G. L. Gustafsson, "Nonlinear structured-illumination microscopy: Wide-field fluorescence imaging with theoretically unlimited resolution," Proc. Natl. Acad. Sci. (2005).
13. E. A. Ingerman, R. A. London, and M. L. Gustafsson, "Signal, noise and resolution in linear and nonlinear structured-illumination microscopy," Report (2013).
14. M. A. A. Neil, R. Juškaitis, and T. Wilson, "Method of obtaining optical sectioning by using structured light in a conventional microscope," Opt. Lett. (1997).
15. J. Mertz, "Optical sectioning microscopy with planar or structured illumination," (2011).
16. D. Xu, T. Jiang, A. Li, B. Hu, Z. Feng, H. Gong, S. Zeng, and Q. Luo, "Fast optical sectioning obtained by structured illumination microscopy using a digital mirror device," J. Biomed. Opt. (2013).
17. H. L. Fu, J. L. Mueller, M. P. Javid, J. K. Mito, D. G. Kirsch, N. Ramanujam, and J. Q. Brown, "Optimization of a Widefield Structured Illumination Microscope for Non-Destructive Assessment and Quantification of Nuclear Features in Tumor Margins of a Primary Mouse Model of Sarcoma," PLoS ONE (2013).
18. T. C. Schlichenmeyer, M. Wang, K. N. Elfer, and J. Q. Brown, "Video-rate structured illumination microscopy for high-throughput imaging of large tissue areas," Biomed. Opt. Express (2014).
19. S. Chowdhury, J. Chen, and J. A. Izatt, "Structured illumination fluorescence microscopy using Talbot self-imaging effect for high-throughput visualization," (2018).
20. S. Behera, M. Kumar, and J. Joseph, "Submicrometer photonic structure fabrication by phase spatial-light-modulator-based interference lithography," Opt. Lett. **41**, 1893–1896 (2016).
21. J. Sun, C. Zuo, L. Zhang, and Q. Chen, "Resolution-enhanced Fourier ptychographic microscopy based on high-numerical-aperture illuminations," Sci. Reports (2017).
22. J. W. Goodman, *Introduction to Fourier optics* (Roberts, Englewood, Colo., 2005), 3rd ed.
23. L. J. Young, F. Ströhl, and C. F. Kaminski, "A Guide to Structured Illumination TIRF Microscopy at High Speed with Multiple Colors." J. visualized experiments : JoVE p. e53988 (2016).
24. K. O'Holleran and M. Shaw, "Polarization effects on contrast in structured illumination microscopy," Opt. Lett. (2012).
25. K. Wicker, "Non-iterative determination of pattern phase in structured illumination microscopy using auto-correlations in Fourier space," Opt. Express **21**, 24692–24701 (2013).
26. K. Wicker, O. Mandula, G. Best, R. Fiolka, and R. Heintzmann, "Phase optimisation for structured illumination microscopy," Opt. Express **21**, 2032 (2013).
27. E. Mudry, K. Belkebir, J. Girard, J. Savatier, E. Le Moal, C. Nicoletti, M. Allain, and A. Sentenac, "Structured illumination microscopy using unknown speckle patterns," Nat. Photonics **6**, 312–315 (2012).
28. M. Geissbuehler and T. Lasser, "How to display data by color schemes compatible with red-green color perception deficiencies," Opt. Express (2013).
29. R. Ayuk, H. Giovannini, A. Jost, E. Mudry, J. Girard, T. Mangeat, N. Sandeau, R. Heintzmann, K. Wicker, K. Belkebir, and A. Sentenac, "Structured illumination fluorescence microscopy with distorted excitations using a filtered blind-SIM algorithm." Opt. Lett. **38** (2013).
30. B. Thomas, M. Momany, and P. Kner, "Optical sectioning structured illumination microscopy with enhanced sensitivity," J. Opt. (United Kingdom) (2013).
31. L. Shao, P. Kner, E. H. Rego, and M. G. Gustafsson, "Super-resolution 3D microscopy of live whole cells using structured illumination," Nat. Methods **8**, 1044–1048 (2011).

3.2.2 Chip SIM - Paper 3

If a high NA objective is used in a single lens SIM setup, it is possible to generate two beams at an angle (with the cover slip) large enough such that they undergo TIR in the cover slip and interfere counter-propagating. This way the highest possible pattern frequency in the evanescent field is achieved. Whether or not the critical angle for TIR is reached, depends on the NA of the objective lens and where the beams enter the lens, as well as the refractive index contrast between cover slip and sample. Since a high refractive index difference is usually unwanted in general to minimize aberrations, TIRF SIM relies on high NA objectives, which reduces the FoV, as discussed above. This way the major advantage of TIRF SIM is the reduced imaging depth associated with the low sample penetration depth given by the evanescent field.

In cSIM the illumination pattern is generated in a transparent waveguide chip, where the geometry of waveguides determines the interference angle. The labeled sample is mounted on top of the waveguide such that the excitation is limited to the evanescent field as in conventional TIRF SIM. The benefit of this method is that it does not require a high NA objective lens in order to obtain a high frequency illumination pattern limited to an evanescent field. Additionally, the pattern frequency can be manipulated by the effective index n_{eff} achieved in the waveguide as it directly relates the speed of light in the medium v to the speed of light in vacuum c ($n_{\text{eff}}v = c$), such that the pattern spacing is given by

$$\delta_{\text{Pattern}} = \frac{\lambda_{\text{vac}}}{2n_{\text{eff}} \sin\theta}, \tag{3.15}$$

with a vacuum wavelength of λ_{vac} and half the angle between the waveguide arms of θ. Materials with a high refractive index like silicon nitride (Si_3N_4) ($n = 2.04$ @ 660 nm), tantalum pentoxide (Ta_2O_5) ($n = 2.12$ @ 660 nm), and titanium dioxide (TiO_2) ($n = 2.57$ @ 660 nm) can be used to achieve high effective mode indices in the waveguide. The resolution limit is then given by

$$\delta = \frac{\lambda_{\text{vac}}}{2\,(\text{NA} + n_{\text{eff}} \sin\theta)}, \tag{3.16}$$

with the NA of the imaging objecctive lens, similar to the calculations shown in table 3.1 for the tSIM approach. The difference is that in cSIM the SBP is increased by improving the pattern resolution due to the high values achieved in n_{eff}.

Basic concept

The concept and different implementations of cSIM are described in figures 1 and 2 in the attached paper 3 at the end of this section. Figure 1 **a)** in paper 3

shows the general concept of TIRF SIM, using a high NA objective to bring two coherent beams to interference in the cover slip. In **b)**, the the proposed waveguide based configuration is depicted. A standing wave is generated in the waveguide using two counter-propagating modes. This way the evanescent field shows a sinusoidal modulation. A standard imaging objective is used to capture the raw data images. Depending on the angle between the waveguides (**d)**), the pattern frequency changes. In **f)** the shift of the OTF depending on the interference angle is depicted schematically for a given high NA objective and waveguide material, similar to what is done for tSIM in fig. 3.14. Using a low NA objective, a shift of the OTF well beyond the original support can be achieved, as illustrated in **i)**. In order to fill the frequency space, intermediate interference angles are used to obtain smaller shift vectors (**j)**), similar to what is presented in fig. 3.15 for tSIM.

In figure 2 **a)** of paper 3, a waveguide design with two inputs is presented. The excitation light has to be split prior to coupling into the waveguide. Furthermore the phase control has to happen before the light is coupled into the chip. Since this configuration only allows for an illumination pattern along one direction, three of these configurations rotated by 60° at the imaging area are merged into one as depicted in **d)**. Although such an off-chip configuration does not show the pattern phase to be as stable as the on-chip solution discussed further down, the multi-angle configuration does automatically provide access to intermediate interference angles as depicted in **d)**. In **b)** the on-chip solution is presented. By splitting the guided mode using a Y-junction, the pattern phase is determined by the length difference in the two pathways. This allows for a far more stable pattern phase but needs a separate waveguide for each phase step. In **e)** the suitable design, providing three pattern angles is presented. As for the off-chip solution, it contains three copies rotated by 60°.

In order to provide interference angles smaller than 180°, a structure as presented in figure 2 **g)** is used. If the light was just coupled into suiting waveguide arms as in **d)**, the stability of the on-chip phase control would be lost. Finally, in **c)** another on-chip implementation is presented. Instead of providing three pathways per pattern orientation in order to achieve phase shifting, thermo-optic phase shifters are employed [44]. The thermo-optic coefficient of a material determines the change of its refractive index with the change in temperature $\frac{\mathrm{d}n}{\mathrm{d}T}$. An electric conductor on the waveguide may then be used to change its optical path length by Joule heating; the thermo-optic phase shifter. This way the the phase of the illumination pattern depends on the voltage applied to the thermo-optic phase shifter, which enables stable on-chip phase control at a reduced number of waveguide paths. In **f)**, and **h)** the options providing three pattern orientations at interference angles of 180° and 50° are shown.

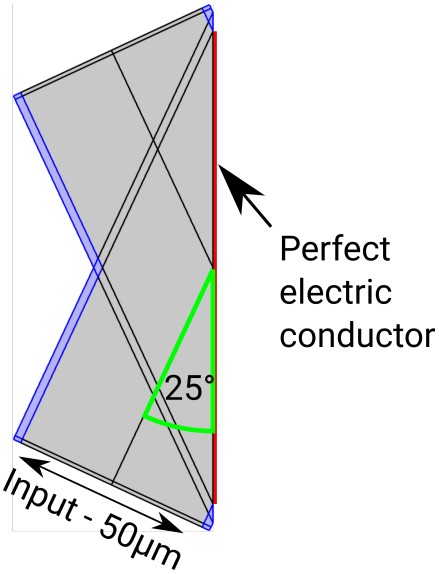

Figure 3.16: A two-dimensional model for the simulation of two 50 µm rib waveguides crossing at an angle of 50°. The highlighted blue regions have a slightly lower refractive index than the gray region. The waveguide is excited at the lower end and the perfect electric conductor exploits the mirror symmetry of the whole proposed configuration.

Waveguide simulations in COMSOL

Considering a rib waveguide (fig. 2.7), the effective refractive indices for two regions, the rib and the slab, are calculated. Here the waveguide is modeled using a substrate of silicon dioxide (SiO_2), a core of Si_3N_4 and a cladding of H_2O, resembling the aqueous sample space. Using eq. (2.29) the effective refractive index for the slab region with a thickness of 145 nm and the rib region of 150 nm (width of 50 µm) are calculated and used in the model in fig. 3.16. The slab region is highlighted in blue, the rib is the whole gray region. Due to mirror symmetry only the left-hand half of the model is simulated using a perfect electric conductor to exploit the symmetry. Light is coupled into the waveguide from the lower end thus simulating two waveguides crossing at an angle of 50°.

Simulation results for the full waveguide are presented in the supplementary information of paper 3. In figure 1, interference patterns for a wavelength of 660 nm and interference angles of 50° and 180° are shown. The refractive index for the fundamental TE mode is found to be $n = 1.7552$. The interference patterns are fitted as described in supplementary note 1, yielding pattern spacings of 445 nm and 188 nm for interference angles of 50° and 180° respectively. The simulation shows, that the crossing waveguides provide illumination pattern

frequencies suited for cSIM. However, due to the drop in modulation depth towards the waveguide edges, an imaging area smaller than what is covered by the waveguide is to be expected.

Imaging simulations

The expected quality of the reconstructed images using cSIM is illustrated in figures 3 and 4, and supplementary note 3, in the supplementary information of the attached paper 3. Using an objective lens with NA = 1.2, the WF image and frequency spectrum are shown in **(a)** and **(b)**. Since these are simulations for which the regarded wavelength may be chosen depending on the application, the scale bar is set to indicate the regarded wavelength. In **(c)** and **(d)** a SIM result using the conventional epifluorescence setup is shown. Using a waveguide with an effective refractive index of 1.7 and an interference angle of 60°, as would be possible using the off-chip design, the reconstruction results for known patterns are shown in **(e)** and **(f)**. The same is done for 180° interference angles in **(g)** and **(h)**. Compared to conventional SIM, cSIM does show a resolution improvement due to the high refractive index of the waveguide.

Since cSIM, like tSIM allows for illumination pattern generation independent of the objective lens, the imaging process is simulated for an NA = 0.6 objective lens in figure 4. A WF/deconvolution image is shown in **(a)** and **(b)** for comparison. Using 60° interference angles for three pattern orientations results in resolution enhancement as shown in **(c)** and **(d)**. Having in mind that TIRF SIM requires high NA objective lenses in order to provide evanescent field excitation, this is a low NA TIRF SIM solution, in which the resolution is not primarily limited by the imaging objective's NA. Interference angles of 120° and 180° produce results as presented in **(e)** and **(f)**, and **(g)** and **(h)**. Similar to the result presented for tSIM, the Fourier space is filled incompletely. This has to do with to few pattern orientations as well as lacking intermediate pattern frequencies (interference angles). Filling the Fourier space using all suggested interference angles (60°, 120° and 180°), the Fourier space can be filled further with the result as presented in **(i)** and **(j)**. An important assumption in this result is that the orientation of the 120° interference pattern is rotated by 30° with respect to the direction of the other two. This happens due to the required selection of waveguides in the off-chip design to achieve a targeted interference angle.

The simulations show that cSIM is suitable to implement low NA TIRF SIM. This does not only benefit from the limited evanescent field excitation but also from the large FoV possible using a low NA objective lens. This way the SBP may be increased similar to tSIM. The off-chip design shows to provide a suitable

flexibility with respect to pattern generation at comparably low complexity. However, the main benefit is the possibility in increase the maximum pattern frequency using waveguide materials with a high refractive index and improve the SBP this way.

Experimental results

Although they are not part of this thesis, experimental results of cSIM are mentioned as they appear in the attached paper 3. In figure 3, off-chip results for interference patterns of 60° are presented. Fluorescent beads of 100 nm size are imaged using an excitation and emission wavelength of 660 nm, and 690 nm respectively. In **l)** an intensity profile through two neighbouring beads is presented for WF and cSIM imaging showing the resolution improvement. The pattern generation using an interference angle of 20° is shown in **d)**.

In figure 4 on-chip cSIM is presented using an interference pattern of 180° only. Due to its phase stability, a dSTORM image of a fluorescent dye layer on the chip could be generated showing a pattern spacing of 195 nm at an excitation wavelength of 660 nm, corresponding to an effective index of ≈ 1.7. In **h)** the intensity profile through be beads, 117 nm apart is show. They are spatially resolved in the cSIM image only.

Paper 3 (submitted): Structured illumination microscopy using a photonic chip

- Manuscript submitted
- Authors:
  - Øystein Ivar Helle,
  - Firehund Tsige Dullo,
  - Marcel Lahrberg,
  - Jean-Claude Tinguely,
  - and Balpreet Singh Ahluwalia
- *Author contributions:* B.S.A. conceived the idea and supervised the project. Ø.I.H. built the setup, performed the experiments and analysed the data. J.C.T and F.S.T designed the waveguide mask. All authors contributed towards chip designs. Ø.I.H., F.T.D. and J.C.T characterized the waveguides. F.T.D. and Ø.I.H. fabricated the on-chip thermo-optics for phase modulation. M.L. performed all the simulation of cSIM. Ø.I.H. and B.S.A. mainly wrote the manuscript and all authors commented to the manuscript.

Structured illumination microscopy using a photonic chip

Øystein Ivar Helle[1], Firehun Tsige Dullo[1], Marcel Lahrberg[1], Jean-Claude Tinguely[1] and Balpreet Singh Ahluwalia[1]

1 Department of Physics and Technology, UiT-The Arctic University of Norway, 9037 Tromsø, Norway.

Correspondence should be addressed to BSA (balpreet.singh.ahluwalia@uit.no)

Structured illumination microscopy (SIM) enables live cell, 3D super-resolution imaging of sub-cellular structures at high speeds. Present day, SIM uses free-space optical systems to generate pre-determined excitation light patterns and reconstruction algorithms to enhance the spatial resolution by up to a factor of two. These arrangements are prone to miss-alignment, often with high initial and maintenance costs, and with the final resolution-enhancement being limited by the numerical aperture of the collection optics. Here, we present a photonic-chip based total internal reflection fluorescence (TIRF) *c*SIM that greatly reduces the complexity of the optical setup needed to acquire TIRF-SIM images. This is achieved by taking out the entire light generation and delivery from the microscope and transferring it to an integrated photonic-chip. Thus, the conventional glass slide is replaced by a planar photonic chip that both holds and illuminates the specimen. A photonic chip consisting of an array of opposing optical waveguides are used to create standing wave interference patterns in different angles, which illuminates the sample via evanescent fields. The phase of the interference pattern is controlled by the use of either on-chip thermo-optical modulation or by off-chip phase modulation of the interfering beams, leaving the footprint of the light illumination path for the *c*SIM system to around 4x4 cm^2. The photonic chips are fabricated using dielectric materials which enables light guidance and illumination of arbitrary large areas. Furthermore, by harnessing high refractive index waveguide materials, such as silicon nitride, 2.3x resolution enhancement was obtained using cSIM, which is beyond the 2x resolution enhancement of conventional SIM. *c*-SIM represents a simple, stable and affordable approach, which could enable widespread penetration of the technique and might also open avenues for high throughput optical super-resolution microscopy.

The spatial resolution of optical microscopy is bound by diffraction effectively limiting the achievable resolution to around 250 nm laterally, and 500 nm axially[1, 2]. The advent of super-resolution fluorescence microscopy, commonly known as nanoscopy, has proven the ability to trick the diffraction limit extending the lateral resolution of the microscope down towards just a few nanometer[3]. Among the existing optical nanoscopy methodologies[4-9], structured

illumination microscopy (SIM)[10, 11] works for most bright fluorophores. Instead of illuminating a sample with a uniform field, in SIM, a sinusoidal excitation pattern illuminates the sample, and the fluorescence emission is captured on a camera. The sinusoidal excitation light is typically generated using interference of two or three beams at the sample plane. The illumination and object functions combine at the sample plane via a multiplication, which in frequency space represents a convolution, mixing the spatial frequencies of the two functions. In this manner, high frequency, un-resolved, content is made available within the passband of the objective lens due to a frequency down-conversion with the resulting fluorescence emission observed as a Moiré fringe pattern. To extract the high frequency content from the Moiré pattern, three or five phase-shifts of the structured illumination is needed for improving the resolution along one axis. For isotropic resolution, the process must be repeated for 3 orientations (angles) of the excitation pattern, for a total of 9 (15) images in case of a 2D (3D) SIM reconstruction. Since SIM only needs 9 (15 for 3D) images to create a super-resolution image over wide-field of view, this method is inherently fast, making it the most popular method for live cell optical nanoscopy.

The development of high-resolution methods like excitation depletion techniques[4, 5] and single-molecule localization microscopy (SMLM)[6-9], yielding resolution down to a few tens of nanometers, has opened new possibilities for discovery within life sciences[12]. However, to find real statistical meaning, the increase in throughput of super-resolution imaging methods would represent the next leap within nanoscopy. SIM already have the temporal ascendancy over the other methods, and with its ease of use, label compatibility and low photo-toxicity the method points in the direction of real high-throughput nanoscopy. To fully harness the utility of fast SIM imaging technique, the achievable spatial resolution, throughput of the method and the system complexity of SIM would need improvement. In conventional SIM, the illumination and collection light paths are coupled (**Fig 1a**), which limits the resolution and hinders the use of low N.A objectives to be used for large area imaging. Furthermore, the generation of the necessary standing wave patterns are usually done with free-space optics, with components to control and maintain the pattern orientation, phase and polarization state. The resulting SIM microscopes are thus both bulky, expensive, and prone to misalignment needing highly qualified personnel which further adds to maintenance costs. The resolution of SIM can be improved by using speckle-illumination[13-15] and blind-SIM[16-18] reconstruction approaches but it comes with a cost of low-temporal resolution due to the need of large number of images (100s). The speckle illumination methods takes away the main concept of “structured” illumination which helps in minimizing the number of frames needed (9-15) by illuminating the sample with pre-determined and highly structured illumination pattern. Thus, efforts to enhance the resolution of SIM keeping structured illumination is worth pursuing.

SIM on a chip. In this work we propose a method that will allow a standard optical microscope to acquire total internal reflection fluorescence (TIRF) SIM[19-21] images using a mass-producible, photonic chip, with better resolution and possibly increased field-of-view (FOV) over conventional SIM. Chip-based fluorescence microscopy relies on total internal reflection of the excitation light inside planar waveguides on a chip[22-25 26, 27], with a part of the excitation light available as an evanescent field exponentially decaying from the surface of the waveguide. In chip-based SIM (*c*SIM), a low-cost upright microscope can gather super-resolved images of the specimen placed directly on top of a planar waveguide surface (**Fig. 1b**). The waveguide is made from a dielectric material with high index contrast (HIC) (such as silicon nitride, Si3N4). By using the interference of spatially coherent light inside single-mode waveguides, standing wave interference fringes are generated on top of the waveguide surface (**Fig. 1, Supplementary note 1, Supplementary Fig. 1**), which are used to excite fluorescence in the labelled sample. An array of single mode planar waveguides, for example six as shown in **Fig. 1c** enables three rotational angles at the overlapping imaging area. By maneuvering the phase of the standing wave of the respective waveguide arm, the necessary data for a 2D TIRF-SIM reconstruction, i.e. 9 images (3 angles and 3 phases steps) can be acquired. At the imaging location, the single mode waveguides are adiabatically tapered[27, 28] to a large area (400 um^2 in the present study).

The proposed *c*SIM methodology opens up the possibility of pushing the resolution enhancement of the SIM technique beyond 2X, and enables scalable resolution over a scalable large field of view. This can be seen if we first consider the fringe period f_s generated by interference in a waveguide as given by

$$f_s = \frac{\lambda_{ex}}{2n_f \sin\frac{\theta}{2}}$$

where λ_{ex} is the excitation wavelength, n_f is the effective refractive index of the guided mode and θ is the angle of interference. Generating the SIM pattern with a planar waveguide thus contributes n_f in to the achievable resolution Δ_{xy} of the method, so the equation describing the theoretical best resolution for *c*SIM takes the form of

$$\Delta_{xy} = \frac{\lambda_{ex}}{2(N.A. + n_f \sin\frac{\theta}{2})}$$

where N.A. is the numerical aperture of the imaging objective lens. If n_f is larger than the N.A. , the resolution of the method exceeds the resolution of conventional SIM, which would have 4N.A. in the denominator (**Supplementary note 2, Supplementary figure 2**). In *c*SIM, the resolution enhancement can be scaled by changing the fringe spacing of the interference pattern using different pairs of waveguides interfering at different angles (**Fig. 1d,**

Supplementary figure 3, Supplementary note 3). A small interference angle between two waveguides produces a large fringe period and thus a low-resolution enhancement, while opposing pair of waveguides (180° between them) yield a very small fringe period and thus a high-resolution enhancement (**Fig. 1d-f**). Moreover, by using waveguides made of HIC material, (n_f=1.7-2.1) the fringe spacing of the standing wave pattern can be made much smaller than what can be achieved by a high N.A. oil immersion objective lens (N.A.=1.49) in conventional SIM. For Si_3N_4 (n=2) waveguides interfering at 180°, the theoretical resolution enhancement possible for *c*SIM (**Supplementary note 2, Supplementary figure 2**) is around 2.4x above the Abbe resolution limit using an N.A. of 1.2. This can be further increased by the use of other HIC dielectric materials with even higher refractive index such as tantalum pentoxide (n=2.1) or titanium dioxide (n=2.6).

In conventional SIM, a high N.A./magnification objective lens is desirable for high-resolution imaging (to generate small fringe pattern); while a low magnification/N.A. objective lens is required for increasing the FOV and the throughput. Thus, the present solution limits either the resolution or the FOV. In case of *c*SIM, since the contribution of n_f in Eq.2 is independent of the objective lens the method can be extrapolated to work with low N.A. and low magnification objectives (**Supplementary note 3, Supplementary Figure 4**). The shift in frequency space is dictated by n_f but the passband of the objective lens is still governed by N.A, thus the frequency shift would remain the same but more interference angles would be needed to fill any gaps in frequency space (**Fig. 1h-j, Supplementary Figure 4**). In this sense, the output of the method would show the same resolution enhancement as the high N.A case, but with the FOV supported by the lower N.A. imaging objective lens. Noticeably, generating the illumination fringes onto the sample via waveguides also alleviates the problem of refractive index oil mismatching as often arises in objective based SIM.

RESULTS

Since the method relies on interference, the laser light must be split in two paths. This can be done either off-chip splitting the light in a 50:50 fibre split and by using two waveguides simultaneously (**Fig. 2a**), or on-chip using a waveguide y-branch (**Fig. 2b,c**). The on-chip light spilt is less prone to any phase vibration originating from outside the chip and thus produces less phase-noise as opposed to the off-chip fibre split (**Supplementary Figure 5**). A key parameter of any SIM imaging method is the accurate control of the illumination patterns phase. For *c*SIM, three routes are proposed. Firstly, for the design proposed in **Fig. 2a**, off-chip phase shifts can be achieved by local heating of one arm of the fibre split. Alternatively, by using three discrete waveguides y-branches illuminating the same imaging area, but each with a different optical path length creates a relative phase shift between the three waveguides

(**Fig. 2b**). Finally, using on-chip thermo-optics phase shifter concept[29] (**Fig. 2c, Supplementary Figure 6**) a pre-determined phase shift can be imparted. This describes resolution enhancement along one axis (**Fig 2 a-c**), however to achieve isotropic resolution the structures need to be copied and rotated to have three equally spaced orientations of the *c*SIM pattern (**Fig. 2d-h**).

For light splitting off-chip (**Fig.2a**), the fringe spacing can be scaled by coupling in to different waveguides on the same structure (**Fig. 2d**) to create interference at different angles. For light splitting on-chip (**Fig. 2b,c**) separate structures can be used for *c*SIM imaging to achieve interference at different angles (**Fig.2e-h**). The method was experimentally verified by imaging a sample of 100nm fluorescent beads using the *c*SIM structure depicted in **Fig. 2d**, having interference angle of 60^{o}. Here, excitation wavelength of 660 nm was used which for this structure give a fringe spacing around 400 nm. The light was sequentially guided from different rotational angles towards the central area where the *c*SIM interference pattern is overlapping for all orientations (**Fig.3a-c**). The presence of the standing wave with phase shifts was directly observed using a fluorescent dye layer (**Fig. 3d**). The standing wave fringe spacing and orientation was further confirmed by the power spectrum showing a distinct peak at the standing wave frequency (**Fig.3e-g**) with the orientation of the peaks in **Fig. 3e-g** corresponding to **Fig. 3a-c**, respectively. By comparing the diffraction limited images (**Fig. 3h,j**) with the cSIM reconstruction (**Fig. 3i,k**) the resolution enhancement is clearly visible. By drawing a line-profile (**Fig. 3l**) across the intensity distribution marked with a green box in **Fig. 3k**, what appears as a continuous distribution in the diffraction limited image (**Fig.3j**) is clearly observed as two beads in the *c*SIM reconstruction (**Fig. 3k**). The line-profile shows that the two beads are separated by 206 nm, note that this is obtained using an imaging objective lens of N.A. 1.2.

Similarly, thermo-optical phase change using the chip designs shown in **Fig 2h**. was demonstrated. A sputtered silver circuit acting as a resistor locally heated a polymer on top of tone of the arms leading towards the interference region (**Supplementary Figure 7**). The resulting change in the effective refractive index yields a phase change in the standing wave interference pattern. Using this method, the phase can be accurately controlled using small increments in the voltage supplied to the silver circuit (**Supplementary Figure 6**). The rise and fall times to achieve a π shift in the phase of the interference pattern was found to be on the microsecond range, which would allow fast live *c*SIM imaging. We confirmed this method by imaging a 100 nm bead sample and the results are shown in **Supplementary Figure 8**.

Furthermore, we demonstrate that *c*SIM can surpass the resolution enhancement of conventional linear SIM, achieved using opposing pairs of waveguides (interfering at 180 ^{o}).

This will generate interference fringes with smaller spacing than what is presently possible using a high N.A. objective lens (e.g. 1.49 N.A.) in conventional TIRF-SIM, and the interference pattern will have a fringe spacing beyond the diffraction limit. Such chip design would enable a resolution enhancement beyond a factor of 2x (as in case of linear SIM). Using the Si_3N_4 waveguide platform and an imaging objective lens of 1.2 N.A. a theoretical resolution enhancement of 2.4x (Supplementary note 1) is possible. 1D counter-propagating waveguides (**Fig. 2b**) was used to investigate this idea. As the fringe pattern were smaller than the diffraction limit of the imaging objective lens, they could not be observed directly. To verify the presence of a sub-diffraction limited standing wave pattern, the surface of the chip was stained using a fluorescent dye and brought in to a blinking state following *d*STORM imaging protocols[30]. This allows a super-resolution image of the evanescent field intensity distribution to be formed, visualizing the standing wave (**Fig. 4a-c, Supplementary Figure 9**). This method both verifies that there is a standing wave present, and importantly confirms the phase stability of the pattern since a *d*STORM measurement consists of thousands of frames over tens of minutes and any phase drift during imaging would have averaged the image making visualization of fringes impossible. A fluorescent bead sample was imaged using both diffraction limited (**Fig. 4 d,f**) and *c*SIM (**Fig. 4e,g**) showing a clear resolution enhancement along one direction. Beads are separable by line-profiles down to around 117 nm **(Fig.4h**), corresponding to 2.3x resolution enhancements while using imaging objective lens of 1.2 N.A. and 660 nm.

DISCUSSION AND CONCLUSION

In this work we have demonstrated a new concept of performing SIM imaging. The main idea is to harness photonic integrated circuits (PICs) to generate the illumination patterns required in SIM instead of using the conventional approach of the objective lens. We outline several advantages of this novel proposed route. Firstly, the photonic chip enables easy generation of user-defined, highly-stable on-chip illumination patterns without needing any free-space optical components. Secondly, by using a photonic-chip the effective refractive index of the guided mode dictates how tightly the light is confined inside the waveguide, allowing for sub-diffraction limited illumination patterns to be formed; as opposed to the high-N.A. objective lens which is diffraction limited. Thirdly, photonic chips made of dielectric materials can generate uniform illumination over arbitrary large areas which is determined by the dimensions (width and length) of the waveguides[25, 26]. This is in contrast to objective lens based illumination that suffers from field-flatness and that generates a illumination pattern with a Gaussian profile over a limited FOV, determined by its magnification. Finally, our proposed *c*SIM is inherently compact and since it is an integrated technology, replying on PICs it will open the avenues for parallelization, automation, high-throughput and miniaturization.

In our proposed method, the entire illumination light path, i.e. light delivery, pattern generation and beam steering are provided using a photonic chip, which can be easily retrofitted allowing any standard microscope **(Supplementary Figure 10**) to acquire super-resolution SIM images (**Fig. 3h-k, 4f-g, Supplementary Figure 8**) Moreover, the proposed setup, together with on-chip light splitting and phase modulation (**Supplementary Figure 5, Fig. 4a-c**) is inherently very stable with minimum bulk optical elements and therefore free from miss-alignment issues. Besides, being compact, we have shown that *c*SIM has the potential to surpass the resolution enhancement provided by conventional objective-based SIM. The interference fringes in *c*SIM are formed at the sample plane using planar waveguides, and are thus not influenced by the imaging objective as is the case when crating the pattern using objective lenses itself. With counter-propagating waveguides made from a HIC dielectric material, the fringe spacing of *c*SIM will be smaller than what can be generated using the high N.A oil-immersion objective lens commonly used, which led to *c*SIM imaging with up to 2.3x resolution enhancement (**Fig. 1, Fig. 4, Supplementary note 1, Supplementary Fig. 9**).

Using simulations we have demonstrated that the chip-based method opens the opportunity of using a low N.A./ magnification objective lens which provides a larger FOV while still maintaining the resolution improvement provided by the waveguide generated illumination pattern (**Supplementary figure 4**). This represent an improvement over conventional SIM, where a use of a low. N.A. objective lens to image large FOV will significantly reduce the supported optical resolution (**Supplementary note 1, Supplementary figure 10**).

Compared to previous approaches where the formation of illumination fringes were shown using surface plasmon interference and localized plasmons[31, 32] with a metal interface, here we demonstrate the advantages of using PICs made of dielectric material. PICs enables easy integration of several optical functions and components such as on-chip splitters, multiplexers, couplers, lens, etc. Moreover, dielectric materials can propagate and delivery light to much longer distances (centimeters, **Fig. 1 c**) as compared to plasmons based on metals. Although, in the present *c*SIM design the imaging area was limited to about 400 um^2, this is not an inherent limitation and the imaging area can easily be expanded using wider adiabatically tapered single mode waveguides[33]. Once the light is coupled, the PICs enables easy manipulation of the light on the chip, opening avenues for user-defined illumination pattern and phase stepping strategies as outlined in **Fig. 1c-d and Fig. 2**. Using PICs we proposed different waveguide designs where light splitting and phase stepping were implemented both off-board (**Fig. 2a,d**) and on-board (**Fig 2. b,c,e-h**) the chip. To maintain stable and repeatable phase steps, the on-chip methods are preferred due to the inherently low phase noise achieved when splitting the light on-chip with waveguides covered by a protective silica top-cladding

(**Supplementary figure 5**). While all the methods for phase-stepping finally worked **(Fig. 3, Fig. 4, Supplementary figure 8**), the methods holding the potential for high-speed imaging are using thermo-optics (**Fig. 2c,f,h**), or on-chip path-length stepping (**Fig. 2b,e,g**). Both of these methods can be made to switch phase very fast, using a voltage supply or fibre-optical switch, respectively. Thus, the final temporal resolution of the method would be dominated by the camera exposure time typically needed for wide-field fluorescence microscopy, which will allow live-speed imaging.

The present implementation of *c*SIM is done using opaque silicon substrates and with an upright microscope equipped with a water immersion objective lens (x60/N.A.1.2). Future, development of *c*SIM will be done using thin transparent substrates. This will enable using an inverted optical microscope configuration equipped with a high-N.A. oil immersion objective lens (e.g. 1.4 instead of 1.2 used in the present study). This will further extend the resolution of *c*SIM, while in the same time keeping the scalability of the method without affecting the benefits of the inverted microscope configuration. Also, in future work, development of 2D SIM with 2.4X resolution enhancement will be studied by designing suitable waveguide geometries.

The chip-based illumination strategy is an lucrative route, although the focus of this work is to report chip-based SIM, it can be foreseen that PICs provides new research directions of performing complex light beam shaping for other nanoscopy methodologies such as stimulated emission depletion microscopy[5, 34] or light sheet microscopy[35]. Intricate waveguide geometries are capable of generating a range of exotic intensity distributions by harnessing multimode light guiding and interference for altogether new illumination strategies within optical microscopy and nanoscopy. Due to the widespread use of microfabrication techniques within mainstream CMOS technology, the fabrication facilities for PICs are already existing, making mass production of photonics chips feasible, with the potential cost per chip could be reduced to just a few Euros.

The relatively new field of on-chip optical nanoscopy could also benefit with the development of on-chip integration of light sources[36] and frequency combs[37], further miniaturizing the optical set-up. Although, on-chip illumination strategy enables excitation over large areas, the light collection is still presently limited by the imaging objective lens. In the future, the marriage of on-chip illumination with micro-lens arrays[38] for light collection could potentially open the avenues for extra-ordinary high-throughput, where illumination and collection both can be done parallel over large areas, completely removing the dependency on a bulky objective lens.

ACKNOWLEDGMENTS

The authors thank Olav G. Hellesø for his inputs on designs and Rainer Heintzmann and Sourov Das, for help with the SIM reconstruction algorithms and design of fibre-optical phase modulator, respectively. This work was supported by the European Research Council (grant no. 336716 to B.S.A.).

COMPETING FINANCIAL INTERESTS

B.S.A. applied for patent GB1705660.7 on SIM-on-chip. The other authors declare no competing financial interest.

AUTHOR CONTRIBUTIONS

B.S.A. conceived the idea and supervised the project. Ø.I.H. built the setup, performed the experiments and analysed the data. J.C.T and F.S.T designed the waveguide mask. All authors contributed towards chip designs. Ø.I.H., F.T.D. and J.C.T characterized the waveguides. F.T.D. and Ø.I.H. fabricated the on-chip thermo-optics for phase modulation. M.L. performed all the simulation of cSIM. Ø.I.H. and B.S.A. mainly wrote the manuscript and all authors commented to the manuscript.

Figure 1 – The concept. (a) Conventional SIM relies on a high N.A. objective lens to both generate the sinusoidal excitation pattern, and to collect the emitted fluorescence. (b) cSIM harness a standing wave interference pattern generated in a planar waveguide to excite fluorescence in samples located directly on top of an integrated photonic chip via evanescent fields. The emitted fluorescence is captured from the top using a microscope. This decouples the excitation and collection light paths compared with the conventional case. (c) The chip used for cSIM have integrated waveguides which interferers at different rotational angles. Here, light inside the different waveguides are shown in pseudo-color. (d) Interference at a low angle between waveguides creates an interference pattern with low fringe spacing, while interference using counter-propagating guided modes yields the smallest fringe spacing. The latter giving better cSIM resolution. (e) The resolution of a microscope is represented in frequency space with the cut-off frequency (Abbe limit) shown with the solid circle. The dotted circle represents the maximum shift of the OTF possible in conventional SIM yielding 2x resolution enhancement. (f) In cSIM different interference angles shifts the OTF according to the fringe spacing of the interference pattern, here shown for Si_3N_4 waveguide material where 100° and 180° interference gives increased resolution over conventional SIM. g) Using materials of even higher refractive index it is possible to scale the resolution even further, here shown with Si_3N_4 ($n\approx2.0$), Ta_2O_5 ($n\approx2.05$) and TiO_2 ($n\approx2.3$). (h) Using a low N.A. objective lens in conventional SIM gives a shift of the OTF corresponding to the N.A., yielding low resolution. (i) In cSIM the excitation and collection light paths are separated, so the shift of the OTF will unaffected by the low N.A, however more interference angles will need to be used to fill the frequency space.

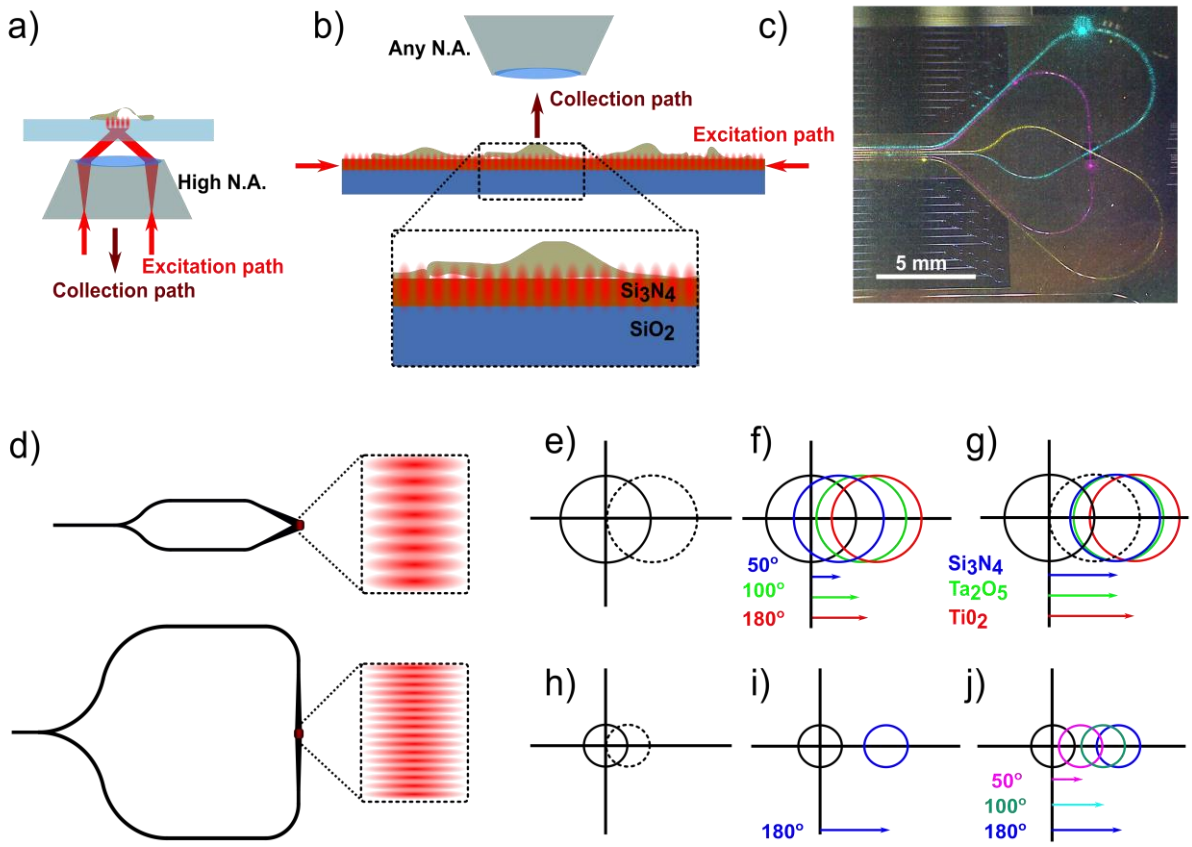
a)
High N.A.
Excitation path
Collection path
b)
Any N.A.
Collection path
Excitation path
Si3N4
SiO2
c)
5 mm
d)
e)
f)
50°
100°
180°
g)
Si3N4
Ta2O5
Ti02
h)
i)
180°
j)
50°
100°
180°

Figure 2 – Waveguide designs for cSIM. (a) Two input waveguides are used to create interference in the image region (marked with a circle). Here, light is split on the optical table using a 50:50 fibre split. This structure will create a 1D cSIM image. For the 2D case the structure needs to be rotated for a total of three rotational angles of the cSIM pattern to get isotropic resolution as shown in (d). Using the structure in (d) different interference angles can be used for scalable resolution, depending on which waveguides are active. b) Light splitting on-chip yields a more phase-stable interference pattern. For this 1D cSIM structure the phase stepping is achieved by coupling light on to three different waveguides merging at the same image area, each with different optical path lengths. To get isotropic resolution the structure must be rotated as shown in (e) for 180° interference, and (g) for 60° interference. c) Using thermos-optics the phase of the interference pattern can be controlled by applying a voltage to a resistive circuit causing heat on of the waveguide arms. A polymer located on the waveguide arm, in contact with the waveguide, will thermally expand giving a change in refractive index which cause the phase change. (f, h) The structure must be rotated to yield isotropic resolution.

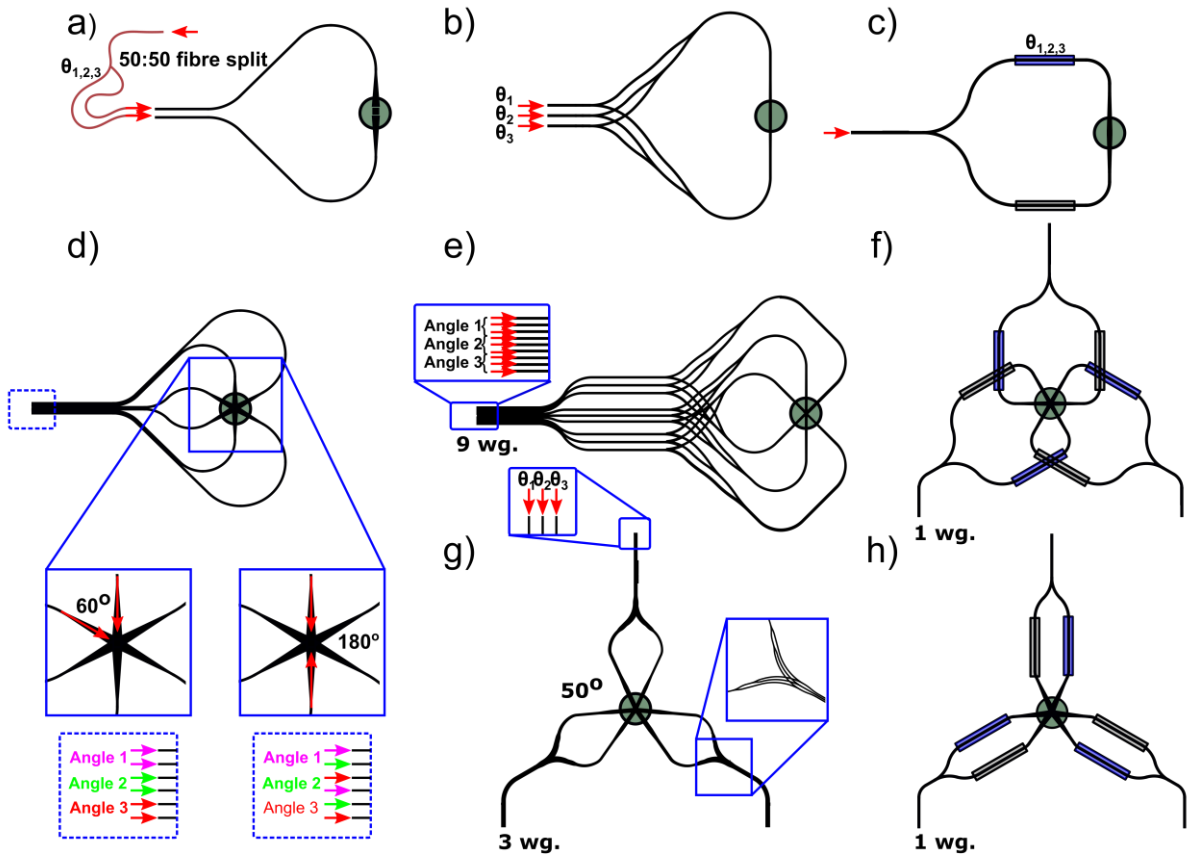

Figure 3 – cSIM imaging. (a) Light is guided in two arms of the waveguide cSIM structure creating interference at 60° where the waveguides meet. (b, c) Different waveguides creates interference with the same fringe spacing at different rotational angles, for isotropic resolution enhancement. d) The cSIM standing wave is directly imaged using a fluorescent dye layer and the line plot show the three phase steps needed for cSIM (20° interference is used for increased contrast). (e-f) The power spectrum, generated by the reconstruction software shows a peak corresponding to the detected standing wave modulation frequency with the orientation corresponding to the orientations standing wave generated in (a-c) respectively. h) Show a diffraction limited, filtered image of a 100 nm fluorescent bead sample while (i) shown the cSIM reconstruction of the same region. A cluster of beads saturates in the centre of the image. (j-k) Show the zoomed images indicated with a white box in (i) with the green box indicating the position of the line-profile shown in (l). Here, two beads located 206 nm apart is resolved using cSIM, but not in the diffraction limited image. The excitation/emission wavelengths used are 660nm/690nm.

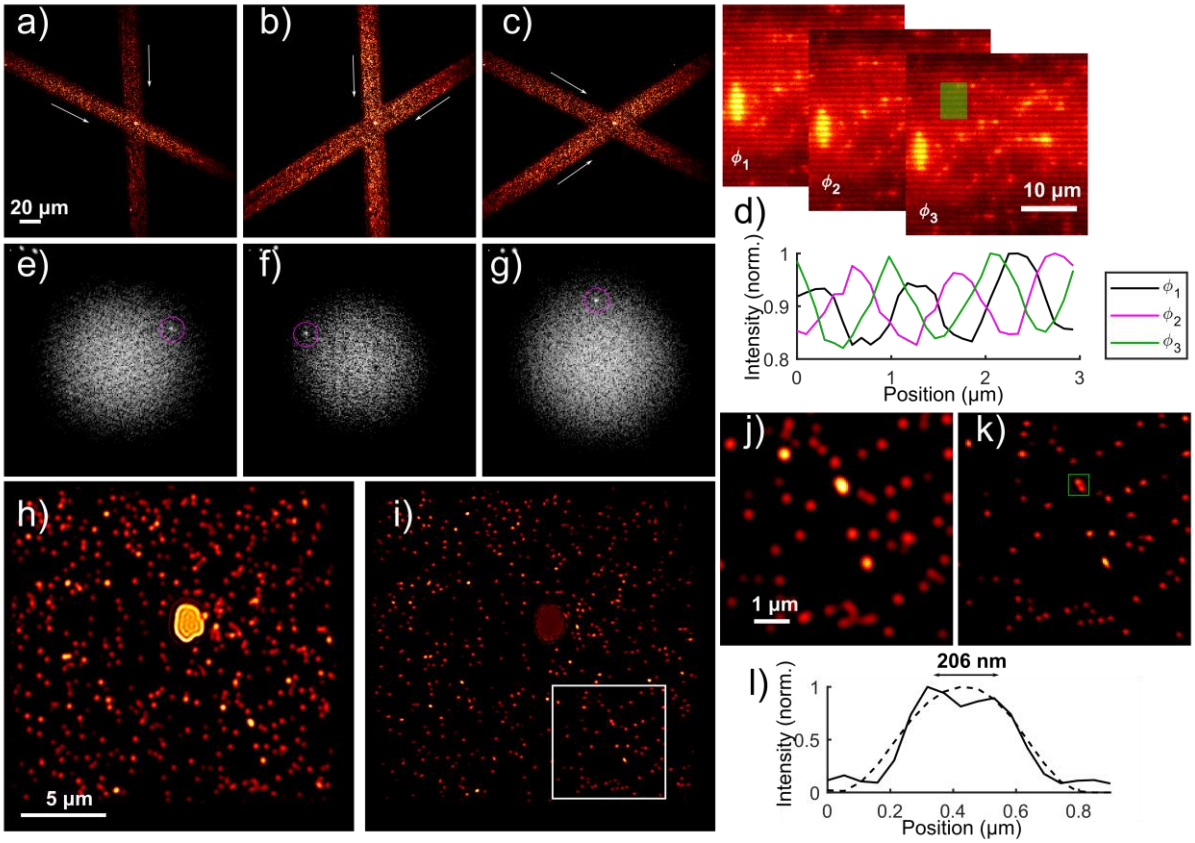
a)
b)
c)
20 μm
d)
ϕ_1
ϕ_2
ϕ_3
10 μm
Intensity (norm.)
1
0.9
0.8
0
1
2
3
Position (μm)
e)
f)
g)
h)
i)
5 μm
j)
k)
1 μm
l)
206 nm
Intensity (norm.)
1
0.5
0
0
0.2
0.4
0.6
0.8
Position (μm)

Figure 4 – cSIM with increased resolution. (a) Counter-propagating light set up a sub-diffraction limit interference pattern not visible using a fluorescence dye layer. (b) The presence of the standing wave is confirmed using *d*STORM imaging of the fluorescent dye layer, visualizing the standing wave having a fringe spacing around 195 nm (c). (d, e) The same 1D structure was used for cSIM, with diffraction limited and 1D cSIM images shown respectively. (f, g) show the zoom indicated with a white box in (d), with a line profile (h) demonstrating two beads separated by 117nm which corresponds to 2.3x resolution enhancement using cSIM. Excitation and emission wavelengths are 660 nm/690 nm.

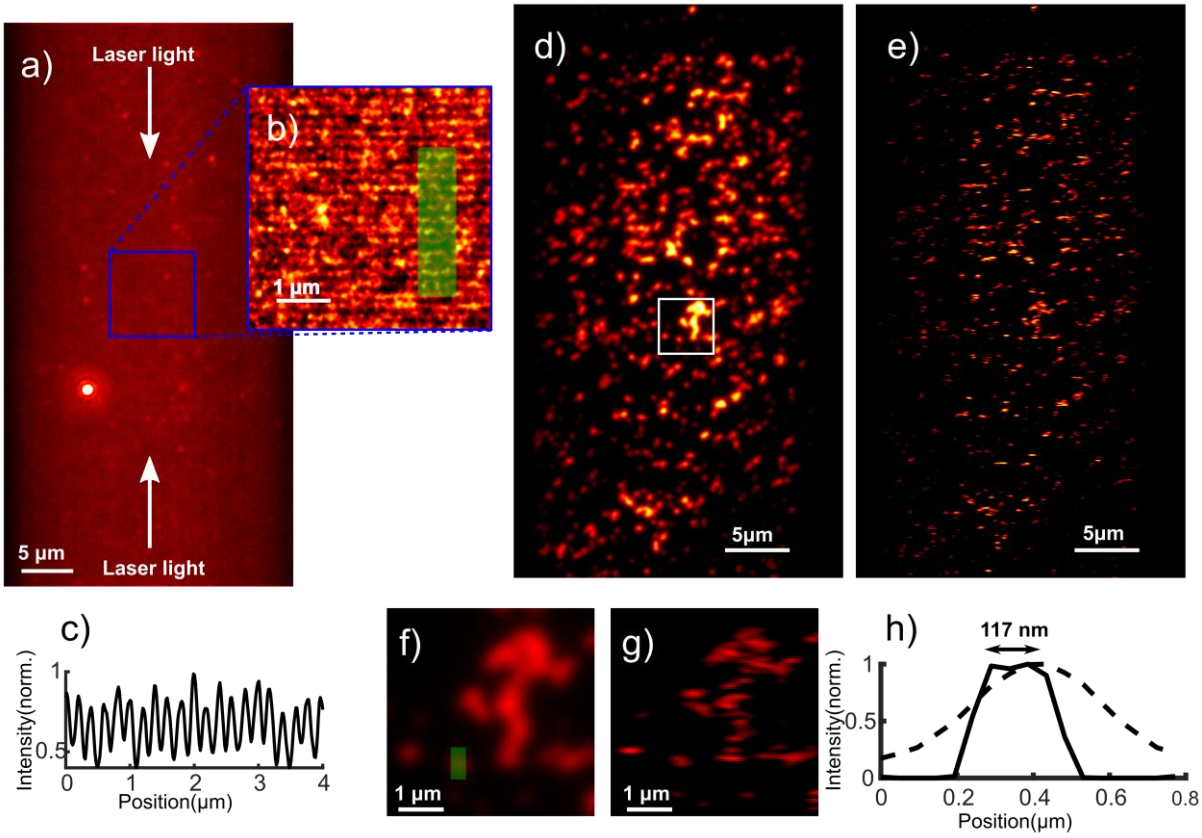

REFERENCES

1 Goodman JW. *Introduction to Fourier Optics*. W. H. Freeman, 2005.

2 Pawley J. *Handbook of Biological Confocal Microscopy*. Springer US, 2010.

3 Eggeling C, Willig KI, Sahl SJ, Hell SW. Lens-based fluorescence nanoscopy. *Quarterly Reviews of Biophysics* 2015, **48**(2)**:** 178-243.

4 Hell SW, Wichmann J. Breaking the diffraction resolution limit by stimulated emission: stimulated-emission-depletion fluorescence microscopy. *Opt Lett* 1994, **19**(11)**:** 780-782.

5 Willig KI, Rizzoli SO, Westphal V, Jahn R, Hell SW. STED microscopy reveals that synaptotagmin remains clustered after synaptic vesicle exocytosis. *Nature* 2006, **440**(7086)**:** 935-939.

6 Rust MJ, Bates M, Zhuang X. Sub-diffraction-limit imaging by stochastic optical reconstruction microscopy (STORM). *Nature Methods* 2006, **3:** 793.

7 Heilemann M, van de Linde S, Schuttpelz M, Kasper R, Seefeldt B, Mukherjee A*, et al.* Subdiffraction-resolution fluorescence imaging with conventional fluorescent probes. *Angewandte Chemie (International ed in English)* 2008, **47**(33)**:** 6172-6176.

8 Betzig E, Patterson GH, Sougrat R, Lindwasser OW, Olenych S, Bonifacino JS*, et al.* Imaging intracellular fluorescent proteins at nanometer resolution. *Science (New York, NY)* 2006, **313**(5793)**:** 1642-1645.

9 Hess ST, Girirajan TPK, Mason MD. Ultra-High Resolution Imaging by Fluorescence Photoactivation Localization Microscopy. *Biophys J* 2006, **91**(11)**:** 4258-4272.

10 Gustafsson MG. Surpassing the lateral resolution limit by a factor of two using structured illumination microscopy. *Journal of microscopy* 2000, **198**(Pt 2)**:** 82-87.

11 Heintzmann R, Cremer CG. *Laterally modulated excitation microscopy: improvement of resolution by using a diffraction grating*, vol. 3568. SPIE, 1999.

12 Sahl SJ, Hell SW, Jakobs S. Fluorescence nanoscopy in cell biology. *Nature Reviews Molecular Cell Biology* 2017, **18:** 685.

13 Kim M, Park C, Rodriguez C, Park Y, Cho Y-H. Superresolution imaging with optical fluctuation using speckle patterns illumination. *Sci Rep-Uk* 2015, **5:** 16525.

14 Guo K, Zhang Z, Jiang S, Liao J, Zhong J, Eldar YC*, et al.* 13-fold resolution gain through turbid layer via translated unknown speckle illumination. *Biomed Opt Express* 2018, **9**(1)**:** 260-275.

15 Yeh L-H, Chowdhury S, Repina NA, Waller L. Speckle-structured illumination for 3D phase and fluorescence computational microscopy. *Biomed Opt Express* 2019, **10**(7)**:** 3635-3653.

16 Mudry E, Belkebir K, Girard J, Savatier J, Le Moal E, Nicoletti C*, et al.* Structured illumination microscopy using unknown speckle patterns. *Nat Photonics* 2012, **6:** 312.

17 Ayuk R, Giovannini H, Jost A, Mudry E, Girard J, Mangeat T*, et al.* Structured illumination fluorescence microscopy with distorted excitations using a filtered blind-SIMalgorithm. *Opt Lett* 2013, **38**(22)**:** 4723-4726.

18 Jost A, Tolstik E, Feldmann P, Wicker K, Sentenac A, Heintzmann R. Optical Sectioning and High Resolution in Single-Slice Structured Illumination Microscopy by Thick Slice Blind-SIM Reconstruction. *Plos One* 2015, **10**(7)**:** e0132174.

19 Cragg GE, So PTC. Lateral resolution enhancement with standing evanescent waves. *Opt Lett* 2000, **25**(1)**:** 46-48.

20 Chung E, Kim D, So PT. Extended resolution wide-field optical imaging: objective-launched standing-wave total internal reflection fluorescence microscopy. *Opt Lett* 2006, **31**(7)**:** 945-947.
21 Kner P, Chhun BB, Griffis ER, Winoto L, Gustafsson MGL. Super-resolution video microscopy of live cells by structured illumination. *Nature Methods* 2009, **6:** 339.
22 Grandin HM, Stadler B, Textor M, Voros J. Waveguide excitation fluorescence microscopy: A new tool for sensing and imaging the biointerface. *Biosensors & Bioelectronics* 2006, **21**(8)**:** 1476-1482.
23 Agnarsson B, Ingthorsson S, Gudjonsson T, Leosson K. Evanescent-wave fluorescence microscopy using symmetric planar waveguides. *Opt Express* 2009, **17**(7)**:** 5075-5082.
24 Agnarsson B, Jonsdottir AB, Arnfinnsdottir NB, Leosson K. On-chip modulation of evanescent illumination and live-cell imaging with polymer waveguides. *Opt Express* 2011, **19**(23)**:** 22929-22935.
25 Diekmann R, Helle OI, Oie CI, McCourt P, Huser TR, Schuttpelz M*, et al.* Chip-based wide field-of-view nanoscopy. *Nat Photonics* 2017, **11**(5)**:** 322-+.
26 Helle ØI, Coucheron DA, Tinguely J-C, Øie CI, Ahluwalia BS. Nanoscopy on-a-chip: super-resolution imaging on the millimeter scale. *Opt Express* 2019, **27**(5)**:** 6700-6710.
27 Tinguely J-C, Helle ØI, Ahluwalia BS. Silicon nitride waveguide platform for fluorescence microscopy of living cells. *Opt Express* 2017, **25**(22)**:** 27678-27690.
28 Fu Y, Ye T, Tang W, Chu T. Efficient adiabatic silicon-on-insulator waveguide taper. *Photon Res* 2014, **2**(3)**:** A41-A44.
29 Harris NC, Ma Y, Mower J, Baehr-Jones T, Englund D, Hochberg M*, et al.* Efficient, compact and low loss thermo-optic phase shifter in silicon. *Opt Express* 2014, **22**(9)**:** 10487-10493.
30 van de Linde S, Löschberger A, Klein T, Heidbreder M, Wolter S, Heilemann M*, et al.* Direct stochastic optical reconstruction microscopy with standard fluorescent probes. *Nature protocols* 2011, **6:** 991.
31 Wei F, Liu Z. Plasmonic Structured Illumination Microscopy. *Nano Letters* 2010, **10**(7)**:** 2531-2536.
32 Wei F, Lu D, Shen H, Wan W, Ponsetto JL, Huang E*, et al.* Wide Field Super-Resolution Surface Imaging through Plasmonic Structured Illumination Microscopy. *Nano Letters* 2014, **14**(8)**:** 4634-4639.
33 Archetti A, Glushkov E, Sieben C, Stroganov A, Radenovic A, Manley S. Waveguide-PAINT offers an open platform for large field-of-view super-resolution imaging. *Nature Communications* 2019, **10**(1)**:** 1267.
34 Schneider J, Zahn J, Maglione M, Sigrist SJ, Marquard J, Chojnacki J*, et al.* Ultrafast, temporally stochastic STED nanoscopy of millisecond dynamics. *Nature Methods* 2015, **12:** 827.
35 Santi PA. Light Sheet Fluorescence Microscopy: A Review. *Journal of Histochemistry & Cytochemistry* 2011, **59**(2)**:** 129-138.
36 Otterstrom NT, Behunin RO, Kittlaus EA, Wang Z, Rakich PT. A silicon Brillouin laser. *Science (New York, NY)* 2018, **360**(6393)**:** 1113-1116.
37 Gaeta AL, Lipson M, Kippenberg TJ. Photonic-chip-based frequency combs. *Nat Photonics* 2019, **13**(3)**:** 158-169.
38 Orth A, Crozier K. Gigapixel fluorescence microscopy with a water immersion microlens array. *Opt Express* 2013, **21**(2)**:** 2361-2368.

39 Prieto F, Sepúlveda B, Calle A, Llobera A, Domínguez C, Abad A*, et al.* An integrated optical interferometric nanodevice based on silicon technology for biosensor applications. *Nanotechnology* 2003, **14**(8)**:** 907.

40 Müller M, Mönkemöller V, Hennig S, Hübner W, Huser T. Open-source image reconstruction of super-resolution structured illumination microscopy data in ImageJ. *Nature Communications* 2016, **7:** 10980.

41 Ovesný M, Křížek P, Borkovec J, Švindrych Z, Hagen GM. ThunderSTORM: a comprehensive ImageJ plug-in for PALM and STORM data analysis and super-resolution imaging. *Bioinformatics* 2014, **30**(16)**:** 2389-2390.

METHODS

Chip Design.

The key parameters in SIM are interference fringe spacing, phase modulation and fringe contrast. For chip-based SIM the dimensions of the active region is also crucial, to ensure that biological specimens are evenly illuminated by the structured illumination. The lateral size of cells are often from 10 µm and upwards.

The waveguide platform has been developed using the high-refractive index material Si3N4. High-index contrast materials enable tight confinement of the light inside the waveguide which entails compact bend radius. This allows for ultra-compact and dense waveguide structures with small footprint benefiting from high intensity in the evanescent field. In the visible range, strong evanescent fields can be achieved by designing waveguides with core thickness between 100-200 nm. For a 150 nm thick core material; single mode condition, adiabatic taper condition and bending losses were previously investigated[27]. It was found that 150 nm thick waveguide core give a strong evanescent field intensity without sacrificing much on the coupling efficiency. For this work single mode condition (**Supplementary figure 11(a)**) is necessary to generate uniform fringe pattern, which can be formed by interfering fundamental mode light guided inside the waveguide. The presence of any residual higher order modes will generate a mode-beat pattern, which is undesirable. Thus, shallow rib waveguides were preferred over strip waveguides. For a shallow rib, fundamental mode guiding can be achieved using waveguide widths (1-1.5 µm wide) (**Supplementary figure 11(b)**) within the reach of fabrication using standard photo-lithography techniques. Waveguides with 4 nm rib height (total height of 150 nm) and around 1-1.5 µm width was adiabatic tapered out to 25 µm or 50 µm with a tapering length of 2 mm or 4 mm, respectively. A significantly low bending loss for a shallow rib waveguides was achieved for a bend radius of 2 mm and more. The optimization of the designed parameters can be found in previous literature[27].

Chip fabrication.

The production of waveguide chips was performed at the Insitute of Microelectronics Barcelona (IMB-CNM, Spain). First, an oxide layer of ca. 2 µm was thermally grown on a silicon slab, followed by low-pressure chemical vapor deposition (LPCVD) of 150 nm Si_3N_4 at 800°. Conventional photo-lithography imprinted the waveguide geometries on a layer of photo-resist. 4 nm rib waveguides were realized using reactive-ion-etching (RIE). In order to prevent cross-talk of light into adjacent waveguide structures, an absorption layer consisting of 200 nm SiO_2 (deposited by plasma-enhanced chemical vapor deposition (PECVD)) followed by 100 nm poly-crystalline silicon (deposited by PECVD at 300°) was designed as a negative image of the first mask with 10 µm added to the waveguide width. RIE was used to etch until 100 nm of

SiO_2 remained, with wet etching (using hydrofluoric acid) removing the remaining material from the waveguide surface. Finally, a 1.5 µm SiO_2 layer (deposited by PECVD) built the cladding layer. The chip fabrication workflow is shown in **supplementary figure 12**. Imaging areas were patterned by a 3rd photo-lithography step. The window openings were realized using RIE until 100 nm SiO_2 was remaining, followed by wet etching to completely remove the oxide layer while preserving the Si_3N_4. Further details of the fabrication optimization and process can be found elsewhere[39].

Experimental setup.

A microscope modified from an Olympus modular microscope (BXFM) was mounted on a XY motorized translation stage. The microscope was fitted with a Hamamatsu Orca flash sCMOS camera. cSIM images were acquired using either Olympus x60/1.3SiO or Olympus x60/1.2W objective lenses. The waveguide chip was mounted on a micrometer xyz-stage using a vacuum chuck to hold the chip. Light was coupled on to the chip using a nine-fiber array adapter. The fibre array adapters are commercially available with fixed spacing (e.g. 127 µm). The waveguides were separated by the same space (127 µmm) as the fibre array, allowing for multiple waveguides to have light coupled at the same time (supplementary figure 7b). For off-chip cSIM (Fig.2a,d), an additional 50:50 fused fibre-split (OZ optics) was used to split the light. Thermo-optical phase stepping was achieved using a 6V voltage supply coupled to the resistive on-chip electro-optical heating elements. A schematic of the setup is shown in **supplementary figure 10**. The image data was analyzed using Fiji open source image processing software and FairSIM[40], an open source SIM reconstruction plugin. cSIM data from the 180° interference waveguides was analyzed with custom software.

Near-field mapping using dSTORM.

dSTORM near field mapping was performed by staining the waveguide surface with a layer of fluorescent molecules. A 1/1000 solution of CellMask deep red (Thermofisher, C10046) in phosphate buffered saline (PBS) was incubated for 20 minutes on the waveguide surface at room temperature. The solution was aspirated and a PDMS micro-chamber positioned on top of the chip was filled with dSTORM switching buffer consisting of an enzymatic oxygen scavenging system and 100 mM β-Mercaptoethylamine (MEA). The surface was excited with the 660 nm laser with sufficiently high power to achieve photo-switching. A stack of 100000 images was acquired at 30 ms exposure time and reconstructed using the Fiji plugin ThunderStorm[41].

Sample preparation.

The chip surface was coated with 0.5% Poly-l-lysine (PLL) solution, aspirated and dried with compressed Nitrogen. Depending on the desired distribution of fluorescent beads the chip would be plasma treated at a high setting for 30s, ensuring hydrophilic surface properties. A 0.5 µl drop of 100nm diameter fluorescent bead stock ((Tetraspeck, Thermofisher T7279) was put at the cSIM image region and allowed to dry completely. The chamber was filled with dH2O and the chip brought to the microscope for imaging.

REFERENCES FOR METHODS

21 Tinguely J-C, Helle ØI, Ahluwalia BS. Silicon nitride waveguide platform for fluorescence microscopy of living cells. *Opt Express* 2017, **25**(22)**:** 27678-27690.

32 Prieto F, Sepúlveda B, Calle A, Llobera A, Domínguez C, Abad A*, et al.* An integrated optical interferometric nanodevice based on silicon technology for biosensor applications. *Nanotechnology* 2003, **14**(8)**:** 907.

33 Müller M, Mönkemöller V, Hennig S, Hübner W, Huser T. Open-source image reconstruction of super-resolution structured illumination microscopy data in ImageJ. *Nature Communications* 2016, **7:** 10980.

34 Ovesný M, Křížek P, Borkovec J, Švindrych Z, Hagen GM. ThunderSTORM: a comprehensive ImageJ plug-in for PALM and STORM data analysis and super-resolution imaging. *Bioinformatics* 2014, **30**(16)**:** 2389-2390.

Structured illumination microscopy using a photonic chip

Supplementary Information

Øystein I. Helle Firehun T. Dullo Jean-Claude Tinguely
Marcel Lahrberg Balpreet S. Ahluwalia

March 2019

Supplementary note 1: Simulation of chip-based interference patterns

The cSIM interference patterns were simulated using finite element method in Comsol Multiphysics. Figure 1(a) shows two waveguides crossing at an angle of 50°. The red arrows indicate the directions of the straight waveguides along which the light propagates. Since the presented model is limited to a two-dimensional representation of the actual waveguide, the effective refractive indices along the third dimension have been calculated approximating those regions as planar waveguides [1]. Given the fundamental transversal electric (TE) mode being exited in each waveguide, the resulting intensity distribution shows the intended sinusoidal structure as well as a Gaussian envelope due to the shape of the waveguide modes. The mode index in the simulated Si_3N_4 structures is found to be $n = 1.7552$ at a vacuum wavelength of $\lambda = 660\,\mathrm{nm}$. In the presented model only the fundamental modes of the waveguides are excited. As it is indicated in Fig. 1(a), in order to estimate the periodicity of the intensity pattern, a sinusoidal function of the form $I(x) = \exp\left(-\left(\frac{x}{a}\right)^2\right)\sin^2(bx)$ has been fitted; the pattern spacing is found to be 445 nm.

Figure 1(b) shows respective simulation results for counter-propagating waveguides, i.e. interfering at an angle of 180°. As for the case of an interference angle of 50°, the intensity distribution was fitted as $I(x) = \sin^2(ax)$ and a period of 188 nm is found.

Although the pattern spacing can be calculated from the effective mode index without running a full numerical simulation of the structure, here the simulation results are used to illustrate the expected intensity distribution over the whole waveguide geometry.

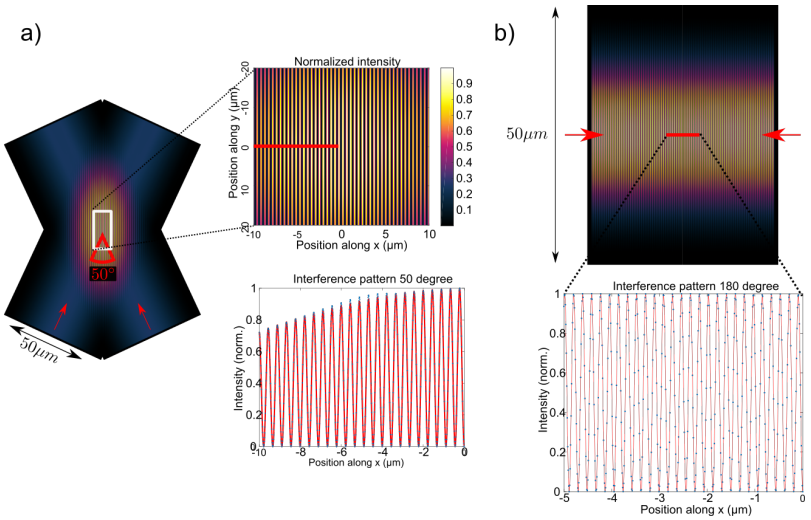

Figure 1: Numerical simulations of the proposed waveguide geometries to generate the illumination patterns for cSIM. The configurations of two waveguides crossing at an angle of 50° (a) generates a pattern with a periodicity of 445 nm. The couterpropagating waveguides (b) create a pattern with a period of 188 nm.

Supplementary note 2: Resolution of cSIM

The microscope objective is inherently a low pass filter, stopping frequency content above a certain value k_0, often refered to as the diffraction limited. Structure illumination microscopy relies on a sinusoidal excitation light to excite fluorescence in the sample. For a sample having frequency $\mathbf{k}$, the multiplication of structured illumination and sample yields a moirè pattern with observable frequencies $|\mathbf{k} - \mathbf{k_1}|$, if these are within the passband of the OTF (k_0) [2]. So as long as $\mathbf{k}$ lies within a circle of radius k_0 centered around $\mathbf{k_1}$, it will be indirectly observed in the moirè fringes. By going through the SIM reconstruction using phase stepping the achievable resolution of the reconstructed image is then $k_0 + k_1$. In this sense, it is desirable to have a large k_1, but since k_1 is formed using lenses, the method is also limited by diffraction, with the highest possible value of k_1 being k_0. Finally this would yield a maximum resolution enhancement of $2k_0$. By generating the structured illumination using waveguides the formation of k_1 is no longer depending on lenses, and is thus not diffraction limited but instead relies on the effective refractive index of the waveguide materials, as outlined below.

The resolution of cSIM is governed by the fringe-spacing of the standing wave interference pattern in addition to the N.A. of the collection optics. By interfering waveguides with changing angles θ the fringe spacing f_s can be changed as

$$f_s = \frac{\lambda_{ex}}{2n_{eff}\sin\theta/2}, \tag{1}$$

where n_{eff} is the effective refractive index of the guided mode. Generating the SIM pattern with a planar waveguide thus contributes n_{eff} in to the achievable resolution Δ_{xy} of the method, so the equation describing the theoretical best resolution for cSIM takes the form of

$$\Delta_{xy} = \frac{\lambda_{ex}}{2(N.A. + n_{eff}\sin\theta/2)}, \tag{2}$$

where N.A. is the numerical aperture of the imaging objective lens. Since n_{eff} is larger than N.A. the resolution of the method can exceed that of conventional SIM, which would have $4N.A.$ in the denominator.

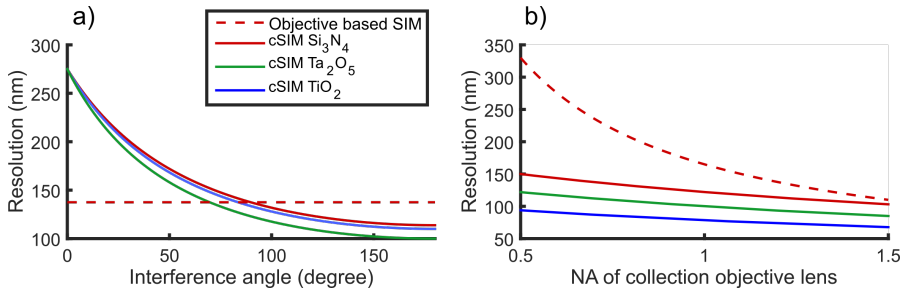

Figure 2: Graphical interpretation of eq. 2 for three different materials is shown. a) The angle of interference is dominating the achievable resoltuion for cSIM, which for interference angles between 70-100° surpass the resolution of conventional objective based SIM, using N.A.=1.2. b) The maximum achievable resolution for different N.A. objective lens, and thus different field of view size is shown for both cSIM (using 180° interference) and objective based SIM. The potential for cSIM to yield high resolution over large fields of view can be harnessed by acquiring several images with different interference angles as shown in Fig.4.

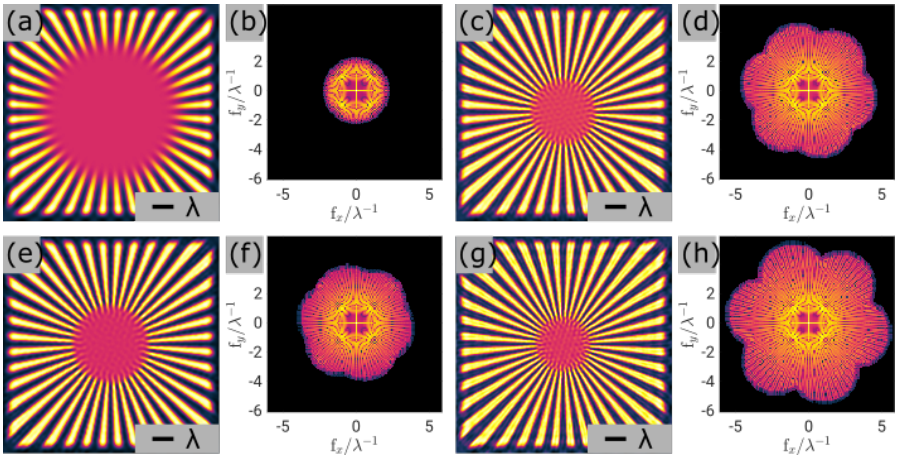

Figure 3: Simulation of SIM using the Siemens star sample. Spatial and freqency images are shown sequentially. a,b) Diffraction limited image. c,d) Conventional SIM image, e,f) cSIM using 60 degree interference angle. g,h cSIM using 180 degree intefernce angle)

Supplementary note 3: Simulation of chip-based SIM

The effect of structured illumination using planar waveguides is presented in Figs. 3 and 4 for two different imaging objective lenses using the Siemens star sample.

In Fig. 3, imaging using an objective lens with N.A. = 1.2 is simulated. Figure 3(a) shows the spatial result using plain illumination, and Fig. 3(b) shows the logarithmic values of the Fourier spectrum. It is visible in the figure that the highest frequency is limited to $2\text{N.A.}/\lambda = 2.4\lambda^{-1}$. Fig. 3 (c) and (d) show the effect of SIM imaging using the conventional objective based approch, having a spatial frequency of the SIM pattern at the OTF cutoff frequency $2\text{N.A.}/\lambda$, yielding a 2x resolution enhancement. For a sample that is illuminated with a sinusoidal stripe pattern using planar waveguides with an effective refractive index of $n_{\text{eff}} = 1.7$ at an angle between the waveguides of 60° the expected SIM result is shown in Fig. 3(e)-3(f). Increasing the interference angle to 180° increases the modulation frequency of the illumination pattern and thus the expected resolution improvement as shown in Figs. 3(g)-3(h).

In a similar fashion cSIM imaging is simulated in Fig. 4 for an objective lens with N.A. = 0.6. Figures 4(a)-4(b) show the result from using plain illumination. It shows a clear reduction in resolution as compared to the result using an imaging objective with a N.A. = 1.2 as in Figs. 3(a)-3(b).

Using an illumination pattern generated by waveguides with an interfering angle of 30° will improve the resolution as presented in Figs. 4(c)-4(d). For cSIM using patterns generated with interference angles of 120° and 180° it is possible to obtain sample information of high spatial frequency as illustrated in Figs.

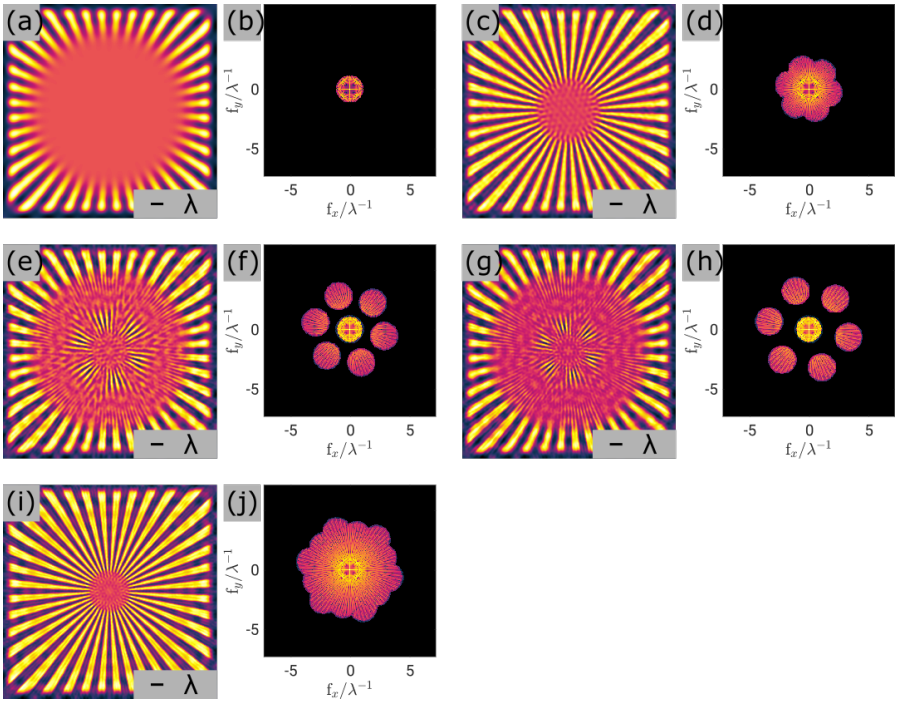

Figure 4: The resolution improvement using chip based SIM is simulated for an imaging objective with $N.A. = 0.6$. (a) and (b) show the result of conventional deconvolution imaging at the indicated wavelength λ and the representation in Fourier space respectively. (c) and (d) show the SIM results for patterns generated at an waveguide interference angle of 60°. (e)-(f) and (g)-(h) show the SIM result using interference patterns generated at angles of 120° and 180° respectively. In (i) and (j) the SIM reconstructions using all interference angles (60°; 120°; 180°) are shown.

4(e)-4(f) and Fig. 4(g)-4(h) respectively. Since the Fourier space is not filled evenly in this approach, a combined use of illumination patterns generated at interference angles of 60°, 120° and 180° as shown in Figs. 4(i)-4(j) will improve the resolution without the loss of frequency bands. Thus, cSIM supports the use of low magnification/N.A. objective lens to enable super-resolution imaging over large field of view (FOV), while the maximum attainable resolution will be supported by the illumination provided by the waveguide as demonstrated in Figs. 4(i)-4(j). In conventional SIM, the illumination and the collection light paths are coupled, thus a use of low. N.A. objective lens to image large FOV will significantly reduce the supported optical resolution.

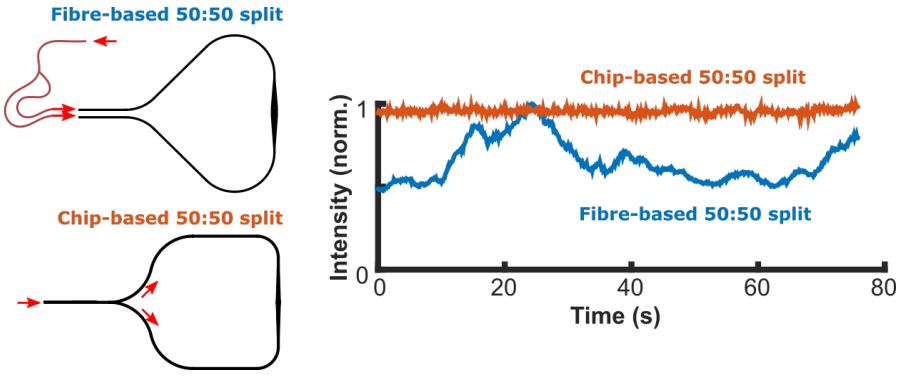

Figure 5: The phase stability of the standing wave SIM interference pattern is shown indirectly by tracking the fluorescence from a bead over time. By splitting the light on the optical table using a 50:50 fibre split the phase of the standing wave is drifting in time, seen with the blue curve. When splitting the light on-chip, the phase is obeserved to be stable over time (red curve).

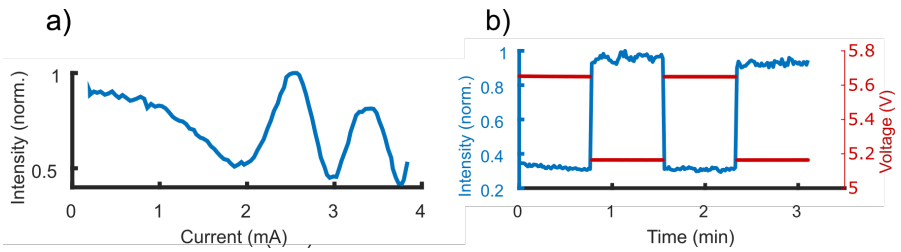

Figure 6: a) By applying current to the thermo-optical element the phase of the SIM interference pattern was changed. A fluorescent bead was tracked while changing the current, thus shifting the SIM pattern phase. b) By selecting the voltages corresponding to a π change in the SIM pattern, the phase was stepped between 0 and π over 3 minutes to demonstrate the reproducibility of the phase stepping method.

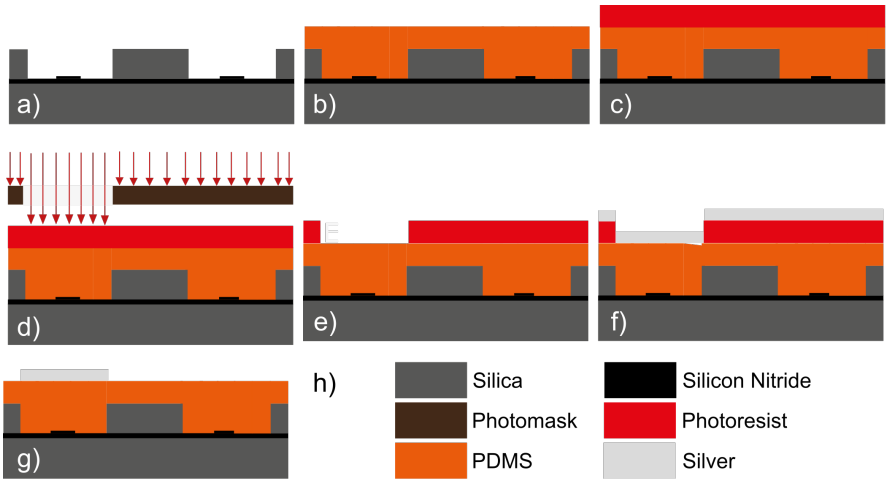

Figure 7: Fabrication of thermo-optic heating element. (a) Both arms of the cSIM structure incorporates opening in the cladding. (b) A cladding layer made from either PDMS or Su-8 covers the entire chip, followed by a photo-resist (c). (d) One of the openings is exposed and the photo-resist was removed. (e) A layer of Ag is sputtered on the entire chip, before the photo-resist is removed leaving only silver on one of the arms.

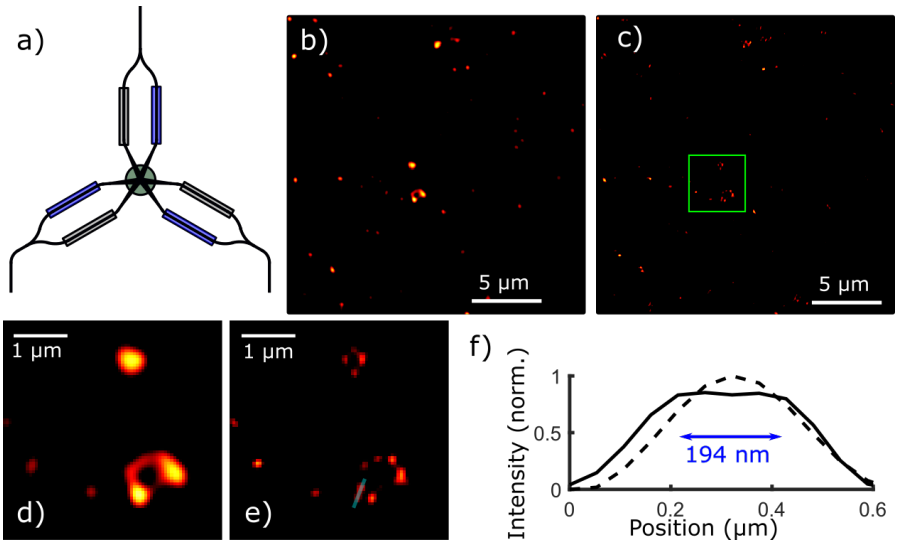

Figure 8: a) cSIM using thermo-optics phase modulation with 50° interference angle. b) Show the diffraction limited image of 100nm fluorescence beads under plain 660nm illumination yielding a diffraction limited image. c) Using the structure shown in a), the cSIM reconstruction shows a clear resolution enhancement. d) and e) shows the zoom indicated with a green box in c). f) Show a line-profile over an intensity distribution comparing the diffraction limited (dotted line) and cSIM reconstruction (solid line). The cSIM image shows two beads separated by 194nm, which is not resolved in the diffraction limited image.

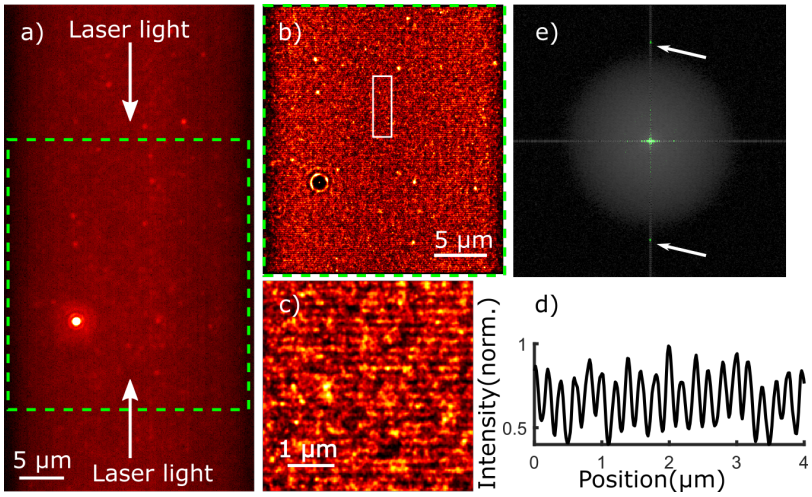

Figure 9: The waveguide surface was stained with a fluorescent dye. a) The standing wave interference pattern is not visible under diffraction limited imaging. b) By using *d*STORM imaging the sub-diffraction limited standing wave pattern was visualized, as better seen in the zoomed image (c). d) A line-profile shows the modulation with a fringe spacing of around 195 nm. d) The power-spectrum of the diffraction limited image (a) and the *d*STORM reconstruction (b) is overlaid, with the green peaks showing the frequency peak of the standing wave at its position outside the span of the OTF.

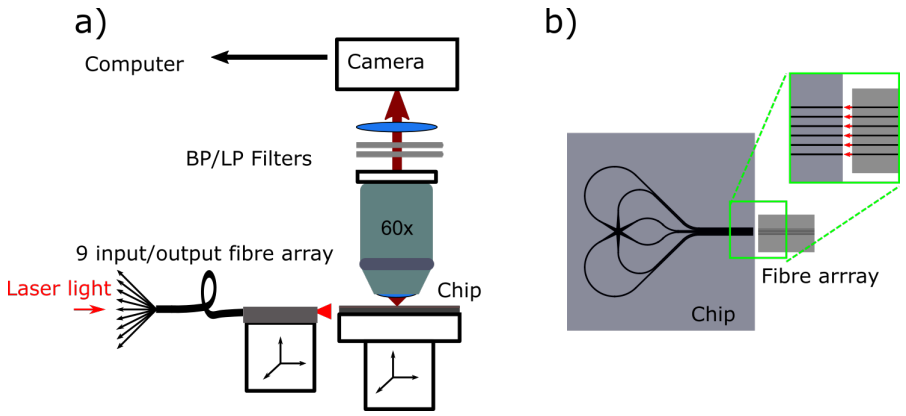

Figure 10: Experimental setup. a) An upright microscope detects the emitted fluorescence. The waveguide chip is held by a vacuum chuck while light is coupled on to the chip via a nine-fibre array adapter. Both sample and coupling stages have xyz movement. b) The fibre array adapter holds 9 optical fibers with equidistant spacing (127 μm), which corresponds to the waveguide spacing on the chip. Each of the 9 optical fibers can be individually activated, according to the chip designs being used.

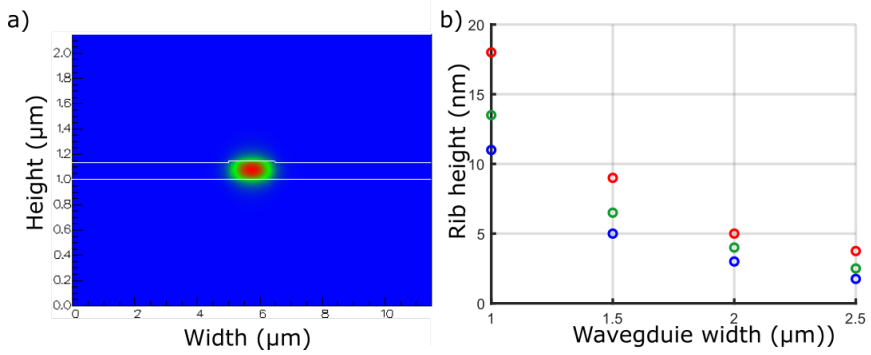

Figure 11: a) Simulation showing the fundamental transverse electric (TE) mode guided in waveguide core, with parts of the light outside the top surface as an evanescent field. b) Simulated threshold rib height values for single mode operation for different waveguide widths and wavelengths (660 nm, 561 nm and 488 nm are shown in the appropriate colors.)

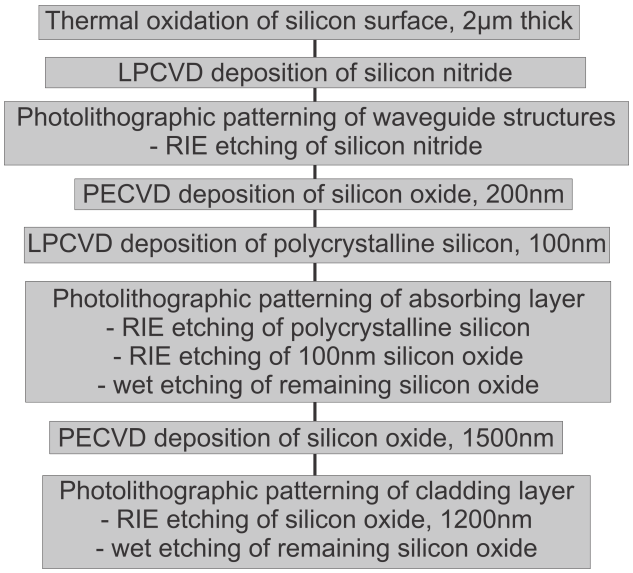

Figure 12: Flow-chart showing the fabrication steps performed in the production of cSIM waveguide chips

References

[1] K. Okamoto, *Fundamentals of Optical Waveguides*, pp. 16–19. 2006.

[2] M. G. L. Gustafsson, "Nonlinear structured-illumination microscopy: Wide-field fluorescence imaging with theoretically unlimited resolution," *Proceedings of the National Academy of Sciences of the United States of America*, vol. 102, no. 37, pp. 13081–13086, 2005.

Conclusion

The presented ideas for an implementation of a large FoV in SIM, tSIM and cSIM make use of a pattern generation independent of any objective lens. This way, higher pattern frequencies than in any conventional epifluorescence SIM implementation are achieved. This excludes techniques like nonlinear SIM [41] and plasmonic SIM [101].

Assuming that the required computational reconstruction of the data, especially the parameter estimation are performed correctly, the SBP in tSIM can be increased significantly, allowing high throughput imaging. As it is demonstrated in first experimental results, the approach is made by modifying the illumination path with a set of mirrors that are capable of generating an illumination pattern over an area of several mm^2. A possible downside of this approach is the increased number of raw data images that need to be acquired to reconstruct the data. Since this implementation does not inherently provide TIRF SIM capability, the most relevant applications are in the biomedical field where thin sample sections are imaged. However, a development towards three-dimensional SIM, using a third beam is not ruled out. The high throughput capability of the proposed design is thus the most important advantage since it allows for a large scale collection of quantitative data.

The approach of cSIM benefits from the stable pattern generation that is independent of free-space bulk optics. The necessary illumination patterns are determined by the waveguide geometry and material that are used to fine-tune the setup without the need for high NA objective lenses. The discussed simulations emphasize the achievable FoV in TIRF SIM as the main benefit with respect to bioimaging application. Although in the initial results of cSIM, the FoV is limited by the waveguide size, it provides inherent evanescent field illumination, even when using a low NA objective lens. The FoV is thus a question of waveguide geometry. However, the high pattern frequencies, made available due to the high refractive index of the waveguide material improve the SBP by increasing the resolution even for high NA imaging objective lenses.

SIM at pattern frequencies reaching well beyond the OTF support of the imaging objective need more advanced image reconstruction than what is currently available. Since the parameter estimation relies on overlapping regions of the frequency components, the Fourier space must be filled using pattern frequencies that do not entirely separate these components from each other. This is the major challenge regarding both, tSIM and cSIM.

4

Chip-based beam shaping

The chip-based imaging as discussed in the previous chapter is limited to the evanescent field on top of a waveguide. In the following, optical waveguides and their ability to generate three-dimensional light patterns and beams in free-space is investigated. If volumetric fluorescence imaging is to be performed, the light has to be coupled out of the waveguide, either by grating structures [99] or at the end face of a waveguide. Coupling using a grating structure depends on the used wavelength and is not considered, having the large range of wavelength (405 nm to 660 nm) used in bioimaging application in mind. Instead, in this chapter, light sheet generation by means of chip-based axicon structures is investigated. Optical waveguides in the form of planar optical chips are used to manipulate light in order to generate excitation patterns with a Bessel beam like structure in one plane. These patterns may then be employed for bioimaging purpose in LSFM. This is extended to static and dynamic light pattern shaping with focus on quasi-Bessel beams (QBBs) [14] and superimposed Bessel beams (SBB) [20]. The QBB is an experimental approximation of a Bessel beam, which is a nondivergent beam and thus well suited to generate light sheet illumination. Experimentally it is possible to generate a QBB by means of an axicon. Here the use of a photonic-chip based axicons for the generation of QBBs in free-space is discussed, using a variety of models in COMSOL. This includes chip designs for QBB and SBB generation as well as chip based optical phased arrays (OPAs) [79] for the dynamic steering of the beam profiles. Within SR bioimaging, optical waveguide chips have mainly been used to provide an evanescent field in chip-based dSTORM and entropy-based SR imaging (ESI) [27, 51] and SIM [52] for the excitation of fluorophores

so far. The work presented in the following relates to light propagating in free space in order to achieve LSFM and lattice light sheet microscopy [21] as well as SIM. Since these techniques usually rely on complex and expensive bulk optics to generate a suitably shaped excitation pattern, the implementation of beam shaping properties on-chip will not only reduce the physical size of the beam shaping component but will also allow for cost-efficient fabrication.

4.1 Introduction

In LSFM, a light sheet is used to excite fluorescence in the focal plane of the sample only, such that phototoxicity and photobleaching are limited to a minimum and out-of-focus signal is reduced. For that purpose, a thin light sheet of constant thickness is used for sample excitation. This may be generated by a cylindrical lens or by scanning a non diverging beam in the focal plane. Here, the generation of a light sheet applying a non diverging profile in one direction is investigated.

Since light has a wavelike nature, it shows diffraction upon hitting an obstacle. This behavior is governed by the Helmholtz equation [38]. However, the Bessel beam is a nondivergent solution of the Helmholtz equation [30, 31]. It has a lateral intensity profile that is described by a Bessel function and does not change along the direction of propagation. In addition, the Bessel beam also shows self-reconstruction, sometimes called self-healing, after hitting an obstacle along the way of propagation [14]. The electric field amplitude of the zeroth-order Bessel beam can be written as [30]

$$E_j(\rho, x) = \mathrm{J}_0(k_{\rho j}\rho) \exp\left[\mathrm{i}\left(k_{xj}x + \phi_j\right)\right], \tag{4.1}$$

where ρ is the transverse distance from the optical axis, x is the direction of propagation along the optical axis, $k_j = \frac{2\pi}{\lambda_j}$ is the wave vector with wavelength λ_j and its radial and longitudinal components $k_{\rho j}$ and k_{xj}, the index j refers to a particular Bessel beam, for differentiation of SBB. The term J_0 is the zeroth-order Bessel function of first kind. The intensity of the Bessel beam is proportional to

$$I_j(\rho) \propto \mathrm{J}_0^2\left(k_{\rho j}\rho\right) \tag{4.2}$$

and is independent of x; which highlights the non-diverging property of an ideal Bessel beam (shown in fig. 4.1). This holds for beams of infinite lateral extend, resulting in an infinite amount of energy in the beam since J_0 is not square-integrable [30]. It is possible though to experimentally realize a QBB that shows the described properties over a finite propagation length without the necessity of infinite lateral extend.

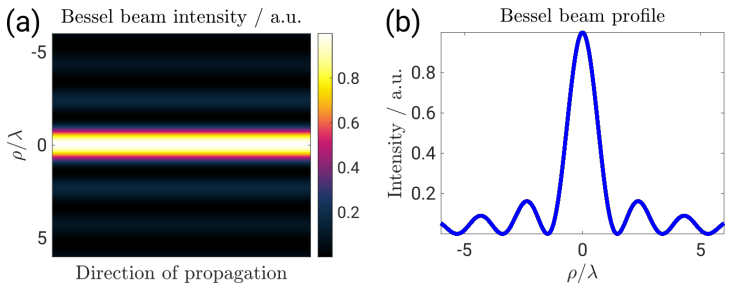

Figure 4.1: The Bessel beam as per eq. (4.2) **(a)** and its profile **(b)**.

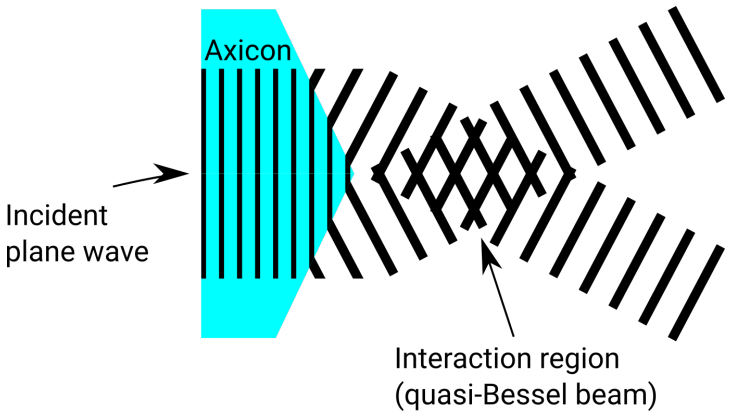

Figure 4.2: A plane wave incident on an axicon. The conical surface manipulates the wavefront such that it converges towards the optical axis. For a limited region after the surface the upper an lower half of the wave may create an interference pattern, the QBB.

The QBB generation by means of an axicon [72] is illustrated in fig. 4.2. A plane wave encountering a conical surface is converging towards the optical axis after exiting the axicon. The axicon generates a line focus along the optical axis as opposed to a regular lens that is usually designed to generate a point focus. A more detailed description is given in the attached paper section 4.2.3, [64], figure 2. There, approximated estimations of the QBB are given as well, based on a mixed geometrical and wave optics description.

It has been shown that the interference of two Bessel beams ($j = 1$ and $j = 2$) with different radial propagation constants generates an interference pattern of the electric field amplitudes $E_1(\rho, x)$ and $E_2(\rho, x)$ propagating on a common optical axis; the SBB whose intensity distribution is proportional to [20]

$$I(\rho, x) \propto \mathrm{J}_0^2\left(k_{\rho 1}\rho\right) + \mathrm{J}_0^2\left(k_{\rho 2}\rho\right) + 2\mathrm{J}_0\left(k_{\rho 1}\rho\right)\mathrm{J}_0\left(k_{\rho 2}\rho\right) \times \cos\left[\left(k_{\mathrm{x}1} - k_{\mathrm{x}2}\right)x + \phi_1 - \phi_2\right]. \quad (4.3)$$

These intensity distributions are illustrated on the right-hand side of figure 9 in the paper. They show intensity voids surrounded by non-zero intensity along the optical axis. This is why SBB are also referred to as bottle beams [71]. It is possible to generate such beams by introducing a second angle in the axicon [4, 5, 109]. A model and geometrical description are presented in figure 3 in the paper. As for the axicon, the original work on the double axicon considered different rotationally symmetric implementations [2, 3]. The descriptions given in the attached paper regard the one-dimensional on-chip implementation, but show the same beam shaping behavior in the chip (xy) plane.

The axicon and double axicon are two ways to perform static beam shaping. In order to achieve dynamic beam shaping, OPAs can be used. They work according to the Huygens principle. An array of waveguides is arranged on a surface and each waveguide is fed by the same source using a set of Y-junctions. By controlling the phase and amplitude at each end, a specific wavefront can be shaped. This is illustrated in figure 10 in the attached paper.

4.2 Simulation of chip-based beam shaping - Paper 4

The work regarding photonic-chip based free space beam shaping and steering attached at the end of section is briefly discussed in the following. The main results found in the attached paper 4 are summarized, as the whole topic is covered there extensively. References to the figures in paper 4 are given.

The work presented in the attached publication can basically be divided into two parts. The first part regards static waveguide configurations in the sense that the surface shaping the wavefront may not be altered after fabrication during an actual experiment. The second part regards OPAs that are manufactured as devices that can actively be used during the experiment to alter the emitted wavefront.

4.2.1 Static beam shaping

The static beam shaping is investigated regarding axicons and double axicons implemented on-chip. These designs are referred to as static since the shape of the generated wavefront depends on the fabrication and can not be altered in the application. Only the overall phase may be manipulated. This is of interest regarding a proposed design generating two counter-propagating beams that produce an interference pattern.

On-chip axicon: one-dimensional QBBs for LSFM

The proposed on-chip axicon is presented in figure 1 of paper 4. Light is coupled into a single-mode rib waveguide that is then expanded laterally, using a linear taper in order to achieve the wanted axicon width as presented in **(a)**. Given a Ta_2O_5 on SiO_2 rib waveguide, covered with water and operating at a visible wavelength of 660 nm, the single-mode conditions at the input are calculated. For a rib and slab height of 50 nm and 200 nm respectively, a rib width of 500 nm shows to have one waveguide mode in **(b)**. A wider rib width potentially supports higher order modes as shown in **(e)**. These considerations are important since the beam profiles achieved in free-space do not only depend on the waveguide geometry, but also on the coupled intensity distributions in the waveguide. This has been exploited in the generation of high-order Bessel beams [9].

In order to estimate the the propagation length or depth of field (DOF) of the generated QBBs, a combined geometrical and wave optics description is given in paper 4. Based on Snell's law and the width of the wavefront exiting the device, an effective interference region can be calculated as well as a rough estimate of the generated interference pattern. However, in order to provide a more realistic analysis of the expected intensity distribution in the sample area, two-dimensional COMSOL simulations are performed as described in paper 4.

The results for a 20 µm wide axicons at a vacuum wavelength of 532 nm and different axicon angles are presented in figure 4. It can be seen that the number

of visible side lobes changes depending on the wedge angle of the axicon. This is basically explained by the size of the region over which the interference takes place. On the other hand it is discussed that the actual number of side lobes is less than what is expected by the description using geometrical and wave optics. This is due to the actual intensity profile in the fundamental waveguide mode not being considered. This is an important result with respect to LSFM since the side lobes of the axicon can be expected to appear as additional light sheets in the chip version. However, it can be seen that the central lobe reaches an intensity maximum along the optical axis well before the side lobes become more intense. The uneven intensity distribution along the direction of propagation is seen in the line profiles in figure 5 **(a)** for the central lobes considering different wedge angles. The figure also includes modulations for larger wedge angles. Since in the LSFM application a larger propagation length is favorable, the smaller wedge angle of 6° showing fewer side lobes and no modulation may be selected. It shows an effective length of the central lobe of about 1 µm with only one major side lobe on each side.

A trade-off must be found with respect to the width of the central lobe. As a smaller wedge angle results in a smaller interference angle, the width of the central lobe will be larger at a smaller wedge angle. This is shown in figure 5 **(b)**. The influence of the size of the axicon is shown in figure 6 of paper 4. Figure 6 **(a)** and **(b)** show the output of axicons with a width of 20 µm and 40 µm, respectively, at an exemplary wedge angle of 8°. In **(c)**, the the intensity profiles for the central lobes are presented. Although the interference area is increased with the size of the axicon, the additional length in the central lobe comes with modulations that have to be taken into account. Furthermore, the extended propagation length is accompanied with additional side lobes.

In order to generate an actual light sheet, the profile that is generated in the xy-plane has to diverge in the z-direction. The divergence in the z-direction depends on the thickness of the waveguide, as demonstrated taking a slab waveguide as an example in fig. 4.3.

Counter-propagating QBBs: one-dimensional lattice light sheets

In order to achieve modulated excitation patterns for the use in SIM, a counter-propagating assembly of two axicons is proposed as shown in figure 7 of paper 4. Light is coupled into a single mode waveguide, as for the single axicon, and the intensity divided equally in two using a Y-junction. Both waveguide arms may then be aligned, facing each other, and tapered out to the intended axicon size. If the waveguide ends are fitted with axicon structures, counter propagating QBBs are generated providing a sinusoidal modulation in the generated beam as shown in figure 8. Simulation results for 6°, 10° and 15° are presented in **(a)** to

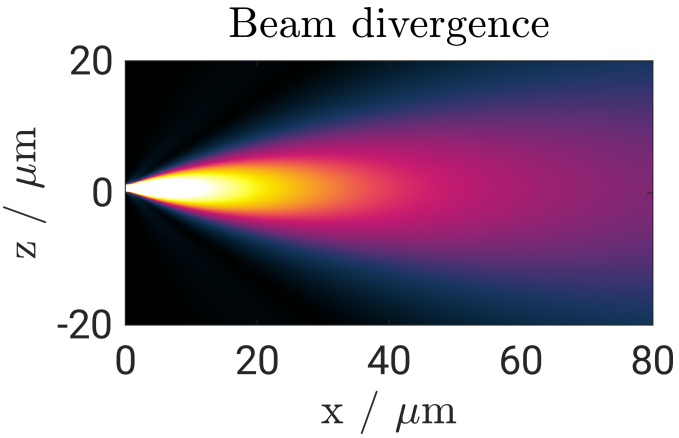

Figure 4.3: The intensity distribution (in arbitrary units) in free-space, after a flat end facet for an exemplary slab waveguide made of a 1 µm thick slab (Si_3N_4) on SiO_2 substrate in water, with light propagating at a vacuum wavelength of 532 nm. The divergence depends on the thickness of the core and allows the QBB profile in the xy-plane to spread out in z-direction to produce a light sheet.

(c). These results confirm the expected dependence of the pattern modulation on the axicon wedge angle as described in equation (6) in paper 4. This means the smaller the wedge angle, the higher the modulation frequency. This way, modulated excitation patterns can be generated using optical waveguides similar to the concept in cSIM but propagating in free space, instead of being confined within the chip. Since QBBs are used, the excitation may still be limited to a thin slice of the sample without being limited to evanescent field excitation at the surface of the waveguide. The necessary phase manipulation of the illumination pattern may be achieved by thermo-optic elements on the waveguide arms [44].

Chip-based double axicons: one-dimensional bottle beams

The double axicon was introduced as a means to generate SBB [4]. Here, simulations are shown to assess a possible waveguide implementation. The schematic design is shown in figure 3, and simulation results are shown in figure 9. The intensity distribution for two overlapping Bessel beams as per eq. (4.3) is presented on the right-hand side of figure 9. The radial propagation constant for the first Bessel beam is determined by $\alpha_1 = 12°$ and the refractive index distribution in the model. The radial propagation constants for the second Bessel beam are determined by α_2 =3° and 6°, respectively, and the refractive index distribution. Since eq. (4.3) describes two ideal Bessel beams overlapping, COMSOL simulations are used to obtain a more accurate estimate of the expected output. As it can be seen from figure 3, the size of the inner

and outer axicons determine the size of the region where the two generated QBBs actually overlap. A ratio of $R_2 = R_1 \frac{\alpha_1}{\alpha_2}$ was empirically found to show an initial result. As it can be seen in figure 9 **(a)**, it is possible to generate a single intensity void in a rather small ($R_1 = 20\,\mu m$) model, but the short propagation length does not leave much room for angle adjustments, as it can be seen in **(b)**, where no intensity void is visible.

4.2.2 Optical phased arrays in free-space beam shaping

At this point, OPAs are introduced as they come with a set of advantages over chip-based axicons. The fabrication of the proposed on-chip axicons and double axicons required a non-flat end facet with a sharp edge. Although a preliminary investigation of hyperbolic deviation of the axicon edge from the ideal model as used in the simulations does not show a significant distortion to the intensity profile, as presented in figure 16 of paper 4, this may actually become a problem if the fabrication process shows to have a larger error margin. Such geometry deviations may be significant, as reported in the literature [17, 92]. Additionally, there is no tapering required in the OPA approach, as can be seen in figure 10. The width of the array is determined by the total number of elements, their width and their spacing.

A set of Y-junctions on a photonic chip is used to distribute coupled light between the elements at the output face. Thermo-optic manipulation of the individual phases in the array elements can be used to achieve wavefronts and interference patterns as achieved in the static (double) axicon implementations, with the ability to dynamically change parameters such as angle and width during the experiment [99]. Two different ways to simulate a variety of OPA configurations are used. The first one is based on the summation of the electric field generated by a set of point sources with a specific phase and amplitude. These are aligned with a defined spacing, as described by equation (8) in paper 4, the so called array factor. The second is a COMSOL model using an array structure of rib waveguides as shown in figure 11.

Considering single mode conditions for Ta_2O_5 on SiO_2 waveguides at 660 nm vacuum wavelength, the simulation results for different configurations are presented in figures 12 to 15. In figure 12, the simulation results for a 16 element (antennas) OPA with a width of 0.5 µm of each element (in the COMSOLmodel) and a distance of 1.5 µm between them is presented. In **(a)**, the approximation using equation (8) is shown, with **(b)** displaying the result of a two-dimensional COMSOL model. Applying a Gaussian amplitude distribution to the single elements as presented in **(c)** and an axicon like phase distribution as presented in **(d)**, the capability of such an implementation to generate a QBB with the central lobe showing non-diffraction properties over

about 60 µm is presented.

The next step is to extend the OPA towards generating SBB. This is shown in figure 13 of paper 4, with the number of antennas being increased to 32 but otherwise same parameters as before. A Gaussian amplitude distribution (**(c)**) is applied and the phase distribution does now have two different slopes (**(d)**, one for each axicon angle. Both, the array factor (**(a)**) and the COMSOL simulation (**(b)**)show the bottle beam structure as described for the SBB. The difference between the array factor and the COMSOL model becomes very clear at this point, since the point sources in the array factor emit the electric field isotropically with a constant amplitude. This produces multiple copies of the SBB at regular tilt angles with the optical axis. The COMSOL model shows a more realistic behavior since actual waveguide modes are used.

Finally, the dynamic manipulation of the SBB is shown in figure 14. The phase distribution of the 32 element OPA that is used for the generation of SBB is altered by adding a phase of $n\pi/2$ to the phase of each element n (**(b)**). This will tilt the generated beam away from the optical axis. Previously, this has been described for focusing OPAs, using a linear phase change to shift the focus laterally, requiring a non-linear correction [75]. From the presented result for the SBB, it is obvious that a linear phase shift does not introduce a lateral shift but a tilt.

The focal length of an aspheric lens depends on the curvature of its surface. In a similar way, the output of an axicon depends on the slope of its two surfaces. Although an axicon produces a line focus such that a focal length is not defined, the term is used in order to indicate a chance in the surface slope. Simulation results are presented in figure 15. The SBB generated in **(a)** comes from a double axicon having a phase gradient (phase change from one antenna to the next) of $\pm 8\pi$ on the inner and $\pm 24\pi$ on the outer axicon as presented in **(c)** in blue. Changing the slopes to $\pm\pi/2$ in the inner and $\pm 16.5\pi$ in the outer axicon as presented in **(c)** in red will stretch the generated pattern along the optical axis as shown in **(b)**. Four intensity minima or bottles are highlighted in **(a)** and **(b)**, indicating the shift.

4.2.3 Conclusion

Chip-based axicons, double axicons and OPAs show to be suitable to generate a diverse set of illumination patterns in free-space using the benefits of waveguide technology. Simulations demonstrate the concepts for the visible spectrum used in fluorescence bioimaging. For this purpose, planar models are used so show the in-plane intensity distribution of different waveguide designs. This way, light sheets can be generated based on using an axicon structure in one

plane and diverging beam properties in the perpendicular plane. Two counter-propagating axicons are shown to produce intensity modulated light sheets with possible application in SIM, similar to lattice light sheet microscopy. Here, the on-chip thermo-optic modulation is used for the necessary pattern phase control. The demonstrated penetration depths cover the general limit to the penetration depth of lattice light sheet microscopy without adaptive optics of 20 µm to 100 µm [21]. The simulation of chip-based double axicons show general feasibility, although the parameters need to be well controlled at the suggested dimensions.

The investigated OPA designs are presented as a means to not only mimic the wavefront shaping properties of axicon and double axicon designs, without the necessity of a well defined angle in the waveguide edge. OPAs show to provide general capability of not only generating QBBs and SBB, but also tilt and shift the whole structure along the optical axis. The generated bottle beam profiles may find application in particle manipulation based on optical trapping.

Paper 4: Photonic-chip based free space beam shaping and steering for advanced optical microscopy application

- Accepted in OSA Continuum, September 2019
- Authors:
  - Marcel Lahrberg,
  - Firehun Tsige Dullo,
  - and Balpreet Singh Ahluwalia
- *Author contributions:* M.L. performed the simulations, analyzed the data, and wrote the manuscript. F.T.D. advised regarding fabrication constraints. All authors reviewed and commented on the manuscript.

Photonic-chip based free space beam shaping and steering for advanced optical microscopy application

MARCEL LAHRBERG, FIREHUN TSIGE DULLO, AND BALPREET SINGH AHLUWALIA*

Department of Physics and Technology, UiT The Arctic University of Norway, NO-9037 Tromsø, Norway
balpreet.singh.ahluwalia@uit.no

Abstract: Photonic-chip-based light illumination has recently found applications in optical microscopy and nanoscopy methodologies. The photonic chip removes the dependency on imaging objective lenses to generate the required illumination patterns for different microscopy methods. Until now all the reported chip-based optical microscopy methods exploit the evanescent field present on top of a waveguide surface and are thus inherently limited to two-dimensional microscopy. Here, we perform systematic simulation studies to investigate different chip-based waveguide designs for static and dynamic shaping of light beams in the free-space. The simulation studies have been carefully designed considering the photo-lithography limitations and wavelength spectrum (405 nm to 660 nm) that is of interest in fluorescence based optical microscopy and nanoscopy. We first report the generation of a quasi-Bessel beam (QBB) using an on-chip axicon made at the end facet of a planar waveguide to mimic light sheet illumination. This is extended to the implementation of a counter propagating QBB for lattice light-sheet applications. The double axicon, a derivative of the axicon generates superimposed Bessel beams (SBB). Its waveguide-based implementation is proposed and analyzed. Finally, we investigate an optical phased array (OPA) approach to allow dynamic steering of the output light in the free-space. The aim of this study is to find suitable waveguide design parameters for free-space beam shaping operating in the visible spectrum opening possibilities for three-dimensional chip-based optical microscopy.

1. Introduction

The last decade has witnessed momentous progress in the field of advanced optical microscopy with focus on two fronts. These are super-resolution (SR) optical microscopy commonly referred to as optical nanoscopy that has overcome what is generally known as the Abbe diffraction limit in the field of optical microscopy, and minimally invasive, three-dimensional light sheet fluorescence microscopy (LSFM) or selective plane illumination microscopy (SPIM). Optical nanoscopy comprises a panel of techniques including structured illumination microscopy (SIM) [1, 2], stimulated emission depletion (STED) [3] microscopy, and single-molecule localization microscopy (SMLM) techniques such as photo activated localization microscopy (PALM) [4] and fluorescence photoactivation localization microscopy (FPALM) [5] as well as stochastic optical reconstruction microscopy (STORM) [6] and direct STORM (dSTORM) [7]. Techniques such as SR optical fluctuation imaging (SOFI) [8] and entropy-based SR imaging (ESI) [9] are based on the analysis of signal fluctuations in an acquired image series. LSFM or SPIM [10], originally developed as orthogonal-plane fluorescence optical sectioning (OPFOS) [11], uses orthogonal illumination of the sample with respect to the imaging objective lens, minimizing out-of-focus light and providing exceptional optical sectioning capability. This has made LSFM a most suitable method for live cell imaging of thick specimens.

Most of the present day advanced optical microscopy uses complex and costly optical

microscopes to deliver specialized illumination patterns required to achieve high-resolution images while the sample lies on a simple glass slide. These advanced microscopy solutions all employ bulk optics for laser beam engineering in free-space and a microscope to deliver the illumination pattern. This approach is prone to misalignment; therefore, successful implementation requires well-calibrated optics hosted on a stable and mechanically rigid platform, consequently increasing their cost and hindering parallelization.

Recently, photonic-chip-based optical fluorescence nanoscopy has emerged as a potential solution to reduce the system complexity and cost of present day optical nanoscopy [12–16]. The light inside the waveguide is guided based on total internal reflection (TIR), generating an evanescent field at the core and cladding interface. In chip-based optical nanoscopy the sample is placed directly on top of an optical waveguide (the core) and is illuminated using the evanescent field present at the interface. The fluorescence signal is collected using any standard upright optical microscope. Waveguide chip illumination generates evanescent field excitation, which is determined by the waveguide geometry (length and width) and is independent of the imaging objective lens. The illumination and collection light paths are therefore decoupled in photonic-chip-based microscopy. These properties of on-chip illumination have recently been exploited in chip-based dSTORM and ESI [17, 18] and SIM [19]. Chip-based optical nanoscopy does not only hold edge over conventional approaches on simplicity and cost but has also pushed the technical frontiers of respective optical nanoscopy methodologies. On-chip dSTORM has demonstrated the largest field of view (FoV) ever reported with super-resolution (70 nm resolution over 500 µm × 500 µm), 100-times larger than the conventional solution. Similarly, on-chip SIM was demonstrated with 2.4-fold resolution enhancement with respect to conventional microscopy, contrary to a 2-fold improvement of conventional SIM.

However, all on-chip optical microscopy and nanoscopy approaches so far have been limited to two-dimensional imaging, as they use the evanescent field present on top of the waveguide surface. Thus only a thin portion of the cell (e.g. 150 nm to 200 nm) touching the waveguide surface can be imaged due to evanescent field excitation. For three dimensional and volumetric imaging of the sample it is necessary to access the light guided inside the waveguide and to perform beam shaping in the free-space. To access the guided light inside the waveguide, there could be different approaches to do so. The end of the waveguide can be cleaved [20, 21] and the light escaping from the end facet can be used for 3D imaging. Alternatively, it is also possible to use a grating coupler to out-couple the guided light inside the waveguide [22]. Most of the grating couplers are optimized for a single wavelength and have less tolerance for a wide span of wavelengths that are intended to be used in fluorescence based optical microscopy, spanning from 405 nm to 660 nm, which is focus of this work. Therefore, in this study the outcoupling is performed by means of cleaved end facets as it would be less prone to errors over a wide wavelength spectrum.

Previous developments related to on-chip beam shaping are silicon on insulator (SOI) based implementations that are inherently restricted to work using infrared wavelengths, opposed to the visible wavelength spectrum (405 nm to 660 nm) that is of interest for optical microscopy. They comprise light detection and ranging (Lidar) [23], near-field-focusing [24], QBB generation [25, 26] and beam steering [22, 27]. Silicon nitride (Si_3N_4) based OPAs have been demonstrated to work at a visible vacuum wavelength of 635 nm [28].

In this work, we investigate on-chip light shaping strategies for the visible wavelength spectrum (405 nm to 660 nm) with the aim to be used in optical microscopy and optical nanoscopy applications. While on-chip axicon like designs have been previously explored, here we extend the scope for photonic-chip-platforms for the generation of self-imaged optical beams and lattice-like light sheets for the first time to the best of our knowledge. Moreover, we extend the use of integrated optical arrays to generate user-defined self-imaged optical beams and Bessel beams at visible wavelength and investigate their usefulness from optical microscopy application.

The light from the cleaved end of the waveguide would diverge rapidly, therefore on-chip lenses at the end facets of the waveguide were simulated and investigated. Here, first we discuss the design and simulation of on-chip integrated lenses (axicons) that are necessary to generate single plane static illumination using a photonic chip in section 2. Such a single plane light illumination will find application in light sheet microscopy. In order to generate steerable light illumination, an integrated OPA approach is explored in section 3. The simulation parameters investigated in this study carefully consider both the fabrication tolerance of the conventional photolightography that governs the waveguide designs, and the practical requirements of the desired illumination pattern, such as dimensions, divergence, wavelength and beam shaping that are essential in optical microscopy for bioimaging applications.

2. Design and simulation of chip-based static beam shaping in free space

The diffraction of light is inextricably connected to its wavelike nature; it is governed by the Helmholtz equation [29]. This means that propagating light shows divergence in most cases, especially after hitting an object along the direction of propagation. However the Bessel beam is a nondivergent solution of the Helmholtz equation [30, 31]. It has a lateral intensity profile that is described by a Bessel function and does not change along the direction of propagation. In addition the Bessel beam also shows self-reconstruction, sometimes called self-healing, after hitting an obstacle along the way of propagation [32]. The electric field amplitude of the zeroth-order Bessel beam can be written as [30]

$$E_j(\rho, x) = \mathrm{J}_0(k_{\rho j}\rho)\exp\left[\mathrm{i}\left(k_{xj}z + \phi_j\right)\right], \tag{1}$$

where ρ is the transverse distance from the optical axis, x is the direction of propagation along the optical axis, $k_j = \frac{2\pi}{\lambda_j}$ is the wave vector with wavelength λ_j and its radial and longitudinal components $k_{\rho j}$ and k_{xj}, the index j refers to a particular Bessel beam. The term J_0 is the zeroth-order Bessel function of first kind. The intensity of the Bessel beam is proportional to

$$I_j(\rho) \propto \mathrm{J}_0^2\left(k_{\rho j}\rho\right) \tag{2}$$

and is independent of x; which highlights the non-diverging property of ideal Bessel beam. This holds for beams of infinite lateral extend resulting in an infinite amount of energy in the beam since J_0 is not square-integrable [30]. It is possible though to experimentally realize a QBB that shows the described properties over a finite propagation length without the necessity of infinite lateral extend.

It has been shown that the interference of two Bessel beams ($j = 1$ and $j = 2$), with different radial propagation constants generates an interference pattern of the electric field amplitudes $E_1(\rho, x)$ and $E_2(\rho, x)$ propagating on a common optical axis; the SBB whose intensity distribution is proportional to [33]

$$I(\rho, x) \propto \mathrm{J}_0^2\left(k_{\rho 1}\rho\right) + \mathrm{J}_0^2\left(k_{\rho 2}\rho\right) + 2\mathrm{J}_0\left(k_{\rho 1}\rho\right)\mathrm{J}_0\left(k_{\rho 2}\rho\right) \times \cos\left[\left(k_{\mathrm{x}1} - k_{\mathrm{x}2}\right)x + \phi_1 - \phi_2\right]. \tag{3}$$

This interference pattern shows zero intensity spots on the optical axis that are surrounded by non-zero light intensity, it may be referred to as a bottle beam. The bottling is governed by the cos-term in eq. (3) for $k_{\mathrm{x}1} - k_{\mathrm{x}2} \neq 0$.

Experimentally a Bessel beam can be generated by passing collimated light through an axicon, for example an annular slit in the focal plane of a lens, generating an interference pattern [34] where the author refers to van Heel [35] who used such a geometry for two-dimensional alignment problems. Although any rotationally symmetric optical element that images a point source into a stretch along the optical axis [36] may be referred to as an axicon, the most common type is a glass cone and the Bessel beam is generated by passing a Gaussian beam through it [37].

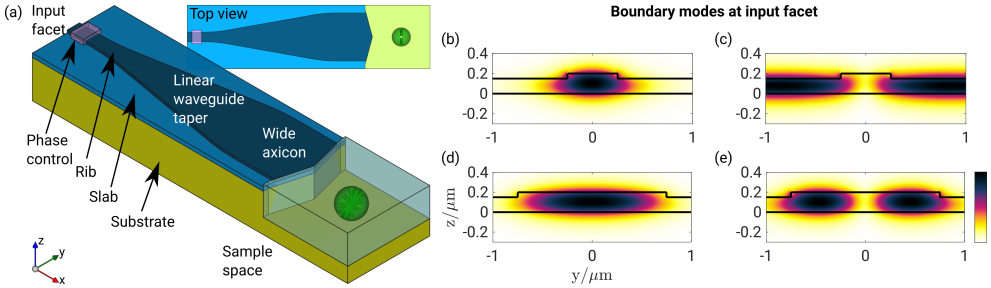

Fig. 1. A rib waveguide using a linear waveguide taper in order to maintain the fundamental mode. Panel **(a)** shows the general rib waveguide under consideration. Boundary modes **(b)**-**(e)** for a model at a vacuum wavelength of 660 nm with materials of refractive indices 1.46 (Substrate, SiO_2), 2.12 (Slab and Rib, Ta_2O_5), and 1.33 (water on top). The slab and rib height are set to 200 nm and 50 nm respectively. In **(b)** the fundamental waveguide mode for a rib waveguide of 500 nm width is shown. It is the only guided mode, the first order mode **(b)** (mode with next lower effective refractive index) is not guided (propagates in the slab). For a rib waveguide with a rib width of 1.5 µm not only the fundamental mode **(d)**, but also the first order mode **(e)** is guided in the waveguide. The boundary modes are presented as the norm of their electric field distribution in arbitrary units, color bar in **(d)**.

It is noted that the described generation of a fundamental QBB is based on feeding a fundamental Gaussian beam (fundamental Laguerre-Gaussian mode) into the axicon. It is possible to generate higher order Bessel beams by passing Laguerre-Gaussian laser modes with a radial or azimuthal index not equal to zero through an axicon. These higher order Bessel beams exhibit a modified beam structure that has also been used to generate bottle beams [38, 39].

2.1. Choice of waveguide material

The careful choice of suitable material is an important first step. In section 2, the waveguide designs are simulated using Si_3N_4 and in section 3 it is based on tantalum pentoxide (Ta_2O_5). High-refractive index material such as Si_3N_4 and Ta_2O_5 enable ultra-compact waveguide structures with small bend radii and thus compact footprint on an integrated optical functions. In particular Si_3N_4 has gained significant popularity in recent years, due to it is compatibility with conventional semiconductor fabrication facilities, high-refractive index (n = 2.0 @ 532 nm) and low loss.

2.2. On-chip axicon design

The light pattern generation presented in the following is based on planar waveguide technology as illustrated in fig. 1. Light coupled into the input facet of the waveguide chip can propagate in well defined modes in the waveguide. Single mode waveguide condition is necessary to control the beam shaping in the free-space. In previous work, single mode conditions at visible wavelengths (405 nm to 660 nm) were achieved using shallow rib geometry [12]. The advantage of rib waveguide geometry over strip waveguide is that it allows single mode behaviour for wider waveguide geometry [12].

Given a small enough rib width (here 500 nm) only the fundamental mode **(b)** is guided. The next waveguide mode (with the next lower effective index) is not guided, it is a slab mode as shown in **(c)**, i.e. propagating outside the waveguide core. However, for bio-imaging the main interest is on wider waveguides to generate a large beam to scan the entire cells (10 µm to 20 µm). A wide waveguide made of Si_3N_4 will not only guide the fundamental mode **(d)** but also the higher order modes, for example the first order mode as shown in **(e)**. To solve this issue, a

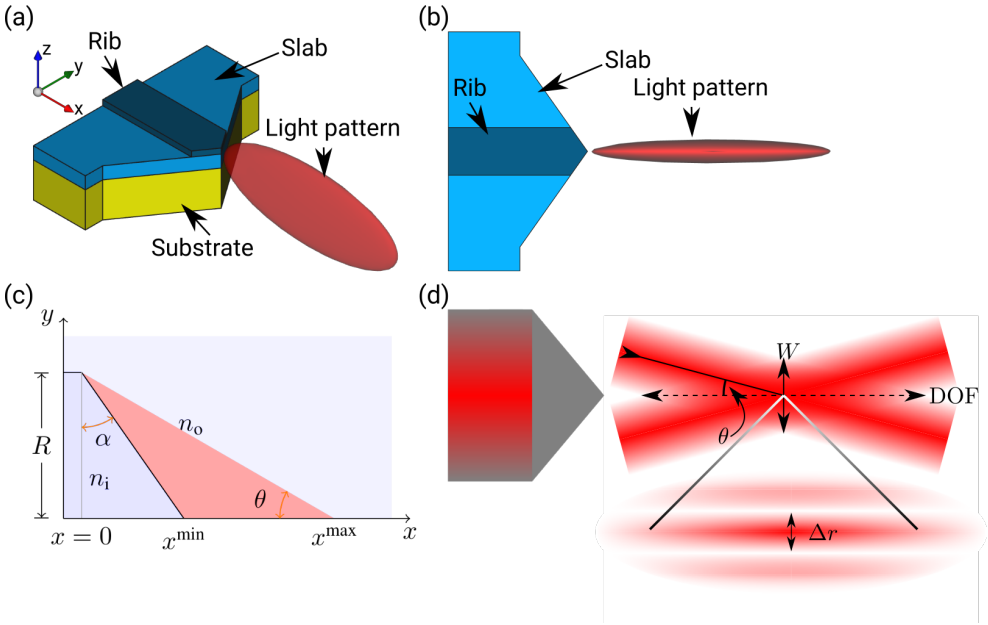

Fig. 2. The chip-based axicon and its ability to form a 1D light sheet as part of 1D-QBB. In **(a)** a general design for an axicon using a planar waveguide and the beam shaping capability is shown. The top view in **(b)** shows the xy-plane where the 1D-QBB intensity profile is generated. Following [26], the DOF of the generated QBB profile can be approximated using the optical properties and geometry shown in **(c)** where only one half of the top view is presented. Describing the QBB as an interference pattern can be done using the sketch in **(d)**, where the axicon is set of to the left for better visualization.

single mode waveguide is used at the input facet and is adiabatically tapered out as illustrated in **(a)**. Light is coupled into the waveguide, only exciting the fundamental mode of the narrow input. The adiabatic waveguide taper expands the mode into the fundamental mode of the wider waveguide part without exciting higher order modes. This way a pure single mode condition can be maintained using a Si_3N_4 rib waveguide. In addition a phase shift of the guided mode can be achieved by means of thermo-optic manipulation as indicated in **(a)**.

In the first approximation, generating a 1D-QBB by means of an axicon can be described in terms of a combination of geometrical optics and wave optics as presented in fig. 2. Figure 2**(a)** shows a general design of a chip-based axicon, with the axicon structure in the xy-plane like a cross section of a conventional rotationally symmetric axicon. The waveguide core, i.e. the slab and the rib is made of Si_3N_4 on a SiO_2 substrate. The light inside the waveguide is tightly confined in both axes, thus it will diverge rapidly from the end facet of the waveguide. For hosting the sample and for the generation of the beam, it will be essential to etch away both the core (rib and slab) and the underlying cladding at the end facet. The axicon at the end facet is used to control the divergence of the beam in the xy-plane, generating a line focus as shown in fig. 2**(b)**. The top view in fig. 2**(b)** indicates the QBB properties of the propagating light in the xy-plane. However, the divergence in the xy-plane is allowed intentionally as shown by the red region of fig. 2**(a)**. The net result is a thin light sheet illumination. Using fig. 2**(c)**, showing one half of the cross section and fig. 2**(d)**, showing a full cross section, the propagation of the light is described in terms of geometrical optics and the wave properties are only taken into account to describe the generated interference pattern. Collimated light propagating along the optical axis enters the axicon from the left-hand side. Assuming that the whole axicon aperture of size $2R$

is filled (R being the half width of the waveguide), the light is refracted by the conical surface (characteristic wedge angle α) and propagates over the red shaded area. The refractive index of the axicon is n_i and the refractive index of the environment n_o, where $n_i > n_o$. Using Snell's law, the light coming from the upper part of the axicon is incident onto the optical axis at an angle $\theta = \arcsin\left(\sin(\alpha)\frac{n_\mathrm{i}}{n_\mathrm{o}}\right) - \alpha$. The length along the optical axis over which light coming from the axicon is incident on the optical axis and thus generating the Bessel beam is given by the DOF (see fig. 2**(c)** and **(d)**)

$$\mathrm{DOF} = x^{\max} - x^{\min}, \tag{4}$$

with $x^{\min} = R\tan(\alpha)$ and $x^{\max} = \frac{R}{\tan(\theta)}$. The maximum width over which the interference takes place is given by $W = \mathrm{DOF}\tan(\theta)$ and the fringe spacing of the resulting interference pattern is given by what is commonly referred to as the Abbe diffraction limit $\Delta r = \frac{\lambda_0}{2\mathrm{NA}}$, with the vacuum wavelength λ_0 and the numerical aperture $\mathrm{NA} = n_0\sin(\theta)$. This allows to calculate the number of intensity lobes to be

$$N_{\mathrm{lobes}} = \frac{W}{\Delta r}. \tag{5}$$

From the physics point of view it seems reasonable to round these values to the nearest odd integer. Viewing the Bessel beam as an interference pattern of plane waves propagating at a fixed angle with the optical axis explains the self-healing properties of the beam since the Bessel beam does not consist of light propagating along the optical axis, liming the shadow of an object along the optical axis depending on its size and the angle θ. For the application in LSFM the Bessel beam should optimally provide a large DOF at a limited Δr with only one strong central lobe. This can be achieved by balancing the values of R and θ [26].

Next, the generation of one-dimensional SBB using a photonic-chip is investigated. In order to generate SBB by overlapping two zeroth order QBBs, three basic principles have been employed so far. First, a screen with two annular slits of different radii and a lens were used to generate the SBB, demonstrating the self imaging effect in a non-diffracting beam [33]. Then the self-imaged bottle beam was introduced by using a hologram on a spatial light modulator (SLM) [40] as well as a photolithography hologram [41]. On the other hand, starting with a highly efficient glass cone axicon, introducing a second wedge angle it is possible to obtain a so called double axicon. Passing a fundamental Gaussian beam through this optical device it is possible to generate two overlapping zeroth-order QBBs with different longitudinal wave vector components, interfering on the optical axis and generating the SBB [42–44].

More involved implementations using an SLM for spatial filtering have been shown to significantly improve the propagation length [45]. A slightly different way to generate self-imaging beams is a volume holographic method using a Bessel readout beam [46].

In fig. 3 the light shaping function of the double axicon, similar to what is done in fig. 2 with respect to the (single) axicon, is described. The refractive index of the axicon is n_i and the refractive index of the environment n_o, where $n_i > n_o$. The axicon has two angles with $\alpha_1 > \alpha_2$. The radii of the axicons are given by $R_1 > R_2$. Again, using Snell's law, the angle between the light coming from the upper part of the axicon and the optical axis is θ_1. The light coming from the lower part of the axicon forms an angle with the optical axis of θ_2. For the given conditions, the refractive indices and axicon angles it follows $\theta_1 > \theta 2$ with $\theta_{1/2} = \arcsin\left(\sin\left(\alpha_{1/2}\right)\frac{n_i}{n_o}\right) - \alpha_{1/2}$. The distance over which light coming from the outer axicon in incident on the optical axis is given by $x_1^{min} = \tan(\alpha_1)(R_1 - R_2) + \frac{R_2}{\tan(\theta_1)}$ and $x_1^{max} = \frac{R_1}{\tan(\theta_1)}$. For the light coming from the lower axicon this distance is given by $x_2^{min} = \tan(\alpha_1)(R_1 - R_2) + \tan(\alpha_2)R_2$ and $x_2^{max} = \tan(\alpha_1)(R_1 - R_2) + \frac{R_2}{\tan(\theta_2)}$.

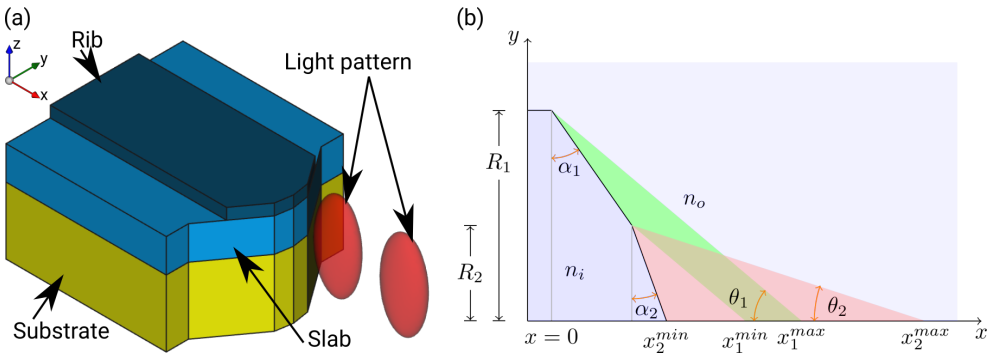

Fig. 3. The chip-based double axicon and its ability to form a light sheet as part of a SBB. In **(a)** a general design for a double axicon using a planar waveguide and the beam shaping capability is shown. In **(b)**, as for the (single) axicon in fig. 2**(c)**, the necessary parameters to approximate the interaction length along the optical axis, where a SBB profile may be generated, is shown.

2.3. Finite element simulation

The on-chip axicon represents a cross-section of an actual axicon that is described as a rotationally symmetric device. It is the deliberate attempt to limit the non-divergent properties of the QBB to one plane and being able to manipulate the light in the direction perpendicular to that plane in a different way. The two-dimensional implementation of the axicon on a planar waveguide is proposed elsewhere [26], where finite-difference time-domain (FDTD) simulations of Si_3N_4 for vacuum wavelength in the infrared (780 nm) are shown. The idea is to perform light sheet microscopy where the light sheet is generated by a one-dimensional axicon. It is estimated that light sheets with a resolution of twice the wavelength of the used light can be generated. In the following two-dimensional simulations of the proposed (double) axicons are performed assuming a waveguide design similar to the sketches in fig. 2**(c)** and fig. 3**(b)** using the refractive index of Si_3N_4 and water at a given vacuum wavelength for the simulation of 532 nm.

2.3.1. Waveguide based axicons

In fig. 4 a two-dimensional simulation for on-chip axicon as described above with $R = 20\,\mu m$ at a visible vacuum wavelength of $\lambda_0 = 532$ nm, $n_i = 2.0559$, $n_o = 1.3371$, and different angles α is presented. The simulations are done using the finite element method (FEM) in COMSOL Multiphysics (COMSOL) and the results are presented as the square of the electric field norm as a measure of the intensity distribution. As can be seen in fig. 4 **(a)** the smaller the wedge angle the larger is the non-diffracting distance of the central core of the Bessel beam. Also, fig. 4 **(a)** shows that the on-chip axicon output does not only consist of the central beam or lobe, but also some weak side lobes. Although the number of lobes according to eq. (5) is rather high with 5, 7, 9, 11 and 15 for **(a)**–**(e)** respectively, it is observed that the further away from the central lobe these side lobes appear, the farther along the propagation direction they show maximum intensity. Even though the side lobes are not desirable for conventional light sheet microscopy, the appropriate placement of the side lobes could be exploited for simultaneous imaging of multiple planes.

This is the reason why the investigation of the proposed waveguide designs, using geometrical optics only is not sufficient anymore and the wavelike nature of light has to be considered more rigorous. The number of lobes to be expected according to eq. (5) would render the investigated axicons with the parameters given in fig. 4 useless with respect to an application in light sheet generation, as it has been pointed out already [26]. As can be seen in fig. 4 the central maximum is rather limited to extend in the first half of the DOF, whereas the side lobes are more prominent

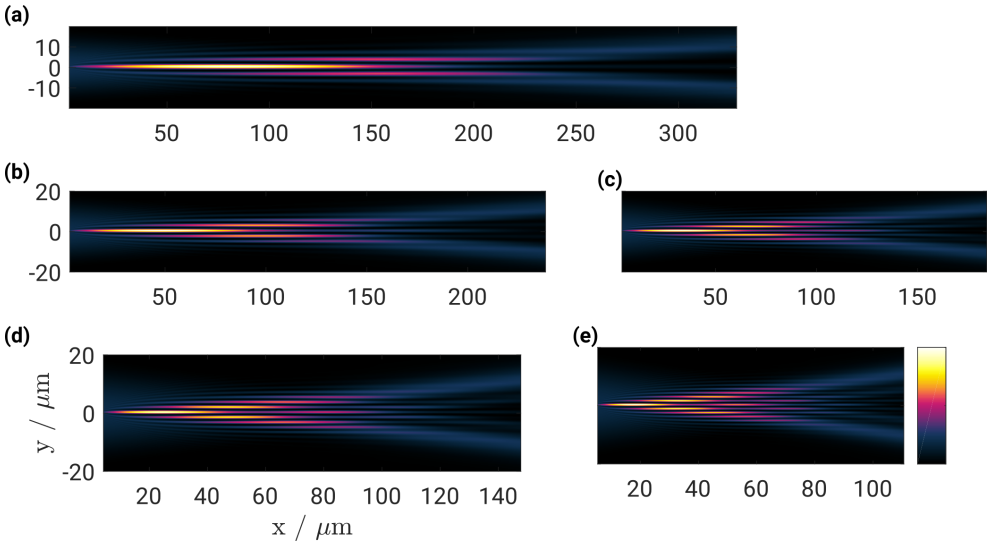

Fig. 4. Simulation results for an axicon with $R = 20\,\mu\text{m}$ at a vacuum wavelength of $\lambda_0 = 532\,\text{nm}$, $n_\text{i} = 2.0559$, $n_\text{o} = 1.3371$. Shown are the values for the electric field norm squared in arbitrary units for **(a)** $\alpha = 6°$, **(b)** $\alpha = 8°$, **(c)** $\alpha = 10°$, **(d)** $\alpha = 12°$, and **(e)** $\alpha = 15°$.

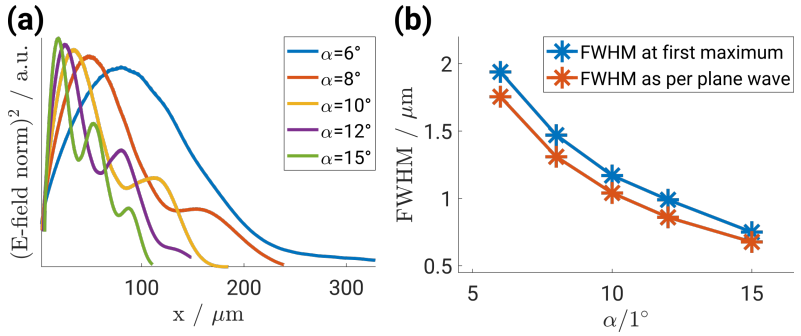

Fig. 5. The central beam along the optical axis as simulated for an axicon with $R = 20\,\mu\text{m}$ at a vacuum wavelength of $\lambda_0 = 532\,\text{nm}$, $n_\text{i} = 2.0559$, $n_\text{o} = 1.3371$ and varying axicon angles α using FEM is evaluated. **(a)** The intensity (here in terms of the electric field norm squared) along the direction of propagation is show for different angles. **(b)** Comparing the FWHM of the central beam at its maximum as given in the simulations is compared to is FWHM given by $\frac{\Delta r}{2}$.

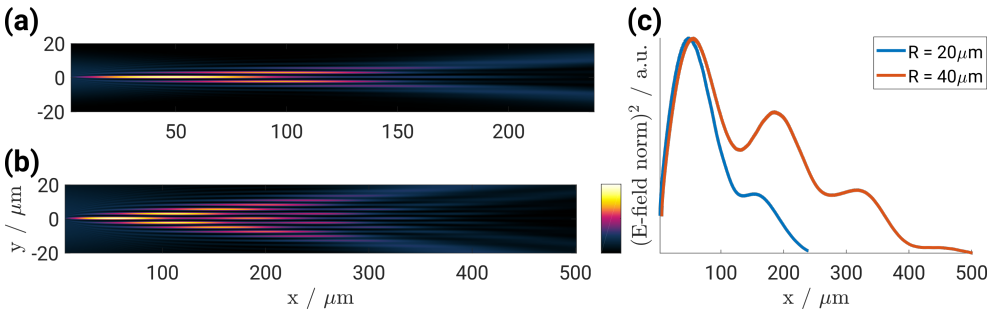

Fig. 6. Simulation results for an axicon with **(a)** $R = 20\,\mu\text{m}$ and **(b)** $R = 40\,\mu\text{m}$ at a vacuum wavelength of $\lambda_0 = 532\,\text{nm}$, $n_\text{i} = 2.0559$, $n_\text{o} = 1.3371$ at an axicon angle of $\alpha = 8°$. Presented is the square of the electric field norm as an indicator of the light intensity. Panel **(c)** shows the intensity profiles along the central part of the output for the two axicon, both normalized to their maximum value. The FWHM at maximum intensity are 1.47 µm and 1.45 µm for the $R = 20\,\mu\text{m}$ and $R = 40\,\mu\text{m}$ axicons respectively. The geometrically expected FWHM is 1.31 µm for both cases.

in the region farther away for the the axicon. This is also visible in fig. 5**(a)** where the intensity profile for the central maximum along the direction of propagation extracted from the results presented in fig. 4 is shown. Increasing the axicon angle does not only shorten the relevant propagation of the central lobe and increase the number of side lobes, but it also introduces intensity variations along the direction of propagation. In order to assess the validity of the geometrical description, the FWHM of the central beam at its maximum (along x) is compared to the FWHM as predicted by $\frac{\Delta r}{2}$ in fig. 5**(b)**. It suggests that the geometrical optics based approach is an overall valid approximation although the physically more precise FEM simulations predict a slightly larger FWHM for the central maximum. The intensity fluctuations along the optical axis as seen in fig. 5**(a)** emphasize the necessity of FEM simulations since these fluctuations cannot be predicted using the geometrical optics based model. Finally it can be observed that the translation invariant property of the field amplitude reduces over a finite length.

2.3.2. Size variation in on-chip axicons

Increasing the size of the axicon from $R = 20\,\mu\text{m}$ to $R = 40\,\mu\text{m}$ changes the interference pattern generated by the axicon as shown in fig. 6. First of all it can be seen that the number of lobes increases. The geometrical approximation predicts 7 and 15 lobes for an axicon angle of 8°. As for the axicon with $R = 20\,\mu\text{m}$, the side lobes appear farther along the direction of propagation especially those that are generated more distant from the optical axis. According to eq. (4) an increase in R also increases the propagation length of the central maximum. Looking at fig. 6**(b)** and **(c)** it can be seen that the intensity along the optical axis does not stay constant but is rather extended in a modulated fashion. This puts a much shorter limit to the application of on-chip axicon for the generation of light sheets for imaging application. For bio-imaging it is desirable that different parts of the sample is illuminated with similar intensities.

Moreover, it can be seen that the relevant propagation distance for the central beam is much shorter than the DOF predicted by the geometry which would be 260 µm for $R = 20\,\mu\text{m}$ and 520 µm for $R = 40\,\mu\text{m}$. In addition to that is the number of lobes with 7 and 15 for $R = 20\,\mu\text{m}$ and $R = 40\,\mu\text{m}$ respectively much larger than the number of lobes appearing over the first 100 µm after the axicon. Most of the lobes appear after that point, where the relevant central lobe has lost most of its intensity already as can be seen in fig. 6**(c)**. The further away from the center these side lobes appear, the farther along the direction of propagation and the weaker they appear. In addition to diminishing of the central beam along the the way, especially the wider on-chip axicon

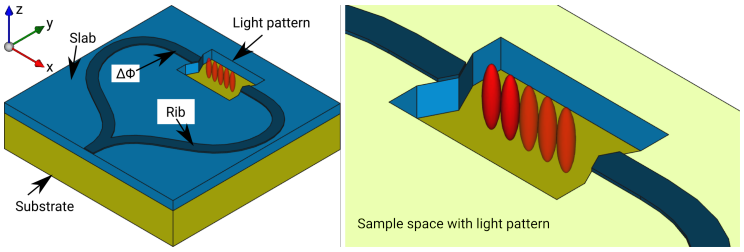

Fig. 7. A photonic chip incorporating two axicons that generate two counter-propagating QBBs with an intensity modulation suitable for SIM. Introducing a phase shift $\Delta\Phi$ in one arm will shift the generated interference pattern along the x-axis. Depending on the axicon width a waveguide taper as shown in fig. 1 may be required. Phase control is achieved by thermo-optic means as indicated in fig. 1.

produces a beam with an additional intensity modulation. Finally do the simulation results not only show that the actually relevant DOF is much shorter than geometrically expected, it should be pointed out that the out-of-plane divergence, depending on the thickness of the waveguide reduces the light intensity that is reached away from the axicon even further.

2.3.3. On-chip axicon counter-propagation

A combination of SIM and LSFM was introduced as lattice light-sheet microscopy [47]. Here, we demonstrate that two opposing axicons as presented in fig. 7 can be used to generate a pattern as presented in fig. 8 thus implementing chip-based 1D-lattice light-sheets. The design is based on a waveguide loop, with two opposing waveguide end-facets, each with on-chip axicon and the sample can be placed inside the well. Again a Si_3N_4 rib waveguide design is considered. The two opposing axicons in fig. 7 generate two counter-propagating 1D-light-sheets as simulated for the axicon. The resulting intensity distribution will resemble to a 1D-light-sheet with additional intensity modulation along the x-axis. The simulation parameters like vacuum wavelength and refractive index are kept the same as for the axicon simulations. The on-chip axicons will basically create structures as the ones described above with an additional modulation along the direction of propagation. This pattern may then be shifted along the optical axis by introducing a phase shift $\Delta\phi$ in one of the waveguide arms. Depending on the angle under which the waves stemming from opposing sides interfere, the modulation frequency can be calculated as

$$d = \frac{\lambda_0}{2\sin(90-\theta)\,n_o}. \tag{6}$$

Cropped data from the center of the simulation results (marked by a white rectangle) were extracted and a sinusoidal function of the form

$$f(x) = a_1 + a_2\cos(2a_3x\pi - a_4) \tag{7}$$

was fitted against the data. The parameters a_1, a_2, and a_4 represent the offset, modulation and phase respectively. The pattern wavelength is given by $d = \frac{1}{a_3}$, yielding values of d = 199 nm, 200 nm and 201 nm for $\alpha = 8°$, 10° and 15° respectively. These values coincide with the values given by eq. (6). It can be appreciated that waveguide chip illumination can easily generate counter-propagating Bessel beams with an interfering angle of 180 degrees and thus creating fringe period much smaller than what would have been possible using an objective lens. Moreover, as the light pattern is not generated by the imaging objective lens, it allows free choice of imaging objective lens of different magnification and N.A. without influencing the light pattern generated by the chip-illumination.

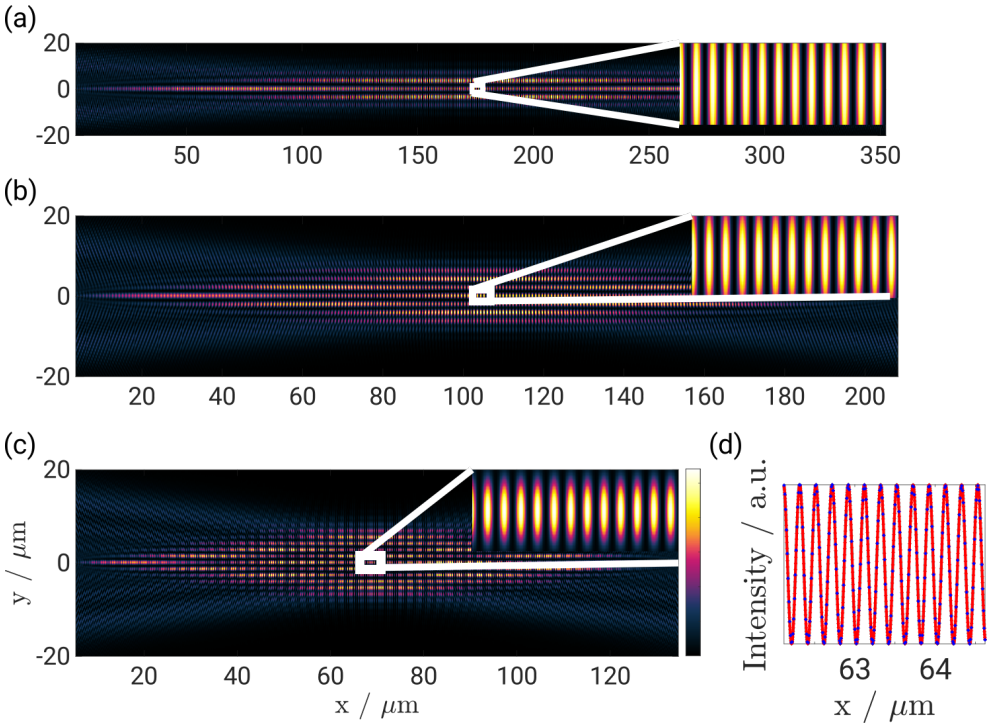

Fig. 8. Using a configuration as presented in fig. 7, the simulated intensity distribution is shown for axicon angles (as defined in fig. 2**(c)**) of $\alpha = 6°$, $10°$ and $15°$ as presented in **(a)** – **(c)** respectively. Data samples are taken from the highlighted rectangular regions and a sinusoidal function (see eq. (7)) is fitted (red curve) to the data (blue dots) to extract the pattern period; an example is shown in **(d)** for the pattern in **(c)**. The pattern periods are found to be 199 nm, 200 nm and 201 nm.

2.3.4. On-chip double axicon

Next, we investigate the generation of self-imaged Bessel beams SBB or bottle beam using a photonic-chip. It has been previously shown that the interference of two Bessel beams with different radial propagation constants generates an interference pattern described by eq. (3). This interference pattern is called SBB or bottle beam since it shows zero intensity spots on the optical axis that are surrounded by non-zero light intensity. It is possible to generate such overlapping Bessel beams using an axicon with two different angles. Here the implementation of a chip based double axicon (fig. 3) is simulated. Simulation results for the chip-based double axicon are presented in fig. 9. On the left-hand side a COMSOL model with a geometry as presented in fig. 3 and $n_\mathrm{i} = 2.0559$, $n_\mathrm{o} = 1.3371$, $\alpha_1 = 12°$, $\alpha_2 = 3°$ and $6°$, $R_1 = 20\,\mu\mathrm{m}$, $R_2 = R_1 \frac{\alpha_2}{\alpha_1}$ is simulated. The fundamental mode propagating in the waveguide is simulated and the intensity distribution after $x_2^{\min}$ is presented. On the right-hand side the intensity distribution of two co-propagating Bessel beams as described in eq. (3) is shown. As opposed to what was done in [40, 43], here $\alpha_1 > \alpha_2$. The reason for that is that the geometrical optics approach to the problem suggests that as shown in fig. 3**(b)** the light stemming from the first axicon angle and the light stemming from the second axicon angle would not overlap which is actually generating the interference.

As can be seen from the results, a clear intensity void is only expected for $\alpha_2 = 3°$, as shown in fig. 9**(a)**. The deviation from the result on the right-hand side is basically due to the far from optimal approximation of the two Bessel beams with respect to the spatial extend. This further

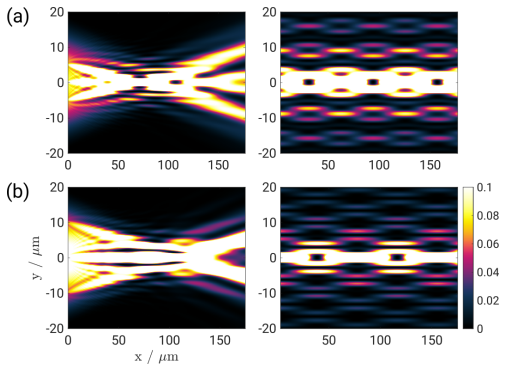

Fig. 9. The output of the on-chip double axicon as simulated in COMSOL on the left-hand side and the corresponding result as per eq. (3) on the right-hand side. Displayed is the normalized intensity, cut off at 10 % to achieve a representation similar to what is shown in [40, 43]. The axicon angles are set to be $\alpha_1 = 12°$ and $\alpha_2 = 3°$ and 6° for **(a)** and **(b)** respectively. The axicon size is set to $R_1 = 20\,\mu\text{m}$ and $R_2 = R_1 \frac{\alpha_2}{\alpha_1}$ to obtain a good overlap of the green and red region in fig. 3**(b)**.

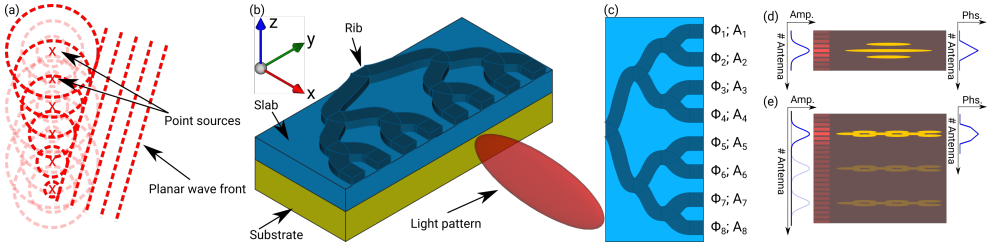

Fig. 10. Beam shaping using an OPA. According to the Huygens principle **(a)** a set of point sources (red x) generates spherical wavefronts (dashed lines) that form a plane wave in the far field. The general concept is presented in **(b)**, the waveguide is presented clinched the x-direction. Manipulating the phases ϕ_n and amplitudes A_n in each arm (**(c)**), wavefronts similar to those generated by a (double) axicon are generated in order to obtain QBBs and SBBs. Depending on the amplitude and phase distribution over the antennas, a QBB (**(d)**) or a SBB ((e)) may be generated. A dynamic manipulation of ϕ_n and A_n allows for dynamic beam shaping and steering. A spatially extended array may also allow for lateral beam shifting without alteration of the beam profile (**(e)**).

suggests that it is beneficial to perform simulations based on finite element method for optimizing the design parameters of on-chip lens for free-space beam shaping.

3. Design and simulation of chip-based dynamic beam shaping in free space

In the preceding section, using an on-chip axicon lens approach, the generation of spatially confined, but static illumination patterns is investigated. Moreover, non-flat ends of the end facet of the waveguides are required for the on-chip axicon. Another possibility of on-chip wavefront shaping to generate user-defined illumination patterns is the OPA as illustrated in fig. 10. According to the Huygens principle each point of a wavefront may be regarded as the source of a spherical wave. The antennas of an OPA mimic a set of point sources. By manipulating their phase and amplitude relation an overall wavefront can be shaped that is desired to generate a QBB for example [26].

Active beam steering in the far-field using OPAs has been demonstrated in SOI designs using

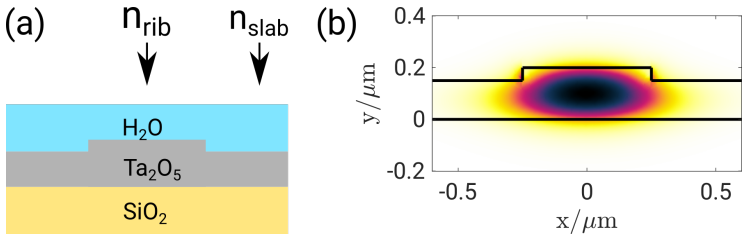

Fig. 11. The waveguide structure in the phased arrays. **(a)** The Ta_2O_5 on SiO_2 structure covert with water is shown. The slab height is 200 nm, the rib height and width are 50 nm and 500 nm respectively. Using a vacuum wavelength of 660 nm only the fundamental TE mode is guided. The distribution of the electric field norm is presented in **(b)** in arbitrary units.

the thermo-optic effect to steer a beam across the array, where the outcoupling was facilitated by grating couplers, enabling steering along the array by using different wavelength of 1500 nm, 1550 nm and 1600 nm [22]. Exploring the capability of OPAs, FDTD simulations of OPAs to shape the wavefront as generated by an axicon have been introduced with an emphasize on the Huygens principle for a vacuum wavelength of 780 nm assuming a cleaved end of the chip instead of grating couplers [26]. A passive far-field-focusing at vacuum wavelength of 1550 nm and 635 nm near the diffraction-limit on a Si_3N_4 platform has been demonstrated [28] as well as near-field-focusing at a vacuum wavelength of 1550 nm with additional grating based outcoupling and focus steering at a variable vacuum wavelength of 1550 nm, 1560 nm and 1570 nm on a SOI platform [24] which has further been developed to generate a QBB [25].

Regarding the OPA as a set of N antennas located at $\mathbf{r}_n$, radiating isotropically with an amplitude a_n, a phases ϕ_n and a wavelength λ, the complex valued far-field radiation pattern is described by the array factor. Similarly for the near-field a quasi-array-factor model was proposed as [24, 25]

$$E(\mathbf{r}) = \sum_{n=1}^{N} = a_n \exp\left[-i\left(2\pi \frac{\|\mathbf{r}_n - \mathbf{r}\|_2}{\lambda}\right) + \phi_n\right]. \tag{8}$$

This way a set of phases ϕ_n can be derived so that N waves constructively interfere at a desired focus spot similar to a plane wave encountering a hyperbolic lens as demonstrated in [24]. In a similar fashion an axially symmetric, linear phase distribution for the generation of a QBB including the required phase distribution have been derived in [25].

3.1. OPA designs at visible wavelengths for one-dimensinal QBB

The influence of the amplitude and phase distribution in OPAs is illustrated in fig. 10. In fig. 10**(c)** a Gaussian amplitude distribution over a set of waveguides (antennas) is combined with a phase distribution that is symmetrically changing from the center in a linear fashion. The resulting light intensity distribution of a QBB is indicated. In fig. 10**(e)** the phase distribution has been changed such that it shows two different slopes, thus generating the SBB. Moreover, a lateral movement of the intensity distribution along a larger set of waveguides is indicated by selectively activating different sets of waveguides. In order to test the feasibility of such a design at visible wavelength, not only the quasi-array-factor is calculated but also a two-dimensional FEM model in COMSOL.

Here a Ta_2O_5 on SiO_2 rib waveguide in an aqueous environment at a vacuum wavelength of 660 nm is considered. Assuming a waveguide array consisting of a set of rib waveguides, cleaved at the end of a chip, it is desirable to have good control over the guided modes, preferably single mode conditions in order to apply phase and amplitude control in an orderly fashion. The rib structure for the proposed design is shown in fig. 11**(a)** and the distribution of the electric field

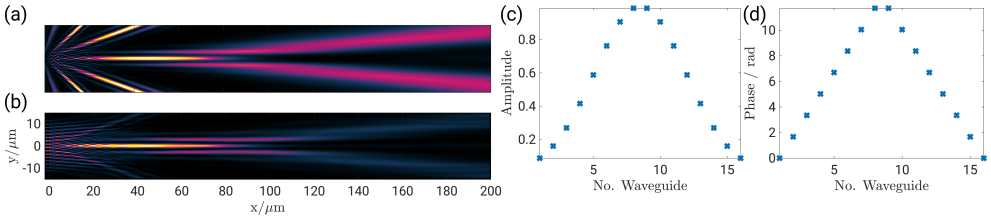

Fig. 12. Given an OPA with 16 elements, the output has been simulated using **(a)** eq. (8) and **(b)** FEM in COMSOL. The applied amplitude and phase distribution among the waveguides is shown in **(c)** and **(d)** respectively.

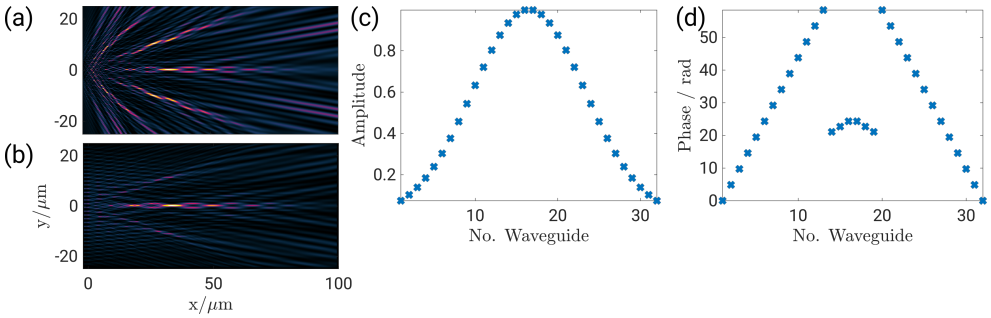

Fig. 13. Given an OPA with 32 elements, the output has been simulated using **(a)** eq. (8) and **(b)** FEM in COMSOL. The applied amplitude and phase distribution among the waveguides is shown in **(c)** and **(d)** respectively.

norm of the only guided TE mode is shown in fig. 11**(b)**. The proposed structure shows single mode conditions for the fundamental TE-mode at the given wavelength. In order to perform the two-dimensional FEM simulations in COMSOL the refractive index for the rib and the slab (n_{rib} and n_{slab} in fig. 11**(a)**) are approximated using the dispersion equation as described in [48]. The two-dimensional model in COMSOL is thus set up using two regions with n_{rib} and n_{slab} for the array and one region with the refractive index of water in which the light is propagating. For the quasi-array-factor model only the refractive index of water is considered since a discrete set of point sources is set up.

In order to generate a QBB using an OPA, simulations have been performed as presented in fig. 12. For an array with 16 antennas, a Gaussian amplitude distribution (fig. 12**(c)**), and a linear phase distribution (fig. 12**(d)**) the generated intensity distribution is simulated. Similar to what has been done for the $N = 64$ array with a spacing (pitch) of d =10 µm and a propagation wavelength of 1550 nm [25], here the set of $N = 16$ antennas is positioned with d =1.5 µm and a wavelength of $\lambda = \lambda_0/n_{H_2O}$ for the calculation of the array factor. The square of the electric field norm as obtained from the array factor eq. (8) is presented in fig. 11**(a)** and the equivalent result of the COMSOL simulation is presented in fig. 12**(b)**. Both results show a similar quality of the generated QBB although the array factor in addition shows tilted versions of the QBB that are less prominent in the FEM simulation that uses actual waveguides of 500 nm width to simulate the array.

In order to generate a SBB as it is described for the double axicon, the $N = 16$ OPA that generates a QBB is extended to $N = 32$ and while maintaining a Gaussian amplitude distribution (fig. 13**(c)**), the phase distribution introduces a second slope angle in order to generate two overlapping QBB. Again the array factor and a COMSOL-model are used to simulate the intensity distribution in terms of the square of the electric field norm in fig. 13**(a)** and fig. 13**(b)** respectively.

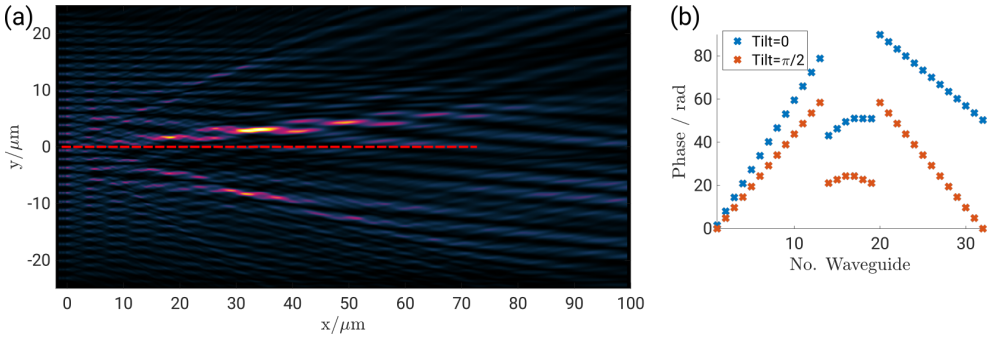

Fig. 14. A similar setup as shown in fig. 13 is used to demonstrate the tilting capabilities of the OPA. A linear phase gradient of $n\pi/2$ with the waveguide number n is added to the original (red) phase distribution thus changing it to the blue distribution in **(b)**. The SBB in **(a)** is thus tilted from its original optical axis (dashed red line) to an angled direction. See also Visualization 1.

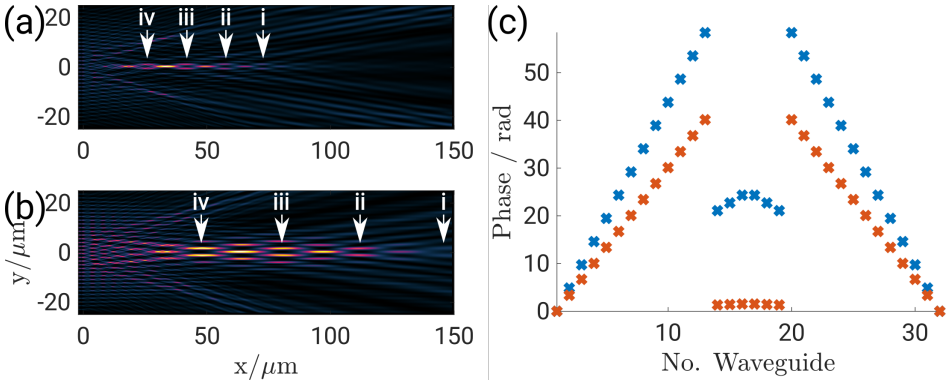

Fig. 15. Manipulating the phase distribution of the OPA in order to shift the intensity minima (i, ii, iii, iv) of the SBB along the optical axis. The intensity distributions presented in **(a)** and **(b)** are generated with the phase distributions presented in **(c)** in blue and red respectively. See also Visualization 2.

As for the QBB the array factor simulation of the SBB shows tilted copies of the intended intensity distribution. This is a feature of the point source model under consideration and the FEM models show a more accurate result since they consider actual waveguide structures.

The individual manipulation of the OPA's phases allows for a steering of the QBB and SBB. This is demonstrated in fig. 14**(a)** where a linear phase gradient is added to the original distribution that is used to generate the SBB (fig. 14**(b)**). This effect has been described with respect to a OPA's ability to shift a focus normal to the optical axis [24], where a linear phase gradient was added as well and the authors find that this approach would not only shift the focus, but will also change the focal length, which has to be corrected for. Looking at the SBB the interpretation is that the beam is not shifted, but tilted and the focal length would actually be the same. An animation of the incremental change for a $-\pi/2$ to a $\pi/2$ distribution is presented in Visualization 1.

On the other hand it is also possible to change the "focal length" of the SBB and thus move the intensity minima along the optical axis. This is achieved by changing the slope of the linear phase gradient introduced in the OPA. Given a slope for the linear phase gradient for the inner part of the double axicon (symmetric to both sides), a constant offset is is used to generate the

slope for the outer part of the double axicon (again in a symmetric manner). Then changing the initial slope for the phase gradient will ultimately shift the SBB along the optical axis. The intensity distribution shown in fig. 15**(a)** is generated using a phase gradient changing by 8π from one antenna to the next for the outer and 24π for the inner part. In fig. 15**(b)** the intensity distribution generated a phase gradient step of $\pi/2$ on the outer part and 16.5π on the inner part is shown. Four minima are indicated in the figures and their shift along the optical axis is the result of a general stretch of the pattern . The phase distributions of fig. 15**(a)** and fig. 15**(b)** are shown in fig. 15**(c)** in blue and red respectively. An incremental shift of the SBB along the optical axis is shown in Visualization 2.

4. Fabrication constraints

The fabrication of an actual axicon does involve a deviation from the perfectly sharp tip of the axicon as modeled in this work towards a rounded shape depending on the fabrication tolerance. These deviations have been modeled and investigated as tips of hyperbolic shape [49], as well as spherically shaped tips [50]. With respect to the generated QBBs a modulation of the intensity along the optical axis, as well as a broadening of the central lobe near the axicon were reported.

In [49] the sharp axicon tip is approximated by a hyperbolic shape of the form

$$x = \sqrt{a^2 + \frac{y^2}{\tan^2(\tau/2)}}, \tag{9}$$

with the parameter a determining the deviation from the perfect shape, the radial coordinate y and the axicon angle $\tau = 180° - 2\alpha$. In order to check the severity of this effect, an axicon as presented in figs. 4 and 5 (with $\alpha = 6°$) was remodeled with a tip shaped using the hyperbolic approximation with $a = 1\,\mu\text{m}$. With the intended micro fabrication process in mind this is a reasonable assumption. This yields a deviation of the tip shape as shown in fig. 16 **(a)**. The intensity profiles along the optical axis are plotted in fig. 16 **(b)**.

The exemplary simulation of a tip showing hyperbolic shape does show a shift of the intensity distribution along the optical axis. However, a modulation as presented in [49] could not be reproduced. The reason for this may be the use of guided modes instead of freely propagating Gaussian modes as used in [49] and the overall dimensions of the targeted axicons. The broadening of the central lobe as demonstrated in [50] due to a spherical shape of the tip was demonstrated to happen mainly near the axicon such that a significant part of the QBB will be available for the intended application.

However, should the fabrication of the on-chip axicon turn out to deviate from the perfectly shaped axicon in such a way, that the generated beam structure may not be applied in the intended way, the use of OPAs can solve this problem. These devices are investigated in section 3 with their ability to generate QBBs among others. The fabrication of flat end faces is not as critical as the fabrication of an axicon and the dynamic phase control allows for adjustment of the intended wavefront.

5. Conclusion

Here, the use of optical waveguides for performing light beam shaping in free-space optimized for three-dimensional bio-imaging application is investigate. We explore both the static and the dynamic light shaping using different chip designs highlighting the suitability and the benefits of integrated photonics in microscopy. This study will lay the foundation of the development of chip-based 3D optical microscopy. The chip-based axicon presents itself as a suitable means to generate light-sheet illumination as used in LSFM, based on a QBB intensity profile. Furthermore the counter propagating configuration of two axicons in combination with thermo-optic phase

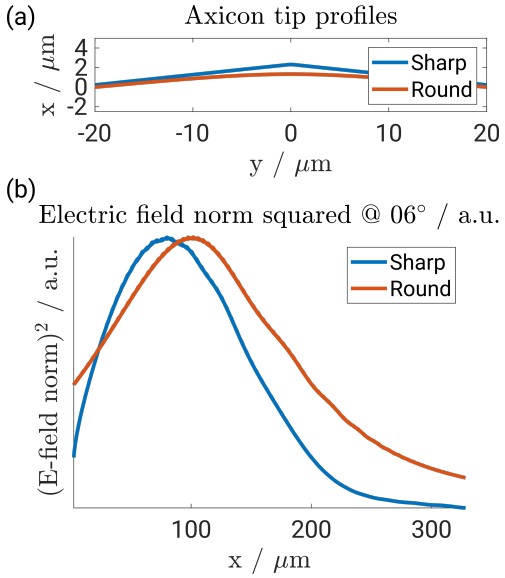

Fig. 16. The profile of the axicon tip is expected to deviate from a perfectly sharp to a round shape due to fabrication limitations. In **(a)** the perfectly sharp and a rounded (hyperbolic) tip profile are shown. The resulting intensity profile of the qbbs are shown in **(b)**.

control has the potential to generate illumination patterns suitable in lattice light-sheet microscopy. The chip enables interference of two counter-propagating Bessel beams with an angle of 180° between them, consequently generating a lattice light-sheet with small interference fringes, which will be beneficial for enhancing the lateral resolution.

Although limited in its extend the simulations of the chip-based double axicon show a general feasibility with respect to SBB generation. The formation of three-dimensional dark spots (bottles) using SBB could find application in chip-based STED. Finally, we explored OPA in the chip-based implementation show to be a useful tool not only in order to generate QBBs and SBB. It is also suitable for dynamic manipulation of the generated beam structure.

It was observed that the FEM simulations in COMSOL provides better overview as opposed to the analytical simulation of the light distribution of the waveguide designs proposed in this work. This facilitates the actual fabrication of planar waveguides that aid in the shaping of different illumination patterns for different microscopy methodologies. All simulation are performed for visible wavelengths that are essentially used in optical microscopy.

The main motivation of this study is to propose the use of photonic-chip for LSFM and its variants, such as lattice light-sheet microscopy. The main advantage of using photonic-chip is that the entire beam generation and beam steering can be performed using a photonic-chip and thus a standard optical microscope equipped with a single objective lens can be used to acquire LSFM images. This will not only make the set-up compact but also allow easy of operation with respect to placement of samples and working distances which are usually restricted with dual-objective lens based LSFM solutions.

Furthermore, the generation of user-defined illumination patterns using a photonic-chips could also have other applications, like optical trapping [51], on-chip Raman spectroscopy [52] and other integrated optical functions.

References

1. R. Heintzmann and C. G. Cremer, "Laterally modulated excitation microscopy: improvement of resolution by using a diffraction grating," in *Proc. SPIE 3568, Optical Biopsies and Microscopic Techniques III,* I. J. Bigio, H. Schneckenburger, J. Slavik, K. Svanberg, and P. M. Viallet, eds. (International Society for Optics and Photonics, 1999), pp. 185–196.
2. M. G. L. Gustafsson, "Surpassing the lateral resolution limit by a factor of two using structured illumination microscopy," J. Microsc. **198**, 82–87 (2000).
3. S. W. Hell and J. Wichmann, "Breaking the diffraction resolution limit by stimulated emission: stimulated-emission-depletion fluorescence microscopy," Opt. Lett. **19**, 780–782 (1994).
4. E. Betzig, G. H. Patterson, R. Sougrat, O. W. Lindwasser, S. Olenych, J. S. Bonifacino, M. W. Davidson, J. Lippincott-Schwartz, and H. F. Hess, "Imaging intracellular fluorescent proteins at nanometer resolution," Science **313**, 1642–1645 (2006).
5. S. T. Hess, T. P. Girirajan, and M. D. Mason, "Ultra-high resolution imaging by fluorescence photoactivation localization microscopy," Biophys. J. **91**, 4258–4272 (2006).
6. M. J. Rust, M. Bates, and X. Zhuang, "Sub-diffraction-limit imaging by stochastic optical reconstruction microscopy (STORM)." Nat. methods **3**, 793–5 (2006).
7. M. Heilemann, S. Van De Linde, M. Schüttpelz, R. Kasper, B. Seefeldt, A. Mukherjee, P. Tinnefeld, and M. Sauer, "Subdiffraction-resolution fluorescence imaging with conventional fluorescent probes," Angewandte Chemie - Int. Ed. **47**, 6172–6176 (2008).
8. T. Dertinger, R. Colyer, G. Iyer, S. Weiss, and J. Enderlein, "Fast, background-free, 3D super-resolution optical fluctuation imaging (SOFI)," Proc. Natl. Acad. Sci. **106**, 22287–22292 (2009).
9. I. Yahiatene, S. Hennig, M. Müller, and T. Huser, "Entropy-Based Super-Resolution Imaging (ESI): From Disorder to Fine Detail," ACS Photonics **2**, 1049–1056 (2015).
10. J. Huisken, J. Swoger, F. Del Bene, J. Wittbrodt, and E. H. Stelzer, "Optical sectioning deep inside live embryos by selective plane illumination microscopy," Science **305**, 1007–1009 (2004).
11. A. H. Voie, D. H. Burns, and F. A. Spelman, "Orthogonal-plane fluorescence optical sectioning: three-dimensional imaging of macroscopic biological specimens," J. Microsc. **170**, 229–236 (1993).
12. J.-C. Tinguely, Ø. I. Helle, and B. S. Ahluwalia, "Silicon nitride waveguide platform for fluorescence microscopy of living cells," Opt. Express **25**, 27678–27690 (2017).
13. B. Agnarsson, A. B. Jonsdottir, N. B. Arnfinnsdottir, and K. Leosson, "On-chip modulation of evanescent illumination and live-cell imaging with polymer waveguides," Opt. Express **19**, 22929–22935 (2011).
14. S. Mittler, "Waveguide evanescent field fluorescence and scattering microscopy: The status quo," in *Springer Series in Optical Sciences,* vol. 218 (2018), pp. 1–24.
15. H. M. Grandin, B. Städler, M. Textor, and J. Vörös, "Waveguide excitation fluorescence microscopy: A new tool for sensing and imaging the biointerface," Biosens. Bioelectron. **21**, 1476–1482 (2006).
16. A. Hassanzadeh, M. Nitsche, S. Mittler, S. Armstrong, J. Dixon, and U. Langbein, "Waveguide evanescent field fluorescence microscopy: Thin film fluorescence intensities and its application in cell biology," Appl. Phys. Lett. **92**, 233503 (2008).
17. R. Diekmann, Ø. I. Helle, C. I. Øie, P. McCourt, T. R. Huser, M. Schüttpelz, and B. S. Ahluwalia, "Chip-based wide field-of-view nanoscopy," Nat. Photonics **11**, 322–328 (2017).
18. Ø. I. Helle, D. A. Coucheron, J.-C. Tinguely, C. I. Øie, and B. S. Ahluwalia, "Nanoscopy on-a-chip: super-resolution imaging on the millimeter scale," Opt. Express **27**, 6700–6710 (2019).
19. Ø. I. Helle, F. T. Dullo, M. Lahrberg, J.-C. Tinguely, and B. S. Ahluwalia, "Structured illumination microscopy using a photonic chip," arXiv preprint arXiv:1903.05512 (2019).
20. O. G. Hellesø, P. Løvhaugen, A. Z. Subramanian, J. S. Wilkinson, and B. S. Ahluwalia, "Surface transport and stable trapping of particles and cells by an optical waveguide loop," Lab on a Chip **12**, 3436–3440 (2012).
21. B. S. Ahluwalia and O. G. Hellesø, "Optical waveguide loop for planar trapping of blood cells and microspheres," in *Optical Trapping and Optical Micromanipulation X,* vol. 8810 (2013), p. 88100T.
22. K. Van Acoleyen, W. Bogaerts, J. Jágerská, N. Le Thomas, R. Houdré, and R. Baets, "Off-chip beam steering with a one-dimensional optical phased array on silicon-on-insulator," Opt. Lett. **34**, 1477–1479 (2009).
23. C. V. Poulton, A. Yaacobi, D. B. Cole, M. J. Byrd, M. Raval, D. Vermeulen, and M. R. Watts, "Coherent solid-state LIDAR with silicon photonic optical phased arrays," Opt. Lett. **42**, 4091–4094 (2017).
24. J. Notaros, C. V. Poulton, M. Raval, and M. R. Watts, "Near-Field-Focusing Integrated Optical Phased Arrays," J. Light. Technol. **36**, 5912–5920 (2018).
25. J. Notaros, C. V. Poulton, M. J. Byrd, M. Raval, and M. R. Watts, "Integrated optical phased arrays for quasi-Bessel-beam generation," Opt. Lett. **42**, 3510–3513 (2017).
26. A. Diaz Tormo and N. Le Thomas, "On-chip axicon for light sheet microscopy," in *Proceedings of the 20th Annual Symposium of the IEEE Photonics Society Benelux Chapter,* (2015), pp. 1–4.
27. D. N. Hutchison, J. Sun, J. K. Doylend, R. Kumar, J. Heck, W. Kim, C. T. Phare, A. Feshali, and H. Rong, "High-resolution aliasing-free optical beam steering," Optica **3**, 887–890 (2016).
28. C. V. Poulton, M. J. Byrd, M. Raval, Z. Su, N. Li, E. Timurdogan, D. Coolbaugh, D. Vermeulen, and M. R. Watts, "Large-scale silicon nitride nanophotonic phased arrays at infrared and visible wavelengths," Opt. Lett. **42**, 21–24 (2017).

29. J. W. Goodman, "Introduction to Fourier Optics, Third Edition," (2004).
30. J. Durnin, "Exact solutions for nondiffracting beams I The scalar theory," J. Opt. Soc. Am. A **4**, 651–654 (1987).
31. J. Durnin, J. Miceli, and J. H. Eberly, "Diffraction-free beams," Phys. Rev. Lett. **58**, 1499–1501 (1987).
32. Z. Bouchal, J. Wagner, and M. Chlup, "Self-reconstruction of a distorted nondiffracting beam," Opt. Commun. **151**, 207–211 (1998).
33. S. Chávez-Cerda, E. Tepichin, M. A. Meneses-Nava, G. Ramirez, and J. M. Hickmann, "Experimental observation of interfering Bessel beams," Opt. Express **3**, 524–529 (1998).
34. J. H. McLeod, "The Axicon: A New Type of Optical Element," J. Opt. Soc. Am. **44**, 592–597 (1954).
35. A. C. S. van Heel, "High Precision Measurements with Simple Equipment*," J. Opt. Soc. Am. **40**, 809–816 (1950).
36. Z. Jaroszewicz, A. Burvall, and A. T. Friberg, "Axicon - the Most Important Optical Element," Opt. Photon. News **16**, 34–39 (2005).
37. R. M. Herman and T. A. Wiggins, "Production and uses of diffractionless beams," J. Opt. Soc. Am. A **8**, 932–942 (1991).
38. J. Arlt and K. Dholakia, "Generation of high-order Bessel beams by use of an axicon," Opt. Commun. **177**, 297–301 (2000).
39. D. McGloin, G. C. Spalding, H. Melville, W. Sibbett, and K. Dholakia, "Three-dimensional arrays of optical bottle beams," Opt. Commun. **225**, 215–222 (2003).
40. B. S. Ahluwalia, X. C. Yuan, and S. H. Tao, "Generation of self-imaged optical bottle beams," Opt. Commun. **238**, 177–184 (2004).
41. B. S. Ahluwalia, X.-C. Yuan, and S. H. Tao, "Transfer of 'pure' on-axis spin angular momentum to the absorptive particle using self-imaged bottle beam optical tweezers system," Opt. Express **12**, 5172–5177 (2004).
42. B. S. Ahluwalia, W. C. Cheong, X.-C. Yuan, L.-S. Zhang, S.-H. Tao, J. Bu, and H. Wang, "Design and fabrication of a double-axicon for generation of tailorable self-imaged three-dimensional intensity voids," Opt. Lett. **31**, 987–989 (2006).
43. B. S. Ahluwalia, X. C. Yuan, S. H. Tao, W. C. Cheong, L. S. Zhang, and H. Wang, "Micromanipulation of high and low indices microparticles using a microfabricated double axicon," J. Appl. Phys. **99**, 113104 (2006).
44. X. C. Yuan, B. S. Ahluwalia, W. C. Cheong, J. Bu, H. B. Niu, and X. Peng, "Direct electron beam writing of kinoform micro-axicon for generation of propagation-invariant beams with long non-diffracting distance," J. Opt. A: Pure Appl. Opt. **9**, 329–334 (2007).
45. L. Li, W. M. Lee, X. Xie, W. Krolikowski, A. V. Rode, and J. Zhou, "Shaping self-imaging bottle beams with modified quasi-Bessel beams," Opt. Lett. **39**, 2278–2281 (2014).
46. R. A. A. G. Jonathan P. Manigo, "Self-imaging, self-healing beams generated by photorefractive volume holography," Opt. Eng. **54**, 1–6 (2015).
47. B. C. Chen, W. R. Legant, K. Wang, L. Shao, D. E. Milkie, M. W. Davidson, C. Janetopoulos, X. S. Wu, J. A. Hammer, Z. Liu, B. P. English, Y. Mimori-Kiyosue, D. P. Romero, A. T. Ritter, J. Lippincott-Schwartz, L. Fritz-Laylin, R. D. Mullins, D. M. Mitchell, J. N. Bembenek, A. C. Reymann, R. Böhme, S. W. Grill, J. T. Wang, G. Seydoux, U. S. Tulu, D. P. Kiehart, and E. Betzig, "Lattice light-sheet microscopy: Imaging molecules to embryos at high spatiotemporal resolution," Science **346**, 1257998 (2014).
48. K. Okamoto, *Fundamentals of Optical Waveguides* (2006).
49. O. Brzobohatý, T. Cižmár, and P. Zemánek, "High quality quasi-Bessel beam generated by round-tip axicon," Opt. Express **16**, 12688–12700 (2008).
50. G. S. Sokolovskii, V. V. Dyudelev, S. N. Losev, M. Butkus, K. K. Soboleva, A. I. Sobolev, A. G. Deryagin, V. I. Kuchinskii, V. Sibbet, and E. U. Rafailov, "Influence of the axicon characteristics and beam propagation parameter M2 on the formation of Bessel beams from semiconductor lasers," Quantum Electron. **43**, 423–427 (2013).
51. B. S. Ahluwalia, P. Løvhaugen, and O. G. Hellesø, "Waveguide trapping of hollow glass spheres." Opt. letters **36**, 3347–9 (2011).
52. P. Løvhaugen, B. S. Ahluwalia, T. R. Huser, and O. G. Hellesø, "Serial Raman spectroscopy of particles trapped on a waveguide," Opt. Express **21**, 2964–2970 (2013).

5

Conclusion

This thesis is part of a large EU project with people working on instrumentation, computational data processing and simulations, and biology. A description of the author's contributions to related publications are given where they are attached. The contributions of the presented thesis to SRM are summarized, followed by an outlook to describe relevant work that can be done in the future based on the presented results. In chapter 3 the subpixel peak localization for high precision parameter estimation in SIM data at pattern frequencies supported by the systems OTF was introduced. It was demonstrated, that it is an efficient way to estimate the pattern wave vector with an error up to 80 % smaller as compared to an estimation using regular peak localization in simulated, two-dimensional SIM data. It turns out to build the basis for subsequent pattern phase estimation if the method relies on precise knowledge of the pattern wave vector. Ultimately the deviation of the reconstruction from the optimal reconstruction can be improved by about one order of magnitude if the parameters are estimated using the subpixel method as compared to the conventional method using full pixels. No prior knowledge regarding the parameters is needed, the computational cost is low and the final reconstruction is improved. This method may be used in any SIM implementation that allows for the pattern frequency to be transmitted by the imaging system.

The SBP is a figure of merit that considers both, the resolution and the FoV of an imaging system. Two new approaches have been introduced in order to circumvent the limitations in SIM, inherent to epifluorescence imaging using a single objective lens for pattern generation and image acquisition at the

same time. The first implementation is tSIM, which uses a set of mirrors to generate sinusoidal illumination patterns by interfering two coherent beams in the sample plane. This way, a low magnification (10×), NA=0.25 objective with a large FoV of 2.2 mm for instance can be used for image acquisition. The pattern generation using the mirror set has been shown to generate a pattern spacing of about 250 nm spacing over a mm^2 area, which provides the high resolution of SIM. Such a pattern spacing could theoretically be achieved with an objective having NA=0.81, which would not have been able to provide such a large FoV. A typical (40×), NA=0.65 objective has FoV of only 0.55 mm in diameter for example. The presented simulations show, that this SIM implementation provides the option to increase the FoV as compared to conventional epifluorescence SIM while maintaining the possible resolution, thus increasing the SBP significantly. They also help to estimate the required amount of raw data images that need to be taken depending on the used hardware, and what happens if minimum requirements are not met. The second option to decouple patternn generation from the objective lens in SIM are photonic chips. Optical waveguide technology is used in cSIM in order to perform high frequency pattern SIM over a potentially large FoV, while maintaining TIRF conditions. As in tSIM here the SBP is improved beyond what is possible when using a single lens for pattern generation and image acquisition at the same time. The pattern generation is illustrated using COMSOL simulations and the imaging requirements are investigated using appropriate simulations of the imaging process.

The photonic chip-based beam shaping, a means to generate light sheet illumination among others was investigated with respect to different waveguide designs and wavelengths using a simple array factor model as well as two-dimensional COMSOL simulations. The idea is to ultimately use waveguide technology in microscopy beyond its ability to shape an evanescent field on top of a waveguide, but use its capabilities for free-space beam shaping. Chapter 4 and the attached paper can be seen as a guide to choose optimal parameters when using a QBB profile generated by an axicon to perform LSFM. Keeping in mind, that the sample has a degrading influence on the generated light-sheet at larger penetration depths, the 20 µm wide axicon with a wedge angle of 6° can be expected to generate a QBB profile that shows one central lobe over a propagation distance of about 150 µm, a reasonable penetration depth. Increasing the wedge angle will yield more side lobes, as will a wider axicon structure. A sinusoidal intensity modulation can be imprinted on the generated light sheet when two opposing on-chip axicons generate counter propagating QBBs. The modulation frequency depends on the selected wedge angles, an thermo-optic modulation may be used to dynamically control the pattern phase. A waveguide model implementing a double-axicon structure to generate SBB profiles, if only for a very limited propagation length. However the simulated and discussed OPA approach has an edge over the suggested axicon and double-

axicon designs as is does not require an angled end facet of the waveguide. In addition to that, dynamic beam shaping through manipulation of the phase and intensity in each array element has been demonstrated. Especially the dynamic steering of a bottle beam profile may find applications with respect to optical trapping for instance. Dynamic steering of light sheets will be beneficial in future LSFM implementations.

5.1 Outlook and future work

Since the subpixel peak localization is a general method to perform a high precision peak detection in the Fourier transform a data set, it may be beneficial to implemented it in order to estimate the pattern wave vector in SIM using the approach presented in equation (9) of paper 1. This approach estimates the pattern wave vector based on the known relative phases of the generated patterns, also by doing a peak localization.

The presented large FoV SIM techniques require more advanced reconstruction algorithms, especially new ways of parameter estimation for the comparably high pattern frequencies generated with respect to the resolution of the objective lens. Since the proposed implementations allow for intermediate pattern frequencies, iterative parameter estimation approaches based on overlapping spectral regions could be a way.

The work on chip-based, free-space beam shaping provides appropriate guide lines and a suitable method for fabrication like photolithography or electron-beam lithography must be found to fabricate the waveguides and test their feasibility for LSFM as proposed.

Bibliography

[1] Ernst Abbe. “Beiträge zur Theorie des Mikroskops und der mikroskopischen Wahrnehmung.” In: *Archiv für mikroskopische Anatomie* 9.1 (1873).

[2] B. S. Ahluwalia, X. C. Yuan, and S. H. Tao. “Generation of self-imaged optical bottle beams.” In: *Optics Communications* 238.1-3 (2004).

[3] B. S. Ahluwalia, X.-C. Yuan, and S. H. Tao. “Transfer of ‘pure’ on-axis spin angular momentum to the absorptive particle using self-imaged bottle beam optical tweezers system.” In: *Optics Express* 12.21 (2004).

[4] B. S. Ahluwalia et al. “Design and fabrication of a double-axicon for generation of tailorable self-imaged three-dimensional intensity voids.” In: *Optics Letters* 31.7 (2006).

[5] B. S. Ahluwalia et al. “Micromanipulation of high and low indices microparticles using a microfabricated double axicon.” In: *Journal of Applied Physics* 99.11 (2006).

[6] G. B. Airy. “On the Diffraction of an Object-glass with Circular Aperture.” eng. In: *Transactions of the Cambridge Philosophical Society* 5 (1835). Ed. by London Natural History Museum Library.

[7] H. Andersson et al. “Autofluorescence of living cells.” In: *Journal of Microscopy* (1998).

[8] Manfred von Ardenne. “Das Elektronen-Rastermikroskop - Theoretische Grundlagen.” In: *Zeitschrift für Physik* 109.9-10 (1938).

[9] J. Arlt and K. Dholakia. “Generation of high-order Bessel beams by use of an axicon.” In: *Optics Communications* 177.1 (2000).

[10] Brent Bailey et al. “Enhancement of axial resolution in fluorescence microscopy by standing-wave excitation.” In: *Nature* 366.6450 (1993).

[11] Eric Betzig et al. “Imaging intracellular fluorescent proteins at nanometer resolution.” In: *Science* 313.5793 (2006).

[12] G Binnig, C F Quate, and Ch. Gerber. “Atomic Force Microscope.” In: *Phys. Rev. Lett.* 56.9 (Mar. 1986).

[13] G. Binning et al. “Surface studies by scanning tunneling microscopy.” In: *Physical Review Letters* (1982).

[14] Z. Bouchal, J. Wagner, and M. Chlup. “Self-reconstruction of a distorted nondiffracting beam.” In: *Optics Communications* 151.4-6 (1998).

[15] Stefan Bretschneider, Christian Eggeling, and Stefan W. Hell. "Breaking the diffraction barrier in fluorescence microscopy by optical shelving." In: *Physical Review Letters* (2007).

[16] Louis de Broglie. "The reinterpretation of wave mechanics." In: *Foundations of Physics* 1.1 (Mar. 1970).

[17] Oto Brzobohatý, Tomáš Cižmár, and Pavel Zemánek. "High quality quasi-Bessel beam generated by round-tip axicon." In: *Optics Express* 16.17 (2008).

[18] Steven K. Buratto. "Near-field scanning optical microscopy." In: *Current Opinion in Solid State and Materials Science* (1996).

[19] Weilun Chao et al. "Soft X-ray microscopy at a spatial resolution better than 15 nm." In: *Nature* (2005).

[20] S. Chávez-Cerda et al. "Experimental observation of interfering Bessel beams." In: *Optics Express* 3.13 (1998).

[21] Bi Chang Chen et al. "Lattice light-sheet microscopy: Imaging molecules to embryos at high spatiotemporal resolution." In: *Science* 346.6208 (2014).

[22] COMSOL. "Introduction to COMSOL Multiphysics 5.3." In: *Manual* (2014).

[23] R. Courant. *Variational methods for the solution of problems of equilibrium and vibrations*. 1943.

[24] Christoph Cremer and Barry R. Masters. "Resolution enhancement techniques in microscopy." In: *European Physical Journal H* (2013).

[25] T. Dertinger et al. "Fast, background-free, 3D super-resolution optical fluctuation imaging (SOFI)." In: *Proceedings of the National Academy of Sciences* 106.52 (2009).

[26] Alejandro Diaz Tormo and Nicolas Le Thomas. "On-chip axicon for light sheet microscopy." In: *Proceedings of the 20th Annual Symposium of the IEEE Photonics Society Benelux Chapter*. 2015.

[27] Robin Diekmann et al. "Chip-based wide field-of-view nanoscopy." In: *Nature Photonics* 11.5 (2017).

[28] Siyuan Dong et al. "Resolution doubling with a reduced number of image acquisitions." In: *Biomed. Opt. Express* 6.8 (Aug. 2015).

[29] G. Donnert et al. "Macromolecular-scale resolution in biological fluorescence microscopy." In: *Proceedings of the National Academy of Sciences* (2006).

[30] J. Durnin. "Exact solutions for nondiffracting beams I The scalar theory." In: *Journal of the Optical Society of America A* 4.4 (1987).

[31] J. Durnin, J. Miceli, and J. H. Eberly. "Diffraction-free beams." In: *Physical Review Letters* 58.15 (1987).

[32] Jörg Enderlein and Claus B Müller. "Image Scanning Microscopy." In: *Physical review letters : PRL ; providing rapid publication of short reports of important fundamental research with coverage of major advances in*

all aspects of physics and of developments with significant consequences across subdisciplines, 2010, 104, 19 (2010).

[33] Rolf Erni et al. "Atomic-resolution imaging with a sub-50-pm electron probe." In: *Physical Review Letters* (2009).

[34] Tanner C. Fadero et al. "LITE microscopy: Tilted light-sheet excitation of model organisms offers high resolution and low photobleaching." In: *Journal of Cell Biology* 217.5 (May 2018).

[35] J. Franck. "Elementary processes of photochemical reactions." In: *Transactions of the Faraday Society* (1926).

[36] Matthias Geissbuehler and Theo Lasser. "How to display data by color schemes compatible with red-green color perception deficiencies." In: *Optics Express* (2013).

[37] Joseph W Goodman. *Introduction to Fourier optics*. eng. 3. ed. Englewood, Colo.: Roberts, 2005.

[38] Joseph W. Goodman. *Introduction to Fourier Optics, Third Edition*. 2004.

[39] K. Greger, J. Swoger, and E. H.K. Stelzer. "Basic building units and properties of a fluorescence single plane illumination microscope." In: *Review of Scientific Instruments* (2007).

[40] Ingo Gregor and Jörg Enderlein. *Image scanning microscopy*. 2019.

[41] M. G. L. Gustafsson. "Nonlinear structured-illumination microscopy: Wide-field fluorescence imaging with theoretically unlimited resolution." In: *Proceedings of the National Academy of Sciences* (2005).

[42] M. G L Gustafsson. "Surpassing the lateral resolution limit by a factor of two using structured illumination microscopy." In: *Journal of Microscopy* 198.2 (2000).

[43] Mats G L Gustafsson et al. "Three-dimensional resolution doubling in wide-field fluorescence microscopy by structured illumination." In: *Biophysical journal* 94.12 (2008).

[44] Nicholas C Harris et al. "Efficient, compact and low loss thermo-optic phase shifter in silicon." In: *Opt. Express* 22.9 (May 2014).

[45] Mike Heilemann et al. "Subdiffraction-resolution fluorescence imaging with conventional fluorescent probes." In: *Angewandte Chemie - International Edition* 47.33 (Aug. 2008).

[46] Rainer Heintzmann and Christoph G. Cremer. "Laterally modulated excitation microscopy: improvement of resolution by using a diffraction grating." In: *Proc. SPIE 3568, Optical Biopsies and Microscopic Techniques III*. Ed. by Irving J. Bigio et al. International Society for Optics and Photonics, Jan. 1999.

[47] Rainer Heintzmann and Thomas Huser. *Super-Resolution Structured Illumination Microscopy*. 2017.

[48] S. W. Hell and M. Kroug. "Ground-state-depletion fluorscence microscopy: A concept for breaking the diffraction resolution limit." In: *Applied Physics B Lasers and Optics* (1995).

[49] Stefan W. Hell. "Far-Field Optical Nanoscopy." In: *Science* 1153.2007 (May 2011).

[50] Stefan W. Hell and Jan Wichmann. "Breaking the diffraction resolution limit by stimulated emission: stimulated-emission-depletion fluorescence microscopy." In: *Optics Letters* 19.11 (1994).

[51] Øystein I. Helle et al. "Nanoscopy on-a-chip: super-resolution imaging on the millimeter scale." In: *Optics Express* 27.5 (2019).

[52] Øystein I. Helle et al. "Structured illumination microscopy using a photonic chip." In: *arXiv preprint arXiv:1903.05512* (Mar. 2019).

[53] John F. W. Herschel. "Light." eng. In: *Treatises on physical astronomy, light and sound contributed to the Encyclopaedia metropolitana.* (1828).

[54] Samuel T. Hess, Thanu P.K. Girirajan, and Michael D. Mason. "Ultra-high resolution imaging by fluorescence photoactivation localization microscopy." In: *Biophysical Journal* 91.11 (2006).

[55] M. Hofmann et al. "Breaking the diffraction barrier in fluorescence microscopy at low light intensities by using reversibly photoswitchable proteins." In: *Proceedings of the National Academy of Sciences* (2005).

[56] Jan Huisken et al. "Optical sectioning deep inside live embryos by selective plane illumination microscopy." In: *Science* 305.5686 (2004).

[57] Vighter Iberi et al. "Maskless lithography and in situ visualization of conductivity of graphene using helium ion microscopy." In: *Scientific Reports* (2015).

[58] Jaroslav Icha et al. *Phototoxicity in live fluorescence microscopy, and how to avoid it*. 2017.

[59] A. Jabłoński. "Über den Mechanismus der Photolumineszenz von Farbstoffphosphoren." In: *Zeitschrift für Physik* (1935).

[60] Joby Joseph et al. "Improving the space-bandwidth product of structured illumination microscopy using a transillumination configuration." In: *Journal of Physics D: Applied Physics* (2019).

[61] Rainer Kaufmann et al. "Imaging label-free intracellular structures by localisation microscopy." In: *Micron* (2011).

[62] Peter Kner et al. "Super-resolution video microscopy of live cells by structured illumination." In: *Nature Methods* 6.5 (2009).

[63] August Köhler. *Mikrophotographische untersuchungen mit ultraviolettem licht*. Vol. 21. Zeitschrift für wissenschaftliche Mikroskopie und für mikroskopische Technik, 1904.

[64] Marcel Lahrberg, Firehun Tsige Dullo, and Balpreet Singh Ahluwalia. "Photonic-chip based free space beam shaping and steering for advanced optical microscopy application." In: *OSA Continuum* 2.11 (2019).

[65] Marcel Lahrberg et al. "Accurate estimation of the illumination pattern's orientation and wavelength in sinusoidal structured illumination microscopy." In: *Appl. Opt.* 57.5 (Feb. 2018).

[66] Joseph R. Lakowicz. *Principles of fluorescence spectroscopy*. 2006.

[67] Frederick Lanni et al. “Excitation field synthesis as a means for obtaining enhanced axial resolution in fluorescence microscopes.” In: *Bioimaging* 1.4 (Dec. 1993).

[68] A. Lewis et al. “Development of a 500 Å spatial resolution light microscope. I. light is efficiently transmitted through $\lambda/16$ diameter apertures.” In: *Ultramicroscopy* (1984).

[69] W Lukosz. “Optical Systems with Resolving Powers Exceeding the Classical Limit.” In: *J. Opt. Soc. Am.* 56.11 (Nov. 1966).

[70] W. Lukosz. “Optical Systems with Resolving Powers Exceeding the Classical Limit II.” In: *Journal of the Optical Society of America* 57.7 (July 1967).

[71] D. McGloin et al. “Three-dimensional arrays of optical bottle beams.” In: *Optics Communications* 225.4-6 (2003).

[72] John H. McLeod. “The Axicon: A New Type of Optical Element.” In: *Journal of the Optical Society of America* 44.8 (1954).

[73] E. Mudry et al. “Structured illumination microscopy using unknown speckle patterns.” In: *Nature Photonics* 6.5 (2012).

[74] Marcel Müller et al. “Open-source image reconstruction of super-resolution structured illumination microscopy data in ImageJ.” In: *Nature Communications* 7 (2016).

[75] J Notaros et al. “Near-Field-Focusing Integrated Optical Phased Arrays.” In: *Journal of Lightwave Technology* 36.24 (Dec. 2018).

[76] Katsunari Okamoto. *Fundamentals of Optical Waveguides*. 2006.

[77] Yasushi Oshikane et al. “Observation of nanostructure by scanning near-field optical microscope with small sphere probe.” In: *Science and Technology of Advanced Materials* (2007).

[78] James B. Pawley. *Handbook Of Biological Confocal Microscopy*. Boston, MA: Springer US, 2006.

[79] Christopher V. Poulton et al. “Large-scale silicon nitride nanophotonic phased arrays at infrared and visible wavelengths.” In: *Optics Letters* 42.1 (2017).

[80] Rayleigh. “XV. On the theory of optical images, with special reference to the microscope.” In: *Philosophical Magazine Series 5* 42.255 (Aug. 1896).

[81] J N Reddy. *An introduction to the finite element method*. New York, 1993.

[82] Robim M. Rodrigues et al. “Autofluorescence microscopy: A non-destructive tool to monitor mitochondrial toxicity.” In: *Toxicology Letters* (2011).

[83] Michael J Rust, Mark Bates, and Xiaowei Zhuang. “Sub-diffraction-limit imaging by stochastic optical reconstruction microscopy (STORM).” In: *Nature methods* 3.10 (Oct. 2006).

[84] Harekrushna Sahoo. *Fluorescent labeling techniques in biomolecules: A flashback*. 2012.

[85] Bahaa E A Saleh and Malvin Carl Teich. *Fundamentals of Photonics , 2nd Edition*. Wiley-Interscience, 2007.

[86] Lothar Schermelleh, Rainer Heintzmann, and Heinrich Leonhardt. *A guide to super-resolution fluorescence microscopy*. 2010.

[87] Lothar Schermelleh et al. *Super-resolution microscopy demystified*. 2019.

[88] Yasir J. Sepah et al. "Fundus autofluorescence imaging: Fundamentals and clinical relevance." In: *Ophthalmological Imaging and Applications*. 2014.

[89] Sapna A. Shroff, James R. Fienup, and David R. Williams. "Lateral superresolution using a posteriori phase shift estimation for a moving object: experimental results." In: *Journal of the Optical Society of America A* 27.8 (2010).

[90] Sapna A Shroff, James R Fienup, and David R Williams. "Phase-shift estimation in sinusoidally illuminated images for lateral superresolution." In: *Journal of the Optical Society of America. A, Optics, image science, and vision* 26.2 (2009).

[91] Mandeep Singh and Kedar Khare. "Accurate efficient carrier estimation for single-shot digital holographic imaging." In: *Opt. Lett.* 41.21 (Nov. 2016).

[92] G S Sokolovskii et al. "Influence of the axicon characteristics and beam propagation parameter M2 on the formation of Bessel beams from semiconductor lasers." In: *Quantum Electronics* 43.5 (May 2013).

[93] Soummer et al. "Fast computation of Lyot-style coronagraph propagation." In: *The Astrophysical Journal Supplement Series* 167 (2006).

[94] Ernst H.K. Stelzer. "Light-sheet fluorescence microscopy for quantitative biology." In: *Nature Methods* (2014).

[95] Florian Ströhl and Clemens F Kaminski. "Speed limits of structured illumination microscopy." In: *Opt. Lett.* 42.13 (July 2017).

[96] E.H. Synge. "XXXVIII. A suggested method for extending microscopic resolution into the ultra-microscopic region." In: *The London, Edinburgh, and Dublin Philosophical Magazine and Journal of Science* (1928).

[97] Makio Tokunaga, Naoko Imamoto, and Kumiko Sakata-Sogawa. "Highly inclined thin illumination enables clear single-molecule imaging in cells." In: *Nature Methods* 5.2 (Feb. 2008).

[98] Bernard Valeur and Mário N. Berberan-Santos. *A brief history of fluorescence and phosphorescence before the emergence of quantum theory*. 2011.

[99] Karel Van Acoleyen et al. "Off-chip beam steering with a one-dimensional optical phased array on silicon-on-insulator." In: *Optics Letters* 34.9 (May 2009).

[100] A. H. Voie, D. H. Burns, and F. A. Spelman. "Orthogonal-plane fluorescence optical sectioning: three-dimensional imaging of macroscopic biological specimens." In: *Journal of Microscopy* 170.3 (1993).

[101] Feifei Wei and Zhaowei Liu. "Plasmonic structured illumination microscopy." In: *Nano Letters* 10.7 (2010).

[102] K Wicker and R Heintzmann. "Resolving a misconception about structured illumination." In: *Nature Photonics* 8.5 (2014).

[103] Kai Wicker. "Non-iterative determination of pattern phase in structured illumination microscopy using auto-correlations in Fourier space." In: *Opt. Express* 21.21 (Oct. 2013).

[104] Kai Wicker et al. "Phase optimisation for structured illumination microscopy." In: *Optics Express* 21.2 (2013).

[105] Yicong Wu and Hari Shroff. *Faster, sharper, and deeper: structured illumination microscopy for biological imaging*. 2018.

[106] Xuejun Xu et al. "An investigation of the mode characteristics of SOI submicron rib waveguides using the film mode matching method." In: *Journal of Optics A: Pure and Applied Optics* (2009).

[107] M Yanoff, J S Duker, and J J Augsburger. *Ophthalmology*. An expert consult title online + print. Mosby Elsevier, 2009.

[108] Laurence J Young, Florian Ströhl, and Clemens F Kaminski. "A Guide to Structured Illumination TIRF Microscopy at High Speed with Multiple Colors." In: *Journal of visualized experiments : JoVE* 111 (2016).

[109] X. C. Yuan et al. "Direct electron beam writing of kinoform micro-axicon for generation of propagation-invariant beams with long non-diffracting distance." In: *Journal of Optics A: Pure and Applied Optics* 9.4 (2007).